

Online monitoring & mitigation of voltage instability in transmission and distribution systems using synchrophasors

by

Amarsagar Reddy Ramapuram Matavalam
(A R Ramapuram Matavalam)

A dissertation submitted to the graduate faculty

in partial fulfillment of the requirements for the degree of

DOCTOR OF PHILOSOPHY

Major: Electrical Engineering

Program of Study Committee:
Venkataramana Ajarapu, Major Professor
Ian Dobson
Govindarasu Manimaran
Umesh Vaidya
Chinmay Hegde

The student author, whose presentation of the scholarship herein was approved by the program of study committee, is solely responsible for the content of this dissertation. The Graduate College will ensure this dissertation is globally accessible and will not permit alterations after a degree is conferred.

Iowa State University

Ames, Iowa

2019

TABLE OF CONTENTS

	Page
LIST OF FIGURES	vi
LIST OF TABLES	xii
ACKNOWLEDGMENTS	xiv
ABSTRACT	xviii
CHAPTER 1. GENERAL INTRODUCTION	1
1.1 Voltage Stability in Power Systems	1
1.1.1 Fault Induced Delayed Voltage Recovery.....	3
1.1.2 Long Term Voltage Stability.....	5
1.2 The Requirements, Opportunities & Challenges for Online Monitoring and Control of Voltage Stability	7
1.2.1 Research Objectives	10
1.3 Research Contributions.....	10
1.3.1 Fault Induced Delayed Voltage Recovery Monitoring & Control	10
1.3.2 Long Term Voltage Stability Monitoring & Control	11
1.4 Thesis Organization.....	12
1.5 References	14
CHAPTER 2. LITERATURE SURVEY	16
2.1 Fault Induced Delayed Voltage Recovery.....	16
2.1.1 Dynamic VAR Planning Based Methods.....	16
2.1.2 Online Measurement Based Methods.....	18
2.1.2.1 Voltage Based Monitoring & Control.....	18
2.1.2.2 Load Model Based Monitoring & Control.....	18
2.1.2.3 Controlling Distribution System Devices to Prevent Instability.....	19
2.2 Long Term Voltage Stability Monitoring.....	19
2.2.1 PV Curve Tracing.....	20
2.2.2 Boundary Tracing in Parameter Space.....	21
2.2.3 Online Measurement Based Methods.....	21
2.2.3.1 Local Thevenin Equivalent Based Methods	22
2.2.3.2 Centralized Thevenin Equivalent Based Methods	22
2.2.3.2 Other Centralized Methods	23
2.2.3.3 Machine Learning Based Methods	23
2.3 References	24
CHAPTER 3. PMU BASED MONITORING AND MITIGATION OF DELAYED VOLTAGE RECOVERY USING ADMITTANCES	28
Abstract.....	28
3.1 Introduction	29
3.2 Examination of the WECC Composite Load Model	30

3.2.1	3-Phase Motor Modelling.....	31
3.2.2	1-Phase Motor Modelling.....	33
3.3	Online Monitoring of FIDVR using Measurements.....	35
3.3.1	Comparison of the behavior of load admittance and voltage during delayed voltage recovery.....	40
3.4	Admittance Based Analysis of Composite Load Model	44
3.4.1	Time to Initiate Thermal Tripping of 1-Phase Motor.....	45
3.4.2	Time to complete thermal disconnection of 1-phase motor	46
3.4.3	Estimating individual component conductance from measurements	48
3.4.4	Discussion on the relation between t_1 , t_2 and admittance.....	51
3.4.5	Disconnecting AC motors to recover from FIDVR	53
3.5	Numerical Results for the IEEE 162 Bus System	56
3.6	Real-Time Cyber-Physical Test-Bed Implementation	64
3.7	Conclusion	68
3.8	References	69

CHAPTER 4. MONITORING & MITIGATION OF DELAYED VOLTAGE RECOVERY IN DISTRIBUTION NETWORKS USING μ PMU

MEASUREMENTS.....	71
Abstract.....	71
4.1 Introduction	72
4.2 Analysis & Recovery Time Estimation of FIDVR.....	73
4.2.1 Time to initiate motor disconnection.....	76
4.2.2 Time to complete motor disconnection	76
4.3 Reduced Distribution System Model.....	77
4.4 Mitigation of FIDVR using DERs and Load Control.....	80
4.4.1 Ensuring voltage recovery beyond a single voltage close to pre-fault voltage	80
4.4.2 Ensuring voltage recovery satisfies fault-ride through requirements.....	83
4.5 Numerical Results on Test System.....	87
4.5.1 Recovery time estimation for monitoring FIDVR	90
4.5.2 Control to ensure voltage recovery close to pre-fault voltage.....	91
4.5.3 Ensuring voltage recovery satisfies voltage-ride through	95
4.6 Conclusion	99
4.7 References	100

CHAPTER 5. DATA DRIVEN LINEAR APPROXIMATION OF THE 3-PHASE INDUCTION MOTOR FOR STABILITY MONITORING APPLICATIONS

Abstract.....	103
5.1 Introduction	104
5.2 Operator Theoretic Description of Dynamical Systems.....	106
5.2.1 Comparison between Koopman linear representations & standard linearization	109
5.3 Data Driven Linear Model Estimation of Induction Motor.....	113
5.3.1 Data generation for learning the linear model.....	113
5.3.2 Validation of the linear model behavior.....	115
5.4 Application of Linear Model of Induction Motor	121

5.4.1	Estimating the rotor speed from admittance measurements.....	121
5.4.2	Estimating fraction of 1-phase motor stalling	123
5.5	Conclusion	124
5.6	References	125
CHAPTER 6. SENSITIVITY BASED THEVENIN INDEX WITH SYSTEMATIC INCLUSION OF REACTIVE POWER LIMITS		126
	Abstract.....	126
6.1	Introduction	127
6.2	Sensitivity Based Thevenin Index	128
6.2.1	Analytical Validation of Sensitivity Based Thevenin Index	133
6.2.2	Numerical Validation of the Sensitivity Based Thevenin Index	134
6.2.2.1	Small 5-Bus system.....	134
6.2.2.2	IEEE 30-Bus System.....	137
6.2.2.3	MATPOWER 3120 Bus System.....	141
6.2.2.4	Performance of STI and LTI in the presence of noise	142
6.2.3	Consequences of the Equivalence between LTI and STI.....	146
6.3	Predicting the Impact of Reactive-Limits on STI & LTI	148
6.3.1	Numerical Validation of STI Including the Generator Reactive Limits ..	152
6.4	Feasibility of Implementing STI in Practical EMS Software.....	157
6.5	Conclusion	158
6.6	References	159
CHAPTER 7. MONITORING LONG TERM VOLTAGE INSTABILITY DUE TO DISTRIBUTION & TRANSMISSION INTERACTION USING UNBALANCED μ PMU & PMU MEASUREMENTS		161
	Abstract.....	161
7.1	Introduction	162
7.2	Impact of Distribution Network on Voltage Stability Indicator at the Transmission Network.....	163
7.2.1	Estimation of Equivalent Circuit Parameters from PMU & μ PMU Measurements for 1 ϕ Circuits	167
7.3	3 Φ Voltage Stability Indicator and Transmission-Distribution Distinguishing Index.....	168
7.3.1	A. Discussion on Load Model.....	171
7.3.2	Validating Results on Unbalanced Load	172
7.3.3	Transmission-Distribution Distinguishing Index	175
7.4	Estimation of Thevenin Equivalent Parameters using PMU and μ PMU Measurements	176
7.4.1	PMU and μ PMU Placement in TN and DN.....	179
7.5	Numerical Results.....	181
7.5.1	Simulation and Validation Setup.....	181
7.5.2	Small Test Case: 9 bus TN + 13 node DN	182
7.5.3	Larger Test Case: 30 bus TN + 37 node DN.....	186
7.6	Conclusion	190
7.7	References	191

CHAPTER 8. GENERAL CONCLUSION	194
8.1 Overall Conclusions	194
8.2 Overall Contributions	197
8.2 Possible Extensions of Work	200
8.4 Publications	201
8.4.1 Journals.....	201
8.4.2 Conferences	201
 APPENDIX A. WASSERSTEIN METRIC BASED QUANTIFICATION OF FIDVR.....	 203
 APPENDIX B. COMPARISON OF POWER BETWEEN VARIOUS MOTORS DURING FIDVR	 208
 APPENDIX C. COMPOSITE LOAD MODEL PARAMETERS.....	 209
 APPENDIX D. REAL-TIME TEST-BED RESULTS	 210

LIST OF FIGURES

	Page
Figure 1.1 Classification of power system stability [3]	1
Figure 1.2 Conceptual delayed voltage recovery waveform at a bus	4
Figure 1.3 Recorded delayed voltage recovery waveform at a 115kV bus in Southern California on July 24, 2004 [13]	5
Figure 1.4 Variation of load voltage as the loading increases. The power grid cannot operate after the critical loading.	7
Figure 1.5 The location of PMU devices in the North American Grid in 2007 and 2013 [21].	9
Figure 3.1 Structure of the composite load model [9].	30
Figure 3.2 Standard model of the 3-Phase Induction Motor.....	31
Figure 3.3 The variation in motor speed when the voltage and the load are reduced	32
Figure 3.4 Active power (left) and Reactive power (right) versus the voltage for the normal and stalled operation for the 1- ϕ induction motor [9].	33
Figure 3.5 The thermal protection logic implemented in the composite load model	34
Figure 3.6 WECC Voltage Performance Criteria [11].....	35
Figure 3.7 Proposed WECC voltage ride-through envelope for generators [11]	36
Figure 3.8 The Voltage time series and the PDF for the voltage series in along with a voltage reference PDF in green [12]......	38
Figure 3.9 The voltage time series at the bus with increasing percentage of induction motor load. The dashed line is the reference voltage.	39
Figure 3.10 The Moving KL-Index of the delayed voltage waveforms. The more the delayed the voltage, the faster the index goes to 0.	39
Figure 3.11 Voltage response with various motor stalling proportion	42
Figure 3.12 Load conductance with various motor stalling proportion. t1 & t2 are indicated for fmD = 0.3	42

Figure 3.13	Flowchart of the expected method to monitor and mitigate FIDVR.....	43
Figure 3.14	Admittance based composite model structure.....	44
Figure 3.15	Flowchart for detecting and monitoring FIDVR using measurements	51
Figure 3.16	The variation of the load and its composition over the course of a day in Portland in July [14]......	53
Figure 3.17	Idealized behavior of the susceptance during FIDVR with AC disconnection.....	54
Figure 3.18	Voltage at Bus 135 for $fmD = 0.10$ to $fmD = 0.45$ with fault at 1s.....	58
Figure 3.19	Load conductance for $fmD = 0.10$ to $fmD = 0.45$ with fault at 1s.....	58
Figure 3.20	Conductance of the components of the CMLD model for $fmD = 0.3$	59
Figure 3.21	Estimated and actual stall conductance for $fmD = 0.15, 0.3$ & 0.45	60
Figure 3.22	Voltage at Bus 135 with and without load control.....	64
Figure 3.23	The lab setup of the real-time cyber-physical test-bed with the various components – Opal-RT, PMU, OpenPDC, Python, OPC.	66
Figure 3.24	The delayed voltage response (left) and the corresponding susceptance plot (right).....	68
Figure 4.1	The structure of the composite load model [14].....	74
Figure 4.2	The simplified composite load model during FIDVR.....	75
Figure 4.3	Radial distribution system with μ PMUS installed in some nodes [17].....	78
Figure 4.4	(a) Generic reduced distribution system model. (b) Sub-model. [17].....	79
Figure 4.5	Example plot for the VRT requirements of DER inverters in distribution system.....	84
Figure 4.6	Flowchart for monitoring and mitigating online FIDVR in distribution systems	87
Figure 4.7	Test system used to validate proposed methodology. The areas in the distribution system are shaded and the red nodes are the μ PMU locations.....	88
Figure 4.8	Voltages at the substation and at μ PMUs for a fault at node 701	89

Figure 4.9 Voltage at node 709 for various faults in the DS	91
Figure 4.10 Voltage at node 709 for various control actions for fault at node 740	93
Figure 4.11 Impact of optimal control to improve voltage for fault at node 740	94
Figure 4.12 Comparison between actual voltage trajectory and estimated voltage trajectory using linear sensitivities for different amounts of A/C load control.....	96
Figure 4.13 Impact of controls on the voltage trajectory and the corresponding VRT. The controls are able to ensure that the voltage recovery satisfies the VRT requirements	98
Figure 4.14 Impact of controls on the voltage trajectory at all the nodes in the system.....	99
Figure 5.1 Comparison of x_1 for the true system, linearized system and the Koopman linear representation starting from the initial condition [1.5, -1].....	111
Figure 5.2 Comparison of x_2 for the true system, linearized system and the Koopman linear representation starting from the initial condition [1.5, -1].....	112
Figure 5.3 Variation of the inputs to the linear model used for validation for the data-driven model.....	117
Figure 5.4 Comparison between the true and estimated rotor speed from the reconstruction of the data-driven linear system.....	117
Figure 5.5 Comparison in the 1 st 5 seconds between the true and estimated rotor speed from the reconstruction of the data-driven linear system.....	118
Figure 5.6 Comparison in the 1 st 5 seconds between the motor conductance outputs of the full model and the estimated outputs from the data-driven linear system.....	118
Figure 5.7 Comparison between the true and estimated rotor speed from the reconstruction of the data-driven linear system when starting outside the training region.....	119
Figure 5.8 Comparison in the 1 st 5 seconds between the true and estimated rotor speed from the reconstruction of the data-driven linear system when starting outside the training region	119

Figure 5.9	Variation of the inputs to the linear model used for validation to initiate stalling in the data-driven model	120
Figure 5.10	Comparison between the true and estimated rotor speed from the reconstruction of the data-driven linear system when stalling occurs.....	120
Figure 5.11	Comparison in the 1 st 5 seconds between the true and estimated rotor speed from the reconstruction of the data-driven linear system when stalling occurs.....	120
Figure 5.12	Comparison in the 1 st 5 seconds between the true and estimated rotor speed from the reconstruction	122
Figure 5.13	Comparison in the 1 st 5 seconds between the true and estimated rotor speed from the reconstruction	122
Figure 6.1	The reduction of the rest-of-the-system into an equivalent Zth and Eth	128
Figure 6.2	A PV curve indicating that the slope of tangent at a point, A, is between the slope of secants, AB ($\Delta\lambda < 0$) and AC ($\Delta\lambda > 0$).	132
Figure 6.3	The single line diagram 5 Bus system with details of the Generator data, Load data & Line data in 100 MVA base.....	135
Figure 6.4	The STI and LTI at Bus 3 versus the system load for various $\Delta\lambda$ in the 5-Bus system. The STI always lies between LTI (0.02) and LTI(-0.02)....	135
Figure 6.5	The STI and LTI at Bus 30 for various $\Delta\lambda$ in the 30-Bus system versus load. The STI is between the LTI with $\Delta\lambda > 0$ & $\Delta\lambda < 0$	137
Figure 6.6	Scatter plot of the LTI versus the STI for various $\Delta\lambda$ at non-zero load buses in the 30-Bus system at load of 330 MW.	139
Figure 6.7	Scatter plot of the LTI versus the STI for various $\Delta\lambda$ at non-zero load buses in the 30-Bus system at load of 760 MW.	140
Figure 6.8	The STI and LTI versus the load at Bus 3111 for various $\Delta\lambda$ in the MATPOWER 3120-Bus system.....	141
Figure 6.9	Scatter plot of the LTI ($\Delta\lambda = 0.05, 0.02, -0.02$ & -0.05) versus the STI at all load buses in the 3120-Bus system 45 GW load.	142
Figure 6.10	The upper limits and lower limits of STI and LTI versus the noise level ϵ_{max} for the 30 Bus system at a system loading of 600 MW with a $\Delta\lambda$ of 0.2%.	144

Figure 6.11 Behavior of the LTI and STI over 300s of operation with $\epsilon_{\max} = \pm 0.0002$ p.u. for the 30 Bus system at a system loading of 600 MW with a $\Delta\lambda$ of 0.2%.	145
Figure 6.12 The STI for the 30 Bus system at a system loading of 600 MW with noise level ± 0.001 p.u and ± 0.0002 p.u.	146
Figure 6.13 The LTI at Bus 3 and 4 as the system load increases in the 5-Bus system. Both the LTI approach 1 at the critical system loading.	147
Figure 6.14 PV Curve of Bus 3 in the 5-Bus system with Reactive Limits enforced. The slope of the tangent changes abruptly when a generator Q-limit is reached.....	149
Figure 6.15 The STI and LTI at Bus 3 for various $\Delta\lambda$ in the 5-Bus system with Reactive Limits enforced. The STI always lies between LTI (0.02) and LTI(-0.02).....	150
Figure 6.16 Comparison between STI ₃ , STI ₃ (1) & , STI ₃ (2) in the 5-Bus system with Q-limits enforced. STI ₃ (1) & STI ₃ (2) can predict the change in STI ₃ when Gen-1 (Gen-2) reaches the reactive limit.....	154
Figure 6.17 Comparison between STI ₃₀ & STI ₃₀ (u) for IEEE 30-Bus system with reactive limits enforced. STI ₃₀ (u) is greater than or equal to STI ₃₀ , even when limits are reached.	156
Figure 7.1 Structure of the conventional Thevenin Equivalent	164
Figure 7.2 Structure of the Thevenin Equivalent including distribution network	165
Figure 7.3 Variation of VSI_T and VSI_D versus load for case-1 in Table 7-1	166
Figure 7.4 Voltage versus total load power with unbalanced load scenario-1	173
Figure 7.5 Voltage versus total load power with unbalanced load scenario-2	174
Figure 7.6 Voltage versus total load power with unbalanced load scenario-3	174
Figure 7.7 Voltage versus total load power with unbalanced load scenario-4	174
Figure 7.8 $VSI_{D-3\phi}$ versus total load power for the load scenarios in Table 7-2.....	175
Figure 7.9 Conceptual example showing the proposed methodology splitting TN & DN so that each load μ PMU + substation PMU has a separate equivalent circuit	177

Figure 7.10	Flowchart using the measurements to estimate $VSI_{D-3\phi}$ and TDDI.....	180
Figure 7.11	Co-simulation methodology between Pypower and GridlabD.....	182
Figure 7.12	Topology of the 9 bus TN and 13 node DN	183
Figure 7.13	$VSI_{D-3\phi}$ at DN-675 at TN 5 & VSI_T at TN 5 v/s load scaling for case 1	184
Figure 7.14	TDDI at DN-675 at TN 5 v/s load scaling for various cases.....	186
Figure A.1	The voltage at the bus with increasing percentage of IM load along with the reference voltage waveform.	205
Figure A.2	The Wasserstein metric based Index of the FIDVR waveforms. The more severe the FIDVR, the faster the index reaches 0.	206
Figure A.3	The Wasserstein metric based Index of the FIDVR waveforms using a moving time windows of 3s.	207
Figure D.1	Comparison between the voltage at Bus 5 in (a) PSSE, (b) RTDS, (c) PMU and (d) Matlab.....	210
Figure D.2	Delayed voltage response (top) and the corresponding W-index (bottom) vs the time in samples (60 samples per sec).....	211
Figure D.3	Voltage instability event (top) and the corresponding Lyapunov Exponent (bottom) vs the time in sample (60 samples per sec).	212

LIST OF TABLES

	Page
Table 3-1 Actual and estimated G_{stall} , t_1 & t_2 with varying 1- ϕ IM proportion.....	61
Table 3-2 Error in prediction of t_1 & t_2 using linear regression.....	62
Table 3-3 Time to recover from FIDVR event in the PSSE simulations by tripping fraction of AC's.....	63
Table 4-1 Various load parameters of the sub-models in an RDSM.....	79
Table 4-2 Sub-model parameters of the load areas.....	89
Table 4-3 Comparison between the actual and estimated recovery times.....	91
Table 4-4 Comparison between the actual and estimated recovery time improvement for various control actions for fault at node 740.....	92
Table 4-5 Comparison between various control actions to improve the voltage recovery with different control constraints for fault at node 740.....	94
Table 4-6 Comparison between the maximum voltage error at different nodes for different amounts of A/C load control.....	96
Table 4-7 Comparison between the amount of load disconnected for the various control constraints and VRT criteria.....	99
Table 5-1 The IM parameters for validation of the linear model.....	116
Table 5-2 The actual and estimated stall proportions using the linear model.....	124
Table 6-1 Comparison of STI and LTI at Total Load of 1000 MW for the 5-Bus system.....	136
Table 6-2 Comparison of STI and LTI at Total Load of 1700 MW for the 5-Bus system.....	137
Table 6-3 Comparison of the STI and the LTI at a few buses in the IEEE 30-Bus system for a system load of 330 MW.....	138
Table 6-4 Comparison of STI3, STI3(1) & STI3(2) for different load levels in the 5-Bus system.....	153
Table 7-1 Various cases and the corresponding P_{crit} , VSI_{T-crit} & VSI_{D-crit}	166

Table 7-2	Network parameters for validating the $VSI_{D-3\phi}$ for unbalanced load	172
Table 7-3	Feeder configuration at various TN buses and critical load	183
Table 7-4	$VSI_{D-3\phi}$ and TDDI at the critical DN node at different TN buses	185
Table 7-5	Increment in critical load for var injection and line addition	186
Table 7-6	Feeder configuration at various TN buses and critical load	187
Table 7-7	$VSI_{D-3\phi}$ at the critical DN node in feeders at different TN buses	188
Table 7-8	TDDI at the critical DN node in feeders at different TN buses.....	188
Table 7-9	Increment in critical load for var injection at various TN buses	189
Table B-1	Power distribution between the various components of the composite load model before and after the fault.....	208
Table C-1	Parameters of the CMLD model for the simulation results in Section 3.5 ...	209

ACKNOWLEDGMENTS

My journey at Iowa State University began six years ago, and there are many people that I would like to thank who have constantly helped and supported me. Without their encouragement, it would have been impossible to complete my Ph.D. successfully.

First and foremost, I would like to express my sincere gratitude to my major professor, Dr. Venkataramana Ajjarapu, for providing me the opportunity to pursue a Ph.D. in his group. I am immensely thankful for his mentoring, his willingness to share knowledge and the freedom to explore various topics during my time in his group that have helped me grow as a researcher. I am also thankful for the support he has provided for attending conferences and meetings to disseminate my work to the wider community and to interact with others in related fields. He will be an ideal that I aspire to for the rest of my career and I hope I can live up to the high standards that he has instilled in me.

I would like to thank Dr. Umesh Vaidya and Dr. Ian Dobson for their regular valuable inputs and guidance. The resources and insights they have provided me in the dynamical systems and power systems fields have greatly helped with my research. I would also like to thank Dr. Govindarasu Manimaran for involving me in his cyber physical test-bed research and Dr. Chinmay Hegde for taking timeout to discuss data-analytics methods and their possible applications to my work. I would like to acknowledge the professors at Iowa State, who instilled the thrill of researching in me and trained me with the skill set to pursue research.

I am also thankful to the ECpE department and Iowa State University for providing me with such a wonderful and enriching atmosphere for carrying out quality research. I would like to thank the staff members at the department of ECpE, for helping with all the

paperwork (especially the reimbursements!) and making my journey smooth. Thank you Vicky, Barbara, Judy, Nadine, Samantha and Sara.

My experience with the Preparing Future Faculty program at Iowa State University has been extremely valuable due the vision and hard work of two extremely talented and generous people, Karen Bovenmeyer and Dr. Holly Bender. Thank you for organizing excellent workshops each week on very relevant topics to the life in academia.

I am very grateful to have a close-knit research group during my time at Iowa State University, and I would not have been able to finish this journey without their support and friendship. The innumerable number of discussions and seminars have always kept me motivated, and helped me to keep my graduate student life exciting. I thank all of my peers with whom I collaborated in various topics over the years at ISU. I would like to specially thank Magesh, Shiyang, Guangchao, Ashraf, Rama, Ekmen, Jorge and Ankit for their collaborations in various projects. I am pleased to express my gratitude to Pranav, Alok, Qian and Nick for their support in a number of ways. I am thankful to my other research group colleagues Atena, Lina, Shikha, Rishi, Santiago, Helena, Armando, Amit, Sambrata, Bowen, Siddharth, Aditya, Abhinav, Xian, Sai, Venkatesh, Gauri, Praneeth and Xu Ma. I am specifically thankful to reach group members of the PowerCyber lab - Vivek, Pengyuan, Krishnan and Gelli and all other former/ current group members for their support during this work.

Words cannot express my emotions and it is almost impossible for me to verbalize my friendship to Srikanth, Arpa, Abhishek, Jyothsna, Prathamesh, Tejaswi, Sunny, Pratyush. Sadhya, and Swetabh. Without their company, my journey would not have been so much gratifying and I would have found it extremely difficult to wade through the highs

& lows of my stay in Ames. I am forever grateful to these awesome folks – Santosh, Mehul, Rohit, Yash, Neel, Rohan, Rucha, Apoorva, Harita, Ashwini, Shubhra, Radhika, Rajat, Debarpan, YKC, Gauri, Viraj, Pranav, Aahilan, Sudarshan, Lalitha, Aishwaria , Amrit, Ravi, Harsha, Kiran, Karthik and Sankalp volunteers. I would also like to take this opportunity to thank my undergraduate friends – Hareen, Tejaswi, Shravan, Ujjwal, Akhil, Kshitij, Amrit, Nikhil, Krishnagiri, Sharath, ATM, Bhagat, Mudit, Gaurav, Sundar, Deepan, Shankar, CSLV and Rakesh, for their devoted and lasting friendship.

A special shout out goes to the members and the advisors of the various student organizations I have been involved in during the past few years. Thank you Sankalp, Indian Student Association, PunkPunditz and Hindu Yuva for organizing activities and events for me to get together with my friends and making sure I do not miss home. Also, a special mention goes to Dr. Athreya and the rest of the Indian Cultural Association of Ames and to the Kannada Sangha in Ames who made me feel at home by organizing cultural programs and family get-togethers with delicious Indian food! ☺

I wish to express my highest appreciation to my parents, Durga Reddy and Vidyasagar Reddy, and my brother, Lalitsagar Reddy, for their unconditional love and support and for always believing in me. The journey would not have been possible without my family. It is only because of their teachings and guidance that I could achieve what I have. I would also like to thank my grandparents, my extended family and friends, who have played a significant role in shaping me into what I am today.

Financial support from National Science Foundation, Department of Energy and Power Systems Engineering Research Center is gratefully acknowledged. The travel grant from PSERC enabled me to interact with industry members in a regular basis and has made

me think of the practical considerations in my research and expanded my world-view.

Thank you PSERC for this wonderful opportunity!

Finally, I would like to apologize to anyone whom I overlooked to thank here and who helped in any possible way for me to be where I am today.

ABSTRACT

With the increasing need for economic operation of the power grid, the system is being operated closer to their limits and there is a need to address the increasing risk of voltage instability in the power grid. In this thesis, methods that can monitor and mitigate the both short-term and long-term voltage instability by utilizing Phasor Measurement Units (PMUs), controllable loads and distributed energy resources are proposed.

In the first part of the thesis, the fault induced delayed voltage recovery (FIDVR) phenomenon is studied. The FIDVR phenomenon is monitored by the load admittance at the substation PMU. The admittance provides the PMU at the substation with an estimate of the stalled motors and can be used to estimate the time to recovery and determine control actions for voltage recovery within a set amount of time. To test the real-time nature of the method, the FIDVR phenomenon is simulated in a real-time test-bed and is shown to be able to determine the control amount in an online manner. This methodology is extended to analyze FIDVR in distribution networks and to estimate the trajectory sensitivities in an online manner which are used in a linear formulation to result in a voltage recovery that prevent DER disconnection. Finally, In order to handle the dynamics of non-linear 3- ϕ motors, a data-driven surrogate linear dynamical model is estimated from data which is used to monitor both 1- ϕ and 3- ϕ motors for short term voltage instability.

In the second part of the thesis, the long term voltage stability phenomenon is studied. A Sensitivity based Thevenin Index (STI) which uses PMU data and (linear) state estimator data is proposed to monitor long term voltage stability. This sensitivity base index can be modified to account for various what-if scenarios (reactive limit reached, line outage, etc.) in a computationally efficient manner. Finally, A 3 ϕ long-term voltage

stability indicator (VSI) using the idea of a 3 ϕ Thevenin equivalent that can identify critical loads in an unbalanced multi-phase system is proposed to account for the impact of distribution networks to long term voltage instability. The estimation of the 3 ϕ Thevenin equivalent is formulated as a convex optimization using PMU & μ PMU measurements, making it possible to calculate VSI in a model-free online manner.

CHAPTER 1. GENERAL INTRODUCTION

1.1 Voltage Stability in Power Systems

Power systems of the future are likely to become more stressed due to the recent trends of (i) large network interconnections and power transfer behavior, (ii) deregulation of the markets giving priority to economic operations, and (iii) integration of renewable energy that are distant from load centers. Due to these evolving behavior of the grid operation, power system voltage stability, which is inherently related to the maximum loading of the system, has become an important phenomenon of interest in the power system community and has been the focus of intense research during the past few decades [1, 2]. An IEEE/CIGRE joint task force [3] proposed various definitions related to power system stability, including voltage stability, and Figure 1.1 summarizes the classification of power system stability. Based on the physical nature of the instability, disturbance size and the time frame; the power system stability is broadly classified into rotor angle stability, frequency stability and voltage stability.

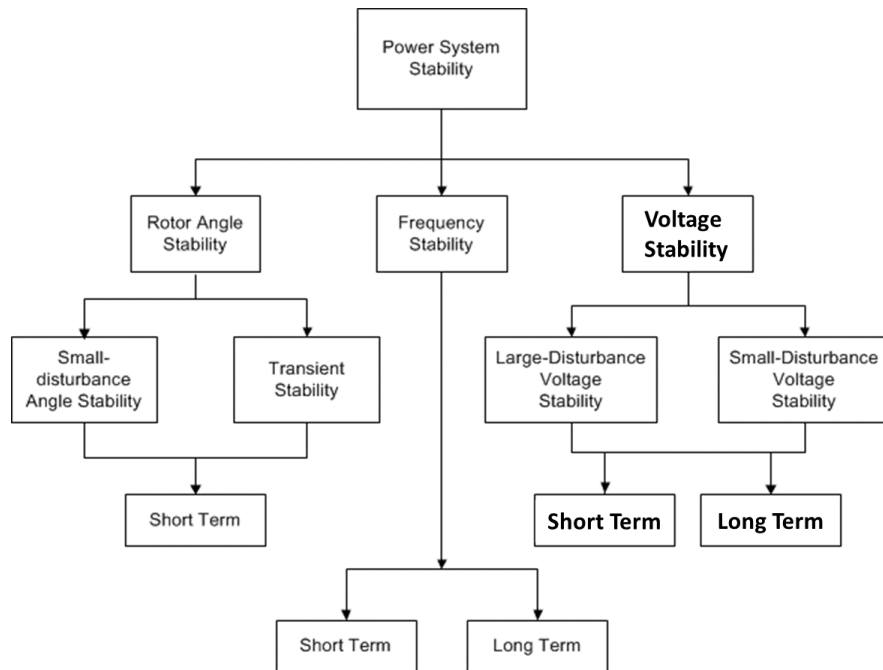


Figure 1.1 *Classification of power system stability [3]*

Voltage stability is defined as the ability of the system to maintain steady voltages at all buses in the system following a disturbance. Voltage instability could lead to progressive rise or fall of voltages at different buses. Based on the type of disturbance, the voltage stability problem can be classified as small and large disturbance stability problem. Large disturbance voltage stability refers to the ability of system to maintain steady voltages when subjected to large disturbances such as three phase faults, loss of generators etc. Small disturbance voltage stability refers to the system's ability to maintain steady voltages when subjected to small perturbations such as incremental changes in the system load. Further, based on the time scale of the phenomenon, the voltage stability problem is classified as short-term and long-term stability problem. The study period of interest for short-term voltage stability problem is in the order of several seconds, and for long term voltage stability it extends to several minutes.

Possible consequences of voltage instability include loss of load in an area, transmission lines tripping and in the most severe cases with cascading, it may lead to a blackout. The term voltage collapse is used to describe "the process by which the sequence of events accompanying voltage instability leads to a blackout or abnormally low voltages in a significant part of the power system" [3]. Few large blackout events have been partially attributed to voltage instability or voltage collapse [4], [5], including the 2003 Northeast blackout that effected more than 50 million people [6]. Thus, to prevent the catastrophic blackouts caused by voltage collapse, various techniques to assess voltage stability and to avoid the instability through timely control are among the most important research tasks of power community. Furthermore, with the shifting behavior of the grid operation and structure, the problem of maintaining voltage stability will remain a challenge in the foreseeable future as well.

Another trend that has been recently observed in the power system community is the incorporation of new sensors in the power grid that are able to measure the voltage and current phasors at a node utilizing the time information in the Global Positioning System (GPS) signal. These devices are called Phasor Measurement Units (PMU), also called as Synchrophasors, and are capable of transmitting the calculated phasors at a high frame rate (up to 120 frames / second) to the control center and so these devices can provide much more visibility to the operator than traditional SCADA devices. Thus, utilizing these sensors for the purpose of voltage stability is of large interest to the power community and this field of study has progressed quite a bit in the past decade [7, 8].

Short-term voltage instability occurs mainly due to the stalling of induction motor loads, and can manifest in the form of fast voltage collapse or delayed voltage recovery. One form of voltage stability is the phenomena of Fault Induced Delayed Voltage Recovery (FIDVR) in which the recovery of the voltage after a disturbance is delayed, resulting in sustained low voltages for several seconds (>15 sec). This work focuses on how the phenomenon of short-term voltage stability, specifically the fault induced delayed voltage recovery (FIDVR), and long term voltage stability can be monitored and mitigated utilizing the capabilities of the PMU devices and the system model information. These phenomena are explained in detail in the next subsections.

1.1.1 Fault Induced Delayed Voltage Recovery

FIDVR is mainly caused in systems with a moderate amount (> 30%) of single phase induction motor (IM) loads. After a large disturbance (fault, etc.), these motors, that are connected to mechanical loads with constant torque, stall and typically draw 5-6 times their nominal current and this leads to the depression of the system voltage for a significant amount of time. The low voltages in the system inherently lead to some load being tripped by protection

devices close to the fault. However, even after this, the concern is that the sustained low voltages (>10 s) can lead to cascading events in the system steering towards a blackout. A typical delayed voltage response after a fault with various features is shown in Figure 1.1.

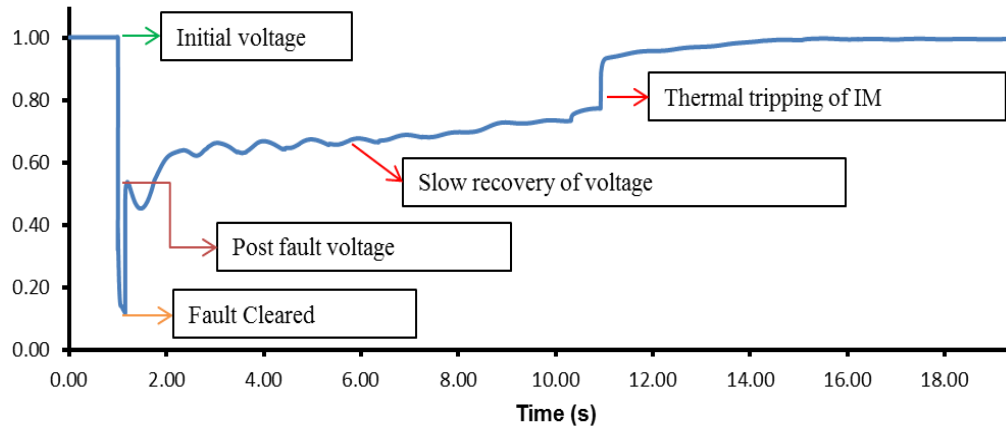


Figure 1.2 *Conceptual delayed voltage recovery waveform at a bus*

Most single phase induction motor are used in residential air-conditioners and so the FIDVR phenomenon has been historically observed in systems where a large number of residential AC's are operational (e.g. summer afternoon in California or Arizona). Most of these devices do not use Under Voltage protection schemes and are only equipped with the thermal protection with an inverse time-overcurrent feature, delaying the tripping upto 20s. Various U.S. utilities have reported experiencing delayed voltage recovery events on their systems, specifically during the summer season. FIDVR events have been observed in Southern California, Arizona, Texas, Florida, and the southeastern part of US [9, 10]. Numerous FIDVR events in the past have led to a significant loss of load [10, 11, 12]. Figure 1.3 shows an FIDVR event on a 115kV bus in Southern California on July 24, 2004. The sustained low voltage was likely caused by stalled AC IM's and the voltage finally recovered to pre-contingency voltage around 25s after the fault. A total of 400 MW of load out 960 MW is tripped by protection devices in residential and commercial units to recover the voltage.

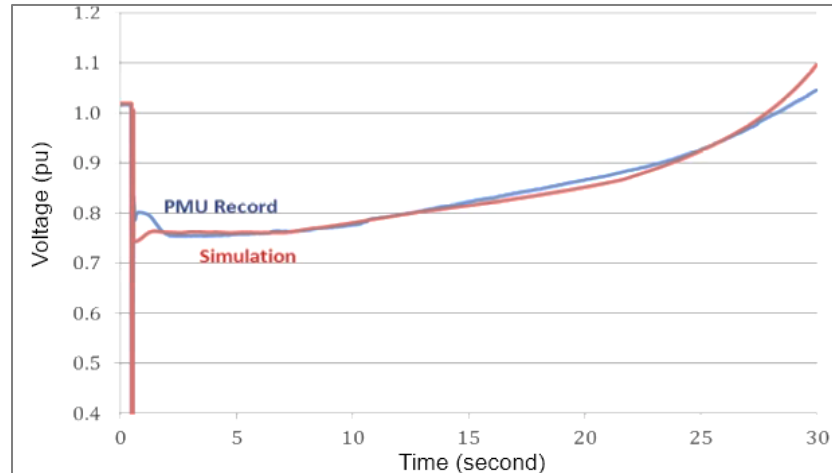


Figure 1.3 Recorded delayed voltage recovery waveform at a 115kV bus in Southern California on July 24, 2004 [13]

In recent years, Southern California Edison (SCE) has observed at least 37 FIDVR events in 2006 and six events during 2007 in its transmission system. The large number of events during 2006 was attributed to use of high AC load because of hot and humid weather conditions [11]. SCE continues to observe FIDVR events, especially during summer monsoonal season. In [14], SCE, in collaboration with Lawrence Berkeley National Lab (LBNL), captured FIDVR events using PQube power quality recorders in SCE's Valley sub-transmission network during 2012 and 2013 summer. An important conclusion is that FIDVR sometimes occurs locally in sub-transmission networks (caused by either lightning strikes, faults, etc.) and does not spread to the transmission system. Hence, it might be the case that the sub-transmission/distribution systems in the regions of California, Texas & Arizona might actually be observing a higher incidence of FIDVR the transmission system. Thus, mitigating this phenomenon is in the interest of the various utilities and reliability coordinators.

1.1.2 Long Term Voltage Stability

The long term voltage stability refers to the stability problems that occurs over a relatively long time frame, such as several minutes. It considers the stability in the long run as

loads slowly increase under various operating conditions and usually involve devices such as generator current limits, thermostatically controlled loads, tap-changing transformers, and voltage regulators that respond to system changes with large time delays (>5 min).

The power system is a nonlinear dynamic system and is generally formulated as a set of Differential-Algebraic equations (DAE). From the theory of singular perturbation and time-scale decomposition of the dynamics [15], while analyzing the long term voltage stability phenomenon, the fast dynamics can be reasonably represented by their equilibrium equations. Also, the dynamics occurring slower than the time scale of interest (load increase, etc.) can be ignored by converting the state variables into parameters that can be varied in the analysis.

A saddle-node bifurcation (SNB) occurs when two equilibrium points of the DAE system described above collide and annihilate each other as a parameter changes over a certain range. This bifurcation mode has been recognized as a major mechanism of voltage collapse in power systems. In the special case where the varying parameters are the load powers, the SNB, which corresponds to the long-term voltage stability critical point, is well approximated by the steady-state loading limit of the overall power system. Thus, it can be analyzed using the equilibrium equations, which are the algebraic non-linear power flow equations.

Thus from the discussion above, a major task of voltage stability analysis is voltage stability assessment which can estimate the voltage stability margin from a given operating point. This margin is determined as the largest increase in a particular parameter from the present operating point and still be able to find a solution to the power flow equations. As the definition implies, this margin is dependent on the parameter chosen to vary and it is standard practice to vary the load in the system for this study, providing us with a voltage stability margin. Figure 1.4 plots the variation in the voltage at a load bus for a simplified system as the

load increases. As the load is increased, it can be seen that the voltage starts to drop in a non-linear manner and after the critical load, there is no longer a viable power flow solution. As the parameter being varied is the load, the resulting margin is referred to as the load margin.

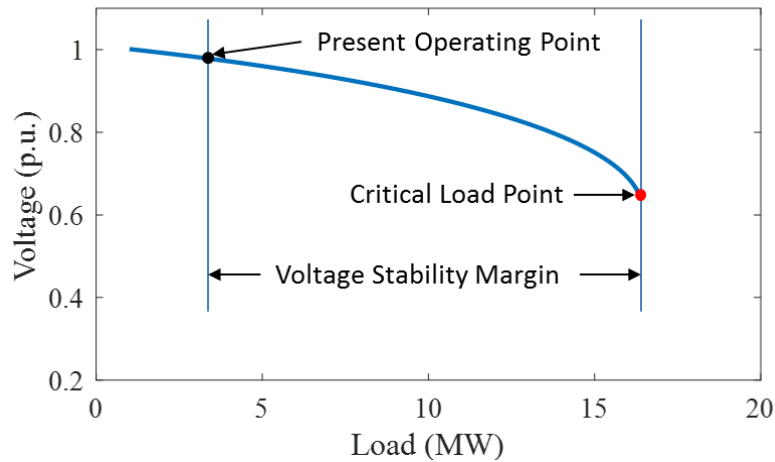


Figure 1.4 Variation of load voltage as the loading increases. The power grid cannot operate after the critical loading.

Since the power flow equations are non-linear, determining the load margin is a computationally expensive task, fast online indices that can quickly indicate how the qualitative distance of the present operating point from the critical load have been proposed [16, 17, 18] utilizing the various properties of the power flow equations. The literature survey in chapter 2 discusses the various indices and the need for a new index based on the idea of thevenin equivalents.

1.2 The Requirements, Opportunities & Challenges for Online Monitoring and Control of Voltage Stability

The NERC standard [19] requires the system operators and utilities to establish the System Operating Limits (SOLs) for power system operations, by requiring that “*the system shall demonstrate transient, dynamic and voltage stability; all Facilities shall be operating within their Facility Ratings and within their thermal, voltage and stability limits*”, under

normal condition or for a credible set of contingencies. These SOLs have been in use in the industry for a long time and operators have been utilizing these quantities to understand the system behavior quickly. However, the SOLs cannot provide quantitative information like VSM to show how far the system is from a voltage collapse. The Federal Energy Regulatory Commission (FERC) has also questioned the effectiveness of directly using the raw measurements, by pointing out that system operators cannot gain situational awareness by simply observing vast amounts of raw data. According to [20], “*while the requirements identify the data to be gathered, they fail to describe the tools necessary to turn that data into critical reliability parameters*”. Also, post-analyses of several blackout events have shown the benefits and the necessity of the adoption of better stability monitoring and control tools [6]. Thus, there is a need to develop tools that can convert the vast amounts of data present in the energy management system (EMS) into meaningful and actionable information that indicates voltage stability in an online manner.

One of the key technological developments that are enabling online applications for voltage stability assessment are Phasor Measurement Units (PMUs). These are measurement devices that are able to measure the phase of the voltage and current phasors at a node utilizing the time information in the Global Positioning System (GPS) signal. These devices send measurements to the control center at a rate of 120 frames/second, which enables them to be used for short-term and long-term voltage stability applications. Their deployment started after the 2003 Northeast blackout and at present there are ~2500 PMUs in North America [21], with various reliability coordinators receiving data in real-time from the grid. Figure 1.5 shows the increasing penetration of the PMU’s in the North American grid from 2007 to 2013 and this provides us an exciting opportunity for developing novel voltage stability assessment tools.

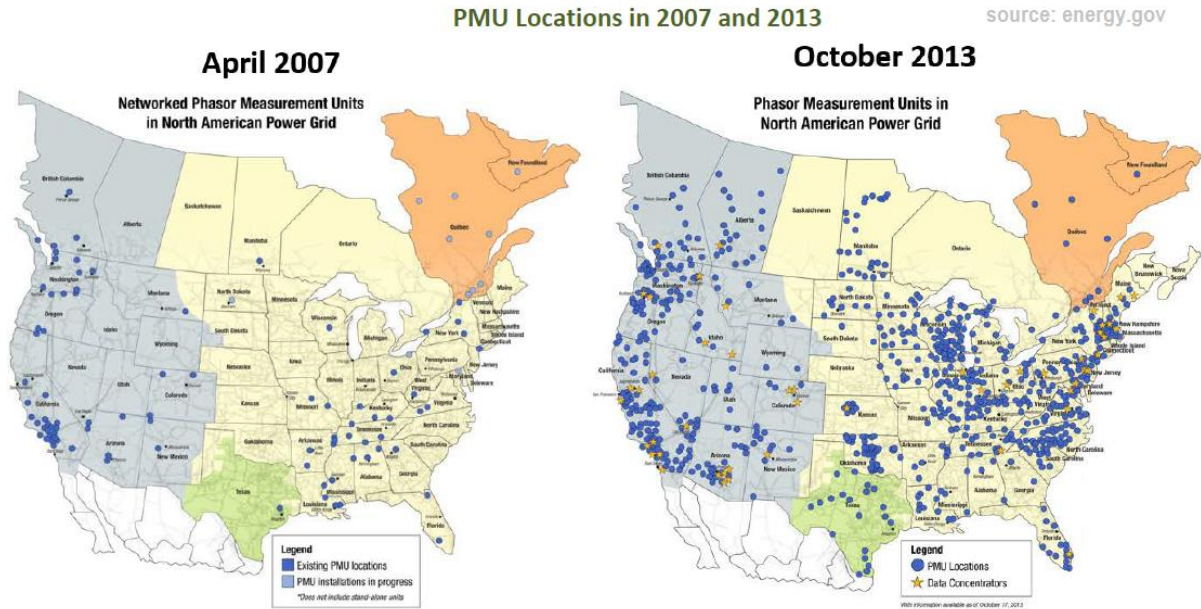


Figure 1.5 *The location of PMU devices in the North American Grid in 2007 and 2013 [21].*

A more recent development in the power system community is the increasing number of controllable devices in the distribution grid. Devices such as smart thermostats, distribution generators, and residential solar are becoming more commonplace, and power utilities are looking at various applications such as demand response and control of distribution energy resources to improve grid operation and to operate the grid in a more economical manner. Some controllable loads, such as air conditioners, can respond in a few seconds [22] as the customers will not observe the change. The collective response of these devices can be used by the short-term and long-term voltage stability tools to improve the system behavior after a large disturbance.

One of the key challenges involved in developing voltage stability assessment tools is the fidelity of the models being used. Depending on the load model being used, the dynamic response might vary, and so the techniques used to analyze a phenomenon might change based on the load model.

1.2.1 Research Objectives

1. To develop a PMU Wide Area Measurements (WAMS) based method to quantify and mitigate the phenomenon of FIDVR in an online manner by utilizing the information of the topology and the composition of dynamic loads.
2. To extend the methodology to monitor and mitigate FIDVR in distribution networks where a majority of the FIDVR events are reported to take place and the extended low voltages can lead to DERs disconnecting due to low voltage ride through requirements.
3. To incorporate the dynamics of 3-phase motors into the monitoring of FIDVR phenomenon when their under voltage relays are not present.
4. To develop an online methodology utilizing PMU measurements to reliably estimate an index for long term voltage stability. The method should be robust to malicious data and should be able to include the impact of generator reactive power limit.
5. Exploit the phasor measurement devices in the distribution networks and propose a measurement based index that can monitor the combined long term voltage stability of the overall transmission and distribution network.

1.3 Research Contributions

1.3.1 Fault Induced Delayed Voltage Recovery Monitoring & Control

1. The proposed monitoring methodology of the FIDVR can successfully identify the stalled behavior of the 1-phase induction motors, even when <10% of load is stalled, and is robust even under the presence of oscillations in the voltage waveform.
2. The proposed control methodology ensures that the system recovers from FIDVR in the expected time. This is the first time control schemes on the composite load model have been used to ensure the voltage recovers swiftly. Existing methods assume that

the FIDVR is caused only by 3-phase motors that does not stall during the fault, which is not what happens in practice.

3. Extend the methodology to monitor and mitigate FIDVR in distribution networks by incorporating targeted load control and DER reactive power injection by utilizing techniques of linear trajectory sensitivity and model predictive control. This monitoring and control scheme ensures that DERs do not disconnect during the FIDVR due to low voltage ride through requirements.
4. Incorporated the dynamics of 3-phase motors into the monitoring of FIDVR phenomenon using admittances. A data-driven model of the 3-phase motors is estimated by using the operator theoretic framework for dynamical systems and allows us to estimate a Bi-Linear model for the 3-phase motor and enables us to employ techniques from linear systems to estimate the speed of the 3-phase motor from admittance measurements at the PMU.
5. Implemented the methodology on a real-time test bed and demonstrated the real-time nature of the FIDVR monitoring and control methodology.

1.3.2 Long Term Voltage Stability Monitoring & Control

1. Proved the explicit relation between the Jacobian of the power flow equations and the Thevenin index calculated at the PMU. This relation provides the mathematical basis for using the PMU measurement based voltage stability indices for multi-bus systems.
2. The proposed index is robust to noise than the local indices and so the proposed index can be used to validate the PMU index and ensure that malicious data does not impact the system operation.
3. Incorporated the reactive limits of the generator into the index calculation and so the index can provide a better assessment of the status of the power grid to the operator.

4. Extended the Thevenin index for 3-phase unbalanced networks and demonstrated a method to perform online Thevenin equivalent estimation from unbalanced voltage and current measurements.

1.4 Thesis Organization

This thesis is organized as follows

- In Chapter 1, the related background, trends in the industry and motivation of the research is presented
- In Chapter 2, a detailed literature survey of short term and long term voltage stability methods is presented
- In Chapter 3, the phenomenon of FIDVR is explained and the composite load model is described. The load model is simplified using physical understanding of the FIDVR phenomenon to derive an admittance based load model and this is used to estimate the recovery time of the FIDVR used as a monitoring index. The simplified model is used to also derive a linear relation between the admittance and the recovery time and this used for estimating control to enhance the voltage recovery. Numerical results on applying the method to the IEEE 162 bus are described.
- In Chapter 4, the phenomenon of FIDVR in distribution systems is studied using the tools of the simplified load model. Linear optimization formulations utilizing the topology of the distribution system and the simplified model are proposed to improve the recovery time and adherence to the voltage ride through requirement via targeted load control and reactive power injection from DERs. Numerical results on applying the method to IEEE 37 node distribution system and the 9 bus transmission system are described.

- In Chapter 5, a data driven method to estimate a linear model from the non-linear 3-phase induction motor dynamics by lifting the model into a functional space in which the trajectories of the simulated data follow a linear relation. The dynamic states can be recovered from the lifted space in a linear manner and techniques from linear systems can be used to perform state estimation and reconstruction in an online manner from output admittance measurements at the PMU, enabling stability monitoring for the non-linear model without model approximations as is usually done in literature.
- In Chapter 6, a relation between the local measurement based Thevenin index and the global sensitivity is mathematically derived. This leads to the Sensitivity based Thevenin Index that can be calculated in real-time and is robust to measurement noise and can incorporate the reactive power limits of generators. Results are described in detail for a 5-Bus system, and verified on larger systems up to 300 buses.
- In Chapter 7, an extension of the traditional Thevenin equivalent is proposed for unbalanced 3 ϕ circuits and a corresponding 3 ϕ long-term voltage stability indicator that can identify critical loads in a 3 ϕ system is proposed. A convex optimization formulation to estimate the 3 ϕ equivalent using measurements is proposed, making it possible to calculate the indicator in an online model-free manner. Numerical simulations performed using co-simulation between Pypower and GridlabD are presented for IEEE transmission networks combined with several modified IEEE distribution networks
- In Chapter 8, the final conclusions and contributions of the thesis are summarized and directions for future work are described.

1.5 References

- [1] N. I. D. T. Force, Survey of the Voltage Collapse Phenomenon. North American Electric Reliability Council, Aug. 1991.
- [2] C. Canizares, I. Dobson, N. Miller, V. Ajjarapu, H. Hamadanizadeh, and F. Rahimi, “Voltage stability assessment: concepts, practices and tools,” Power System Dynamic Performance Committee/Power System Stability Subcommittee, IEEE/PES Power System Stability Subcommittee Special Publication, Aug. 2002.
- [3] P. Kundur, J. Paserba, V. Ajjarapu, G. Andersson, A. Bose, C. Canizares, N. Hatziargyriou, D. Hill, A. Stankovic, C. Taylor, T. V. Cutsem, and V. Vittal, “Definition and classification of power system stability IEEE/CIGRE joint task force on stability terms and definitions,” IEEE Trans. Power Syst., vol. 19, no. 3, pp. 1387–1401, Aug. 2004
- [4] C. W. Taylor, Power system voltage stability. McGraw-Hill, 1994.
- [5] V. Ajjarapu, Computational techniques for voltage stability assessment and control, Springer Science Business Media, LLC, 2006.
- [6] “Final report on the august 14, 2003 blackout in the United States and Canada: causes and recommendations,” U.S.-Canada Power System Outage Task Force, Tech. Rep., April 2014.
- [7] S. Corsi and G. Taranto, “A real-time voltage instability identification algorithm based on local phasor measurements,” IEEE Trans. Power Syst., vol. 23, no. 3, pp. 1271–1279, 2008.
- [8] M. Glavic and T. Van Cutsem, “Wide-area detection of voltage instability from synchronized phasor measurements. Part I: Principle,” IEEE Trans. Power Syst., vol. 24, no. 3, pp. 1408–1416, 2009.
- [9] B. Williams, W. Schmus, and D. Dawson, “Transmission voltage recovery delayed by stalled air conditioner compressors,” Power Systems, IEEE Transactions on, vol. 7, no. 3, pp. 1173 –1181, Aug. 1992.
- [10] L. Taylor and S.-M. Hsu, “Transmission voltage recovery following a fault event in the metro Atlanta area,” in Power Engineering Society Summer Meeting, 2000. IEEE, vol. 1, 2000, pp. 537 –542 vol. 1.
- [11] M. Glavic, D. Novosel, E. Heredia, D. Kosterev, A. Salazar, F. Habibi-Ashrafi, and M. Donnelly, “See it fast to keep calm: Real-time voltage control under stressed conditions,” IEEE Power and Energy Magazine, vol. 10, no. 4, pp. 43–55, 2012.
- [12] DOE, “DOE - NERC FIDVR Workshop,” [Online]:<http://www.nerc.com/files/FIDVR-Conference-Presentations-4-22-08.pdf>, April 22 2008.
- [13] WECC Modeling and Validation Work Group, “Report on Composite Load Model for Dynamic Simulations”, 2012

- [14] Armando Salazar, "Synchronized phasor measurement technology and load monitoring", WECC/JSIS Meeting, April 2016.
- [15] A. J. Korsak, "On the question of uniqueness of stable load-flow solutions," IEEE Trans. Power App. Syst., vol. PAS-91, no. 3, pp. 1093–1100, May 1972.
- [16] A. M. Chebbo, M. R. Irving, and M. J. H. Sterling, "Voltage collapse proximity indicator: behaviour and implications," Transmission and Distribution IEE Proceedings, vol. 139, no. 3, pp. 241–252, May 1992.
- [17] C. Canizares, A. De Souza, and V. Quintana, "Comparison of performance indices for detection of proximity to voltage collapse," IEEE Trans. Power Syst., vol. 11, no. 3, pp. 1441–1450, 1996.
- [18] M. M. El-Kateb, S. Abdelkader, and M. S. Kandil, "Linear indicator for voltage collapse in power systems," Transmission and Distribution IEE Proceedings-Generation, vol. 144, no. 2, pp. 139–146, Mar. 1997.
- [19] System Operating Limits Methodology for the Operations Horizon, North American Electric Reliability Corporation (NERC) Std. TOP-006-3, November 2015.
- [20] FERC, "Federal energy regulatory commission staff preliminary assessment of the North American electric reliability councils proposed mandatory reliability standards," FERC, Tech. Rep. RM06-16-000, 2006.
- [21] Silverstein, A. "Synchrophasors & the Grid.". Presentation at NARUC Summer Meeting July 2017. Available [online]: <https://www.naspi.org/node/648>
- [22] A. Radaideh, U. Vaidya and V. Ajjarapu, "Sequential Set-point Control for Heterogeneous Thermostatically Controlled Loads Through an Extended Markov Chain Abstraction," in IEEE Transactions on Smart Grid, vol. PP, no. 99, pp. 1-1

CHAPTER 2. LITERATURE SURVEY

2.1 Fault Induced Delayed Voltage Recovery

Traditionally to solve the issue of FIDVR, utilities have relied on planning studies to determine the possible risk of FIDVR in their system and then based on the results, decided the location of Dynamic VAR devices. More recently, measurement based methods have been proposed as well that utilize the behavior of voltage and current phasors to detect the onset of FIDVR or stalling and take an action that either prevents FIDVR or ensures fast recovery from FIDVR. These methods are briefly described below.

2.1.1 Dynamic VAR Planning Based Methods

The main idea behind this approach is that the occurrence of the FIDVR in the system is a manifestation of a deeper problem in the system – that the reactive resources in the system are no longer sufficient to support the voltage. To overcome this, utilities performing planning tasks to choose the location and size of various kinds of reactive injection devices such as STATCOMs, SVCs, etc. Selecting the optimal location and appropriate size of the reactive power injection devices is a very challenging multi-objective optimization problem as it inherently is non-linear (the power flow equations) and includes discontinuous variables (location of device). Furthermore, FIDVR is a dynamic phenomenon and so the optimization formulation should incorporate the dynamical equations that can cause FIDVR. This is extremely complicated and so, initial efforts concentrated on formulating the problem using steady-state equations. Recent advances in the computational and optimization methods have enabled researchers and utilities to formulate and solve this problem including the system dynamics as well.

Planning DVAR resources traditionally used techniques like OPF to identify the optimal locations and amount with time domain simulations being used for verifying that the transient voltage performance is satisfactory. Along with OPF, other techniques such as PV, QV analysis in conjunction with time-domain dynamic simulations have been used in ERCOT reactive power study [1]. Similarly, the identification of the reactive requirements and the criteria used for the DVAR planning in Entergy system is presented in [2]. Formulating the problem as a mixed linear optimization problem that are iteratively solved is another route in literature [3]. A comprehensive survey of tools and methodologies for the identification of reactive power requirements is provided in [4]. However, just based on the steady state behavior, it is impossible to detect the locations where FIDVR is most likely and so proper representation of appropriate load models is necessary for effective DVAR planning.

Instead of incorporating the full dynamics, [5] uses a quasi-steady state load models coupled with quasi-dynamic models of generators to ensure that the system dynamics are considered during the VAR planning. Trajectory sensitivity methods [6] have also been used to linearize the non-linear optimization problem to make it tractable to solve using linear programming techniques. In contrast, [7] formulates the problem as a mixed integer dynamic optimization problem and is solved by a mixed integer non-linear solver. However, due to the explosion in the amount of variables for large systems, implementing this method for large practical systems is challenging. Recently, methods [8], [9] that incorporate the time-domain power system simulator into the optimization directly have been proposed that ensure that the optimization does not have to explicitly consider the load dynamics. These methods have been shown to work on large practical systems [8] and also provide information on the system to the operator via concepts such as dynamic voltage control areas [9].

2.1.2 Online Measurement Based Methods

2.1.2.1 Voltage Based Monitoring & Control

The straight forward method to use relays or phasor measurement devices to mitigate short term voltage stability is to utilize the voltage behavior after a dynamic event (fault, lightning strike, etc.) is cleared. The enhanced voltage instability predictor (VIP) method, which represents the power system as a Thevenin equivalent, is used in [10] to identify FIDVR and short term voltage stability problems. This method assumes that the Thevenin impedance remains constant between successive estimations, but the Thevenin and load do vary during the dynamic events. In [11], slope based voltage recovery calculation is used to predict FIDVR events. Successive voltage measurements are used to calculate the slope of the voltage recovery trajectory and this slope is used to calculate the time to recovery. The load is shed in successive steps to ensure that the voltage recovers in a pre-specified time. However, this method cannot handle oscillations that occur due to the other system dynamics. The MVA-volt index is proposed [12] as an integral error based measure to detect FIDVR, but it cannot differentiate between voltage trajectories showing moderate recovery and another showing fast recovery over a shorter period of time.

2.1.2.2 Load Model Based Monitoring & Control

The load model is a key component of the short term voltage instability phenomenon and so utilizing the load model parameters to estimate the internal states or monitoring a more appropriate physical quantity/index that estimates the risk of stalling will improve the behavior of the methodology. [13] presents a method to derive the kinetic energy of an equivalent induction motor by measuring voltage and current phasors. The derived kinetic energy is used to decide how much load to shed to recover from the risk of stalling. Similarly, [14] proposes a method to quantify the FIDVR using the measured active and reactive power to calculate an

index. This index is then used to quantify the amount of load to shed. [15] proposes a method under speed load shedding by estimating the speed of the 3-phase motor load using phasor measurement and a 1st order model of the motor. It is shown that these techniques disconnect less amount of load than under voltage relays, the main drawback with these methods is that the induction motor modelled (the 3-phase motor) is not the true reason for FIDVR in practice and thus, need to be modified to account for the 1-phase motor dynamics.

2.1.2.3 Controlling Distribution System Devices to Prevent Instability

Instead of a corrective control action, the prevention of the FIDVR might be possible using certain devices in the distribution system that can act as mini-dynamic VAR resources – PV inverters, Plug-In Hybrids, etc. Recent studies [16], [17] have been performed with distributed energy sources and utility scale energy sources to test if these have the capability to support the reactive requirements of the 1-phase induction motors during a fault in the system. EMTP simulations demonstrate that the reactive support necessary might be larger than the rating of the distributed sources, but as it is only for a short amount of time, it is a possibility. Further, as more distributed energy sources such as hybrid vehicles [18] are integrated into the system, it seems more possible that the distribution energy sources can aid the system in times of extreme need.

2.2 Long Term Voltage Stability Monitoring

In practice, the monitoring of the long term voltage stability is done using the PV curve tracing methods at the control center. This is the most reliable way to calculate the long term voltage stability margin as it considers the detailed model of system – discrete switching, PV-PQ switching, line flow limits– during load increase. However, in recent years with the increasing penetration of PMUs various online methods have been proposed for both corrective and preventive paradigms.

2.2.1 PV Curve Tracing

The most accurate method for estimating the margin to long term voltage instability is the PV curve tracing, via continuation power flow [18], [19], [20] or by consecutively the solving power flow with increasing load. This is the most reliable way to calculate the long term voltage stability margin as it can consider the detailed model of system that captures the complicated behavior of various components – discrete switching, PV-PQ switching, line flow limit dependence – during load increase. However, as this method is solving a non-linear set of equations while considering the various possibilities of the discrete quantities in the system, this method is computationally expensive. Furthermore, the resulting margin is very much dependent of the model data and the scenario chosen. Thus, this method cannot directly monitor the long term voltage stability in an online manner for large systems. For online application, it is usually kept in the stand-by mode in Energy Management System (EMS) to validate VSM prediction from other fast methods in case of a flag being raised, or to provide detailed analyses for selected critical contingencies. As a benchmark, this method has been widely commercialized in many ESM applications [21], [22].

Various methods have been proposed to speed-up the process of the PV curve tracing for multiple severe scenarios, among which, [23], [24] describe tools to achieve real-time PV Curve tracing for practical utility scale systems. The key method that improves the computational performance is the stressing process that is realized by a “case-worsening procedure”. This procedure ensures that the scenario chosen is a worse scenario than all the previous scenarios chosen. The fast case-worsening procedure first simplifies the system by short-circuit current network transformation and by aggregating fictitious load centers, and then estimates the severity using $\Delta Q/\Delta V$ as collapse point indication. These simplifications enable the computations to be possible in an online manner but might introduce errors.

2.2.2 Boundary Tracing in Parameter Space

Another model-based method is the idea of a boundary tracing for a parameter space. In the PV curve tracing, a single load increase direction is chosen and all the parameters are varied along this direction till the nose point. A different approach is to not look at the PV curve but at the parameter values right at the nose point of the PV curve. The parameter value at the nose point is a limiting point for a particular load increasing direction. If all the parameter values that occur at the nose points are collected [24], [25], they form a boundary in the high dimension parameter space and so the distance from a present operating point to the boundary can be used as a measure of the distance to the long term instability. Quite a few techniques have been developed to obtain the boundary through sampling fitting [26], [27], tangent hypersurface [28], [29], or polynomial approximation for the power flow equations [30].

These high dimensional boundaries can be computed offline and the distance to these boundaries can be computed in an online manner using the EMS state estimation results. One of the concerns with this method is that this suffers from the curse of dimensionality as the larger the system, the larger the number of parameters that need to be analyzed leading to an extremely complicated boundary in the higher dimension.

2.2.3 Online Measurement Based Methods

There have been recent efforts done to utilize the online measurements to estimate the margin or an index that can be used as a proxy for the long term voltage stability. They can be split into methods requiring local measurements and centralized measurements. As the Thevenin methods are of interest in this dissertation, they are discussed in more detail. The main idea behind the Thevenin methods is to estimate an equivalent circuit for the system at the critical load and utilize the ratio between the load impedance and Thevenin impedance as an indicator of long term voltage stability.

2.2.3.1 Local Thevenin Equivalent Based Methods

The early Thevenin methods used only local PMU measurements and independently calculated the Voltage Stability Index (VSI) at each monitoring bus [31], [32]. The VSI was either used to initiate local control actions or transmitted to a centralized location for visualization or control applications. These techniques exploit the high sampling rate of the PMUs (30 samples per second) to capture small variations in the bus voltage at a quasi-steady state operating point and calculate a Thevenin equivalent circuit at each monitored bus. The estimated Thevenin equivalent parameters are then used to calculate the VSI at a bus. To improve accuracy, a multi-bus equivalent is proposed for load areas with several tie-lines [33] and an analytical derivation of the maximum power is used to monitor voltage stability.

One drawback of the local approaches is the reliance on the quasi-steady state nature of the system. The small variations could be due to a specific phenomenon (forced oscillations, etc.) that skew the measurements and provide a false equivalent. Furthermore, measurement noise in the PMU can cause the LTI to oscillate wildly. This is a well-documented problem and [32] use multiple measurements over a time window to smooth out the errors by mathematical techniques. However, these methods assume a certain noise profile and might not work in presence of certain system behavior. Despite these drawbacks, the simplicity and local nature of these methods make them attractive to utilities and they have been implemented commercially in the field and can trigger emergency corrective actions [10].

2.2.3.2 Centralized Thevenin Equivalent Based Methods

The centralized Thevenin methods are calculated at the EMS where the state estimation results and PMU measurements are available for the entire system. Since these methods do not utilize any quasi steady state nature of the system for the Thevenin equivalent calculation, they are more robust to noise compared to the local methods. However, the centralized nature means

that these methods cannot be used for corrective schemes and instead are best used for preventive schemes. The initial method utilized a simplifying assumption to define the L-index [34], without explicitly calculating a Thevenin equivalent. This idea was formalized by the concept of coupled single-port circuit model [35] which is used to explicitly define a Thevenin equivalent. By utilizing the network equations relating the voltages and currents, the entire system can be equivalently described by an extended Thevenin circuit which includes an extra component (source, load, or impedance) to reflect the coupling with current injections at other load buses and generators. The more recent methods have included the reactive limits into the method by fitting a cubic curve and estimating the generators reaching the limit [36]. [37] presents a method to estimate the maximum power transfer in a transmission corridor utilizing the line admittances. A different paradigm by using the system Jacobian along with the admittance matrix to calculate the Thevenin impedance is proposed in [38]. However, no theoretical explanation is present as to how the method can monitor the voltage stability.

2.2.3.2 Other Centralized Methods

Many indices have been proposed to measure the long-term voltage stability – Determinant, smallest eigenvalue, smallest singular value of the Jacobian, and certain sensitivity of voltage with respect to power injection. However, as they do not have a normalized range, they cannot be used for comparing stability among different systems. Definitions and comparisons of these indices can be found in [39].

2.2.3.3 Machine Learning Based Methods

The recent trends in machine learning is to utilize historical and operational data in complex systems for estimating a non-trivial quantity of the system behavior. This is exactly the same problem of the computation of the voltage stability margin and so the recent advances in machine learning can be used for this problem. Recent reported literature seems to suggest

that using deep neural networks can indeed be used to get a reasonable estimate of the voltage stability margin from the measurements [40]. This area is still in its infancy and much progress is necessary in this field to match accuracy of existing methods.

2.3 References

- [1] ABB, “Ercot crez reactive power compensation study,” FACTS Seminar Presentations, St.Paul Minnesota, March 28 2012.
- [2] V. Kolluri and S. Mandal, “Determining reactive power requirements in the southern part of the entergy system for improving voltage security - a case study,” in Power Systems Conference and Exposition, 2006. PSCE '06. 2006 IEEE PES, 2006, pp. 119–123.
- [3] V. Krishnan, H. Liu, and J. McCalley, “Coordinated reactive power planning against power system voltage instability,” in Power Systems Conference and Exposition, 2009. PSCE '09.IEEE/PES, march 2009, pp. 1–8.
- [4] P. Pourbeik, R. Koessler, and B. Ray, “Addressing voltage stability related reliability challenges of san francisco bay area with a comprehensive reactive analysis,” in Power Engineering Society General Meeting, 2003, IEEE, vol. 4, 2003, pp. –2639 Vol. 4.
- [5] A. Meliopoulos, G. Cokkinides, and G. Stefopoulos, “Voltage stability and voltage recovery: Load dynamics and dynamic var sources,” in Power Systems Conference and Exposition, 2006. PSCE '06. 2006 IEEE PES, 29 2006-nov. 1 2006, pp. 124–131.
- [6] B. Sapkota and V. Vittal, “Dynamic var planning in a large power system using trajectory sensitivities,” Power Systems, IEEE Transactions on, vol. 25, no. 1, pp. 461–469, feb. 2010.
- [7] A. Tiwari and V. Ajjarapu, “Optimal allocation of dynamic var support using mixed integer dynamic optimization,” Power Systems, IEEE Transactions on, vol. 26, no. 1, pp.305–314, feb. 2011.
- [8] M. Paramasivam, A. Salloum, V. Ajjarapu, V. Vittal, N. B. Bhatt, Shanshan Liu, “Dynamic Optimization Based Reactive Power Planning to Mitigate Slow Voltage Recovery and Short Term Voltage Instability,” Power Systems, IEEE Transactions on, vol. 28, no. 4, pp. 3865–3873, Nov. 2013
- [9] M. Paramasivam, S. Dasgupta, V. Ajjarapu, and U. Vaidya, “Contingency analysis and identification of dynamic voltage control areas,” Power Systems, IEEE Transactions on, vol. 30, no. 6, pp. 2974–2983, Nov. 2015
- [10] M. Glavic, D. Novosel, E. Heredia, D. Kosterev, A. Salazar, F. Habibi-Ashrafi, and M. Donnelly, “See it fast to keep calm: Real-time voltage control under stressed conditions,” IEEE Power and Energy Magazine, vol. 10, no. 4, pp. 43–55, 2012.

- [11] S. Halpin, K. Harley, R. Jones, and L. Taylor, "Slope-permissive under-voltage load shed relay for delayed voltage recovery mitigation," *Power Systems, IEEE Transactions on*, vol. 23, no. 3, pp. 1211–1216, aug. 2008.
- [12] S. Halpin, R. A. Jones, and L. Taylor, "The mva-volt index: A screening tool for predicting fault-induced low voltage problems on bulk transmission systems," *Power Systems, IEEE Transactions on*, vol. 23, no. 3, pp. 1205–1210, 2008.
- [13] H. Bai and V. Ajjarapu, "A novel online load shedding strategy for mitigating fault-induced delayed voltage recovery," *IEEE Trans. Power Systems*, vol. 26, no. 1, pp. 294–304, Feb. 2011
- [14] A. Mahari and H. Seyedi, "A fast online load shedding method for mitigating FIDVR based on novel stability index," 2013 21st Iranian Conference on Electrical Engineering (ICEE), Mashhad, 2013, pp. 1-6
- [15] Y. Dong, et. al., "An Emergency-Demand-Response Based Under Speed Load Shedding Scheme to Improve Short-Term Voltage Stability," in *IEEE Trans. on Pow. Sys.*, vol. 32, no. 5, pp. 3726-3735, Sept. 2017.
- [16] C. A. Baone, Yan Xu and J. D. Kueck, "Local voltage support from distributed energy resources to prevent air conditioner motor stalling," 2010 Innovative Smart Grid Technologies (ISGT), Gaithersburg, MD, 2010, pp. 1-6
- [17] C. Roe, Y. M. Al-Abdullah, D. Desai, G. K. Stefopoulos, G. J. Cokkinides and A. P. Meliopoulos, "Fault-Delayed Voltage Recovery Control with Plug-In Hybrid Electric Vehicles," 2010 43rd HICSS, Honolulu, HI, 2010, pp. 1-9
- [18] K. Iba, H. Suzuki, M. Egawa, and T. Watanabe, "Calculation of critical loading condition with nose curve using homotopy continuation method," *IEEE Trans. Power Syst.*, vol. 6, no. 2, pp. 584–593, May 1991
- [19] V. Ajjarapu and C. Christy, "The continuation power flow: a tool for steady state voltage stability analysis," *IEEE Trans. Power Syst.*, vol. 7, no. 1, pp. 416–423, 1992.
- [20] H.-D. Chiang, A. J. Flueck, K. S. Shah, and N. Balu, "CPflow: a practical tool for tracing power system steady-state stationary behavior due to load and generation variations," *IEEE Trans. Power Syst.*, vol. 10, no. 2, pp. 623–634, May 1995.
- [21] L. Sandberg and K. Roud'en, "The real-time supervision of transmission capacity in the swedish grid," *Real-time Stability Assessment in Modern Power System Control Centers*, pp. 279–305, 2008
- [22] H.-D. Chiang and P. Causgrove, "Study of co-optimization stochastic superopf application in the CAISO system," Bigwood Systems, Inc., Tech. Rep., sep 2015
- [23] S. C. Savulescu, "Fast assessment of the distance to instability," *Real-Time Stability in Power Systems: Techniques for Early Detection of the Risk of Blackout*, p. 31, 2006

- [24] F. Wu and S. Kumagai, "Steady-state security regions of power systems," *IEEE Trans. Circuits Syst.*, vol. 29, no. 11, pp. 703–711, Nov. 1982.
- [25] Y. Yu, "Security region of bulk power system," in *Proc. Int. Conf. Power System Technology*, vol. 1, Oct. 2002, pp. 13–17 vol.1
- [26] J. Su, Y. Yu, H. Jia, P. Li, N. He, Z. Tang, and H. Fu, "Visualization of voltage stability region of bulk power system," in *Proc. Int. Conf. Power System Technology*, vol. 3, 2002, pp. 1665–1668 vol.3
- [27] J. D. McCalley, S. Wang, Q. L. Zhao, G. Z. Zhou, R. T. Treinen, and A. D. Papalexopoulos, "Security boundary visualization for systems operation," *IEEE Trans. Power Syst.*, vol. 12, no. 2, pp. 940–947, May 1997.
- [28] G. Wang, X. Zhang, and S. Mei, "Quadratic approximation analysis of static voltage stability region boundary," in *Proceedings of the CSEE*, vol. 28, no. 19, 2008, pp. 0–35
- [29] C. Hamon, M. Perninge, and L. Sder, "A stochastic optimal power flow problem with stability constraints —part i: Approximating the stability boundary," *IEEE Trans. Power Syst.*, vol. 28, no. 2, pp. 1839–1848, May 2013
- [30] Y. Qiu, H. Wu, Y. Zhou, and Y. Song, "Global parametric polynomial approximation of static voltage stability region boundaries," *IEEE Trans. Power Syst.*, vol. PP, no. 99, p. 1, 2016.
- [31] K. Vu, M. M. Begovic, D. Novosel and M. M. Saha, "Use of local measurements to estimate voltage-stability margin," in *IEEE Transactions on Power Systems*, vol. 14, no. 3, pp. 1029-1035, Aug 1999
- [32] S. Corsi and G. N. Taranto, "A Real-Time Voltage Instability Identification Algorithm Based on Local Phasor Measurements," in *IEEE Transactions on Power Systems*, vol. 23, no. 3, pp. 1271-1279, Aug. 2008
- [33] F. Hu, K. Sun, A. Del Rosso, E. Farantatos and N. Bhatt, "Measurement-Based Real-Time Voltage Stability Monitoring for Load Areas," in *IEEE Transactions on Power Systems*, vol. 31, no. 4, pp. 2787-2798, July 2016
- [34] Kessel P., and Glavitsch, H., "Estimating the Voltage Stability of a Power System," *IEEE Transactions Power Delivery*, Vol. PWRD- 1, pp 346-354, 1986.
- [35] Y. Wang, I. R. Pordanjani, W. Li, W. Xu, T. Chen, E. Vaahedi, J. Gurney, "Voltage stability monitoring based on the concept of coupled single-port circuit", *IEEE Trans. Power Syst.*, vol. 26, no. 4, pp. 2154-2163, Nov. 2011
- [36] H. Y. Su and C. W. Liu, "Estimating the Voltage Stability Margin Using PMU Measurements," in *IEEE Transactions on Power Systems*, vol. 31, no. 4, pp. 3221-3229, July 2016

- [37] L. Ramirez and I. Dobson, "Monitoring voltage collapse margin with synchrophasors across transmission corridors with multiple lines and multiple contingencies," 2015 IEEE Power & Energy Society General Meeting, Denver, CO, 2015, pp. 1-5.
- [38] S. S. Biswas and A. K. Srivastava, "Voltage Stability Monitoring in Power Systems, " U.S. Patent, Feb. 25, 2014
- [39] M. Glavic and T. Van Cutsem, "A short survey of methods for voltage instability detection," in Power and Energy Society General Meeting, 2011 IEEE, 2011, pp. 1–8
- [40] Li, Shiyang, and Venkataramana Ajarapu. "Adaptive Online Monitoring of Voltage Stability Margin via Local Regression." Power Systems, IEEE Transactions on, 2017 (accepted).

CHAPTER 3. PMU BASED MONITORING AND MITIGATION OF DELAYED VOLTAGE RECOVERY USING ADMITTANCES

Modified from a manuscript accepted for publication in IEEE Transactions in Power Systems

Amarsagar Reddy Ramapuram Matavalam and Venkataramana Ajjarapu

*Department of Electrical and Computer Engineering, Iowa State University, Ames, IA 50011,
United States of America.*

Abstract

This paper analyzes the delayed voltage recovery phenomenon by simplifying the Western Electricity Coordinating Council (WECC) composite load model using the load admittance and the thermal relay dynamics. From this analysis, a closed form expression approximating the recovery time is derived and the key load parameters impacting the behavior of voltage recovery are identified. A monitoring scheme based on the measured load admittance is then proposed to detect the onset of stalling, even in the presence of voltage oscillations, and estimate the duration of the delayed voltage recovery. A mitigation scheme utilizing smart thermostats and offline learning is also derived to ensure that the voltage recovers to the pre-contingency voltage within a specified time. Both the monitoring and mitigation schemes only need local measurements at a substation making them promising for online applications. Results for the IEEE 162 bus system validating the various assumptions used for the analysis and establishing the connection between the delayed voltage recovery phenomenon and load admittance.

3.1 Introduction

The deregulation of the power grid operation is giving priority to economic operations, there has been an increasing push to utilize the electric grid infrastructure to the best extent possible. This transformation in grid operations is causing the operators to operate the grid in more stressed conditions than usual, making it more likely for the problems to be manifested in the grid. One such problem is the phenomenon of short-term voltage instability which occurs mainly due to the stalling of induction motor loads, and can manifest in the form of fast voltage collapse or delayed voltage recovery.

During Fault Induced Delayed Voltage Recovery (FIDVR), the recovery of the voltage after a disturbance is delayed resulting in sustained low voltages for several seconds (>10 sec) [1] – [2] FIDVR is mainly caused in systems with a moderate amount of single phase induction motor (IM) loads. After a large disturbance (fault, etc.), these motors, that are connected to mechanical loads with constant torque, stall and draw ~ 6 times their nominal current and leading to the depression of the system voltage for several seconds. There have been two kinds of solutions in literature to mitigate the FIDVR phenomenon – supply side methods (injection of dynamic VARs via SVC, etc.) [3] – [5] and demand side methods (disconnection of loads using measurements, etc.) [6] - [8]. All the existing methods utilize the dynamic model of the 3- ϕ IM which is **not** the true cause of the conventional FIDVR phenomenon as the stalling of 1- ϕ IM is the recognized cause of the FIDVR. Hence there is a need for analysis and a method to assess and control FIDVR in an online manner while incorporating the stalling of 1- ϕ IM. As far as the authors know, there is a gap in the literature with regards to considering and analyzing the thermal relay dynamics during the FIDVR and this paper is targeted towards filling this important gap. We will start by analyzing the load model that can replicate the FIDVR phenomenon.

3.2 Examination of the WECC Composite Load Model

In order to enable the utilities and system operators to simulate the FIDVR phenomenon to estimate the amount of VAR support required, a dynamic load model has been developed recently by WECC called as the Dynamic Composite Load Model [9]. The composite load (CMLD) model essentially aggregates the various kinds of dynamic loads in the sub-transmission network into several 3- ϕ IM (representing high, medium and low inertias) and an aggregate 1- ϕ IM (representing the AC loads). Furthermore, the protection schemes that trip a proportion of the loads are also implemented for each of the motor representing the Under Voltage and Under Frequency protections policies. An equivalent feeder is also present that tries to emulate the impact of voltage drop in the distribution system when a large current is drawn. The overall structure of the composite load model is shown in Figure 3.1.

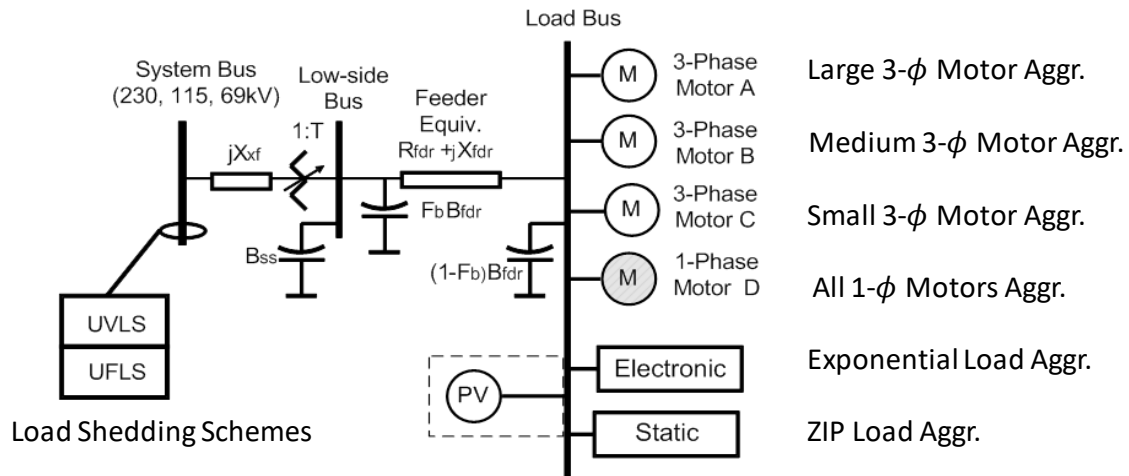


Figure 3.1 Structure of the composite load model [9].

The composite load model has a large number of parameters (132 to be exact) and discrete controls (Under Voltage Load Shedding & Contactors) compared to a conventional load model. Moreover, the model specifications [9] only mention the behavior of most of the components and do not specify the actual equations used. Thus, engineering judgement needs

to be made with regards to developing equations for analysis. For this purpose, understanding the 3-phase IM model and the 1-phase IM model along with their protection components are key. These are detailed in the following sub-sections.

3.2.1 3-Phase Motor Modelling

A standard way to model the 3- ϕ IM is by an equivalent circuit [10] where the stator and rotor impedances along with the mutual inductances are specified (R_A , X_A , X_m , R_1 , R_2 , X_1 & X_2) and is shown in Figure 3.2. The equations are well studied and it is intuitively understandable as the current in the equivalent circuit directly enables the user to estimate the electric torque.

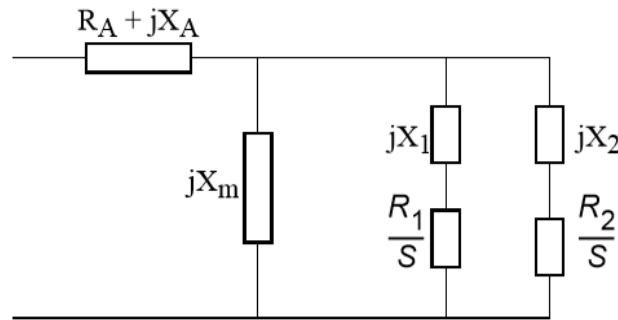


Figure 3.2 *Standard model of the 3-Phase Induction Motor*

However, as per WECC model specifications, the 3- ϕ IM is specified by the transient and sub-transient parameters (L_s , L_p , L_{pp} , T_{p0} & T_{pp0}). The equations for this model are not easily analyzed as they are in the dq frame of reference and so it becomes hard to estimate the impact of load on the electric torque. Thus, we need to convert the sub-transient quantities into corresponding resistance and reactance and analyze the resulting induction motor characteristics. The equations for this conversion are presented in (3-1).

$$L_s = (X_A + X_m)/\omega_{base} \quad (3-1)$$

$$L_p = (X_A + (X_1 \cdot X_m) / (X_1 + X_m)) / \omega_{base}$$

$$L_{pp} = (X_A + (X_1 \cdot X_2 \cdot X_m) / (X_1 \cdot X_2 + X_2 \cdot X_m + X_m \cdot X_1)) / \omega_{base}$$

$$T_{p0} = (X_1 + X_m) / (\omega_{base} \cdot R_1)$$

$$T_{ppo} = (X_2 + (X_1 \cdot X_m) / (X_1 + X_m)) / (\omega_{base} \cdot R_2)$$

As per the WECC CMLD specifications [9], the 3-Phase motors are all equipped with appropriate UV relays that ensure that load is reduced as the voltage drops. This is pictorially represented in Figure 3.3, with the load torque proportional to the square of the rotation speed. The motor speed is given by the intersection of the load-torque curve and the induction motor torque curve. As the supply voltage drops to 50% nominal, the speed reduces and the chance of stalling increases. Before this can happen, the UVLS relay takes effect and reduces the load torque. This reduction in load ensures that the rotor speed of the 3-Phase motors is close to the rated speed and so the slip (s) varies in a tight range (around 0.04 at nominal operation to an extreme of 0.1 at the low voltage condition). While the diagram is for quadratically varying load torque, the same idea holds for the linear load torque and constant load torque curves.

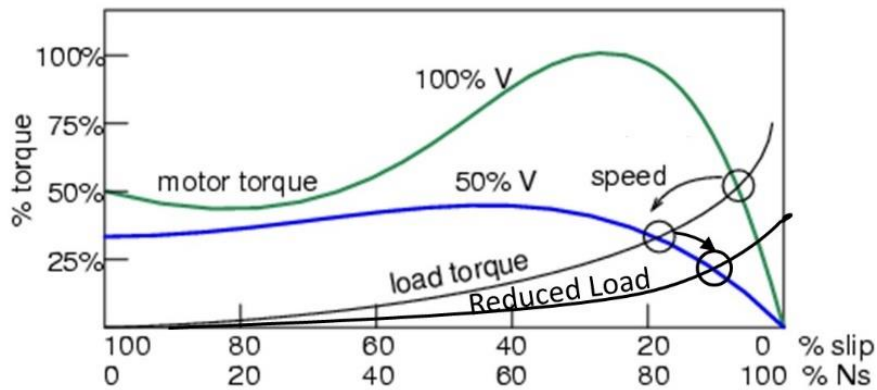


Figure 3.3 *The variation in motor speed when the voltage and the load are reduced*

In fact, given the terminal voltage and the load-torque curve, it is straightforward to estimate the speed of the motor. This fact will be used later on in the monitoring of FIDVR.

3.2.2 1-Phase Motor Modelling

The 1- ϕ induction motor is the main reason why the FIDVR is observed. The 1- ϕ IM model has representations of the AC compressor motor, compressor motor thermal relay, under-voltage relays and contactors. Depending upon the input voltage, the motor operates either in 'running' or 'stalled' state. The behavior of the motor as a function of the voltage can be understood based on the power consumption of the motor and Figure 3.4 plots the active and reactive power demand as a function of the voltage for the normal operation and stalled operation.

From Figure 3.4, it can be seen that in the stalled state, the active power demand is ~ 3 times the nominal amount and the reactive demand is $\sim 5-6$ times the nominal amount compared to the normal 'running' state. This large demand is the reason why the voltage reduces at the substation causing FIDVR. This demand naturally is reduced via thermal protection that takes around 10-15 seconds.

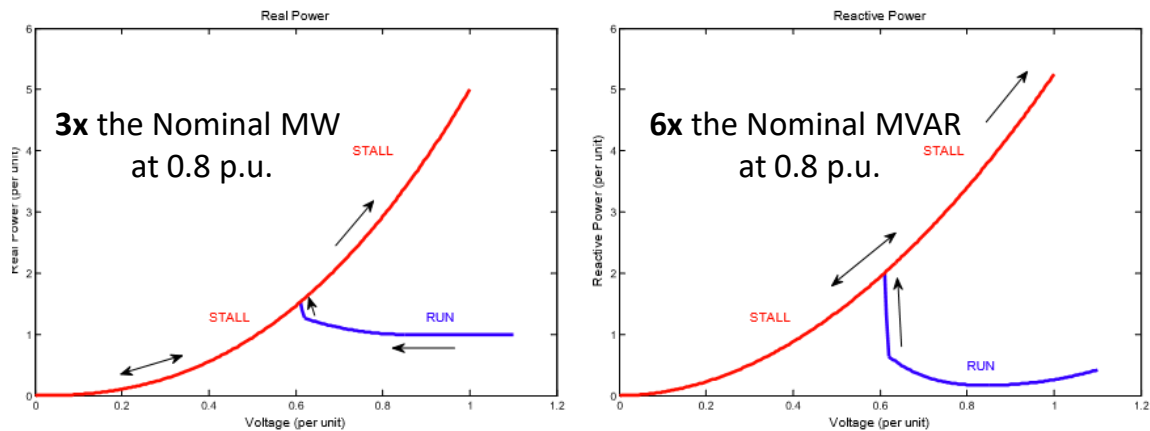


Figure 3.4 Active power (left) and Reactive power (right) versus the voltage for the normal and stalled operation for the 1- ϕ induction motor [9].

The reason why the stalled 1-phase motor power increases so rapidly with the voltage is due to the representation of the 1-phase motor as an admittance after stalling. This is

physically accurate as the stalled motors essentially act as constant admittances and as the terminal voltage increases, the active and reactive power drawn by these stalled motors increases in a quadratic manner.

Another important characteristic of the 1-phase motor are the various control schemes. Just as the 3-phase motor has UV protection devices to reduce the load when the voltage drops, the 1-phase motor also has UV protection, but the percentage of load that has this protection is very small (~5%-10% of the 1-phase motors). On top of the UV relays, there are also contactors that reduce the load below 0.65 p.u. voltage. However, the main protection device is the thermal protection logic that is present in *all* the 1-phase motors. The thermal tripping logic is shown in Figure 3.5, where f_{TH} is the fraction of 1-phase motors connected, θ is the internal motor temperature, T_{th} is the thermal delay time constant in the protection logic with the thermal power dissipated in the motor given by $V^2 \cdot G_{stall}$.

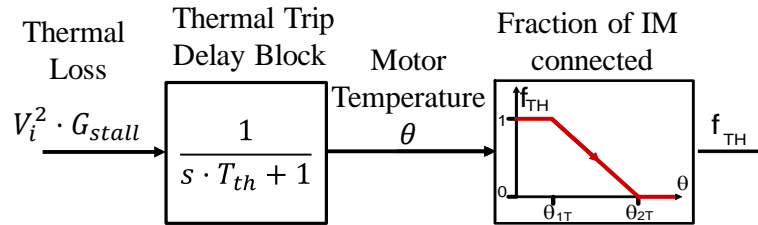


Figure 3.5 *The thermal protection logic implemented in the composite load model*

After a fault that initiates the FIDVR event, the thermal loss in the motor increases suddenly and the thermal trip logic is initiated. The thermal delay block simulates the time delay of the rise in the temperature of the motor coil. This estimated motor coil temperature is what determines the fraction of 1-phase motor connected to the grid. The fraction of 1-phase motors connected is determined by the θ_1 & θ_2 parameters. A temperature that is lesser than θ_1 does not change the admittance and keeps the fraction connected (f_{TH}) as 1. When the motor

temperature is between θ_1 and θ_2 , the f_{TH} is reduced linearly from 1 to 0. And when the temperature reaches θ_2 , there are no more 1-phase motors connected to the grid and the voltage has recovered to a value slightly higher than the pre-contingency voltage. The parameters θ_1 and θ_2 are key in determining the time that the FIDVR event persists and analytically deriving the time taken for the temperature to reach θ_2 is a way to estimate the time to recover from FIDVR.

3.3 Online Monitoring of FIDVR using Measurements

To prevent uncontrolled loss of load in the bulk electric system, NERC, WECC and other regulatory bodies have specified transient voltage criteria that utilities and system operators need to satisfy after a fault has been cleared. Figure 3.6 provides a pictorial representation of the WECC transient criteria.

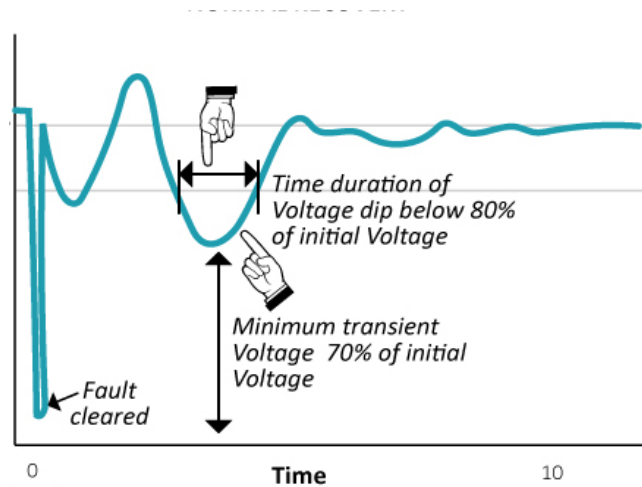


Figure 3.6 WECC Voltage Performance Criteria [11]

The WECC transient criteria is defined as the following two requirements [11]

1. Following fault clearing, the voltage shall recover to 80% of the pre-contingency voltage within 20 seconds of the initiating event.

2. Following fault clearing and voltage recovery above 80%, voltage at each applicable bulk electric bus serving load shall neither dip below 70% of pre-contingency voltage for more than 30 cycles nor remain below 80% of pre-contingency voltage for more than two seconds.

The WECC transient voltage performance criteria was originally proposed using the rotor angle stability requirements. However, the criterion has been used by many utilities for general transient voltage performance studies. To analyze FIDVR events, the WECC modeling and validation group is working on a voltage ride through envelope for generators during FIDVR events [11]. Figure 3.7 shows the proposed WECC voltage ride-through for generators.

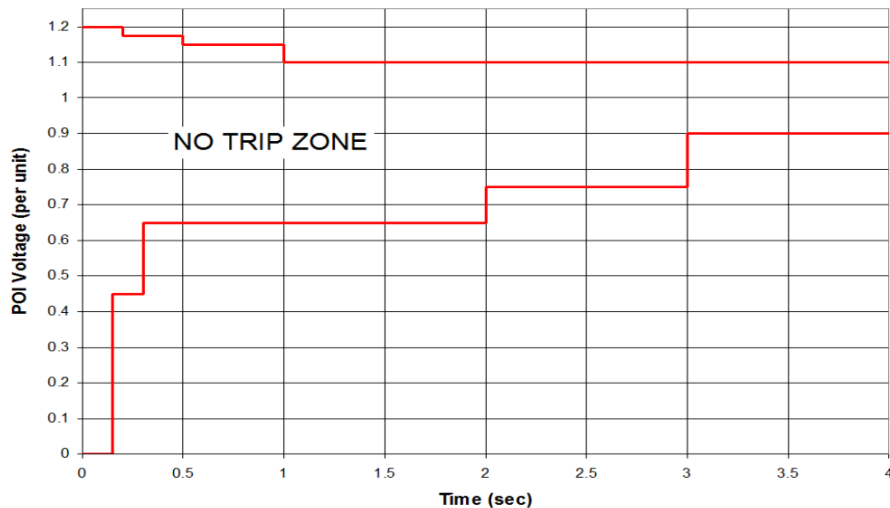


Figure 3.7 Proposed WECC voltage ride-through envelope for generators [11]

This simplified voltage criterion can be used by utilities and to ensure that the trajectory of the recovering voltage must be in the no-trip zone. Similarly, the ERCOT criterion for transient voltage response requires that voltages recover to 0.90 p.u. within 10 seconds of clearing the fault [11]. The utilities ensure that the voltage recovery satisfies the guidelines specified by their regulatory authority during their planning phase and operational phase by

either installing VAR devices (STATCOM, SVC, etc.) in critical regions and by ensuring that sufficient dynamic VARS are available during operation.

The voltage measured at a PMU after a fault is cleared can be compared to the voltage recovery guidelines and the deviation between the two can be used to estimate the amount of FIDVR observed in real-time. This is possible as the PMU calculates the phasors at 60 frames per second and can enable the fast detection of the FIDVR event. A straightforward methodology would be to use the difference between measured voltage and the reference voltage (that symbolizes the expected voltage guideline). However, instead of using the voltages directly, an entropy based approach is proposed in [12] and is shown to quantify the behavior of the FIDVR reliably, where it is used for planning reactive reserves [5]. The authors propose to quantify the distance between the two waveform using the KL divergence metric between two probability densities derived from the measured waveform and the reference waveform.

Figure 3.8 plots the measured voltage at the bus (left) and the corresponding probability density function (PDF) of the measured voltage (right-blue) and reference PDF (right-green). A real-time variation of the KL Divergence method proposed in [13] is used to quantify the FIDVR from the PMU measurements. The probability density functions over a moving time window are used to get a KL divergence for every instant of time. The KL divergence metric between a probability p and a reference probability p_{ref} is given by equation (3-2), where p_i & $p_{ref,i}$ is the probability in the i^{th} bin of the measured waveform and the reference waveform respectively.

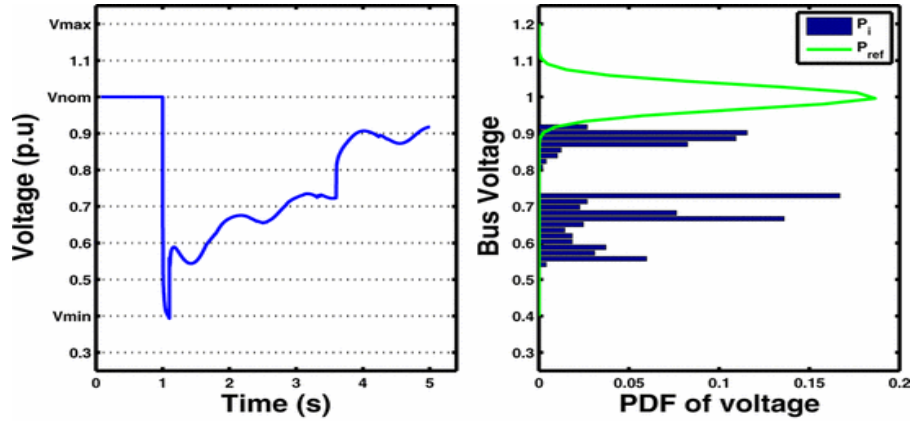


Figure 3.8 The Voltage time series and the PDF for the voltage series in along with a voltage reference PDF in green [12].

$$KL = \sum_{i=1}^n p_i \ln \left(\frac{p_i}{p_{ref,i}} \right) \quad (3-2)$$

This methodology is tested on the FIDVR response in PSSE at a bus with increasing percentage of IM load (from 5% to 30%) for faults of 3 cycles. The increasing amounts of IM load increased the delay in the recovery of voltage and this led to the KL-index for the increasing amount of IM load. The plots of the voltage and the resulting KL-Index are plotted below in Figure 3.9 and Figure 3.10 respectively.

It can be observed that the KL-index with the least amount of IM is the most negative while the KL-index with the largest amount of IM is the least negative and even goes positive for a small amount of time. As the time increases, all the voltages recover to the pre-contingency voltage and so the KL-index of all the voltages goes to 0 as time increases. Hence, the moving KL-index can differentiate between the various scenarios and can quantify the FIDVR in an online manner.

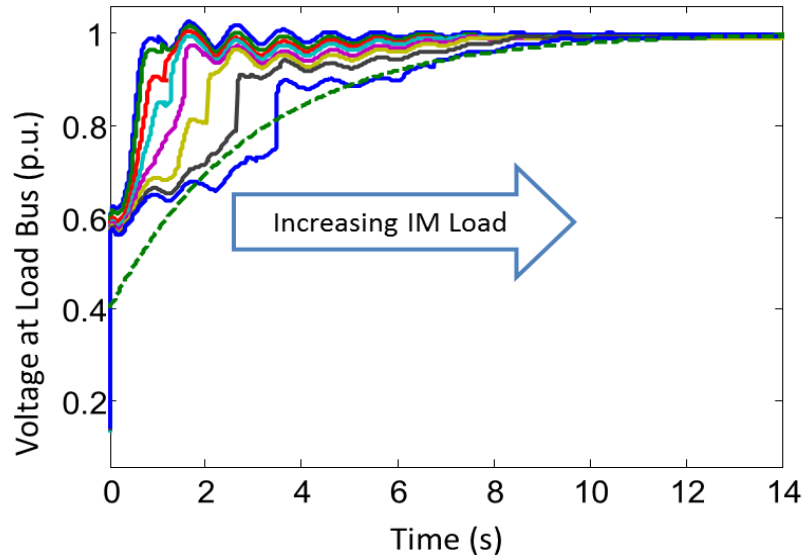


Figure 3.9 The voltage time series at the bus with increasing percentage of induction motor load. The dashed line is the reference voltage.

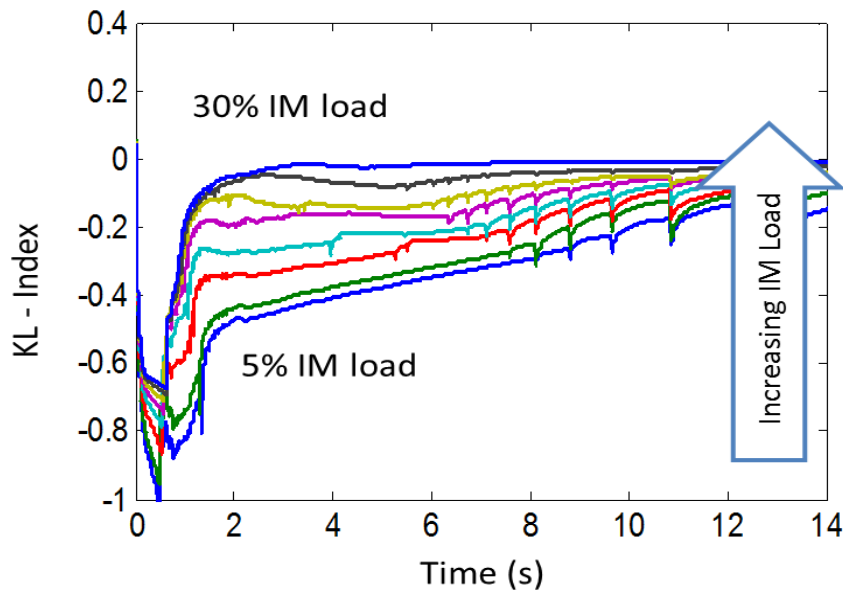


Figure 3.10 The Moving KL-Index of the delayed voltage waveforms. The more the delayed the voltage, the faster the index goes to 0.

There are a few issues with using the KL-index in a realistic setting with noise and sudden outliers. The ‘log’ function in the KL expression is a nonlinear term and can cause the divergence to go very high. Also, the division of two probability densities can be impacted by

sudden switching actions and unexpected behavior, especially when $p_i > 0$ and $p_{ref,i} \sim 0$. This scenario causes the KL index to be negative with a high value due to the division and logarithm function. Thus, the KL index gives a large weight to the bins where p_{ref} is close to zero but p is not close zero. Hence, a smoother metric is preferred for use in the real-time setting and for this purpose the Wasserstein Metric is chosen. The results using this metric are described in Appendix A.

3.3.1 Comparison of the behavior of load admittance and voltage during delayed voltage recovery

After analyzing the results, we recognized that the voltage based quantification methods do not have the capability to give insight into the amount of control necessary to correct the FIDVR. This is because the resulting voltage at a bus facing FIDVR is due to the various causes such as the topology, generator set-points, etc. To overcome this, we tried to use the other parameters of the load to reliably detect and quantify FIDVR. After testing various possibilities, the load admittance is chosen as it demonstrated very clearly the ability to monitor and quantify FIDVR. The voltage and the load power can be used to calculate the load conductance (G) and susceptance (B) using (3-3) & (3-4).

$$G_{load} = P_{load}/V^2 \quad (3-3)$$

$$B_{load} = Q_{load}/V^2 \quad (3-4)$$

As a preliminary exercise, Figure 3.11 & Figure 3.12 plot the voltages and the load conductance (real component of the admittance) for a normal, moderately severe (30% motor stalling) and very severe (60% motor stalling) delayed voltage recovery after a disturbance. The first observation is the voltage waveforms for both normal recovery and delayed recovery have oscillations due to the behavior of the other components in the system. In comparison, the conductance waveform is much better behaved for the normal recovery and delayed

recovery. The oscillations in the voltage are due to the dynamic behavior of the external system (e.g. the generator exciter) and so the impact of these oscillations in the conductance are minimal as the oscillations do not impact the load behavior.

The next observation is that the voltage immediately after the fault is lower for higher amount of motor stalling. Similarly, the load conductance after the fault is cleared increases as the percent of motor stalling increases. However, it is not easy to quantify the severity of the FIDVR event from the voltages as the drop in voltage is not easily related to the severity and depends on the external network parameters. In contrast, the conductance makes it easy to quantify the severity of the event as the conductance increases in a nearly linear manner to the amount of motors stalled. Thus, it provides a quick way to characterize the severity of the FIDVR and enables monitoring and control schemes based on this quantification. The conductance during normal recovery quickly (< 1 sec) returns to the pre-contingency value. On the other hand, the conductance of the delayed voltage scenario has a sudden rise due to the stalling of the 1- ϕ IMs. The sudden rise can be used as a reliable indicator of the onset of the FIDVR phenomenon. The same cannot be said for the voltage as a severe FIDVR on a bus will depress voltages in neighboring buses even if there is no stalling in the neighboring buses.

Finally, the conductance for the delayed voltage scenario can be split into two parts – a flat region and a monotonically decreasing region. The flat region corresponds to the time to initiate the thermal tripping of 1- ϕ IM (t_1) and the region where the conductance reduces which corresponds to the time taken to complete the thermal tripping of 1- ϕ IM (t_2). It is much easier to distinguish between these phases of operation from the conductance plots compared to the voltage plots as the oscillations and other phenomenon can mask the exact time of transition.

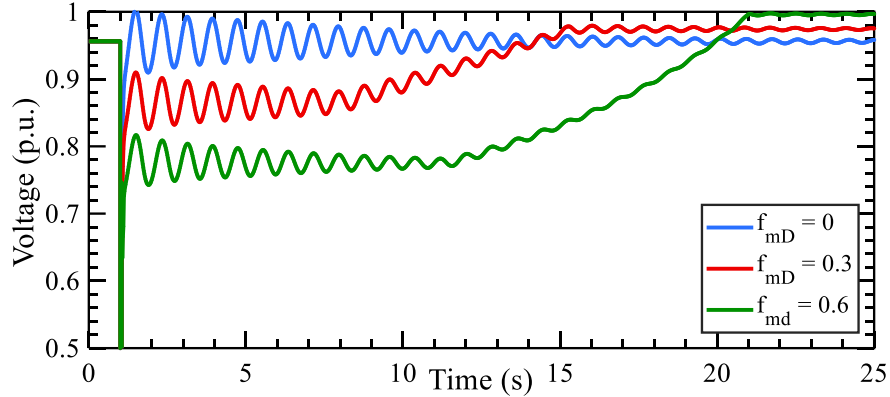


Figure 3.11 Voltage response with various motor stalling proportion

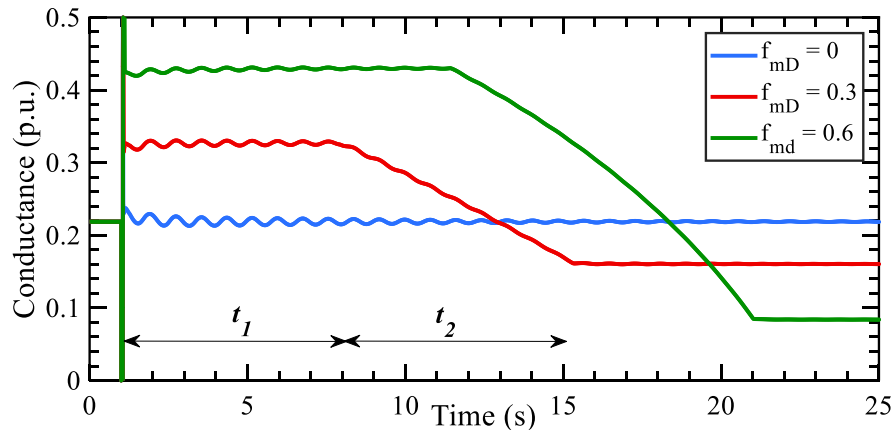


Figure 3.12 Load conductance with various motor stalling proportion. t_1 & t_2 are indicated for $f_{mD} = 0.3$

By observing various conductance (susceptance) plots for various proportions of stalled motor, two observations can be made: (1) the load conductance (susceptance) is nearly constant till the motor thermal protection triggers (2) the slope of conductance (susceptance) due to the thermal disconnection is almost constant. Similar observations can be made FIDVR events in the field both in distribution and transmission systems. Based on these observations, the following hypothesis is suggested - by measuring the admittance just after the FIDVR begins, the values of t_1 and t_2 can be estimated from the load parameters using the admittance based model. Also, if the parameters of the load model were known, then it is even possible to

estimate the times t_1 & t_2 from which the time for the FIDVR to recover can be estimated. If this estimation is greater than a pre-specified duration, then control actions need to be taken to speed up the voltage recovery, either by disconnecting AC loads via smart thermostats and by injecting reactive power via shunts. The overall strategy to monitor and mitigate the FIDVR is presented in the flowchart shown in Figure 3.13.

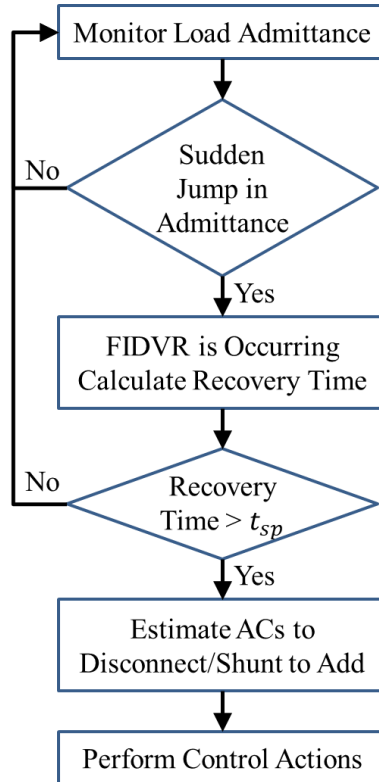


Figure 3.13 *Flowchart of the expected method to monitor and mitigate FIDVR*

The load admittance at the substation is continuously being calculated by the PMU. If it sees a substantial rise in the admittance (given by the load parameters), it can be concluded that the Motor-D is stalled and FIDVR is occurring. Then, based on the load parameters, the time to recovery can be estimated. If the recovery time is less than the specified time (t_{sp}), there is no need to initiate controls as the natural recovery is sufficient. If the recovery time is greater than the specified time, then the control necessary to recover the voltage faster have to

be determined. In this particular case, the control actions are the proportion of AC's disconnect and the amount of reactive support to provide via shunts. To understand how these actions can be performed by analyzing the admittance, an admittance based analysis of the CMLD model is presented in the next section.

3.4 Admittance Based Analysis of Composite Load Model

Figure 3.14 shows the structure of the admittance based composite load model with the load connected to a generator with voltage E and a transmission line with admittance $\mathbf{Y}_{\text{trans}}$. The equivalent feeder admittance is denoted by \mathbf{Y}_{fd} , and includes the substation tap transformer and the shunt compensation to compensate for the voltage drop in the feeder. The PMU is present at the substation before \mathbf{Y}_{fd} and measures V_0 & load current which can be used to calculate the internal voltage from \mathbf{Y}_{fd} . Thus, in the derivations and results, we assume that we know the value of V_i . The A, B & C motors, electronic loads and static loads are represented by $\mathbf{Y}_{\text{ABCES}(V_i)}$ and the 1- ϕ motor is represented by \mathbf{Y}_{mD} . The admittance $\mathbf{Y}_{\text{ABCES}(V_i)}$ is a function of the voltage in order to account for the dynamics of the A, B & C motors and is not constant with time. After a severe fault, the stalled 1- ϕ IM admittance is given by $\mathbf{Y}_{\text{stall}}$. The fraction of 1- ϕ IM connected after stalling is determined by the fraction f_{th} which is the output of the thermal relay.

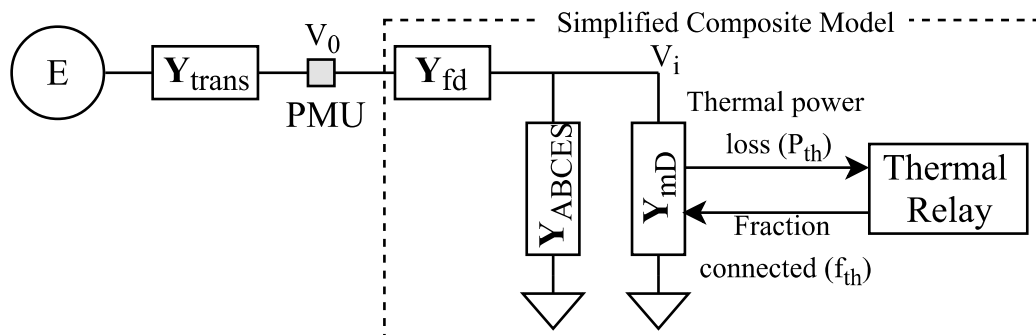


Figure 3.14 Admittance based composite model structure

The PMU is present at the substation and can measure the voltage V_0 , the active power and the reactive power of the load during the FIDVR. The behavior of the static load and the electronic load is directly related to the voltage at the terminal and the power drawn by them can be calculated based on load parameters. The parameters of the load can be taken from the utilities that use them for planning studies or from load modelling studies. A possible source of the parameters is a Load Model Data Tool [14] developed by Pacific North-West National Laboratory (PNNL) to estimate the CMLD parameters of a particular feeder based on the time of day, the weather patterns of the particular location, etc. The total time is made up of two parts – the time to initiate the thermal tripping of the 1-Phase motor (t_1) and the time to complete the thermal tripping of the 1-Phase motor (t_2). By using the CMLD parameters, the time to recover from FIDVR can be estimated and this is presented in the following subsections.

3.4.1 Time to Initiate Thermal Tripping of 1-Phase Motor

From Figure 3.5, the time taken to initiate the thermal tripping of the 1-phase motor is the time taken by the motor to reach the temperature of θ_1 . As the stalling condition occurs suddenly, the input to the thermal delay block can be approximated by a step function. This step input passes through a 1st order time delay block with a delay T_{TH} , and the time taken for the output to reach a temperature of θ_1 needs to be calculated. Using this description and standard definitions, the following equations can be written.

$$V_i^2 = \frac{E^2 \cdot |Y_{eff}|^2}{|Y_{eff} + Y_{ABCES(V_i)} + Y_{mD}|^2}; Y_{eff} = \frac{Y_{fd} \cdot Y_{trans}}{Y_{fd} + Y_{trans}} \quad (3-5)$$

$$V_{i_{post}}^2 = \frac{E^2 \cdot |Y_{eff}|^2}{|Y_{eff} + Y_{ABCES(V_i)} + Y_{stall}|^2} \quad (3-6)$$

$$P_{th_{post}} = V_{i_{post}}^2 \cdot G_{stall} \quad (3-7)$$

$$\theta_1 = P_{th_{post}} (1 - e^{(-t_1/T_{th})}) \quad (3-8)$$

$$t_1 = -T_{th} \cdot \ln \left(1 - \theta_1 / (V_{i_{post}}^2 \cdot G_{stall}) \right) \quad (3-9)$$

The time t_1 can be further approximated using the Taylor expansion $\log(1 - x) \approx -x$, for $x \ll 1$, giving rise to (3-10).

$$t_1 \approx T_{th} \cdot \theta_1 / P_{th} = \frac{T_{th} \cdot \theta_1}{V_{i_{post}}^2 \cdot G_{stall}} \cdot \frac{(Y_{fd} + Y_{rest}(V_i) + Y_{mD})^2}{(Y_{fd})^2} \approx \frac{T_{th} \cdot \theta_1}{V_{i_{post}}^2 \cdot G_{stall}} \quad (3-10)$$

Thus, it seems like $t_1 \propto 1 / (V_{i_{post}}^2 \cdot G_{stall})$, but as $V_{i_{post}} \propto 1/G_{stall}$, the time taken for the thermal tripping to initiate is directly proportional to the value of G_{stall} .

3.4.2 Time to complete thermal disconnection of 1-phase motor

Now that the behavior of the system is understood before θ_1 , we can determine the time taken for the motor temperature to rise to θ_2 from θ_1 by understanding how the thermal trip fraction f_{TH} varies with time. (3-11) to (3-13) follow from the definitions and by utilizing the differential equation relation between the thermal power (P_{TH}) and the motor temperature (θ).

$$\dot{\theta} = \frac{1}{T_{Th}} (P_{TH} - \theta) \quad (3-11)$$

$$f_{TH} = 1 - \left(\frac{\theta - \theta_1}{\theta_2 - \theta_1} \right) \Rightarrow \theta = (\theta_2 - \theta_1) \cdot (1 - f_{TH}) + \theta_1 \quad (3-12)$$

$$\frac{d f_{th}}{dt} = \frac{1}{T_{th}(\theta_2 - \theta_1)} \left(\theta_2 - V_{i(f_{th})}^2 G_{stall} - (\theta_2 - \theta_1) f_{th} \right) \quad (3-13)$$

The complication in solving the above equation is that the value of the voltage V_i changes as the fraction of connected 1-phase motors reduces. This causes the equation (3-13) to be a non-linear equation with no analytical solution. Furthermore, the relation between the voltage V_i and fraction f_{th} is dependent on the system parameters such as closest generator

voltage, other load behavior, etc. A possible way to estimate the time to recover is by considering various limiting cases from the physics of the scenario. Initially, the value of the voltage V_i is low (around 0.75 p.u.), the value of f_{th} is 1 and the value of the slope df_{th}/dt is negative implying that the f_{th} will reduce from 1 and the voltage V_i will increase in magnitude. As the voltage increases and the f_{th} decreases, the slope becomes even further negative and increasing the rate of increase of V_i . Finally, as the value of f_{th} reaches 0, the voltage V_i reaches around 1 p.u. at which time all the 1-phase motors are disconnected and the thermal trip relay stops operating. Thus, the time taken by the f_{th} to go from 1 to 0 is dependent on the V_i and how V_i changes with f_{th} and is denoted by the term t_2 .

The largest value of t_2 occurs if we assume the V_i in (3-13) to be at the minimum value which is equal to the post-contingency value. This is the worst case scenario and the corresponding differential equation and value of t_2 is given by (3-15).

$$\left. \frac{df_{th}}{dt} \right|_{worst-case} = \frac{1}{T_{th}(\theta_2 - \theta_1)} (\theta_2 - V_{i_{post}}^2 G_{stall} - (\theta_2 - \theta_1)f_{th}) \quad (3-14)$$

$$t_{2-worst} = T_{th} \cdot \log \left(1 - \frac{(\theta_2 - \theta_1)}{(V_{i_{post}}^2 G_{stall} - \theta_1)} \right) \quad (3-15)$$

Similarly the smallest value of t_2 occurs if we assume the V_i in (3-13) to be at the maximum value which is the pre fault voltage. This is the best case scenario and the corresponding differential equation and value of t_2 is given by (3-17).

$$\left. \frac{df_{th}}{dt} \right|_{best-case} = \frac{1}{T_{th}(\theta_2 - \theta_1)} (\theta_2 - G_{stall} - (\theta_2 - \theta_1)f_{th}) \quad (3-16)$$

$$t_{2-best} = T_{th} \cdot \log \left(1 - \frac{(\theta_2 - \theta_1)}{(V_{i_{pre}}^2 G_{stall} - \theta_1)} \right) \quad (3-17)$$

Thus the actual t_2 lies between t_{2-best} and $t_{2-worst}$ that can be calculated immediately after the FIDVR starts. This range might be too large in some cases and so fact that can be used is that the behavior of the slope of the susceptance in Figure 3.12 is almost linear. This observation means that an average of the slopes of df_{th}/dt just as the FIDVR begins and just as the FIDVR ends can be used to estimate the t_2 . This is derived in the equations below.

$$\left. \frac{df_{th}}{dt} \right|_{initial} = \frac{1}{T_{th}(\theta_2 - \theta_1)} (\theta_1 - V_{i_{post}}^2 G_{stall}) \quad (3-18)$$

$$\left. \frac{df_{th}}{dt} \right|_{final} = \frac{1}{T_{th}(\theta_2 - \theta_1)} (\theta_2 - V_{i_{pre}}^2 G_{stall}) \quad (3-19)$$

$$\left. \frac{df_{th}}{dt} \right|_{mean} = \frac{1}{2} \left(\left. \frac{df_{th}}{dt} \right|_{initial} + \left. \frac{df_{th}}{dt} \right|_{final} \right) \quad (3-20)$$

$$\left. \frac{df_{th}}{dt} \right|_{mean} = \frac{1}{2T_{th}(\theta_2 - \theta_1)} (\theta_1 + \theta_2 - (V_{i_{pre}}^2 + V_{i_{post}}^2) G_{stall}) \quad (3-21)$$

$$t_{2-approx} = \frac{2T_{th}(\theta_2 - \theta_1)}{(\theta_1 + \theta_2 - (V_{i_{pre}}^2 + V_{i_{post}}^2) G_{stall})} \quad (3-22)$$

This value of t_2 can then be used to estimate the time for the FIDVR to end. It can be seen from (3-22) that the t_2 seems to be inversely proportional to G_{stall} , but as the $V_{i_{post}}^2$ is inversely proportional to G_{stall} , the measured t_2 is directly proportional to G_{stall} . Since the standard construction of the 1-phase motors is such that the $G_{stall} = B_{stall}$, we can use the B_{stall} instead of G_{stall} in equations (3-10) and (3-22). As the load susceptance change is larger than the conductance change during FIDVR, the susceptance can actually be used as a more reliable indicator of the stalling condition and can be used to estimate the times to recover.

3.4.3 Estimating individual component conductance from measurements

To determine the stall conductance, the conductance of the remaining part of the composite load (G_{ABCES}) is determined using the parameters of the composite load model.

G_{ABCES} is a function of the load voltage and its value is then subtracted from the total load conductance calculated from the PMU measurements during the initial period of the FIDVR to arrive at the stall conductance. The load composition is first used to estimate the total conductance of the load at normal operation as follows and it is clear from expression (3-25) that the conductance is a function of the load voltage.

$$P_{load} = P_{ABCE} + P_{st} \cdot (V^2 \cdot f_{stz} + V \cdot f_{stl} + f_{stp}) + P_{mD} \quad (3-23)$$

$$P_{ABCE} = (f_{mA} + f_{mB} + f_{mC} + f_{Elec}) \cdot P_{load} \quad ; P_{st} = f_{st} \cdot P_{load} \quad (3-24)$$

$$G_{load}(V) = \frac{P_{ABCE}}{V^2} + P_{st} \cdot \left(f_{stz} + \frac{f_{stl}}{V} + \frac{f_{stp}}{V^2} \right) + \frac{P_{mD}}{V^2} \quad (3-25)$$

Next, the expression for G_{ABCES} during the FIDVR condition is derived. Due to the time scales involved in the FIDVR phenomenon, we can assume that the A, B & C motors and electronic loads can be approximated as constant power loads. This is valid as the dynamics of these components is very fast compared to the FIDVR and so the steady state of these components is reached in 1s-2s after the fault is cleared. Ideally, the equivalent circuit of the 3-phase motor [10a] ought to be used to estimate the conductance. But this needs many more parameters and the machine slip. In the interest of needing as less number of parameters as possible, the assumption of constant power loads is used. We observed in several numerical simulations that this is a reasonable assumption and using this leads to <5% error in the estimation of G_{ABCES} . The power of the A, B & C motors and electronic load can be written in terms of the pre-fault load power as (3-26). This expression also includes the output fraction from the under-voltage relays (f_{UV}) of these components as the protection schemes modify the power of each component by disconnecting load during the initial low voltage of the FIDVR. The final expression for G_{ABCES} is given by (3-28) and is a function of the voltage V_i .

$$P_{ABCE_{post}} = \left(\begin{array}{l} f_{mA} \cdot f_{UVA} + f_{mB} \cdot f_{UVB} \\ + f_{mC} \cdot f_{UVC} + f_{Elec} \cdot f_{UVElec} \end{array} \right) P_{load_{pre}} \quad (3-26)$$

$$P_{st_{post}} = f_{UVst} \cdot f_{st} (V_i^2 \cdot f_{stz} + V_i \cdot f_{stl} + f_{stp}) P_{load_{pre}} \quad (3-27)$$

$$G_{ABCES}(V_i) = (P_{ABCE_{post}} + P_{st_{post}}) / V_i^2 \quad (3-28)$$

As motor-D stalls quickly after a fault (<0.1s), the conductance of motor-D during the initial phase of FIDVR (post-contingency) is equal to G_{stall} . Thus, the total conductance of the load during post-contingency can be written as the sum of G_{ABCES} and G_{stall} which can be calculated from PMU measurements of load power and voltage. Thus, the stall conductance of the composite load can then be estimated using the expression (3-30). The same expression can be used to estimate the conductance of motor-D by substituting the value of the load voltage any time after FIDVR begins.

$$G_{load_{post}} = \frac{P_{load_{post}}}{V_{i_{post}}^2} \approx G_{ABCES}(V_{i_{post}}) + G_{stall} \quad (3-29)$$

$$G_{stall} \approx \frac{P_{load_{post}}}{V_{i_{post}}^2} - G_{ABCES}(V_{i_{post}}) \quad (3-30)$$

Thus, using PMU measurements along with the fraction of the A,B,C motors, electronic loads, static ZIP parameters and UV protection fraction, the stall conductance can be calculated during the first 1s-2s of an FIDVR event. It can be observed that the key parameters that impact the recovery time from (3-9) & (3-22) are G_{stall} , B_{stall} , θ_1 , θ_2 , & T_{th} . Also, as V_i is estimated from V_0 , Y_{fd} is important. These parameters have been shown to be the most crucial parameters that impact the behavior of FIDVR using simulations on actual utility data [15]. The derivation for the recovery time presented here is from first principles and provides a theoretical basis for these parameters to be the most critical parameters determining the behavior of the FIDVR response. An interesting observation is that even though a simplified equivalent of the system

is used to derive the equations, the terms E & Y_{trans} do not appear in the final expressions as their impact is indirectly present in the voltage measurements. Thus, there is no need to estimate E & Y_{trans} for predicting the recovery time. Figure 3.15 summarizes the proposed methodology for detection and monitoring of FIDVR using admittances as a flow chart.

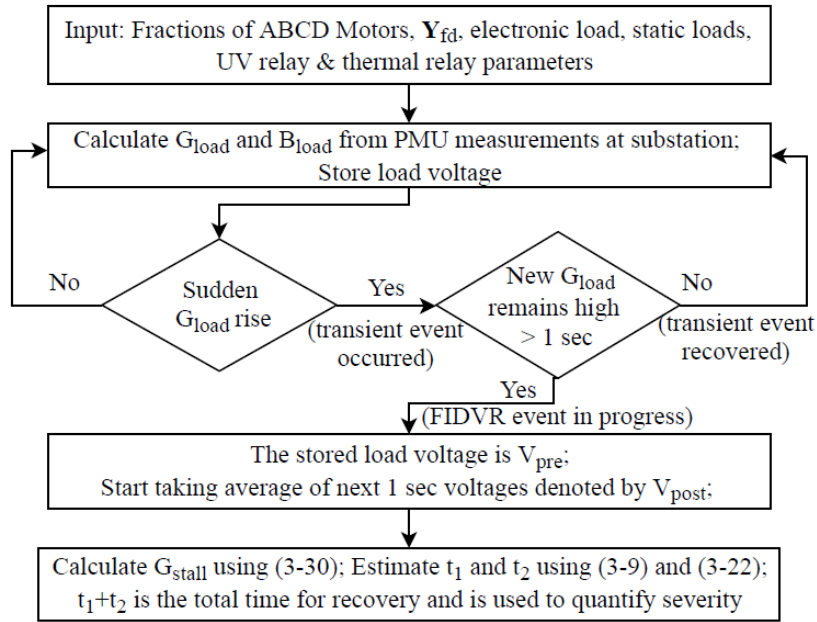


Figure 3.15 Flowchart for detecting and monitoring FIDVR using measurements

3.4.4 Discussion on the relation between t_1 , t_2 and admittance

All the expressions derived in the previous section relating t_1 & t_2 to the admittance include the term V_0 , which is the voltage at the load bus just after the FIDVR has started. This voltage is dependent on the parameters of the system such as the topology, behavior of other loads, etc. While it is true that t_1 & t_2 are directly proportional to the value of the admittance, the relation inherently involves V_0 which is not easy to analytically analyze. One way to overcome this limitation is to perform multiple simulations with varying parameters of the load and analyze how the time to initiate thermal tripping and the time to complete thermal tripping are related to the measured susceptance after the FIDVR event occurs. This is possible as the

fraction of the load that is distributed between Motors A, B, C & D, the Electronic load and the Static load is something that the utilities have information about for a particular substation. The fractions vary within a range over the course of the day and depend on the season and the load type (residential, commercial etc.). As an example, Figure 3.16 plots the load variation and the load composition over the course of 24 hours in Portland in July [14].

It can be seen that the total load varies over a wide range but the load composition varies over a smaller range and this variation will be used to create multiple scenarios to test in a time domain simulator. The majority of the load parameters such as the stall impedance, stator resistances, etc. are not changed in these simulations as they are automatically scaled based on the fractions. From the simulations results the values of the load susceptance immediately after the stalling (B_0) and the times t_1 and t_2 are recorded. Based on the results of the simulations, mathematical relations between B_0 and t_1 and between B_0 and t_2 need to be estimated. The standard techniques from linear regression are utilized to get the coefficients $\alpha_0, \alpha_1, \beta_0$ & β_1 that satisfy the following linear relation

$$t_1 = \alpha_0 \cdot B_0 + \alpha_1 \quad (3-31)$$

$$t_2 = \beta_0 \cdot B_0 + \beta_1 \quad (3-32)$$

Once the coefficients $\alpha_0, \alpha_1, \beta_0$ & β_1 are determined, they are used to estimate the values of t_1 and t_2 in an online manner from the measured load admittance. They can also be used to estimate the amount of control action to be taken to ensure that the voltage can recover within a specified time and this is presented in the next section.

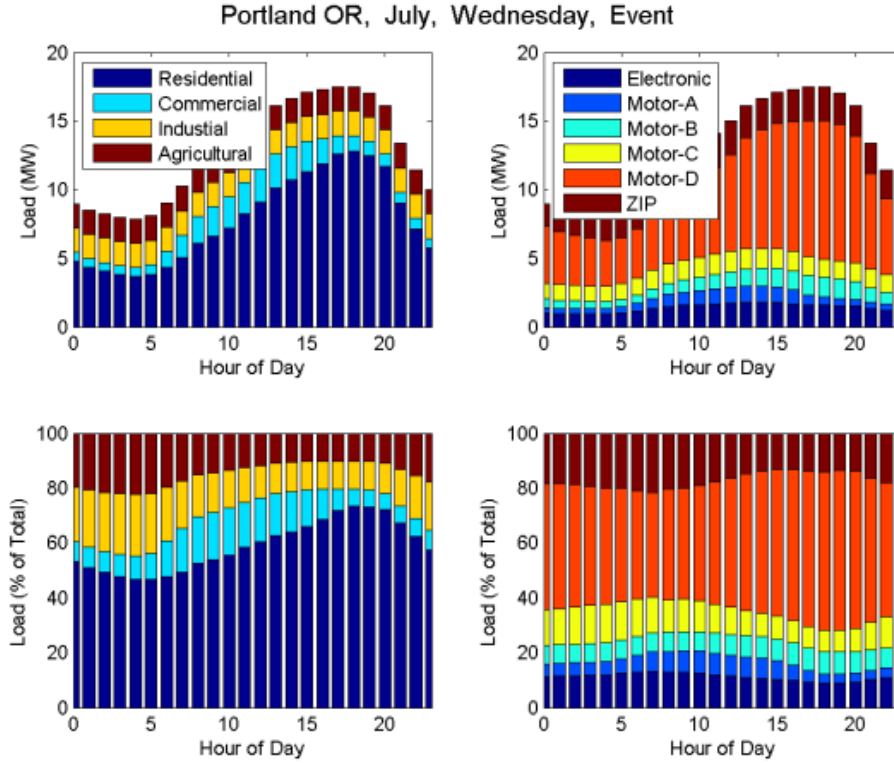


Figure 3.16 *The variation of the load and its composition over the course of a day in Portland in July [14].*

3.4.5 Disconnecting AC motors to recover from FIDVR

Now that we have methodology to estimate the time to recover from FIDVR using load admittances, utilizing a control scheme based on the same framework is the next step. If the estimated time to recovery is more than a specified time, then a control scheme needs to be triggered that ensures that the voltage recovers faster. As the majority of the stalled motors are the residential air conditioners that are not equipped with the under voltage (UV) relays, these motors are chosen for improving the recovery of FIDVR (see Appendix B).

The increasing use of smart thermostats in modern residences enables the utility to utilize the thermal capacity of the residences to improve the overall system. The smart thermostats can turn the AC's off very quickly when they receive a signal from the utility [16]. The disconnection of the stalled air conditioner has the following advantages:

1. A stalled AC motor is not actually performing any useful work as it is not operating as usual and so disconnecting this motor will not impact the customer.
2. A stalled AC motor will disconnect naturally via thermal protection anyhow (after around 15-25 sec) and will reconnect after the excess heat is dissipated, which might take almost 15min - 30 min. The proactive disconnection via a smart thermostat implies that the temperature inside the motor is not high and the excess heat to dissipate is minimal, ensuring that the motor reconnects more quickly.

The motors that are stalling always seem to be the present in the same feeders [17] and so the utilities can determine the motors to target for the installation of the smart thermostats. To determine how much proportion of the AC load should be tripped, the behavior of the susceptance with disconnection of a certain proportion of the AC loads should be understood. Figure 3.17 plots the expected idealized behavior of the susceptance during FIDVR with a proportion of the AC load disconnected after time τ_0 .

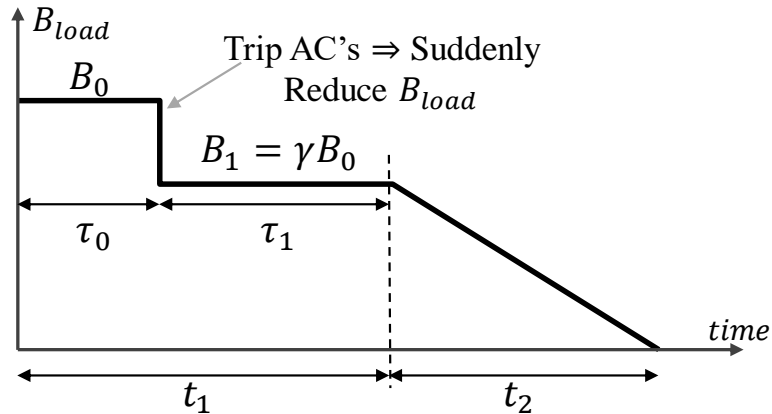


Figure 3.17 *Idealized behavior of the susceptance during FIDVR with AC disconnection*

The initial susceptance at the beginning of FIDVR is B_0 , the AC load is disconnected at a time τ_0 , the susceptance immediately after the disconnection is γB_0 and $(1 - \gamma)$ proportion of the AC load is disconnected by the smart thermostats. The time τ_0 is the time when the AC

smart thermostats disconnect from the grid and takes the latency of the control signal and other communication delays into account and is usually of the order of 1 – 3 seconds. The total recovery time for the FIDVR is given by $t_1 + t_2$ and this time is specified by the utility.

As the time t_1 is determined by the heating of the motor coil, an average susceptance value can be used as a first order approximation to determine it from the susceptance. Thus, t_1 is determined by the weighted average susceptance of B_0 and B_1 weighted by τ_0 and τ_1 and the time t_2 is determined by B_1 . The utility would like to estimate the amount of AC's to trip at a particular time τ_0 so that the total time to recovery is equal to a specified time, t_{sp} . The following equations are derived from their definitions.

$$B_{avg} = \frac{\tau_0 B_0 + \tau_1 B_1}{\tau_0 + \tau_1} = \frac{\tau_0 + \gamma \tau_1}{\tau_0 + \tau_1} B_0 \quad (3-33)$$

$$t_1 + t_2 = t_{sp} \quad (3-34)$$

$$\tau_0 + \tau_1 = t_1 \quad (3-35)$$

As described in the previous section, t_1 and t_2 can be approximated as linear functions of the susceptance. Thus, using equations (3-31) & (3-32), the following equations can be written.

$$t_1 = \alpha_0 \cdot B_{avg} + \alpha_1 = \alpha_0 \cdot \frac{\tau_0 + \gamma \tau_1}{\tau_0 + \tau_1} B_0 + \alpha_1 \quad (3-36)$$

$$t_2 = \beta_0 \cdot B_1 + \beta_1 = \beta_0 \cdot \gamma \cdot B_0 + \beta_1 \quad (3-37)$$

The coefficients $\alpha_0, \alpha_1, \beta_0$ & β_1 are known from offline studies as described in section 3.4.3. Combining the above equations, the following equation (3-38) can be obtained. This is

a quadratic equation that can be solved easily to estimate the value of γ . There are 2 solutions and only the solution with $\gamma < 1$ and $\gamma > 0$ is physically realizable.

$$(t_{sp} - \beta_0 B_0 \gamma - \beta_1)(t_{sp} - \beta_0 B_0 \gamma - \beta_1 - \alpha_1 - \alpha_0 \gamma B_0) = \alpha_0 \tau_0 B_0 (1 - \gamma) \quad (3-38)$$

After solving (3-38), the resulting γ implies that $(1 - \gamma)$ fraction of the AC load has to be tripped at τ_0 time instant to ensure that the FIDVR event is resolved within the specified time. To test this method on a multi-bus system, the IEEE 162 bus system is used. Multiple offline studies are performed with the varying proportion of 3-phase motors and 1-phase motors and the results are described below.

3.5 Numerical Results for the IEEE 162 Bus System

The IEEE 162 bus system has 17 generators, 111 loads, and 238 transmission lines with a total generation of 15,546 MW and a total load of 15,387 MW. The load buses that are most sensitive to faults are buses numbered 111, 133, 134, 135, 136, 137, 139, 140, 143, 144, 145 & 146 [18]. These 12 load buses were stepped down through distribution transformers to the 12.47 kV level, and the composite load model represented by CMLD in PSSE is used at these 12.47 kV load buses in the dynamic simulation studies. Several simulation runs in PSSE are conducted by varying the load fraction of 3-phase motors, 1-phase motors and Static Load. The results for the following cases are tabulated.

1. Case-1: $f_{mA} = 0.15, f_{mB} = 0.05, f_{mD} = 0.1, f_{Elec} = 0.15, f_{stat} = 0.55$
2. Case-2: $f_{mA} = 0.15, f_{mB} = 0.05, f_{mD} = 0.15, f_{Elec} = 0.15, f_{stat} = 0.50$
3. Case-3: $f_{mA} = 0.15, f_{mB} = 0.05, f_{mD} = 0.2, f_{Elec} = 0.15, f_{stat} = 0.45$
4. Case-4: $f_{mA} = 0.15, f_{mB} = 0.05, f_{mD} = 0.25, f_{Elec} = 0.15, f_{stat} = 0.40$
5. Case-5: $f_{mA} = 0.15, f_{mB} = 0.05, f_{mD} = 0.3, f_{Elec} = 0.15, f_{stat} = 0.35$
6. Case-6: $f_{mA} = 0.15, f_{mB} = 0.05, f_{mD} = 0.35, f_{Elec} = 0.15, f_{stat} = 0.30$

7. Case-7: $f_{mA} = 0.15, f_{mB} = 0.05, f_{mD} = 0.4, f_{Elec} = 0.15, f_{stat} = 0.25$
8. Case-8: $f_{mA} = 0.15, f_{mB} = 0.05, f_{mD} = 0.45, f_{Elec} = 0.15, f_{stat} = 0.20$

At 1 second, a 3-phase to ground fault is applied at bus 120 for 3 cycles (50 ms) and this leads to FIDVR being observed at load buses with 1- ϕ IM. The voltage and the load conductance at bus 135 for the various scenarios is plotted in Figure 3.18 and Figure 3.19. For all the scenarios, the load voltage oscillates making it is hard to detect motor stalling just from the voltages, especially for the cases with small percentage of 1- ϕ IM. Also, the oscillations make it hard to quantify the severity of the FIDVR event as the distance between the voltages get closer to each other with the same proportion of the increment in the proportion of the 1- ϕ IM. Furthermore, it is hard to detect the instant when the thermal relay begins disconnection just using the voltage information. In contrast, the stalling can be clearly detected by the sudden rise of load conductance after the fault and the less amount of oscillations in the conductances make it easy to quantify the severity of an event. The severity of the FIDVR is calculated based on the amount of conductance rise from the base case as the distance between the conductances is nearly constant with the same increment in the proportion of the 1- ϕ IM. Additionally, it is easy to identify the instant when the disconnection of the 1- ϕ IM begins as it is the instant when the conductance plot starts to decrease. Thus, the behavior of the conductance is easier to analyze in order to understand the FIDVR phenomenon for larger systems as well.

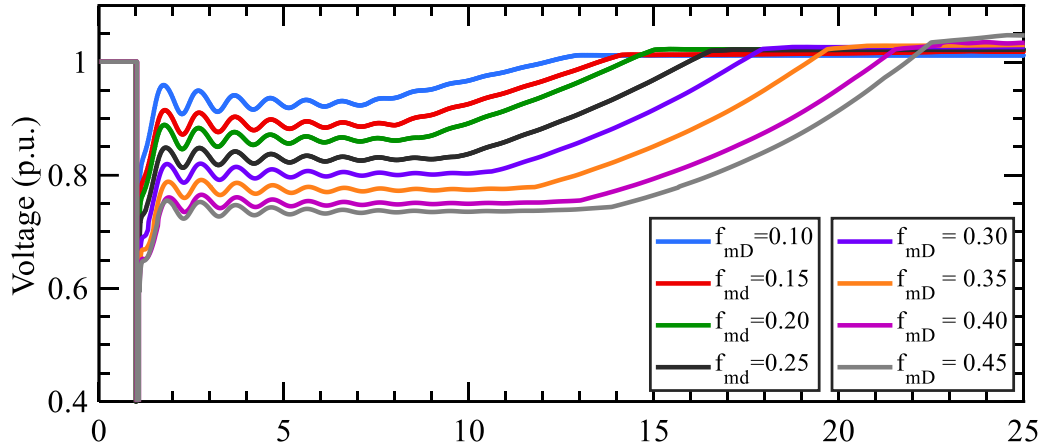


Figure 3.18 Voltage at Bus 135 for $f_{mD} = 0.10$ to $f_{mD} = 0.45$ with fault at 1s

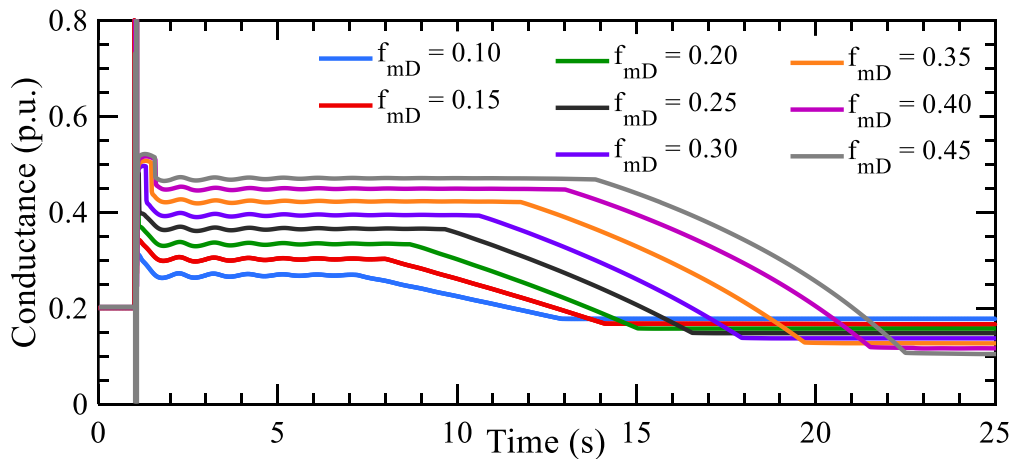


Figure 3.19 Load conductance for $f_{mD} = 0.10$ to $f_{mD} = 0.45$ with fault at 1s

In order to validate the assumption that the behavior of the 1- ϕ IM dominate the overall load behavior, the conductance of the individual A,B,C,D motors, electronic and static load is plotted versus time in Figure 3.20 for the case with $f_{mD} = 30\%$. The conductances before the fault are approximately in the same proportion to their powers as the voltages are close to 1 p.u. After the FIDVR event, the conductance of the 1- ϕ IM rises to several times its nominal value while the conductance of the other components changes by a much smaller amount. Thus, the increment of the load conductance is mainly due to the change of the conductance of

the 1- ϕ IM due to the stalling. This validates the key proposition that the time to recover from FIDVR is mainly dependent on the behavior of the 1- ϕ IM.

Next, to verify that the expression in (3-30) can indeed estimate the stalled motor conductance, the estimated 1- ϕ IM conductance along with the actual 1- ϕ IM conductance is plotted versus time in Figure 3.21 for three different proportions of 1- ϕ IM. It can be observed that the estimated motor conductance has some switching transients and oscillations due to the behavior of the other components of the composite load. But after a short time (~ 1 sec), the estimated conductance matches with the actual 1- ϕ IM conductance. Even though we are only interested in the 1- ϕ IM conductance just after the FIDVR event begins, the expression in (3-30) is able to estimate the conductance over the entire FIDVR event, validating the various assumptions that we made for the derivation.

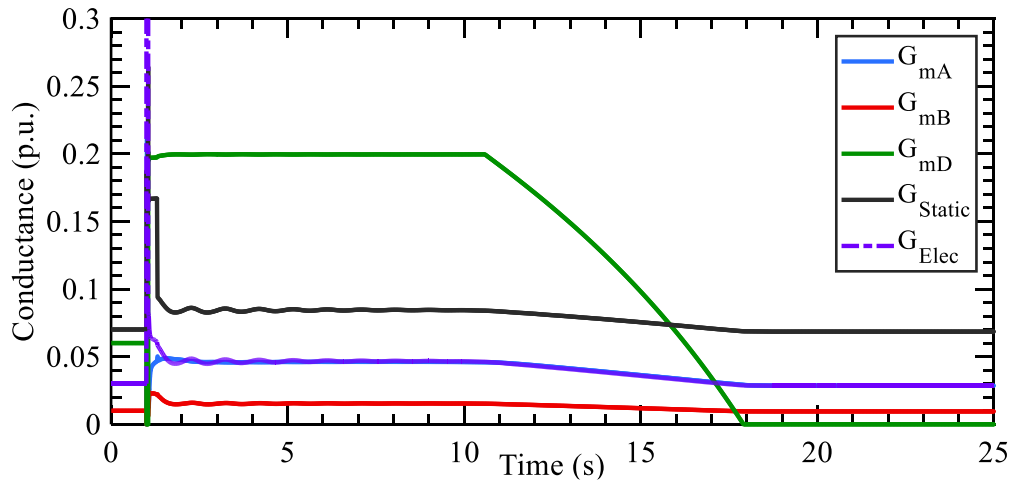


Figure 3.20 Conductance of the components of the CMLD model for $f_{mD} = 0.3$

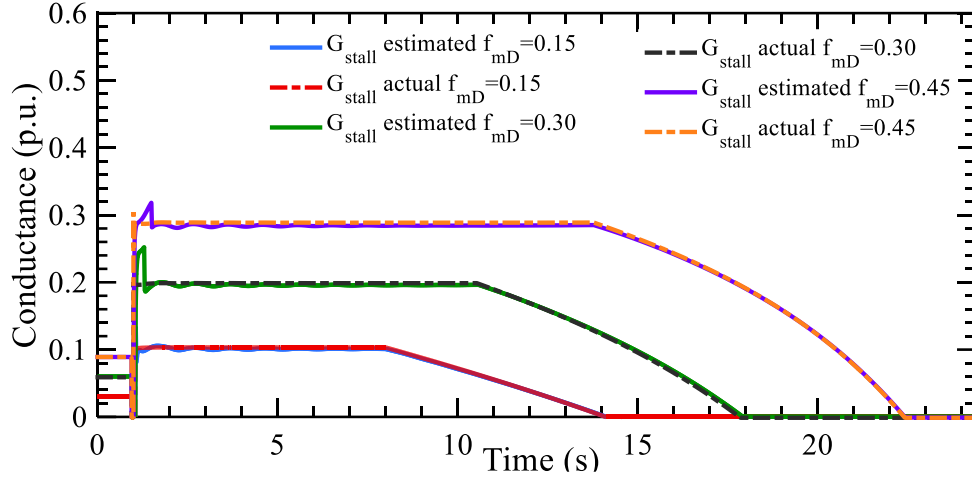


Figure 3.21 Estimated and actual stall conductance for $f_{mD} = 0.15, 0.3$ & 0.45

Now that the simplifying assumptions of the model have been validated, the times t_1 and t_2 that characterize the FIDVR event can be estimated from equations (3-9) & (3-22) using the estimated stall conductance and the measured pre-contingency and post-contingency voltage. As there are oscillations present in the voltages, the average voltage between 1 sec & 2 sec after the fault is cleared is used for the post-contingency voltage. The results of the actual times along with the estimated times for the FIDVR with varying amounts of f_{mD} is presented in Table 3-1. It can be seen that the estimated stall conductance and the estimated times t_1 and t_2 have an error less than 5% of the true measured values. The maximum error occurs when the f_{mD} percent is less due to the fact that the impacts of the dynamics of A,B,C motors are comparable in these scenarios. As the f_{mD} percent increases, the estimated times get closer to the actual values and start becoming more than the actual values, validating the various approximations made in the derivations of the expressions for recovery time. As the measurements are all at a single substation, the proposed method is a local method to detect and quantify FIDVR recovery time in an online manner.

Table 3-1 Actual and estimated G_{stall} , t_1 & t_2 with varying $1-\phi$ IM proportion

f_{md}	G_{stall} actual	t_1 actual	t_2 actual	G_{stall} estim.	t_1 estim.	t_2 estim.
10%	0.07	6.3 s	5.6 s	0.068	6.1 s	5.3 s
15%	0.10	7.0 s	6.1 s	0.097	6.85 s	5.9 s
20%	0.13	7.7 s	6.3 s	0.124	7.6 s	6.3 s
25%	0.17	8.7 s	6.8 s	0.166	8.6 s	6.9 s
30%	0.20	9.7 s	7.2 s	0.195	9.55 s	7.3 s
35%	0.23	10.9 s	7.7 s	0.225	10.7 s	7.9 s
40%	0.26	12.1 s	8.4 s	0.254	12.0 s	8.5 s
45%	0.29	12.9 s	8.7 s	0.285	13.0 s	8.9 s

Now that we have a local method to estimate FIDVR recovery time, a control scheme based on the same framework is the next step. If the estimated recovery time is more than a specified time (determined by the utility), then a control scheme needs to be triggered that ensures that the voltage recovers faster. The main reason for mitigating FIDVR is that depressed voltages over several seconds can lead to generators reaching their field current limits as they try to supply the excessive reactive power required by the load [1]. At present, utilities mitigate FIDVR by installing SVC's using extensive simulations [4]. However, by using the PMU's to detect FIDVR in real-time, we can utilize the flexibility of the loads to mitigate FIDVR.

As the majority of the stalled motors are the residential air conditioners that are not equipped with the UV relays, disconnecting these motors by smart thermostats is used to recover from FIDVR. The increasing use of smart thermostats in modern residences enables the utility to utilize the thermal capacity of the residences to improve the system behavior. The smart thermostats can turn the AC's off quickly when they receive a signal. A stalled AC is

not actually performing any useful work as it is not operating as usual and so disconnecting this motor will not impact the customer. To determine how much proportion of the AC load should be tripped, we utilize the approximate linear relation between the recovery time and the load susceptance. To identify the regression coefficients of t_1 and t_2 to B_0 , a regression problem is solved to get an expression for t_1 and t_2 in terms of B_0 . The resulting expressions are shown in (3-39) & (3-40).

$$t_1 = 39.5 \cdot B_0 + 2.4 \quad (3-39)$$

$$t_2 = 17.5 \cdot B_0 + 4 \quad (3-40)$$

While estimating the linear relation from offline studies, the scenarios with larger t_1 and t_2 are given more weightage as we need more accuracy when the amount of FIDVR is high. To test the generalizability of the linear expressions for the recovery time, a fault at bus 75 is used, which is in the same contingency cluster [19] but is different from the trained scenario. The FIDVR recovery time is measured from the simulations and is compared with the estimated time from (3-39) & (3-40) are listed in Table 3-2.

Table 3-2 *Error in prediction of t_1 & t_2 using linear regression*

f_{md}	B_0	t_1 actual	t_2 actual	t_1 estim.	t_2 estim.
10%	0.07	6.3 s	5.6 s	5.2 s	5.2 s
15%	0.1	7.0 s	6.1 s	6.4 s	5.8 s
20%	0.13	7.7 s	6.3 s	7.5 s	6.3 s
25%	0.16	8.7 s	6.8 s	8.7 s	6.8 s
30%	0.19	9.7 s	7.2 s	9.9 s	7.3 s
35%	0.22	10.9 s	7.7 s	11.1 s	7.9 s
40%	0.245	12.1 s	8.4 s	12.1 s	8.3 s
45%	0.27	12.9 s	8.7 s	13.1 s	8.7 s

It can be seen that the times estimated from the linear expressions for the cases with $f_{mD} > 20\%$ are within 0.25 sec of the true recovery time, demonstrating that the linear expressions for the bus are accurate for the severe FIDVR events. Next, using the coefficients estimated in (3-39) & (3-40), the amount of the control action (in this case AC disconnection) necessary to recover the voltage within a specified time can be determined by solving for γ in (3-38). To demonstrate this, the scenario with $f_{md} = 30\%$ with the fault at bus 75 is chosen in which voltage recovers in 16.9 sec. The amount of ACs to disconnect is estimated using (3-38) for recovery time of 14 sec and 13 sec with a τ_0 of 2 sec and 3 sec, leading to 4 test cases. Table 3-3 lists the actual values of time to recover from the FIDVR event with a fraction of AC load tripped as determined by solving equation (3-38) for different cases.

Table 3-3 *Time to recover from FIDVR event in the PSSE simulations by tripping fraction of AC's*

Time to recover from FIDVR (t_{sp})	Time to trip AC's (τ_0)	AC tripped calculated by (3-38)	Actual time to recover from PSSE simulations
14 sec	2 sec	37 %	13.45 s
14 sec	3 sec	40 %	13.35 s
13 sec	2 sec	49 %	12.70 s
13 sec	3 sec	54 %	12.75 s

It can be seen that the error percent in the total recovery time for these cases is within 5%, validating the estimation of the percent of ACs to disconnect. It can also be observed that the percent of the ACs to disconnect increases as the specified time reduces and the τ_0 increases, which is intuitive. The corresponding voltages plotted in Figure 3.22 demonstrate that the voltages recover to the pre-contingency voltage in a controlled manner after the AC disconnection. Hence, the expressions for the time to recovery can be used to determine the

percentage of AC's to trip to ensure that the FIDVR event is over within a pre specified amount of time.

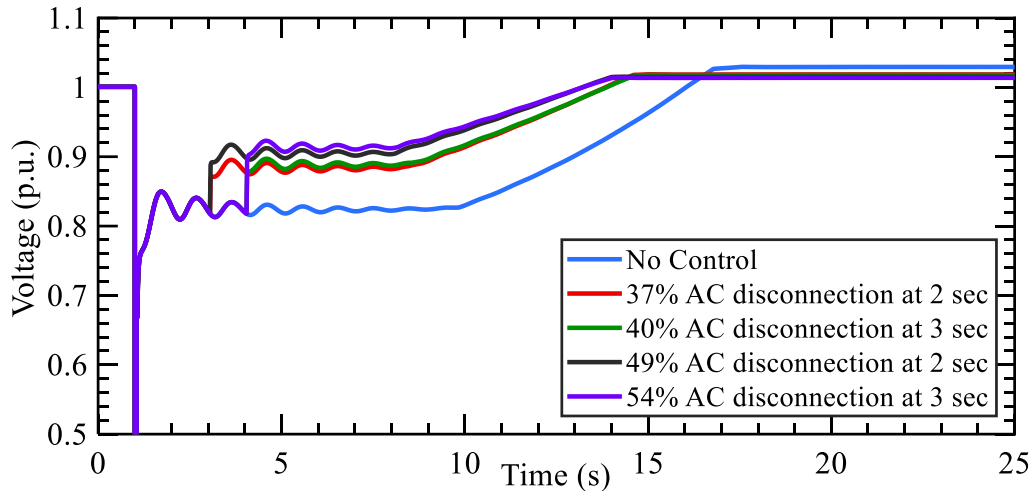


Figure 3.22 *Voltage at Bus 135 with and without load control*

3.6 Real-Time Cyber-Physical Test-Bed Implementation

The application of synchrophasors to improve the voltage stability in the short term is still an untested application in the field and is ideal for implementation in a Real-Time Test-Bed. There is a need to test it in a realistic situation to ensure that the proposed methodology can indeed be utilized in real-time in the field by including the various non-idealities that occur in the field (measurement noise, data drop and delays, etc.). For this purpose, Real-Time Cyber-Physical Test-Bed at ISU is used to simulate the power system in real-time along with the actual hardware used in the industry such as PMU's and relays.

The main components of the Cyber Physical Test-Bed are the following

1. Real time Power System Simulator
2. Phasor Measurement Units (PMU's) with GPS
3. Phasor Data Concentrator to aggregate the data (OpenPDC)
4. Historian database to store the data

5. Analytics Program (Matlab, Python, etc)

A schematic displaying the interfaces between the various components is shown in Figure 3.23. A brief description of the two power system simulators in the test bed is given below

1. Real Time Digital Simulator (RTDS): This simulator uses an Electro Magnetic Transient Program (EMTP) algorithm with short time steps (50 micro sec) to simulate the power system, making it closer to the field than phasor based programs like PSSE or PSLF. It has Analog and Digital cards that output the actual signal at various nodes in the simulation model and allow hardware to be connected. It can also process digital packets of data as input to trip or close lines in the model while running in real-time.
2. Opal-RT Simulator: This is another real time simulator for power systems. The specialty of this simulator is that we can simulate systems either in EMTP representation, with short time steps (50 μ s) and in Phasor representation, with coarse time steps (10 ms). This feature allows us to simulate comparatively large systems (1000 bus systems) in real time using the Phasor representation. Opal-RT also has Analog and Digital cards that output the signal at various nodes in the simulation and allow hardware to be connected.
3. Phasor Measurement Units (PMU's) with GPS: 3 Schweitzer Relays with PMU capability (SEL-421) are present in the lab and are interfaced to the Real-Time simulators using the low-level interface. The Real-Time simulators also have the provision for directly streaming out simulated PMU data from a few nodes in the power system onto the network (called as virtual PMUs). This is convenient as we want to

simulate systems with large nodes and it is unrealistic to have all the data from physical PMUs. A GPS is present to give the clock signal to the Physical and Virtual PMUs.

4. Phasor Data Concentrator (PDC) & Historian: A Phasor Data Concentrator is necessary to time align the various samples from different PMU's and to put the data packets in order. Furthermore, we need to store the data that is being streamed from the PMU's in a reliable manner. The usual standard is to store the data in a Historian database and this is programmed right in the PDC. Simple filtering schemes can also be implemented right at the PDC.
5. Analytics Program: The final component in the Test-Bed and also the one with which the user can understand and view the results in real time. Presently, we have programmed and interface between PDC and python to analyze the data and display it as plots in a python window. The python program can also send signals to the Opal-RT via an OPC Server so that the controllable components can be included in the simulation.

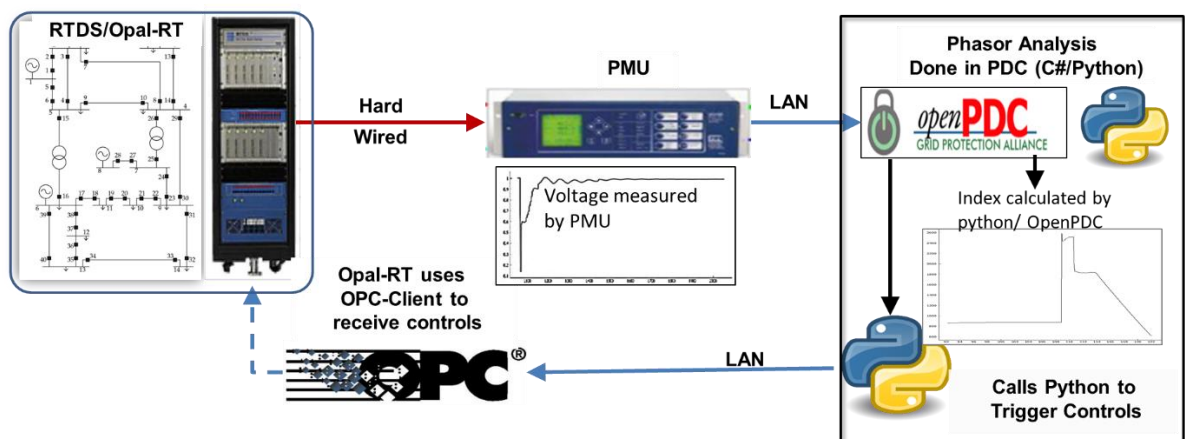


Figure 3.23 The lab setup of the real-time cyber-physical test-bed with the various components – Opal-RT, PMU, OpenPDC, Python, OPC.

While using a real-time power system simulator, it is always important to keep the phenomenon of interest in mind. These test-beds provide quite a bit of flexibility to implement a system and it is easy to get consumed by the details while trying to simulate a system. This is because of the fact that the largest system that can be simulated in hardware is limited due to the real-time nature of the simulation. In contrast, a conventional time domain simulation program running on a workstation does not have this limitation.

For example, if the phenomenon of interest has a time scale of hundreds of milliseconds (voltage stability) to seconds (Inter-area Oscillations), then there is no need for EMTP scale simulations. The phenomenon can be captured reasonably well with phasor based simulations and this enables us to simulate larger systems as the time step can be increased to tens of milliseconds (ms). On the other hand, if the phenomenon of interest is in timescales less than 1 millisecond (analyzing harmonics due to power converters, etc.), then there is a need for EMTP simulations. This will limit the number of nodes in the system as the time step needs to be in tens of microseconds. In the present case of simulating FIDVR and controlling AC motors to disconnect, it is sufficient to do this simulation in a phasor domain simulation.

A load model that can demonstrate FIDVR is modelled in open-modelica [20] and is loaded into the real-time simulator to demonstrate FIDVR. The PMU is connected via hardware outputs to receive the voltage waveform when the fault clears and the FIDVR occurs. The PMU data is streaming to a PDC where the admittance is monitored in real-time. The voltage at the load bus goes to around 0.9 p.u. and recovers to pre-contingency voltage in around 20 seconds. By sending a control action to disconnect 30% of the AC loads after 2 seconds of fault clearing, the voltage recovers to pre-contingency level in 12.3 seconds. This

is demonstrated in Figure 3.24 with the voltage waveform and the admittance waveform. More results from the real-time test-bed are presented in Appendix D.

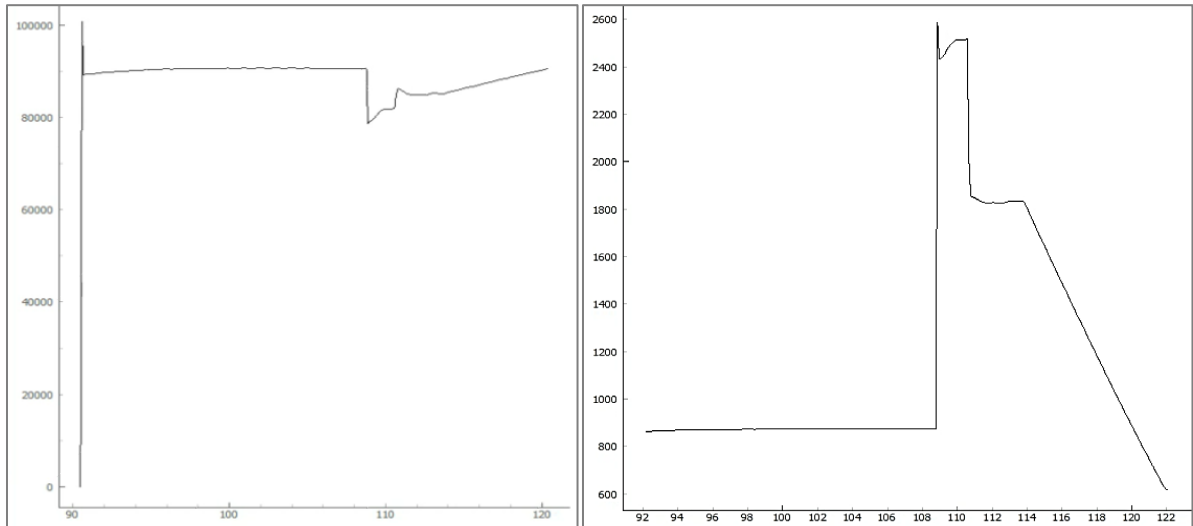


Figure 3.24 *The delayed voltage response (left) and the corresponding susceptance plot (right).*

3.7 Conclusion

In this chapter, the problem of monitoring and mitigating FIDVR is addressed by utilizing the high sampling rate of PMU's and understanding the physics underlying the FIDVR problem to issue control signals to smart thermostats and shunt devices in real-time.

The initial methodology to understand and monitor is based on the voltage measurements being made at the transmission substation where the FIDVR is manifested. The Wasserstein metric is proposed to quantify the FIDVR phenomenon in real time while ensuring that it calculated at the PMU is robust and reliable. To determine the control, just utilizing the voltage did not provide sufficient information as several varying parameters of the load can lead to similar voltages. To overcome this, the composite load model is studied in detail and is simplified based on engineering judgment and it is shown that an admittance approach is well

suited for this purpose. Analytical relations were derived by approximations of expressions and the time to recovery in terms of the measured admittance is derived. This is verified on PSSE simulations and the error between the expected times and the measured times to recovery were less than 1 second.

The low error provides confidence to utilize this method for control ensuring that the FIDVR recovers within a pre-specified time. The only control schemes that can mitigate FIDVR are shown to be the tripping of Air Conditioners or the injection of reactive power via Shunt devices. An analytical expression for the magnitude of control action as a function of trip time is derived and this is also tested in PSSE with accuracy of 1 second with control actions upto 30% Air conditioner tripping, providing a use case for the utilities to implement smart thermostats in their distribution network.

3.8 References

- [1] DOE-NERC FIDVR Conf., Sep. 29, 2009. [Online]. Available: <http://www.nerc.com/files/FIDVR-Conference-Presentations-9-29-09.pdf>.
- [2] B. R. Williams, W. R. Schmus, and D. C. Dawson, "Transmission voltage recovery delayed by stalled air conditioner compressors," *IEEE Trans. Power Syst.*, vol. 7, no. 3, pp. 1173–1181, Aug. 1992.
- [3] V. Krishnan, H. Liu, and J. D. McCalley, "Coordinated reactive power planning against power system voltage instability," in *Proc. IEEE/PES Power Systems Conf. Expo., 2009 (PSCE '09)*, Mar. 2009, pp. 1–8
- [4] B. Sapkota and V. Vittal, "Dynamic var planning in a large power system using trajectory sensitivities," *IEEE Trans. Power Syst.*, vol. 25, no. 1, pp. 461–469, Feb. 2010.
- [5] M. Paramasivam, S. Dasgupta, V. Ajjarapu and U. Vaidya, "Contingency Analysis and Identification of Dynamic Voltage Control Areas," in *IEEE Transactions on Power Systems*, vol. 30, no. 6, pp. 2974-2983, Nov. 2015.
- [6] S. M. Halpin, et. al, "Slope permissive under-voltage load shed relay for delayed voltage recovery mitigation," *IEEE Trans. Power Syst.*, vol. 23, no. 3, pp. 1211–1216, Aug. 2008.

- [7] S. V. Kolluri, et. al, "Relay-based undervoltage load shedding scheme for Entergy's Western Region," 2015 IEEE Power & Energy Society General Meeting, Denver, CO, 2015, pp. 1-5.
- [8] H. Bai, and V. Ajjarapu "A novel online load shedding strategy for mitigating fault-induced delayed voltage recovery" IEEE Trans. Power Syst. vol. 26 no. 1 pp. 294-304 Feb. 2011.
- [9] Modeling and validation work group, "WECC Dynamic Composite Load Model Specifications," Western Electricity Coordinating Council, Technical Report, January 25, 2015
- [10] Paul Krauss, "Analysis of Electric Machinery and Drive Systems", 2nd Edition
- [11] North American Transmission Forum, Transient voltage criteria reference document, September 2016.
- [12] S. Dasgupta, M. Paramasivam, U. Vaidya and V. Ajjarapu, "Entropy-Based Metric for Characterization of Delayed Voltage Recovery," in IEEE Transactions on Power Systems, vol. 30, no. 5, pp. 2460-2468, Sept. 2015
- [13] A. R. R. Matavalam and V. Ajjarapu, "Implementation of user defined models in a real-time cyber physical test-bed," 2016 National Power Systems Conference (NPSC), Bhubaneswar, 2016, pp. 1-6
- [14] D. P. Chassin, et. Al, "ARRA Interconnection Planning - Load Modeling Activities", PNNL-24425 Report June 2015
- [15] W. Wang, et. al., "Time Series Power Flow Framework for the Analysis of FIDVR Using Linear Regression," in IEEE Trans. on Pow. Del., vol. 33, no. 6, pp. 2946-2955, Dec. 2018.
- [16] A. Radaideh, U. Vaidya and V. Ajjarapu, "Sequential Set-point Control for Heterogeneous Thermostatically Controlled Loads Through an Extended Markov Chain Abstraction," in IEEE Transactions on Smart Grid, vol. PP, no. 99, pp. 1-1
- [17] Robles, Steven. "2014 FIDVR Events Analysis on Valley Distribution Circuits". Prepared for Lawrence Berkeley National Laboratory by Southern California Edison, 2015
- [18] Modeling and validation work group, "White paper on modeling and studying FIDVR events," Western Electricity Coordinating Council, Technical Report, October 20, 2011
- [19] M. Paramasivam, "Dynamic optimization based reactive power planning for improving short-term voltage performance", PhD Thesis, [online] <https://lib.dr.iastate.edu/etd/14945/>
- [20] <https://www.openmodelica.org>

**CHAPTER 4. MONITORING & MITIGATION OF DELAYED VOLTAGE
RECOVERY IN DISTRIBUTION NETWORKS USING μ PMU MEASUREMENTS**

Modified from a manuscript to be submitted to IEEE Transactions in Smart Grid

Amarsagar Reddy Ramapuram Matavalam and Venkataramana Ajjarapu

*Department of Electrical and Computer Engineering, Iowa State University, Ames, IA 50011,
United States of America.*

Abstract

This paper proposes a new method to monitor and mitigate fault induced delayed voltage recovery (FIDVR) phenomenon in distribution systems using μ PMU measurements in conjunction with a Reduced Distribution System Model (RDSM). The recovery time estimated from a dynamic analysis of the FIDVR is used to monitor its behavior and a linear optimization is formulated to control air conditioner loads and DER reactive power injection to mitigate the FIDVR severity. The RDSM is made up of several sub-models, each of which is analogous to the Composite Load Model (CLM) with selected parameters. The linear formulation in combination with the RDSM reduces the computation time, enabling online execution. A linear trajectory sensitivity based formulation is also proposed when the voltage recovery constraints are specified as a step function due to voltage ride through requirements. Simulated μ PMU measurements from the IEEE 37 node distribution system connected to the IEEE 9 bus system under various fault scenarios are used to evaluate the proposed methodology. The resulting mitigation schemes are validated using combined transmission-distribution system simulations, thereby demonstrating that μ PMU measurements along with the RDSM enable FIDVR mitigation by optimal control of reactive power injection from DERs with minimal load disconnection.

4.1 Introduction

In today's ever evolving power grid, advanced monitoring and control schemes to mitigate abnormal grid behavior such as short term voltage instability are vital for the reliability. The phenomenon of short term voltage stability deals with the behavior of the power system in the first few seconds after a disturbance. A special case of interest is the Fault Induced Delayed Voltage Recovery (FIDVR) phenomenon which occurs in regions where the 1 ϕ induction motor (IM) load portion is more than 30% [1]-[2]. FIDVR is a precursor to short term voltage instability since the generator excitation and the transmission lines are stressed due to motor stalling, thus increasing the risk of cascading. FIDVR is mainly observed in systems with a moderate proportion of 1 ϕ IM loads, which are present mainly in air conditioner (A/C) loads. After a large disturbance (fault, etc.), these motors can stall and draw ~6 times their nominal current, leading to the depression of the system voltage for several seconds (>15 sec).

Two types of methodologies have been proposed in literature to mitigate the FIDVR phenomenon – supply side methods (injection of dynamic VARs via SVC, etc.) and demand side methods (disconnection of loads using measurements, etc.). Utilities usually employ the supply side solution by determining the amount and location of the SVCs and STATCOMs during the offline planning phase [3][4]. These methods use contingency sets along with extensive time domain simulations to ensure that FIDVR is mitigated over a wide range of operating conditions. The widespread adoption of Phasor Measurement Units (PMUs) by utilities has led to the development of measurement based methods to estimate the severity of FIDVR in real-time and take appropriate control actions to prevent further voltage reduction [5][6][7].

Until recently, distribution systems (DS) have lacked high-quality real-time measurement data. There has been a compelling motivation for using advanced measurement data from accurate, high resolution devices in distribution networks [8]. High-precision micro phasor measurement units (μ PMUs), when tailored to the particular requirements of power distribution, can support a range of monitoring, diagnostic and control applications [8]. They can also enable a new approach for managing distribution systems, particularly in the presence of significant renewable penetration [9] and can reveal phenomenon that were not usually thought to occur in distribution systems. In fact, it was recently shown from μ PMU measurements that FIDVR occurred more frequently in distribution systems than transmission systems (TS) [10].

To mitigate FIDVR in distribution systems, [11][12][13] have proposed utilizing the reactive support from DER inverters based on voltage reduction at the inverter. However, as FIDVR phenomenon is driven by the load dynamics, targeted load control in regions with large motor stalling will lead to a faster recovery. This approach is adopted in this paper where we demonstrate that the μ PMU measurements provide sufficient visibility to identify and localize motor stalling in distribution systems. Furthermore, by analyzing the dynamics of FIDVR, we are able to estimate the recovery time from measurements to enable improved mitigation schemes by targeted control of A/C smart thermostats and DERs. These targeted schemes are shown to mitigate FIDVR with lesser load control than widespread disconnections throughout the system.

4.2 Analysis & Recovery Time Estimation of FIDVR

In order to study the FIDVR phenomenon, the Composite Load Model (CLM), which is one of the most comprehensive dynamic load models, has been developed by Western Electricity Coordinating Council (WECC) [14]. This model aggregates the various loads in a

region into static loads, 3 ϕ IM (also referred as motor-A, B, C), and 1 ϕ IM (also referred as motor-D), representing the residential A/C loads. The overall structure of the composite load model is shown in Figure 4.1. The 1 ϕ IM model represents the A/C compressor motor, thermal relay, and contactors and is the main reason why the FIDVR occurs. Depending on the load voltage, the 1 ϕ IM operates either in 'running' or 'stalled' state.

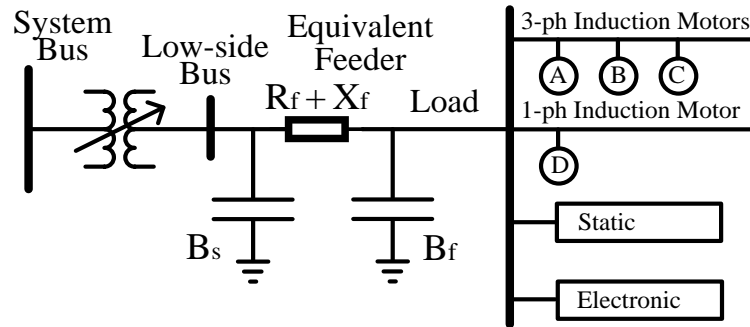


Figure 4.1 *The structure of the composite load model [14]*

The 1 ϕ IM is in the running state for normal operating voltage and when the voltage goes below the stall voltage for a time greater than the stall time, the 1 ϕ IM goes into the stalled state. In the stalled state, the active power demand is ~ 3 times the nominal amount and the reactive power demand is ~ 6 times the nominal amount [4][14] compared to the normal 'running' state. This large increase in the reactive power demand is the reason why the voltage at the load drops during stalling. This power demand is naturally reduced via thermal protection and takes around 10-15 seconds to operate. Despite the recovery, the concern is that the sustained low voltages can lead to events such as generator exciters reaching limits or disconnection of DG inverters that can initiate cascading phenomenon [15].

Figure 4.2 shows the simplified structure of the composite load model during stalling of the 1 ϕ motor with the equivalent feeder admittance denoted by Z_f . The μ PMU is present at the node before Z_f and measures the voltage & load current which can be used to calculate the

load voltage V_L . As the thermal relay dynamics is much slower compared to the dynamics of the 3ϕ IM, the dynamics of the 3ϕ IM can be neglected for this particular phenomenon. The 3ϕ motor, electronic loads, static loads and DER are represented by admittance Y_{3ESDER} and the stalled 1ϕ motor is represented by admittance Y_{stall} . The admittance Y_{3ESDER} is a function of V_L in order to account for the dynamics of the 3ϕ motor and is not constant with time. After a severe fault, the stalled 1ϕ IM admittance is given by $Y_{stall} = G_{stall} - j \cdot B_{stall}$. The fraction of 1ϕ IM connected after stalling is determined by the fraction f_{th} which is the output of the thermal relay.

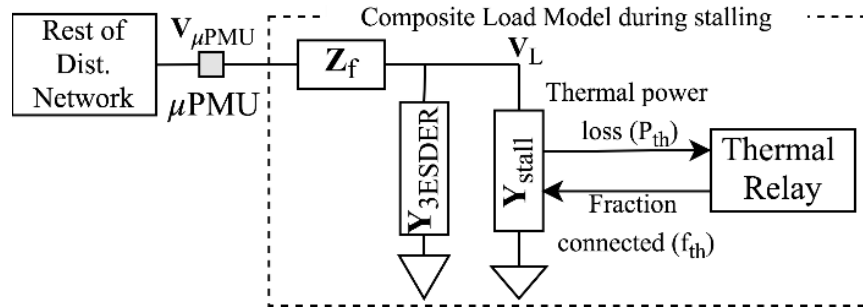


Figure 4.2 *The simplified composite load model during FIDVR*

The load susceptance for the delayed voltage phenomenon can be split into two parts – a flat region and a monotonically decreasing region [16]. The flat region corresponds to the time to initiate the thermal tripping of 1ϕ IM (t_1) and the region where the susceptance reduces which corresponds to the time taken to complete the thermal tripping of 1ϕ IM (t_2). It is much easier to distinguish between these phases of operation from the susceptance plots compared to the voltage plots as the oscillations and other phenomenon can mask the exact time of transition. These observations and modelling assumptions lead to the admittance based representation of the composite load model [16]. Analysis of this simplified model along with the thermal relay dynamics is discussed next to estimate times t_1 & t_2 and total recovery time from measurements.

4.2.1 Time to initiate motor disconnection

The expression for the load voltage V_L is given by (4-1). After the 1 ϕ IM motor stalling, the thermal power dissipated is given by (4-2) and the corresponding differential equation for the temperature is given by (4-3). Initially the internal temperature is zero and the thermal loss is zero. As the stalling condition occurs suddenly, the input to the thermal delay block is a step function with value P_{th} and the internal temperature increases exponentially as shown in (4-4). G_{stall} remains same as f_{th} is equal to 1 till the temperature reaches θ_1 and the time taken for the temperature to reach θ_1 can be calculated by substituting (4-2) in (4-3) to get (4-5).

$$V_L = V_{\mu PMU} - I_L \cdot (R_f + j \cdot X_f) \quad (4-1)$$

$$P_{th} = V_L^2 \cdot G_{stall} \quad (4-2)$$

$$\frac{d\theta}{dt} = \frac{1}{T_{Th}} (P_{th} - \theta) \Rightarrow \theta = P_{th} (1 - e^{(-t/T_{th})}) \quad (4-3)$$

$$\theta_1 = P_{th} (1 - e^{(-t_1/T_{th})}) \quad (4-4)$$

$$t_1 \approx -T_{th} \cdot \ln(1 - \theta_1 / (V_L^2 \cdot G_{stall})) \quad (4-5)$$

Next, we can determine the time taken for the motor temperature to rise from θ_1 to θ_2 by understanding how the thermal trip fraction f_{th} varies with time.

4.2.2 Time to complete motor disconnection

The thermal trip fraction f_{th} is a linear function of the internal temperature and is given by (4-6). To derive an expression describing how the thermal trip fraction varies with time, (4-6) is differentiated and the expression in (4-6) is substituted, leading to expression (4-7). In this expression, the voltage is an implicit function of the fraction f_{th} .

$$f_{th} = 1 - \frac{(\theta - \theta_1)}{(\theta_2 - \theta_1)} \quad (4-6)$$

$$\frac{d f_{th}}{dt} = \frac{-d\theta/dt}{(\theta_2 - \theta_1)} = \frac{(\theta_2 - (\theta_2 - \theta_1) \cdot f_{th} - V_L^2 \cdot G_{stall})}{T_{th}(\theta_2 - \theta_1)} \quad (4-7)$$

Equation (4-7) enables us to understand the behavior of the thermal relay. Initially, the value of the voltage is low and the value of f_{th} is 1, leading to a negative value of df_{th}/dt and implying that the f_{th} will reduce from 1 increasing the voltage magnitude. As the voltage increases and the f_{th} decreases, the slope becomes further negative and increases the rate of rise of voltage. Finally, as the value of f_{th} reaches 0, the voltage is close to the pre-contingency voltage at which time all the 1 ϕ IM are disconnected and the thermal trip relay operation ends. The differential equation (4-7) is non-linear and can be numerically solved for a particular scenario but is difficult to analyze for a general case. In [16], we analyzed the differential equation (4-7) and derived an approximate expression for t_2 and the final expression is presented in (4-8) which needs the recovery voltage level at the bus when the FIDVR is complete. This is usually between 0.95 p.u. to 1 p.u.

$$t_2 \approx \frac{2T_{th}(\theta_2 - \theta_1)}{\left((V_L^2 + V_{L_{recover}}^2)G_{stall} - \theta_1 - \theta_2 \right)} \quad (4-8)$$

$$t_{total} = t_1 + t_2 \quad (4-9)$$

The total time to recovery (t_{total}) is the sum of t_1 & t_2 and thus, the time to recover from FIDVR can be determined using the voltage and admittance measurements from the μ PMU along with the load parameters. The recovery time is used as an indicator for FIDVR severity.

4.3 Reduced Distribution System Model

In order to implement the FIDVR monitoring scheme that has been described in the previous section using few μ PMUs, it is essential to aggregate a group of loads into a single load model. Consider a radial distribution network shown in Figure 4.3 with N nodes with each

node comprising of static, electronic, motor loads (3 ϕ and 1 ϕ AC motors) and PV inverters. Measurement devices such as μ PMUs measure load voltage and power in the distribution lines/loads at sub-second intervals. The objective is to reduce the number of nodes and represent the load at each measurement node using an aggregated dynamic model that captures the overall dynamic behavior of the full downstream model. We assume that they are placed at nodes where secondary feeders and large loads are connected to the primary feeder.

The proposed Reduced Distribution System Model (RDSM) is made up of several sub-models connected in a structure similar to the original topology as shown in Figure 4.4 (a). The sub-model is analogous to the composite load model with selected parameters to represent relevant portions of the distribution network with an equivalent feeder impedance, a load tap changing transformer and a load block as shown in Figure 4.4 (b). The load block includes static load, IM loads, and PV inverter. The static load parameters correspond to the conventional ZIP model. The 3 ϕ IM (A, B, C type motors of the composite load model) are lumped into one motor and the 1 ϕ IM (Type D of the composite load model) represents the motors used in residential A/C compressors.

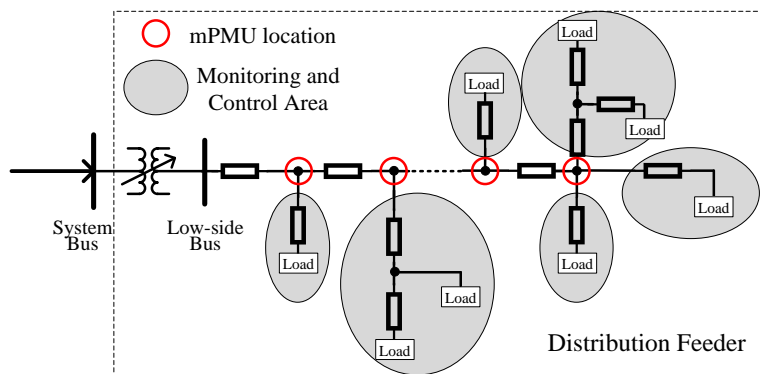


Figure 4.3 Radial distribution system with μ PMUS installed in some nodes [17]

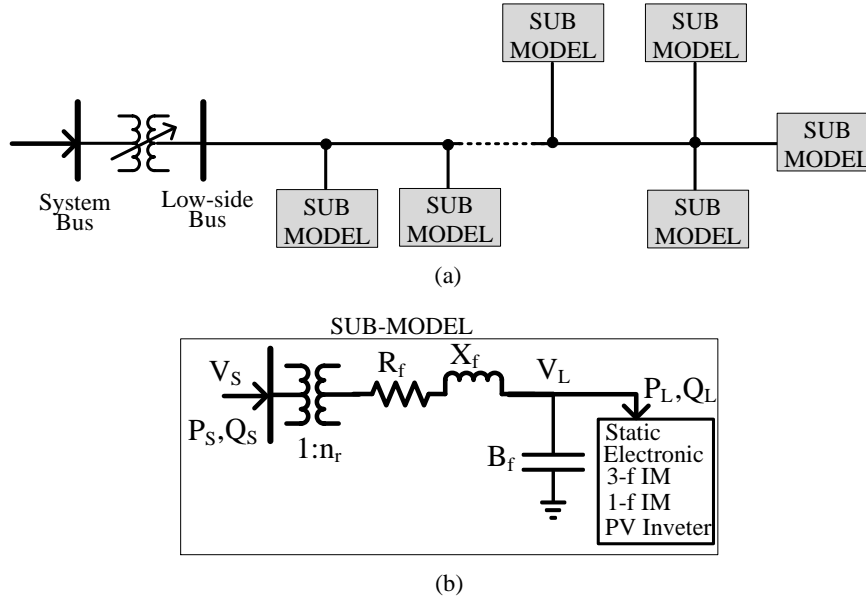


Figure 4.4 (a) Generic reduced distribution system model. (b) Sub-model. [17]

Table 4-1 shows the relevant parameters of the sub-model that would represent the portion of the distribution network. Here, F_s , F_{m1} , F_{m3} are the fractions of the corresponding loads and F_{pv} is the fraction of the equivalent PV in that portion of the network. R_f , X_f , B_f and n_r are the parameters of the equivalent feeder impedance. The static load, the 3 ϕ IM and the 1 ϕ IM and PV inverter are represented by the parameters in the respective columns in Table 4-1 and these parameters are defined in the WECC CLM specifications [14].

Table 4-1 Various load parameters of the sub-models in an RDSM

Load Fraction	Equiv. Feeder	Static (ZIP)	3 ϕ IM	1 ϕ IM	PV
F_s	R_f	$Pz0$	R_s	V_{stall}	P_{pv}
F_{m1}	X_f	$Qz0$	X_{ls}	T_{stall}	Q_{pv}
F_{m3}	B_f	$Pi0$	X_m	R_{stall}	
F_{pv}	n_r	$Qi0$	R_{r1}	X_{stall}	
		$Pp0$	X_{lr1}	T_{th}	
		$Qp0$	R_{r2}	θ_1	
		$Qsh0$	X_{lr2}	θ_2	
			H		

More details on the methods to estimate the RDSM model from a distribution system topology and individual load models using the dynamics co-simulation platform are present in

[17]. Using the RDSM, the control and monitoring applications can be run from μ PMU measurements from only a few nodes.

4.4 Mitigation of FIDVR using DERs and Load Control

The FIDVR phenomenon is of concern to the system operator as sustained low voltages are not expected by the various components in the system and they might disconnect, leading to uncontrolled loss of generation/load. Usually, utilities have two types of voltage recovery criteria

- (1) A voltage recovery criteria that ensures that the system can recover close to the pre-fault voltage after a fault (e.g. 0.95 p.u. in 10s [18]). During FIDVR, this criteria can be violated (e.g. 0.95 p.u. in 13s) and so we need to take control to improve recovery time (by 3s in this case) to ensure the voltage satisfies the criteria.
- (2) A voltage recovery criteria that provides bounds for the voltage range of the response. For example, the voltage should always be above 0.8 p.u. after 2s and above 0.9 after 5s of fault clearing. This criteria is usually associated with fault-ride through requirements [19] of DER devices. During FIDVR, this criteria can be violated several times over the course of the voltage recovery trajectory and so the control should be able to incorporate the voltage recovery constraint in a meaningful manner.

These two kinds of voltage recovery criteria lead to different kinds of control schemes.

4.4.1 Ensuring voltage recovery beyond a single voltage close to pre-fault voltage

As the voltage recovery in this case is to a single voltage that is close to the pre-fault voltage, the expressions (4-5) and (4-8) can be used to estimate the recovery time and use these expressions as a starting point for estimating the control. A change in the values of t_1 & t_2 at bus- i can only occur due to a change in the voltage at bus- i as all other variables are fixed

after an FIDVR event. The change in the values of t_1 & t_2 due to the change in the load voltage is approximated by a linear expression shown in (4-10). The expressions for dt_{1i}/dV_{L_i} and dt_{2i}/dV_{L_i} can be analytically derived from (4-5) and (4-8).

$$\Delta t_{1i} \approx \frac{dt_{1i}}{dV_{L_i}} \cdot \Delta V_{L_i}; \Delta t_{2i} \approx \frac{dt_{2i}}{dV_{L_i}} \cdot \Delta V_{L_i} \quad (4-10)$$

Various controls (Load disconnection, reactive power injection, etc.) at different locations in the network can lead to different magnitude of change in the voltage at bus-i. By linearizing the network equations, ΔV_{L_i} can be written as a linear combination of all possible controls scaled by the partial derivative as shown in (4-11). The total change in the recovery time due to the control throughout the network is then given by (4-12). The quantity $\partial V_{L_i}/\partial u_j$ is the change in the voltage at bus-i due to the j^{th} control action and can be determined from the network parameters and the node voltages. These sensitivities need to be calculated during the early phase of FIDVR using the measurements from the μ PMUs.

$$\Delta V_{L_i} \approx \sum_{j=1}^m \frac{\partial V_{L_i}}{\partial u_j} \Delta u_j \quad (4-11)$$

$$\Delta t_{total_i} = \Delta t_{1i} + \Delta t_{2i} \approx \left(\frac{dt_{1i}}{dV_{L_i}} + \frac{dt_{2i}}{dV_{L_i}} \right) \cdot \sum_{j=1}^m \frac{\partial V_{L_i}}{\partial u_j} \Delta u_j \quad (4-12)$$

Equation (4-12) can be written in a matrix form (4-13), where $D_{t_1,V}$ & $D_{t_2,V}$ are diagonal matrices of size $n \times n$ and the element (i, i) is given by dt_{1i}/dV_{L_i} and dt_{2i}/dV_{L_i} respectively. $S_{V,L,u}$ is a matrix of sensitivities of size $n \times m$ and the element (i, j) is given by $\partial V_{L_i}/\partial u_j$ and Δu is a column vector of size $m \times 1$ which correspond to the various control schemes possible. The increasing number of active components in the DS provide the means to mitigate FIDVR and various kinds of control can be integrated into this formulation. In this paper, we

concentrate on the reactive power injection from PV inverters and A/C on/off control via smart thermostats [20]. Thus, the control vector $[\Delta u]$ can be written as $[\Delta u_{PV} \quad \Delta u_{AC}]^T$ and the expression for the change in recovery time is written as (4-14).

$$[\Delta t_{total}] = [D_{t_1,V} + D_{t_2,V}] \cdot [S_{V_L,u}] \cdot [\Delta u] \quad (4-13)$$

$$[\Delta t_{total}] = [D_{t_1,V} + D_{t_2,V}] \cdot [S_{V_L,u_{PV}} \quad S_{V_L,u_{AC}}] \cdot \begin{bmatrix} \Delta u_{PV} \\ \Delta u_{AC} \end{bmatrix} = [A] \cdot \begin{bmatrix} \Delta u_{PV} \\ \Delta u_{AC} \end{bmatrix} \quad (4-14)$$

All the elements in 'A' and Δt_{total} are negative as Q-injection and load disconnection will reduce the recovery time. In this manner, we have derived a linearized expression to estimate the change in recovery time and this expression can be used to estimate the control necessary to ensure voltage recovery within a specified amount of time. It is important to remember that the true system is non-linear and so this linearization is bound to have errors, especially as the amount of control increases.

The control of PV devices essentially amounts to reactive power injection (assuming no curtailment of active power) and so the $S_{V_L,u_{PV}}$ matrix is estimated from the change in voltages due to reactive power injection at nodes with PV penetration. This is efficiently implemented as solving a set of linear equations from the power flow jacobian during the FIDVR event and is parallelized for multiple buses, speeding up the estimation of $S_{V_L,u_{PV}}$. Similarly, the control of A/C devices is equivalent to reducing the amount of active and reactive power demand at various nodes and so the $S_{V_L,u_{AC}}$ matrix is estimated from the change in voltages due to reducing active and reactive power at various nodes and can also be parallelized, ensuring that the $S_{V_L,u_{AC}}$ estimation is done in an online manner. As the matrices $D_{t_1,V}$ & $D_{t_2,V}$ have analytical expressions, their values are calculated very quickly and so the full matrix 'A' relating the control inputs to the change in recovery time can be calculated in

an online manner and this is used to determine the effective regions and types of control for a specific FIDVR occurrence.

To determine the locations and amount of control, a linear optimization can be formulated using the linear relation (4-14). The formulation is shown in (4-15).

$$\begin{aligned} \min c^T \cdot \Delta u \\ -A \cdot \Delta u \geq -\Delta t_{total} \\ \Delta u_{min} \leq \Delta u \leq \Delta u_{max} \end{aligned} \quad (4-15)$$

This formulation minimizes the control cost with coefficients ‘c’ and ensures that the recovery time improves by a minimum of Δt_{total} while keeping the control within the bounds. The negative sign in the inequality constraint is present as all the elements in ‘A’ and Δt_{total} are negative. Δt_{total} is the change in the recovery time to ensure the recovery satisfies the voltage criteria and the constraints in (4-15) ensures that the voltage recovery improves at all the nodes.

4.4.2 Ensuring voltage recovery satisfies fault-ride through requirements

The voltage ride through (VRT) criteria is a voltage performance criteria after a fault is cleared in the system and ensures that the generation devices such as DERs remain connected to the grid for a few seconds of low voltage to provide support and ensure that the voltage recovery is fast. However, there is a limit to how long these devices can remain connected at low voltages and this is captured by the VRT criteria. A standard VRT specification for DERs is given by the IEEE 1547 standard and is generally provided as a plot shown in Figure 4.5. The plot shows a region of voltage recovery where the DER device remains connected and a region where the DER device will disconnect. This disconnection can lead to further delay in the voltage response and so, the control objective is to make sure that the voltage remains in the no-trip region of the VRT plot.

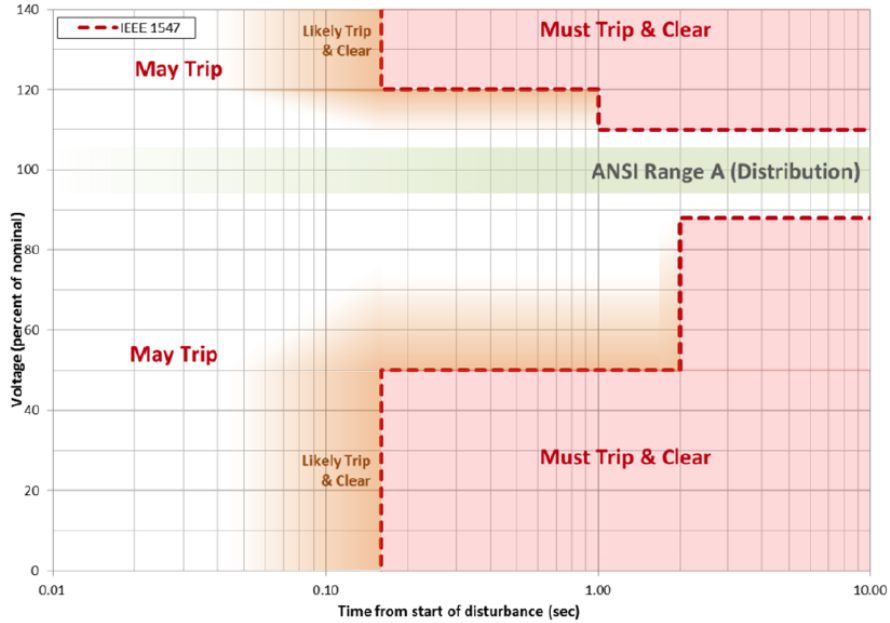


Figure 4.5 Example plot for the VRT requirements of DER inverters in distribution system

To ensure that the voltage recovery satisfies a voltage criteria for a range of times after the fault is cleared, the actual dynamics of the FIDVR phenomenon has to be considered as the approximate expressions for the recovery time are not designed for low voltages and thus cannot be used for this case. The dynamics of the power system is generally represented as a set of nonlinear differential-algebraic equations (DAEs), shown in (4-16).

$$\begin{aligned} \dot{x} &= f(x, y, \lambda) \\ 0 &= g(x, y, \lambda) \end{aligned} \quad (4-16)$$

where x is the vector of dynamic states, y is the vector of algebraic states and includes the node voltages and λ is the vector of parameters that can be varied over a range of values. Usually, λ is a parameter characterizing load parameters, transmission line impedance or generator bus initial voltage levels. λ as a parameter can also incorporate various controls such as disconnection of load and injection of reactive power. The variation of λ is expected to change the trajectory of the DAE and we are interested to quantify how much the trajectory of all the states varies over time with the variation in the λ . This is a very complicated problem and instead of solving it exactly, the power

system community has adopted the idea of linear trajectory sensitivities [21][22] to approximate the variation in the trajectories in a linear manner with respect to λ .

In order to estimate this trajectory sensitivity, the original DAE in (4-16) is augmented with a set of DAE equations that track the evolution of the trajectory sensitivity over time. The augmented equations for a single parameter λ_i are shown in (4-17). The sensitivity of dynamics states to parameter λ is given by $\frac{\partial x}{\partial \lambda_i}$ and the sensitivity of algebraic states to parameter λ is given by $\frac{\partial y}{\partial \lambda_i}$. These are the unknown quantities in (4-17) and will be evaluated at each time step of system evolution using standard integration techniques such as trapezoidal methods [23] in conjunction with Newton line search methods [24]. Furthermore, the impact of the sensitivities of different parameters are independent of each other. These can be evaluated in parallel using an appropriate parallel computing architecture, enabling additional savings in time [23]. The interested reader can refer to [21] – [24] for more details on the trajectory sensitivity method.

$$\begin{aligned} \frac{\partial \dot{x}}{\partial \lambda_i} &= \frac{\partial f}{\partial x} \cdot \frac{\partial x}{\partial \lambda_i} + \frac{\partial f}{\partial y} \cdot \frac{\partial y}{\partial \lambda_i} + \frac{\partial f}{\partial \lambda_i} \\ 0 &= \frac{\partial g}{\partial x} \cdot \frac{\partial x}{\partial \lambda_i} + \frac{\partial g}{\partial y} \cdot \frac{\partial y}{\partial \lambda_i} + \frac{\partial g}{\partial \lambda_i} \end{aligned} \quad (4-17)$$

Once the linear trajectory sensitivities are estimated, then the trajectory of a specific perturbation is estimated by a first order approximation as shown in (4-18) and (4-19). Thus, after estimating the trajectory sensitivities $\frac{\partial x(t)}{\partial \lambda}$ & $\frac{\partial y(t)}{\partial \lambda}$, the trajectory of the system due to any perturbation can be approximated as a linear combination of the sensitivities scaled by the amount of perturbation of each parameter λ_i .

$$x_{new}(t) = x_{old}(t) + \begin{bmatrix} \frac{\partial x}{\partial \lambda_1} & \frac{\partial x}{\partial \lambda_2} & \cdots & \frac{\partial x}{\partial \lambda_k} & \frac{\partial x}{\partial \lambda_m} \end{bmatrix} \cdot \begin{bmatrix} \lambda_1 \\ \lambda_2 \\ \vdots \\ \lambda_k \\ \lambda_m \end{bmatrix} = x_{old}(t) + \frac{\partial x(t)}{\partial \lambda} \lambda \quad (4-18)$$

$$y_{new}(t) = y_{old}(t) + \begin{bmatrix} \frac{\partial y}{\partial \lambda_1} & \frac{\partial y}{\partial \lambda_2} & \cdots & \frac{\partial y}{\partial \lambda_k} & \frac{\partial y}{\partial \lambda_m} \end{bmatrix} \cdot \begin{bmatrix} \lambda_1 \\ \lambda_2 \\ \vdots \\ \lambda_k \\ \lambda_m \end{bmatrix} = y_{old}(t) + \frac{\partial y(t)}{\partial \lambda} \lambda \quad (4-19)$$

This linear approximation can be used to formulate an optimization problem (4-20) to identify the control parameters that ensures the trajectory is above a pre-specified minimum reference voltage which is the voltage-ride through requirement of the DERs in the distribution system. In (4-20), the parameters have been explicitly represented as Δu , as they are control parameters and the constraint is on the voltage of the nodes which is an algebraic state. As (4-20) is a linear problem in the control parameter, it is easy to solve in an online manner for reasonably sized systems. One challenge with solving (4-20) is that the constraint on the voltage is a continuous time constraint making it computationally challenging. In practice, the continuous time constraint is discretized and is imposed at a time step that can capture the dynamics of the phenomenon being controlled.

$$\begin{aligned} & \min c^T \cdot \Delta u \\ & V_{old}(t) + \frac{\partial V_{old}(t)}{\partial \Delta u} \cdot \Delta u \geq V_{ref}(t) \\ & \Delta u_{min} \leq \Delta u \leq \Delta u_{max} \end{aligned} \quad (4-20)$$

As the proposed control scheme needs to estimate the load control and the DER reactive power injection 1s – 2s after the FIDVR is detected, the trajectory sensitivities and the optimization needs to be performed in an online manner. This implies that using the full dynamics of the load model such as the 3-phase motor dynamics, etc. is unrealistic and so we fall back to the admittance based simplified admittance based load model described in Section 4.2 that

captures most of the voltage recovery dynamics [16]. As this load dynamics has only 1 dynamic state (corresponding to motor temperature) for each load area that is comparatively slowly varying, the complexity of the overall DAE is minimized and the time step for simulation can be large ($\sim 0.5s$). This simplification enables us to estimate the uncontrolled voltage trajectory and perform the trajectory sensitivity calculation for various controls in an online manner.

The overall flowchart for the monitoring and mitigation of FIDVR in distribution systems is shown in Figure 4.6

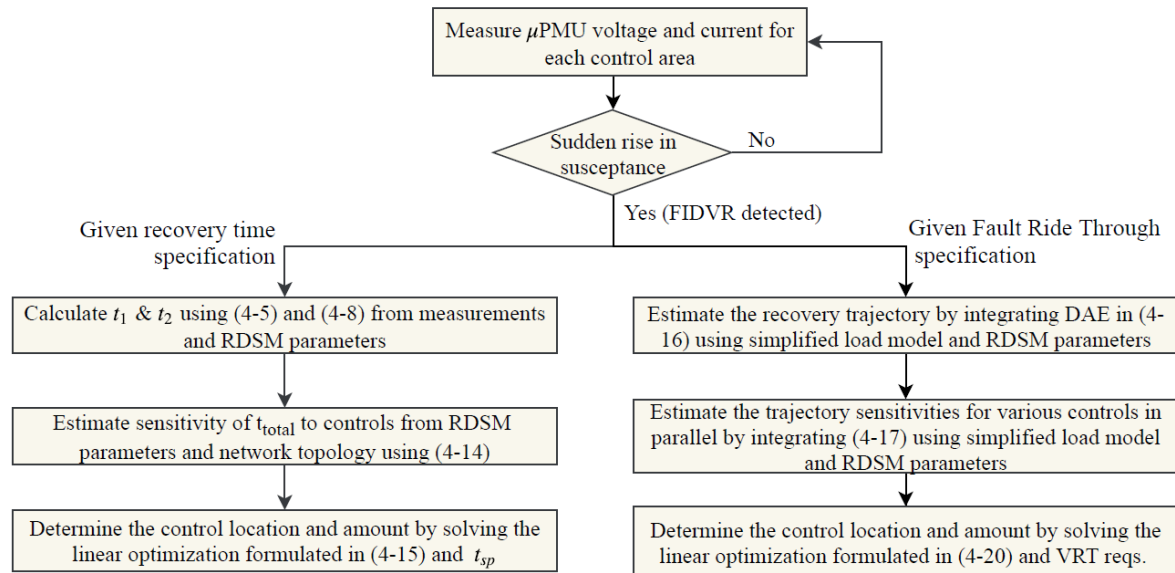


Figure 4.6 Flowchart for monitoring and mitigating online FIDVR in distribution systems

4.5 Numerical Results on Test System

An IEEE 9-bus TS and an IEEE 37-node DS [25] is considered for implementing the control scheme that is developed to mitigate the FIDVR. Figure 4.6 shows the interconnection of these systems with the IEEE 37-node system connected to Bus 6 of the IEEE 9-bus TS. The power demanded by the DS is 2.5 MW and so the remaining power at the transmission bus is assigned to other feeders that are not under study. The DS is also shown in Figure 4.6 and is

divided into 6 load areas with the root node voltage and the currents in each area being measured by a μ PMU (in red) as shown in Figure 4.6. Observe that a few areas share the same root node and the μ PMU located here should measure the currents into load area separately.

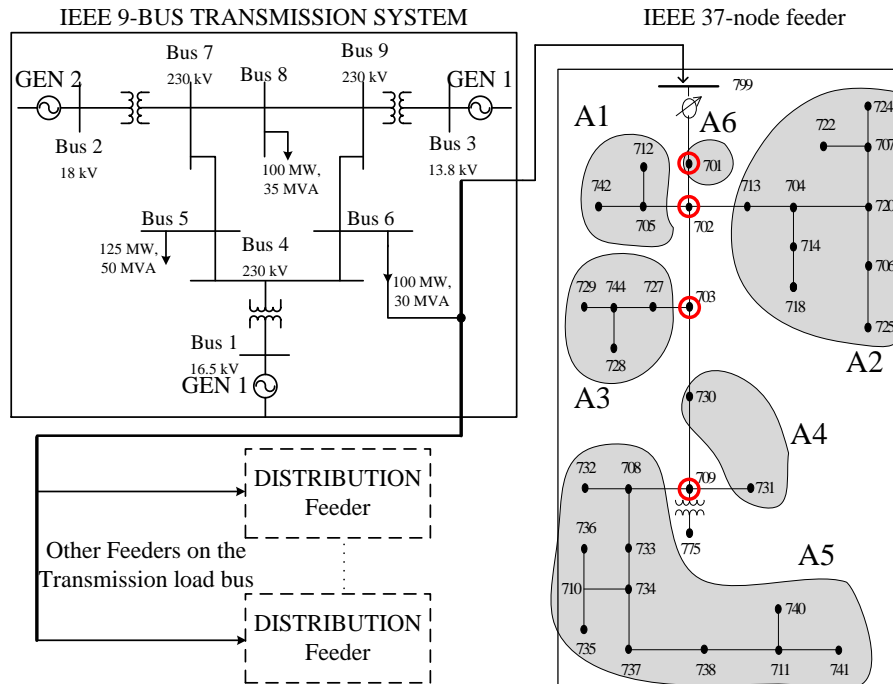


Figure 4.7 Test system used to validate proposed methodology. The areas in the distribution system are shaded and the red nodes are the μ PMU locations

Each of the DS loads in the IEEE 37-node feeder is separated into the composite load model components including static, electronic, 3 ϕ IM and 1 ϕ A/C IM. In order to simulate a realistic scenario, the fraction of loads of each type (F_s , F_{el} , F_{m3} and F_{m1}) is assigned according a normal distribution around a mean value which is estimated based on the type of loads (residential, industrial or commercial) present in each location [26]. In addition, each of the motor load types which have their own set of parameters to characterize them and have variability included by connecting several motors with a normal distribution of parameters. This procedure leads to a comprehensive and detailed model of the DS.

To test the system behavior, a fault is created at node 701 in the DS for a duration of 80 ms and the voltages observed by the μ PMUs and the substation are plotted in Figure 4.7. It can be seen that FIDVR is observed in all the μ PMUs due to the high proportion of the 1 ϕ IM in the feeder. As the FIDVR occurs on only a single distribution feeder whose load (2.5 MW) is small compared to the load at the TS (100MW), the TS is not impacted by this fault and this is reflected in the substation voltage being nearly flat during the FIDVR. These voltage profiles are similar to the FIDVR data from μ PMUs in the Southern California Edison system [10].

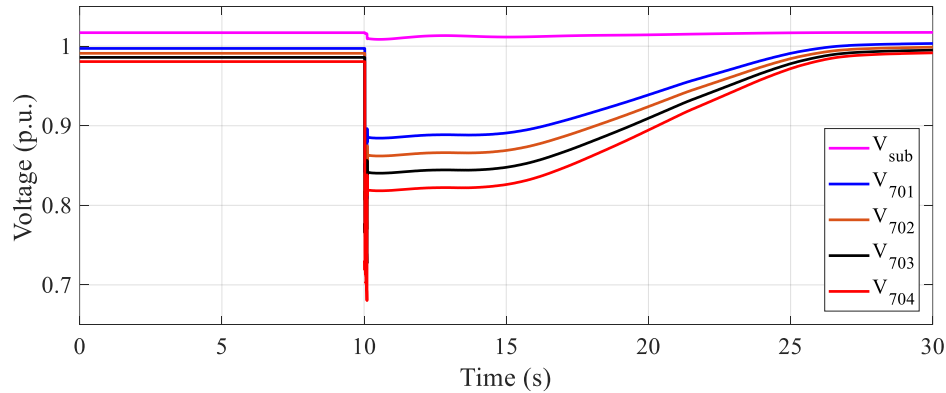


Figure 4.8 Voltages at the substation and at μ PMUs for a fault at node 701

From the different sets of data obtained from CoTDS, the sub-model parameters for each of the 6 areas are determined [17]. A few key parameters for each of the control area are listed in Table 4-2.

Table 4-2 Sub-model parameters of the load areas

Parameter	Root Node and Sub-Model Parameter Values					
	A1	A2	A3	A4	A5	A6
Root Node	702	702	703	709	709	701
P _{load} (kW)	178	538	245	160	684	420
F _s	0.61	0.46	0.49	0.49	0.47	0.2
F _{m1}	0.39	0.54	0.29	0.51	0.53	0.1
F _{m3}	0	0	0.22	0	0	0.7

Rstall	0.061	0.092	0.057	0.074	0.072	0.080
Xstall	0.073	0.112	0.058	0.077	0.091	0.090
T _{th}	17.84	12.00	15.14	13.99	13.62	15.00
θ_1	0.714	0.452	0.450	0.653	0.739	0.800
θ_2	3.025	1.949	3.750	3.222	2.615	3.000

4.5.1 Recovery time estimation for monitoring FIDVR

To validate the expressions in (4-5) and (4-8), various faults in the DS are created in the full CoTDS simulation and the actual recovery time is measured from the resulting FIDVR profile. This is compared to the estimated recovery time calculated using (4-9) and the μ PMU measurements at the root nodes of areas A1 – A6. Figure 4.9 plots the voltage response at node 709 in the DS for the three fault locations with varying fault duration applied in various areas of the distribution feeder. The recovery times are presented in Table 4-3 and they demonstrate that the estimated recovery time lies within 15 % of the actual time in all the cases with the largest errors occurring in scenarios with low fault durations. The recovery time can be estimated in <0.5s after the FIDVR event is detected and enables the fast detection of events that are likely to exceed the recovery time specified by the utility (e.g. 10s). The fast detection and recovery time estimation of FIDVR makes it possible to initiate control schemes to improve recovery time and this is described next.

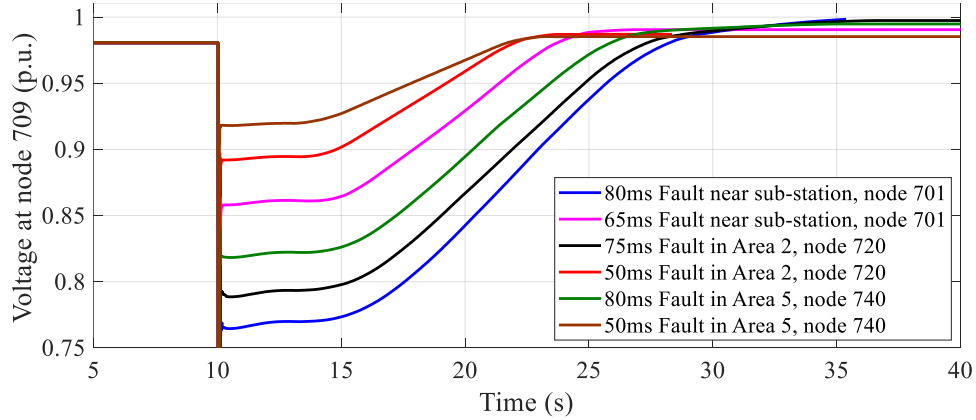


Figure 4.9 Voltage at node 709 for various faults in the DS

Table 4-3 Comparison between the actual and estimated recovery times

Fault location	Fault duration	Actual t_{total}	Estimated t_{total}	Abs. Error (%)
701 (near substation)	80 ms	15.7 s	14.9 s	5 %
	65 ms	11.4 s	12.1 s	6 %
720 (in A2)	75 ms	14.7 s	14.1 s	4 %
	50 ms	9.2 s	10.2 s	11 %
740 (in A5)	80 ms	13.6 s	13.4 s	1.5 %
	50 ms	7.9 s	9.0 s	13.5 %

4.5.2 Control to ensure voltage recovery close to pre-fault voltage

To verify that the expression in (4-14) can predict the FIDVR recovery time improvement, the case with a fault at bus 740 for 80 ms is chosen. FIDVR is detected by the sudden rise in susceptance and the sensitivities are calculated at the FIDVR condition from measurements, topology & RDSM parameters. The controls (A/C load disconnection and reactive power injection from PV inverters ($f_{PV} = 25\%$)) are implemented in the full CoTDS and are triggered 1.5s after the FIDVR is detected. This time delay is to account for the communication delays and computation time to estimate sensitivities and execute the optimization. As there are no measurements within each load area to identify the particular motors that are stalled, a specified percentage of motors are randomly disconnected in each

area. This is the practical scenario as we cannot identify the individual stalled motors. The recent IEEE 1547 [19] standard mandates that new PV inverters should be able to inject reactive power corresponding to 44% of its rating without active power curtailment and is implemented in the CoTDS for reactive power control. The various control scenarios are listed in Table 4-4 along with the actual and estimated Δt_{total} and Figure 4.10 plots the voltage at node 709 for the various control scenarios.

It can be seen from the results that the estimated Δt_{total} for various controls closely match the actual Δt_{total} from the CoTDS. This validates the derivation of the variation in recovery time using sensitivities in (4-14). However, as the phenomenon is inherently non-linear and the sensitivities are a linearized representation, it is expected that as the control amount increases, the error between the actual and estimated values will increase and this is precisely what is observed from Table 4-4.

Table 4-4 *Comparison between the actual and estimated recovery time improvement for various control actions for fault at node 740*

Control Description	Load disconnected	Actual Δt_{total}	Estimated Δt_{total}
10% A/C disconnection in all areas; no Q from PV	91.7 kW	-0.95 s	-0.9 s
20% A/C disconnection in all areas; no Q from PV	183.4 kW	-2.05 s	-1.85 s
30% A/C disconnection in all areas; no Q from PV	275.1kW	-3.40 s	-2.8 s
30% A/C disconnection in Area 5; no Q from PV	108.8 kW	-2.10 s	-1.8 s
44% Q-Injection from PV ($f_{PV}=0.25$) in all areas	-	-0.65 s	-0.7 s

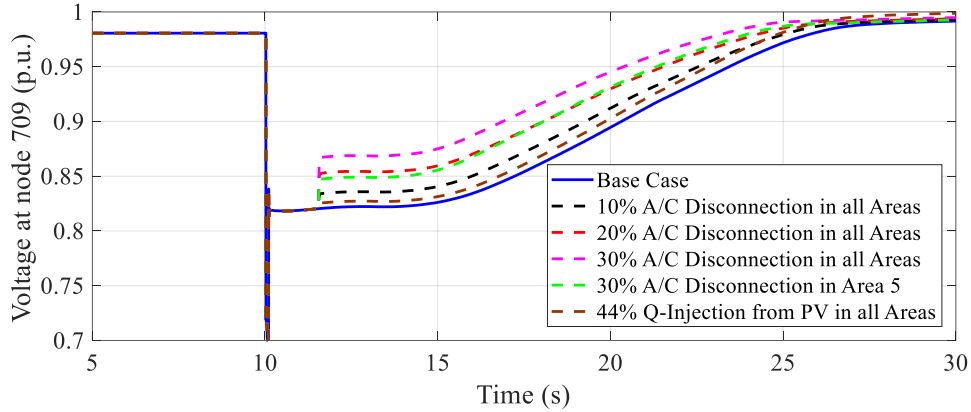


Figure 4.10 Voltage at node 709 for various control actions for fault at node 740

It can also be seen that the same improvement in the recovery time can be realized by disconnecting 108.8 kW of A/C load in area 5 versus 183.4 kW of A/C load in the overall DS – A reduction of 40% in the load disconnected. This is also captured by the estimated Δt_{total} as the calculated sensitivities of the control in area 5 are the highest in magnitude. Thus, the sensitivity based method can estimate the Δt_{total} and can be used for determining effective control locations. Next, the optimization formulation (4-15) is implemented in Matlab to estimate the minimum A/C disconnection to improve voltage recovery by various Δt_{total} values. A control constraint of 50% disconnection in each area is imposed for A/C load control. The estimation of the sensitivities and the execution of the linear optimization took $<0.5s$. Two control limits for the PV inverters were evaluated – normal unity power factor and 44% maximum Q-injection. The resulting optimal control schemes for a 3 scenarios with varying Δt_{total} are listed in Table 4-5 and the voltage responses at node 709 are plotted in Figure 4.11.

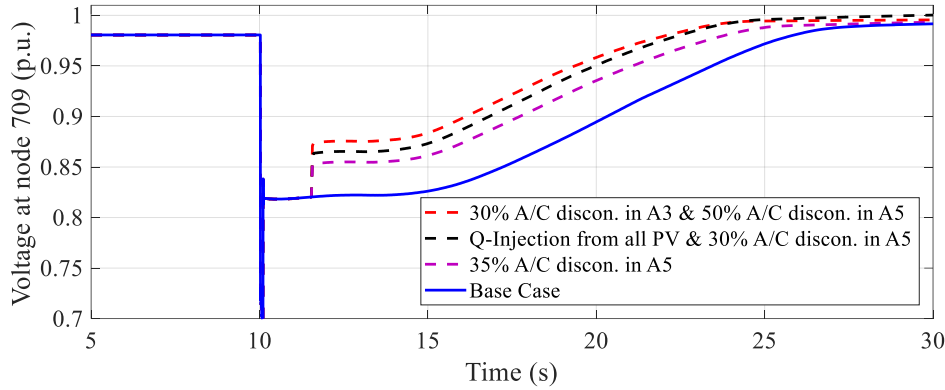


Figure 4.11 Impact of optimal control to improve voltage for fault at node 740

Table 4-5 Comparison between various control actions to improve the voltage recovery with different control constraints for fault at node 740

u_{max} Constraints	Δt_{total}	Optimal Control Description	Load disconn.	Actual Δt_{total}
No PV-Q 50% A/C	-2 s	A5 - 33% A/C load	120 kW	-2.35 s
No PV-Q 50% A/C	-3.4 s	A3 - 30% A/C load A5 - 50% A/C load	200 kW	-3.65 s
44% PV-Q 50% A/C	-3.4 s	Full Q from PV A5 - 30% A/C load	145 kW	-3.5 s

For the 1st case, the Δt_{total} is short enough so that control in A5, which has the highest sensitivity, is sufficient to satisfy the optimization constraints. For the 2nd case, the control limit in the A5 is reached and the optimization selects the next sensitive load area, A2, for control. The Δt_{total} in this case corresponds to 30% load disconnection in all areas in Table 4-4. It can be observed that the amount of load disconnection dropped from 275 kW to 200 kW - a reduction of 28%, demonstrating the benefit of the proposed methodology. If the unity power factor constraint is relaxed and the PV inverters are allowed to inject reactive with no active power curtailment, the load disconnection is further reduced to 145 kW – an overall reduction by 47%, validating the utility of controlling reactive injection from DERs. While we have concentrated on one fault scenario here, the proposed methodology is able quickly (<0.5s)

calculate the A/C load disconnection and Q-injection from DERs to mitigate FIDVR due to faults in various locations with similar reduction in A/C load disconnection compared wide spread control in the overall distribution system.

With these results, we have verified the accuracy of the proposed methodology to recover the voltage to a value close to the pre-fault value and demonstrated the reduction in load disconnection by utilizing the DERs in proposed control scheme.

4.5.3 Ensuring voltage recovery satisfies voltage-ride through

To demonstrate the utility of using the linear trajectory sensitivity methodology and its accuracy in predicting the trajectory of the FIDVR phenomenon, the case with a fault at bus 740 for 80 ms is chosen. FIDVR is detected by the sudden rise in susceptance and the trajectory sensitivities are calculated at the FIDVR condition from measurements, topology & RDSM parameters. The parameters that are used for the trajectory sensitivities are the various controls (A/C load disconnection and reactive power injection from PV inverters ($f_{PV} = 25\%$)) from the various load areas. In order to speed up the computations, the simplified admittance based composite load model with the 3-phase motors simplified as constant power load is used. It is expected that these controls are triggered 1.5s after the FIDVR is detected and the trajectory sensitivities corresponding to these controls are calculated.

After the linear trajectory sensitivities are estimated, the new trajectories can be estimated using the equation (1-49) and they can be compared with the full CoTDS simulation that accounts for the various load dynamics. Figure 4.12 plots the voltage prediction at node 709 using the full CoTDS simulation and the linear trajectory sensitivities for varying amount of A/C load disconnection in the load areas. Table 4-6 lists the maximum voltage error between the estimated and actual voltages at various nodes for different %A/C disconnections.

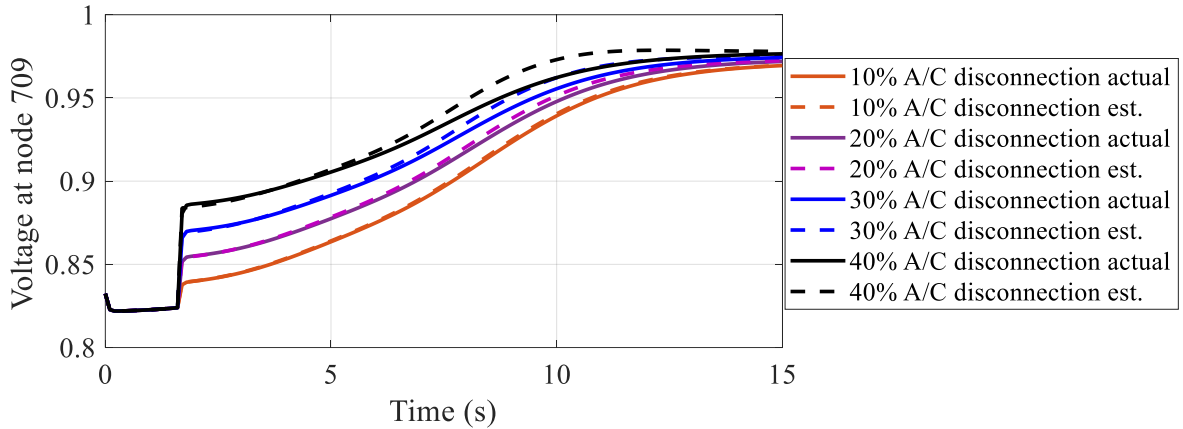


Figure 4.12 Comparison between actual voltage trajectory and estimated voltage trajectory using linear sensitivities for different amounts of A/C load control

Table 4-6 Comparison between the maximum voltage error at different nodes for different amounts of A/C load control

% A/C disconnection in all areas	Load disconnected	Max voltage error at Node 701	Max voltage error at Node 702	Max voltage error at Node 703	Max voltage error at Node 709
10% A/C disconnection	91.7 kW	0.0008 p.u.	0.001 p.u.	0.0015 p.u.	0.002 p.u.
20% A/C disconnection	183.4 kW	0.002 p.u.	0.0025 p.u.	0.003 p.u.	0.004 p.u.
30% A/C disconnection	275.1kW	0.004 p.u.	0.005 p.u.	0.006 p.u.	0.007 p.u.
40% A/C disconnection	366.8 kW	0.006 p.u.	0.008 p.u.	0.095 p.u.	0.012 p.u.

It can be observed from Figure 4.12 and Table 4-6 that the estimated voltage trajectory is able to track the actual trajectory for different kinds of control with an error < 0.01 p.u. over a wide range of control amounts. Furthermore, it can be observed from Figure 4-12 that the estimated voltage deviates more from the actual voltage as the amount of control increases as the estimated voltage is a linear approximation. Even in these cases, the estimated trajectory has a good match with the actual trajectory till around 6s after the fault is cleared. This increase in the error is also seen from the Table 4-6 where the maximum deviation from the estimated

and actual voltages increases at all nodes as the amount of control increases. It can also be observed that the maximum deviation occurs at node 709 for all the cases. This is because the fault is closest to this node and the load at this node has the most amount of stalling leading to a non-linear behavior. An important aspect of the methodology to take into account is the amount of computation time taken to calculate the trajectory sensitivities and the estimated trajectories. For the system under study, the amount of time taken to estimate the trajectory sensitivities for various kinds of control is < 0.5 s as we used the simplified admittance model and in the DAE equations. In comparison, the CoTDS simulation took > 50 s as it accounted for all the dynamics of the load. Thus, calculating the trajectory sensitivities using the simplified model is fast enough for online applications and also accurate as the errors in Figure 4.12 and Table 4-6 also include the errors due to the model simplification.

Next, we will utilize the trajectory sensitivities to estimate the control necessary to ensure a voltage recovery that will satisfy the voltage ride through requirements of DERs and will ensure no disconnection during low voltage. Two VRT criteria ((a) recover to at least 0.85 p.u. in 3 s and (b) recover to at least 0.9 p.u. in 3 s) are tested along with various control constraints. The controls are estimated based on the linear trajectory sensitivities by solving the linear optimization (4-20) and the controls are triggered 1.5s after the FIDVR is detected. The plot of the voltages with the estimated controls are simulated in the CoTDS and are plotted in Figure 4.13. Figure 4.13 also plots both the VRT criteria. It can be seen that the voltages after control are above the VRT criteria waveform and so the control schemes that are designed on linear sensitivities are actually able to ensure that the voltage is satisfying the VRT criteria.

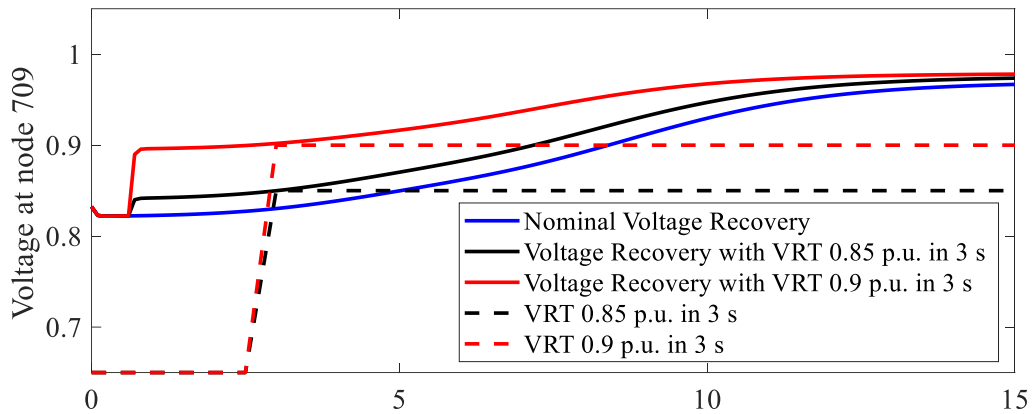


Figure 4.13 *Impact of controls on the voltage trajectory and the corresponding VRT. The controls are able to ensure that the voltage recovery satisfies the VRT requirements*

Different control constraints were used to estimate the control distribution among the various areas and the resulting voltage trajectory was very similar for the various control schemes even if the control dispatched was different. The amounts of total load control for different control constraints and VRT criteria are listed in Table 4-7. The constraint enforcing the same proportion disconnection in all areas simulates non-targeted load control and it can be seen that the total load disconnection in this scenario is the highest as the FIDVR phenomenon is a local phenomenon and targeted load control will help. Allowing each load area to disconnect varying proportion of loads ensured that more load was disconnected at the region with more motor stalling and this leads to a reduced amount of total load disconnection. Allowing DERs to inject reactive power support during the low voltage to exploit the capabilities of smart inverters further reduces the amount of load disconnection. The overall reduction in load disconnection compared to overall load disconnection is 45% for recovery to 0.85 p.u. in 3 sec and 32% for recovery to 0.9 p.u. in 3 sec. Figure 4.14 plots the voltages at all the nodes with controls that ensure for recovery to 0.9 p.u. in 3 sec for all the node voltages. Thus, the control scheme utilizing linear trajectory sensitivities from the simplified admittance

based load model ensures that the VRT criteria is satisfied with minimal amount of load control in an online manner.

Table 4-7 Comparison between the amount of load disconnected for the various control constraints and VRT criteria

Control Constraints	VRT Criteria	Load disconn.
No PV-Q 50% A/C; Same proportion A/C disconn. in all areas	0.85 p.u. in 3 sec	110 kW
No PV-Q 50% A/C; Free to choose A/C disconn.	0.85 p.u. in 3 sec	78 kW
44% PV-Q 50% A/C; Free to choose A/C disconn.	0.85 p.u. in 3 sec	60 kW
No PV-Q 50% A/C; Same proportion A/C disconn. in all areas	0.9 p.u. in 3 sec	480 kW
No PV-Q 50% A/C; Free to choose A/C disconn.	0.9 p.u. in 3 sec	420 kW
44% PV-Q 50% A/C; Free to choose A/C disconn.	0.9 p.u. in 3 sec	330 kW

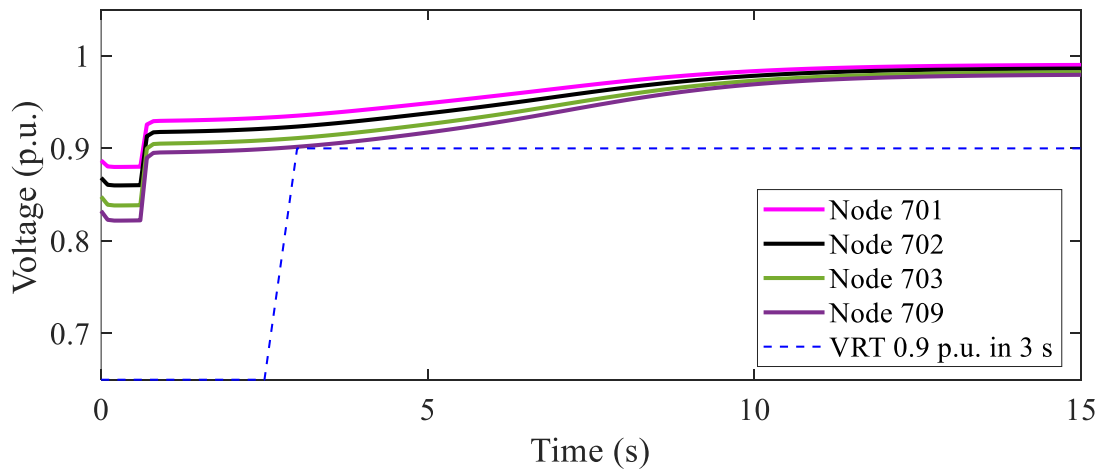


Figure 4.14 Impact of controls on the voltage trajectory at all the nodes in the system

4.6 Conclusion

In this section, a methodology to monitor and mitigate the phenomenon of FIDVR in the distribution networks is proposed using μ PMU measurements. The expressions for recovery time are derived by simplifying the composite load model during FIDVR. A

linearization of the non-linear expressions is then done to estimate the change in recovery time under various control schemes and a linear optimization problem is formulated to estimate the minimal control action necessary to recover faster. Further, the simplified load model is used to quickly estimate the linear trajectory sensitivities to ensure that the voltage recovery satisfies voltage ride through criteria of DERs.

In order to apply this method to a DS with few μ PMUs, the Reduced Distribution System Model is proposed which is composed of sub-models that are analogous to the WECC CLM and aggregates the DS into load areas while ensuring the overall dynamics are retained. To test the proposed scheme, a dynamic co-simulation is performed with several fault scenarios on the IEEE 37 node DS connected to IEEE 9 bus TS. This RDSM is shown to capture the dynamic behavior of the full distribution system under various fault scenarios. The optimal control actions calculated by using the linear sensitivities are quickly (<0.5 s) able to identify the critical regions for control for both recovery time improvement and adherence to VRT requirements of DERs. We demonstrate that optimal control reduces the amount of load control significantly and by incorporating Q-injection by DERs into the optimization, the load control is further reduced ($>35\%$). Thus, the proposed methodology enables online monitoring and mitigation of FIDVR by utilizing Q-injection from DERs with minimal load disconnection making it a promising application of μ PMU measurements to enhance operation of the distribution systems.

4.7 References

- [1] DOE-NERC FIDVR Conf., Sep. 29, 2009. [Online]. Available: <http://www.nerc.com/files/FIDVR-Conference-Presentations-9-29-09.pdf>.

- [2] B. R. Williams, W. R. Schmus, and D. C. Dawson, "Transmission voltage recovery delayed by stalled air conditioner compressors," *IEEE Trans. Power Syst.*, vol. 7, no. 3, pp. 1173–1181, Aug. 1992.
- [3] B. Sapkota and V. Vittal, "Dynamic var planning in a large power system using trajectory sensitivities," *IEEE Trans. Power Syst.*, vol. 25, no. 1, pp. 461–469, Feb. 2010.
- [4] M. Paramasivam, "Dynamic optimization based reactive power planning for improving short-term voltage performance", PhD Thesis, [online] <https://lib.dr.iastate.edu/etd/14945/>
- [5] S. M. Halpin, et. al, "The MVA-volt index: A screening tool for predicting fault-induced low voltage problems on bulk transmission systems," *IEEE Trans. Power Syst.*, vol. 23, no. 3, pp. 1205–1210, Aug. 2008.
- [6] S. V. Kolluri, et. al, "Relay-based undervoltage load shedding scheme for Entergy's Western Region," 2015 IEEE Power & Energy Society General Meeting, Denver, CO, 2015, pp. 1-5.
- [7] H. Bai, and V. Ajjarapu "A novel online load shedding strategy for mitigating fault-induced delayed voltage recovery" *IEEE Trans. Power Syst.* vol. 26 no. 1 pp. 294-304 Feb. 2011.
- [8] R. Argghandeh, "Micro-Synchrophasors for Power Distribution Monitoring, a Technology Review", <https://arxiv.org/abs/1605.02813>
- [9] A. von Meier, et. al., "Precision Micro-Synchrophasors for Distribution Systems: A Summary of Applications", *IEEE Transactions on Smart Grid*, , vol. 8, no. 6, pp. 2926-2936, Nov. 2017.
- [10] S. Robles, "2012 FIDVR Events Analysis on Valley Distribution Circuits". Prepared for LBNL by Southern California Edison, 2013
- [11] R. J. Bravo, "DER volt-VAR and voltage ride-through needs to contain the spread of FIDVR events," 2015 IEEE PESGM, Denver, 2015, pp. 1-3.
- [12] P. Mitra, et. al, "Impact of Distributed Energy Resources (DER) Voltage Regulation and Ride-Through Settings on Distribution Feeder Voltage Recovery", *Proc. CIGRE USNC 2017 Grid of the Future Symposium*.
- [13] C. A. Baone, Yan Xu and J. D. Kueck, "Local voltage support from distributed energy resources to prevent air conditioner motor stalling," 2010 Innovative Smart Grid Technologies (ISGT) , 2010, pp. 1-6.
- [14] WECC MVWG Dynamic Composite Load Model Specifications (Jan 2015) [online].
- [15] R. Venkatraman, S.K. Khaitan, V. Ajjarapu, "Impact of Distribution Generation Penetration on Power System Dynamics considering Voltage Ride-Through Requirements," *Proc. IEEE PES General Meeting*, 2018.

- [16] A.R.R. Matavalam, V. Ajjarapu "PMU based Monitoring and Mitigation of Delayed Voltage Recovery using Admittances," under review in IEEE Trans. Power Sys. [Preprint online]: <https://arxiv.org/abs/1809.08088>.
- [17] R. Venkatraman, "Combined Transmission-Distribution System Co-Simulation Modeling and its Applications for Dynamic Studies", Iowa State University PhD Thesis.
- [18] North American Transmission Forum, Transient voltage criteria reference document, September 2016. [online]
- [19] IEEE standard 1547-2018 - IEEE Standard for Interconnection and Interoperability of Distributed Energy Resources with Associated Electric Power Systems Interfaces
- [20] A. Radaideh, U. Vaidya and V. Ajjarapu, "Sequential Set-point Control for Heterogeneous Thermostatically Controlled Loads Through an Extended Markov Chain Abstraction," in IEEE Transactions on Smart Grid, vol. PP, no. 99, pp. 1-1
- [21] M. J. Laufenberg, M. A. Pai, "A new approach to dynamic security assessment using trajectory sensitivities," IEEE Trans. Power Syst., v. 13, No. 3, pp. 953 –958, 1998
- [22] I. A. Hiskens, M. A. Pai, "Power system applications of trajectory sensitivities," IEEE PES Winter Meeting, 2002, v. 2, pp. 1200 – 1205
- [23] J. S. Chai, N. Zhu, A. Bose, D. J. Tylavsky, "Parallel newton type methods for power system stability analysis using local and shared memory multiprocessors," IEEE Trans. on Power Syst., v. 6, No. 4, pp. 1539 – 1545, Nov. 1991
- [24] G. Hou," Trajectory Sensitivity Based Power System Dynamic Security Assessment", Arizona State University PhD Thesis, [online]
- [25] IEEE Distribution System Analysis Subcommittee. Radial Test Feeders[Online].Available: <http://sites.ieee.org/pes-testfeeders/>
- [26] Chassin D.P., et al, "Load Modeling Activities", Report-24425 by PNNL. http://www.pnnl.gov/main/publications/external/technical_reports/PNNL-24425.pdf

CHAPTER 5. DATA DRIVEN LINEAR APPROXIMATION OF THE 3-PHASE INDUCTION MOTOR FOR STABILITY MONITORING APPLICATIONS

Modified from a manuscript to be submitted to IEEE Transactions in Power Systems

Amarsagar Reddy Ramapuram Matavalam, Venkataramana Ajjarapu and Umesh Vaidya

*Department of Electrical and Computer Engineering, Iowa State University, Ames, IA 50011,
United States of America.*

Abstract

This paper proposes a method to estimate a linear model from the non-linear 3-phase induction motor dynamics using techniques from linear operator theory. The method is a data-driven approach that uses simulated data from the full non-linear system and lifts the model into a functional space in which the trajectories of the simulated data follow a linear relation and leads to a bi-linear model of the non-linear dynamics. The functional space is chosen so that the dynamic states and the outputs of the original system can be recovered from the lifted space in a linear manner. This implies that the techniques from linear systems can be used to perform state estimation and reconstruction in an online manner from output admittance measurements at the PMU, enabling stability monitoring for the non-linear model without model approximations as is usually done in literature. The proposed method is validated on a detailed induction motor model and the data-driven linear model is able to capture non-linear behavior of the induction motor such as stalling, etc. The proposed method can also be used to estimate the fraction of 1-phase motor stalling from PMU measurements of the admittance due to its linear nature making it the first time these two kinds of motors can be monitored at the same time.

5.1 Introduction

The induction motor (IM) is a highly dynamical load, and is usually represented as a set of differential and algebraic equations. There are several models for the 3-phase induction motor in literature ranging from the simplest first order to the complex fifth order model [1]. As this work deals with stability, the dynamics of the 3-phase loads are very critical and so the detailed fifth order induction motor model as described in [1] is analyzed. A summary of the governing equations of the 3-phase IM are given in (5-1)

$$\begin{aligned}
 \frac{d\phi_{ds}}{dt} &= \omega_b \left[V_{ds} - R_s \cdot \frac{X_r}{X_e^2} \cdot \phi_{ds} - \phi_{qs} + R_s \cdot \frac{X_M}{X_e^2} \cdot \phi_{dr} \right] \\
 \frac{d\phi_{qs}}{dt} &= \omega_b \left[V_{qs} - R_s \cdot \frac{X_r}{X_e^2} \cdot \phi_{qs} + \phi_{ds} + R_s \cdot \frac{X_M}{X_e^2} \cdot \phi_{qr} \right] \\
 \frac{d\phi_{dr}}{dt} &= \omega_b \left[-R_r \cdot \frac{X_s}{X_e^2} \cdot \phi_{dr} - (1 - \omega_r) \phi_{qr} + R_r \cdot \frac{X_M}{X_e^2} \cdot \phi_{ds} \right] \\
 \frac{d\phi_{qr}}{dt} &= \omega_b \left[-R_r \cdot \frac{X_s}{X_e^2} \cdot \phi_{qr} + (1 - \omega_r) \phi_{dr} + R_r \cdot \frac{X_M}{X_e^2} \cdot \phi_{qs} \right] \\
 \frac{d\omega_r}{dt} &= \frac{1}{H} \left[\frac{X_M}{X_e^2} (\phi_{ds} \cdot \phi_{qr} - \phi_{dr} \cdot \phi_{qs}) - T_L \cdot \omega_r^{T_e} \right]
 \end{aligned} \tag{5-1}$$

where the states of the dynamic model are ϕ_{ds} , ϕ_{qs} , ϕ_{dr} & ϕ_{qr} which correspond to the flux linkages along the d and q axis of the stator and rotor and the rotor speed (ω_r). R_r , R_s , X_r , X_s , X_M and H are the parameters of the induction motor with $X_e = \sqrt{X_s X_r - X_M^2}$ and ω_b is the synchronous rotor speed. T_L is the mechanical load torque coefficient and T_e is the mechanical load torque exponent (In practice $T_e < 2$). The input to this model are the voltages that are on the stator side and are V_{ds} & V_{qs} which correspond to the d- and q-axis components of the grid voltage. The active and reactive power consumed by the IM model can be written in terms of the states and the inputs and is given by (5-2).

$$\begin{aligned}
P &= \frac{V_{ds}}{X_e^2} \cdot (X_r \cdot \phi_{ds} - X_M \cdot \phi_{dr}) + \frac{V_{qs}}{X_e^2} \cdot (X_r \cdot \phi_{qs} - X_M \cdot \phi_{qr}) \\
Q &= \frac{V_{ds}}{X_e^2} \cdot (X_r \cdot \phi_{qs} - X_M \cdot \phi_{qr}) - \frac{V_{qs}}{X_e^2} \cdot (X_r \cdot \phi_{ds} - X_M \cdot \phi_{dr})
\end{aligned} \tag{5-2}$$

As the methods in Chapters 3 & 4 measure and analyze the admittance, it is convenient to use the admittance to monitor the dynamics of the 3-phase IM as well. The conductance and susceptance of the IM can be estimated from the active and reactive power as shown in (5-3).

$$\begin{aligned}
G &= \frac{P}{V_{ds}^2 + V_{qs}^2} = \frac{V_{ds}}{X_e^2} \cdot \frac{(X_r \cdot \phi_{ds} - X_M \cdot \phi_{dr})}{V_{ds}^2 + V_{qs}^2} + \frac{V_{qs}}{X_e^2} \cdot \frac{(X_r \cdot \phi_{qs} - X_M \cdot \phi_{qr})}{V_{ds}^2 + V_{qs}^2} \\
B &= \frac{Q}{V_{ds}^2 + V_{qs}^2} = \frac{V_{ds}}{X_e^2} \cdot \frac{(X_r \cdot \phi_{qs} - X_M \cdot \phi_{qr})}{V_{ds}^2 + V_{qs}^2} - \frac{V_{qs}}{X_e^2} \cdot \frac{(X_r \cdot \phi_{ds} - X_M \cdot \phi_{dr})}{V_{ds}^2 + V_{qs}^2}
\end{aligned} \tag{5-3}$$

The overall dynamics of the IM load can be written succinctly as (5-4) where x is the column vector of dynamic states, u is the column vector of inputs to the model and y is the column vector of the measured outputs of the IM.

$$\begin{aligned}
\dot{x} &= f(x, u); y = g(x, u); \\
x &= [\phi_{ds} \quad \phi_{qs} \quad \phi_{dr} \quad \phi_{qr} \quad \omega_r]^t; u = [V_{ds} \quad V_{qs}]^t; y = [G \quad B]^t
\end{aligned} \tag{5-4}$$

The following observations can be drawn from the structure of the dynamic equations (5-1)

- The system of equations represents a non-linear dynamical system
- Except the term ω_r^T , the non-linearity in the system are due to polynomials with degree two where the coupling between the states is represented by the multiplication of two states.
- The inputs appear linearly into the dynamical system and directly impact only the first two states. The effect of the inputs on the other states is via these states.

In literature [2], [3], the study of the IM dynamic equations is usually performed by simplifying the dynamic equations into a 1st order system by using the argument of time scales.

The time constant of the 1st four states - ϕ_{ds} , ϕ_{qs} , ϕ_{dr} & ϕ_{qr} - is usually very small and so they are simplified and only the dynamical equation for the rotor speed remains. This dynamical equation is then converted to a discrete time system by using the Euler approximation and this is used for monitoring the rotor speed to detect under-speed that can lead to motor stalling[3]. The advantage of this approximation is the simplicity in the calculation involved as the complexity of the dynamics is significantly reduced. However, as the phenomenon of stalling is highly non-linear and so these simplifications might not be able to capture all the cases of stalling. Furthermore, these simplifications will not work in presence of other dynamics such as thermal dynamics of 1-phase motors disconnection, etc. Thus, a different methodology is necessary to capture the full dynamics of the system while retaining the computation efficiency and simplicity is necessary. For this, we turn to a data-driven methodology that exploits the offline computational capabilities and function approximation capabilities of recently developed techniques in the fields of dynamical systems and machine learning. Specifically, we utilize the operator theoretic framework of dynamical systems to simplify the dynamics in (5-1).

5.2 Operator Theoretic Description of Dynamical Systems

Consider a continuous time dynamical system of the form (5-5) where $x \in X \subset R^n$ and the vector f is assumed to be continuously differentiable.

$$\dot{x} = f(x) \tag{5-5}$$

Let $\phi_{\Delta t}(x_0)$ be the solution of the system (5-5) after a time Δt starting from initial state x_0 . Let \mathcal{O} be the set of all observables $\varphi: X \rightarrow \mathbb{C}$. For this dynamical system, there exists a semi-group of operators $\mathbb{U}_{\Delta t}: \mathcal{O} \rightarrow \mathcal{O}$ with the following definition

$$[\mathbb{U}_{\Delta t}(\varphi)](x) = \varphi(\phi_{\Delta t}(x)) \quad (5-6)$$

This operator is referred to the Koopman Operator [4] and the physical intuition on the behavior of the operator is as follows – given an observable φ , a point x_0 in the state space from which the system evolves to a new state x_1 after a time period Δt . The Koopman operator outputs another observable $\mathbb{U}_{\Delta t}\varphi$ with the property that the value of the new observable at x_0 is equal to the value of the original observable at x_1 . It can also be seen that repeatedly applying the Koopman operator on an observable tracks how the dynamics of the system will act on the original observable with a corresponding time delay.

A key property of the Koopman operator is the fact that this is a linear operator in the space of observables, even if the underlying dynamics is non-linear [4]. The tradeoff that has occurred is that we have now been lifted into an infinite dimensional space or operators from a finite dimensional state space. Despite this tradeoff, there have been recent advances in the theory that suggest a finite dimensional approximation of the Koopman operator is sufficient for monitoring and control purposes [5], [6]. This is done by approximating the space of observables using a set of dictionary functions using the method of extended dynamic mode decomposition (EDMD) [7].

Consider snapshots of data - $x[0], x[1] \dots, x[m]$ - obtained from simulating the dynamical system (5-5) with a time-step of Δt . Now let $\mathcal{D} = \{\psi_1 \ \psi_2 \ \dots \ \psi_K\}$ be the set of dictionary functions and let Ψ define a vector-valued function $\Psi: X \rightarrow \mathbb{C}^K$ as (5-7) and is the mapping from the physical state space to feature space.

$$\Psi(x) = [\psi_1(x) \ \psi_2(x) \ \dots \ \psi_K(x)]. \quad (5-7)$$

Let $\mathcal{G}_{\mathcal{D}}$ denote the span of \mathcal{D} and so functions $\phi, \hat{\phi} \in \mathcal{G}_{\mathcal{D}}$ can be written as (5-8) for some set of coefficients $\mathbf{a}, \hat{\mathbf{a}} \in \mathbb{C}^K$. Let ϕ & $\hat{\phi}$ share the property (5-9), i.e. $\hat{\phi}$ is projection into $\mathcal{G}_{\mathcal{D}}$ of the output of the Koopman operator on ϕ .

$$\phi = \sum_{k=1}^K a_k \psi_k = \mathbf{\Psi}^T \mathbf{a}, \quad \hat{\phi} = \sum_{k=1}^K \hat{a}_k \psi_k = \mathbf{\Psi}^T \hat{\mathbf{a}} \quad (5-8)$$

$$\mathbf{\Psi}(x[i+1]) = (\mathbb{U}_{\Delta t} \mathbf{\Psi})(x[i]) + r \quad (5-9)$$

To find the optimal mapping which can minimize this residual, let \mathbf{K} be a finite dimensional approximation of the Koopman operator. Then the matrix \mathbf{K} can be obtained as a solution of the least-square problem formulated as follows in (5-10) [7].

$$\min_{\mathbf{K}} \sum_{i=0}^{m-1} |\mathbf{\Psi}(x[i+1]) - \mathbf{K}^t \cdot \mathbf{\Psi}(x[i])|_2^2 \quad (5-10)$$

The approximation of the Koopman operator can then be used to propagate the system dynamics much faster the dynamics in the lifted space is now a linear system shown in (5-11).

$$\mathbf{\Psi}(x[i+1]) = \mathbf{K}^t \cdot \mathbf{\Psi}(x[i]) \quad (5-11)$$

We can also estimate a reconstruction matrix \mathbf{R} that is able to recover the original state space from the lifted functional space. This is again estimated from the data from the least square optimization formulation in (5-12).

$$\min_{\mathbf{R}} \sum_{i=0}^{m-1} |x[i] - \mathbf{R}^t \cdot \mathbf{\Psi}(x[i])|_2^2 \quad (5-12)$$

While the various optimization formulations above estimated a discrete-time data-driven linear model, similar techniques can be used to estimate a continuous-time linear system that approximates the behavior of the true dynamical system. To compare the operator theoretic based methods to standard linearization techniques, a simple example is described next.

5.2.1 Comparison between Koopman linear representations & standard linearization

Consider the two-state continuous-time dynamical system in (5-13). It is shown in [6] that this system has a single fixed point at the origin $x_1 = x_2 = 0$.

$$\begin{bmatrix} \dot{x}_1 \\ \dot{x}_2 \end{bmatrix} = f(x_1, x_2) = \begin{bmatrix} -0.5 \cdot x_1 \\ -(x_2 - x_1^2) \end{bmatrix} \quad (5-13)$$

The standard linearized methodology is to differentiate the dynamical system with respect to the states at the equilibrium of the dynamical system. This will lead to a linear dynamical system with new states that are equal to the difference between the coordinates and the equilibrium point. As the equilibrium point is the origin in this case, the states of the linearized system correspond to the states of the original system. Thus, the linearized system represented by (5-14) with states l_1 & l_2 . If the original system in (5-13) is linear, then the linearized system (5-14) will match the response of (5-13). In this scenario, the difference between the states x_1 & l_1 will be zero. However, if the system in (5-13) is non-linear, then the response of the linearized system will not be identical and so the error between the states x_1 & l_1 can be used as a measure of the accuracy of the linearization. One important fact to note is that the derivation of the linearized system needs an explicit expression for the dynamics of the true system. This might not always be possible and is a disadvantage with this method.

$$\begin{bmatrix} \dot{l}_1 \\ \dot{l}_2 \end{bmatrix} = L(l_1, l_2) = \begin{bmatrix} -0.5 & 0 \\ 0 & -1 \end{bmatrix} \begin{bmatrix} l_1 \\ l_2 \end{bmatrix} \quad (5-14)$$

The Koopman operator based linear representation is very much dependent on the dictionary functions Ψ that are used as basis functions for the span of the observable functions that remain invariant under the dynamics of the system in (5-13). Based on mathematical analysis [6], the three dictionary functions shown in (5-15) have been shown [6] to enable a continuous-time linear representation of the dynamics of (5-13) in the lifted space of

observables. The dynamics of the observables are given by (5-16), where the $\dot{\Psi}$ represents the rate of change of the particular observables of the system in (5-15).

$$\Psi(x_1, x_2) = \begin{bmatrix} \psi_1(x_1, x_2) \\ \psi_2(x_1, x_2) \\ \psi_3(x_1, x_2) \end{bmatrix} = \begin{bmatrix} x_1 \\ x_2 \\ x_1^2 \end{bmatrix} \quad (5-15)$$

$$\dot{\Psi} = \mathbf{A} \cdot \Psi \quad (5-16)$$

It can be seen that the expression for (5-16) represents a linear dynamical system and the matrix \mathbf{A} can be estimated from state measurements of the true systems by solving (5-10). For this particular system and the choice of the dictionary functions, the estimate of the matrix \mathbf{A} is shown in (5-17). It is important to note that the linear representation in (5-16) is estimated from data and not from a model directly. This makes it possible to apply the method to settings where the true dynamics of a system are not available as a mathematical expression but where data from the system can be extracted by performing simulations/experiments.

$$\mathbf{A} = \begin{bmatrix} -0.5 & 0 & 0 \\ 0 & -1 & 1 \\ 0 & 0 & -1 \end{bmatrix} \quad (5-17)$$

To compare the accuracy of the standard linearization (5-14) and the Koopman linear representation (5-16) with the true dynamics of the system (5-13), the systems are initialized from the same state values and the state evolution versus time of the two states are compared. As the states are present in the list of dictionary functions, there is no need to estimate a separate recovery matrix in this case. For the sake of exposition, the initial state of $x_1 = 1.5$ & $x_2 = -1$ is used for the comparison. The systems are simulated in Matlab using the ode45 routine for 20s and a time step of 0.1s.

Figure 5.1 and Figure 5.2 plot the evolution of the states x_1 & x_2 for the true system, the linearized system and the Koopman linear representation. It can be observed from figure

5.1 that the evolution of x_1 is identical for all the three system representations. This is because the expression describing the evolution of x_1 in the true system (the first equation in (5-13)) is a linear expression that is independent of x_2 . This property makes the evolution of x_1 identical in the standard linearized representation and the Koopman linear representation.

Next, it can be observed from figure 5.2 that that the evolution of x_2 is identical for the true system and the Koopman linear representation for the entire simulation period while the evolution of the linearized representation is different from the true system in the initial few seconds when the non-linear behavior is the most dominant. After a few seconds, the linearized system also converges to the stable equilibrium point. The mismatch between the true system and the linearized system is due to the fact that the linear system is only valid over a small region around the equilibrium point and the linearized system cannot replicate the true system behavior for large deviations from the equilibrium point. The Koopman representation has much less error as the non-linear basis functions (5-15) enhance the expressiveness of the linear representation in (5-16) to replicate the true systems behavior.

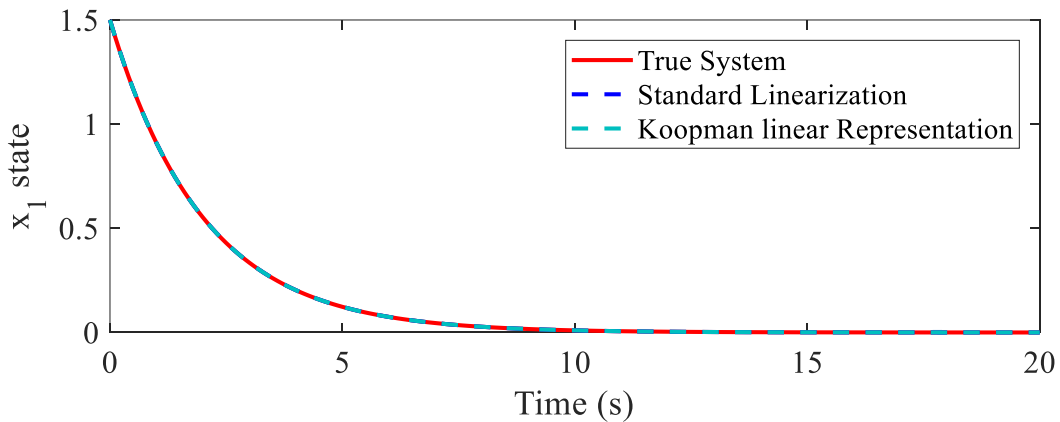


Figure 5.1 Comparison of x_1 for the true system, linearized system and the Koopman linear representation starting from the initial condition [1.5, -1]

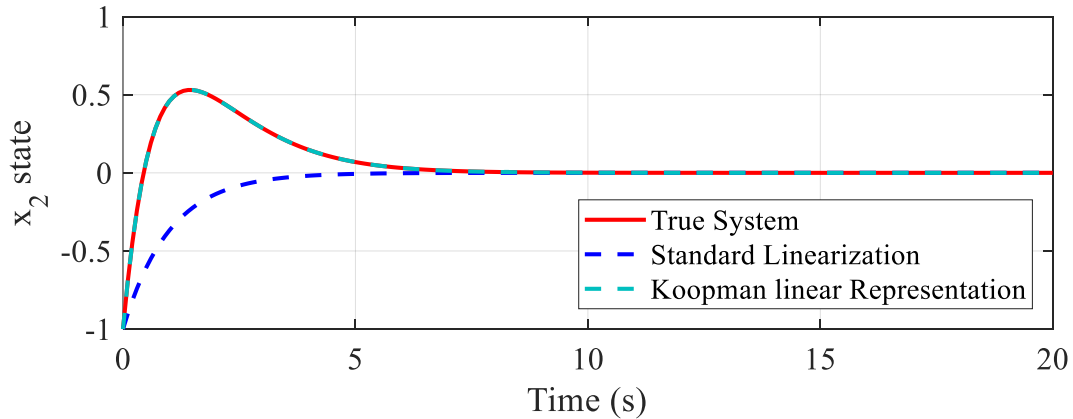


Figure 5.2 Comparison of x_2 for the true system, linearized system and the Koopman linear representation starting from the initial condition $[1.5, -1]$

From the observations for this simple example system, the key advantages of the Koopman representation can be summarized below

- a. The non-linear dictionary functions provide the expressive capacity to the Koopman linear representation to replicate non-linear behavior over a wide range of operating conditions. This is not possible by conventional linearized methods that are only valid over a small region around the equilibrium point.
- b. The estimation of the Koopman linear representation does not need the explicit expression of the system dynamics and can be performed in a data-driven manner by linear-techniques and simulation/experimental data. Conventional linearized methods need the explicit expression of the dynamics as they perform a symbolic differentiation of the expressions to derive the linear representation. Thus, they cannot exploit the data recorded from simulation/experiments.

While the original Koopman theory was developed for non-actuated dynamical systems, an extension to the theory that incorporates the inputs to the dynamical system have been proposed recently and the resulting dynamical system in the lifted space is now a bi-linear dynamical system [8]. This is described in the next section in the context of induction motors.

5.3 Data Driven Linear Model Estimation of Induction Motor

Based on the Koopman theory for controllable dynamical systems, the lifted dynamical system for the induction motor is likely to have the form shown in (5-18).

$$\Psi(x[i+1]) = \mathbf{K}^t \cdot \Psi(x[i]) + V_{ds}^2[i] \cdot \mathbf{B}_1 \cdot \Psi(x[i]) + V_{qs}^2[i] \cdot \mathbf{B}_2 \cdot \Psi(x[i]) \quad (5-18)$$

The inputs to the motor are squared in this system and they arise due to the fact that the states are interacting as polynomials of degree 2. It can be seen that the system in (5-18) is bi-linear with the inputs appearing as squares. As the model has outputs that are measured, they also need to be written in terms of the lifted dynamics and the input. The form of the outputs is shown in (5-19).

$$y[i] = \mathbf{C} \cdot \Psi(x[i]) + V_{ds}^2[i] \cdot \mathbf{D}_1 \cdot \Psi(x[i]) + V_{qs}^2[i] \cdot \mathbf{D}_2 \cdot \Psi(x[i]) \quad (5-19)$$

The reconstruction of the states back from the lifted space is of the form shown in (5-20)

$$x[i] = \mathbf{R} \cdot \Psi(x[i]) + V_{ds}[i] \cdot \mathbf{E}_1 \cdot \Psi(x[i]) + V_{qs}[i] \cdot \mathbf{E}_2 \cdot \Psi(x[i]) \quad (5-20)$$

The various matrices in the dynamics of the system in the lifted space such as \mathbf{K} , \mathbf{R} , \mathbf{B}_1 , \mathbf{B}_2 , \mathbf{D}_1 , \mathbf{D}_2 , \mathbf{E}_1 & \mathbf{E}_2 need to be estimated from the IM behavior under various input conditions and can be estimated using least square techniques on simulated data. The simulation of data and the dictionary functions used for the IM model are explained in the following subsection.

5.3.1 Data generation for learning the linear model

There are two key aspects that determine the accuracy of the proposed data-driven method to estimate the non-linear dynamics using a linear system in the lifted space. They are

- a. The number and behavior of the dictionary functions used in Ψ
- b. The amount of perturbation provided to the model from the inputs during the training phase

It is shown in literature that the most appropriate dictionary functions have the behavior that they span the entire state space with minimal overlap between themselves. The Gaussian radial basis functions satisfy these criteria and are used as the dictionary functions. The number of dictionary functions is a trickier problem as it is very much dependent on the dynamical system. The usual practice is to try for a reasonable number (say twice the number of states) and test it to see if the behavior of the lifted system is able to capture the dynamics of the original system. If it is not able to, then the dictionary function size is increased till the error between the two systems is below a threshold.

Next, the amount of perturbation in the system is very critical for proper learning of the model if we are to use it over a wide range of inputs. As we are expected to use this data-driven model during FIDVR phenomenon which has sustained low voltages, the IM model needs to be provided comparable inputs during the training phase where the lifted system is identified. Thus, the data generation is a key part of the exercise to ensure accurate model estimation. Furthermore, instead of training the model on a single trajectory from a single initial point, it is suggest to train on short trajectories that originate from several initial conditions.

Considering all the above discussion, the data for estimating the lifted dynamical system that is trained offline is generated in the following manner:

1. Fix a time step for the simulation. A time step of 0.025s is used as it is close to a PMU measurement time step.
2. Choose a random initial state x_0 for the IM
3. Choose a random input waveform for V_{ds} & V_{qs} that is varying with the same time step. The range of the input is between 0 and 1.

4. Perform simulations of (5-1) starting from x_0 for 200 time steps (5s) with a varying input waveform.
5. Record the trajectories of the states, the inputs and the outputs.
6. Go to Step 2 and repeat for 400 instances of initial conditions and input perturbations

This completes the data collection phase of the procedure. Next, the dictionary functions are chosen to be Gaussian radial functions with the variance designed such that they cover the entire region of operation of an IM. This variance is dependent on the number of dictionary functions chosen. The least squares optimization is performed to estimate the various matrices and after testing on different parameters of the IM it was observed that 10 dictionary functions were able to capture most of the dynamics of the IM for a majority of cases and gave minimal reconstruction error. The validation results are described next that show the results of the linear model.

5.3.2 Validation of the linear model behavior

To validate the behavior of the linear model, the outputs and the state reconstruction of the lifted dynamics are compared with the true outputs and states of the IM for a varying input waveform. The parameters of the IM model are listed in Table 5-1. One interesting observation is that the torque exponent is not a whole number and so this is going to be a challenging case for the linear model. The model is initialized at x_0 slightly less than the synchronous speed and the corresponding initial value of the lifted state Ψ_0 is calculated using the dictionary functions. The full nonlinear system is then simulated in Matlab using an ODE solver with time varying voltage inputs and the data-driven model is independently advanced in time using the same time varying voltage inputs from Ψ_0 using (5-18).

Table 5-1 *The IM parameters for validation of the linear model*

Parameter	Value (p.u.)
R_s	0.04
X_{ls}	0.06
X_M	1.7
R_{r1}	0.05
X_{lr1}	0.06
R_{r2}	0.2
X_{lr2}	0.14
H	0.9
T_L	2.8
T_e	0.9
Δt	0.025 s

Figure 5.3 plots the input voltages used for the validation of the data-driven model. The voltage is oscillatory in behavior to simulate how the power system would behave after a fault. The overall magnitude of the voltage is low initially and then it rises to its steady state value in around 10s. The trajectory in the original state space is estimated by the reconstructing equation (5-20) from the trajectory in the lifted space. Figure 5.4 plots the true and estimated rotor speed of the IM and it can be observed that the estimated rotor speed very closely follows the true trajectory of the rotor speed. The maximum error between the true and estimated rotor speed is 0.02 p.u. The maximum error occurred in the initial 5 sec, as shown in Figure 5.5. This is because the voltage inputs are most varying and are farthest from their nominal value. All the other estimated flux states - ϕ_{ds} , ϕ_{qs} , ϕ_{dr} & ϕ_{qr} - also matched well with their true values.

Figure 5.6 plots the true conductance output of the IM and estimated conductance outputs from the data-driven model for the 1st 5 seconds. It can be seen that the error between the true and estimate values are the maximum at the beginning of the trajectory but they soon converge to the true value in ~ 3 s. The maximum error in the conductance estimation is ~ 0.1 p.u. and the nominal value is 3 p.u. , demonstrating the error percentage is small.

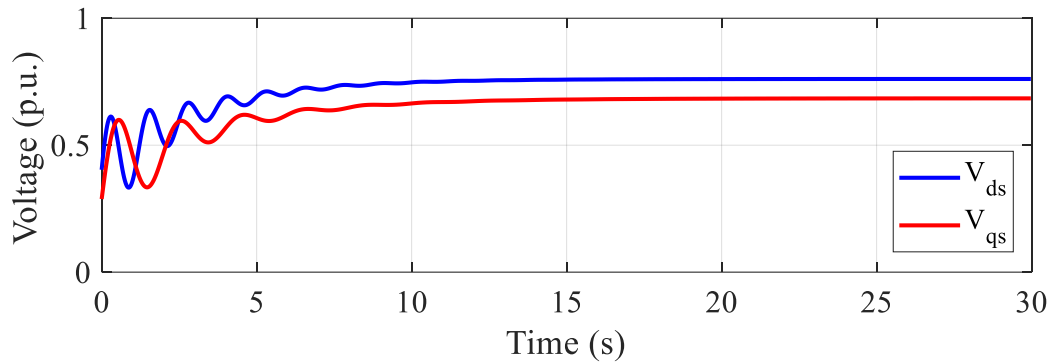


Figure 5.3 *Variation of the inputs to the linear model used for validation for the data-driven model*

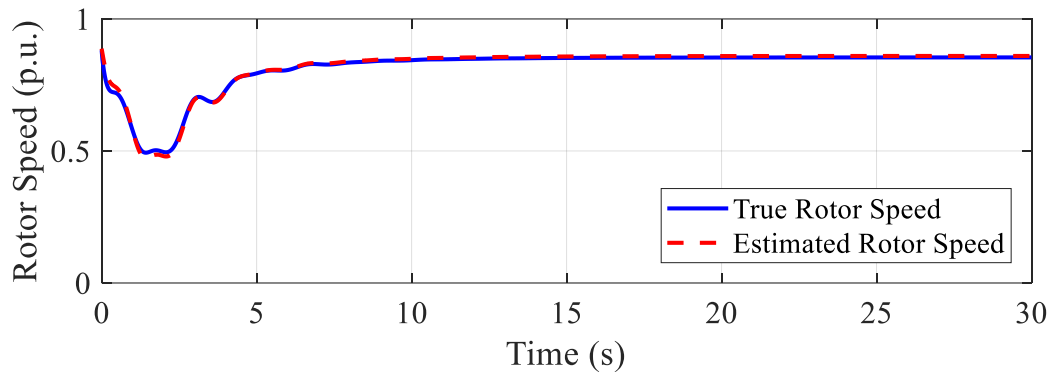


Figure 5.4 *Comparison between the true and estimated rotor speed from the reconstruction of the data-driven linear system.*

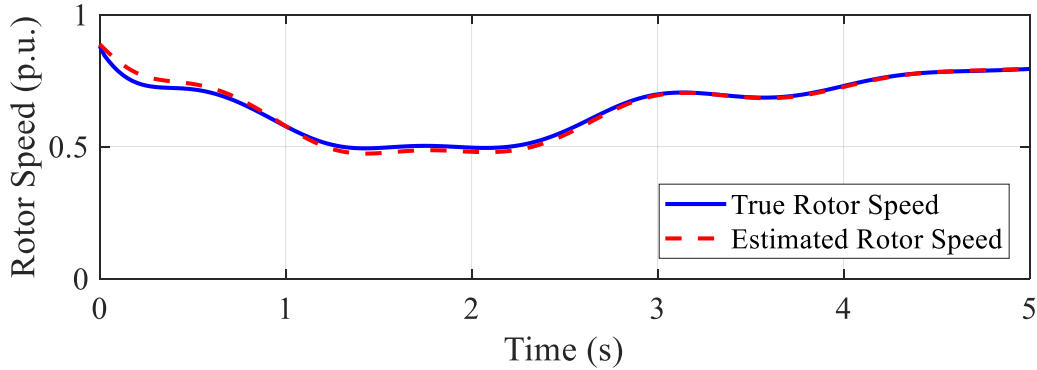


Figure 5.5 Comparison in the 1st 5 seconds between the true and estimated rotor speed from the reconstruction of the data-driven linear system

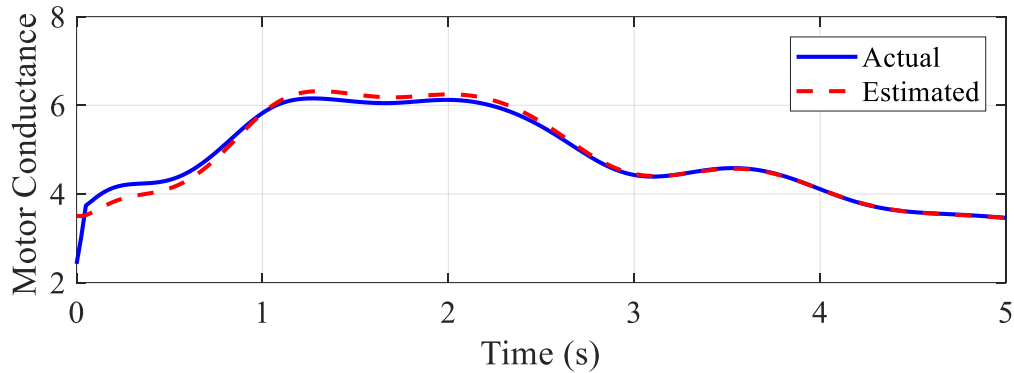


Figure 5.6 Comparison in the 1st 5 seconds between the motor conductance outputs of the full model and the estimated outputs from the data-driven linear system

As the data-driven model is based on training data, it is important to verify its limits and identify when the linear model behavior is not proper. The system is initialized at a rotor speed more than the synchronous speed which is not present in the training set. Figure 5.7 plots the actual and estimated rotor speeds with a time varying input. It seems like the overall trend such as the steady state value and the lowest speed is captured well by the proposed method. However, if we look at the zoomed in version, in Figure 5.8, there is a comparatively large error of 0.2 p.u. at the beginning which very quickly reduces in < 1 s. This demonstrates that the data-driven method is a bit too much dependent on the training data and so incorporating the various condition that we expect in practice is recommended.

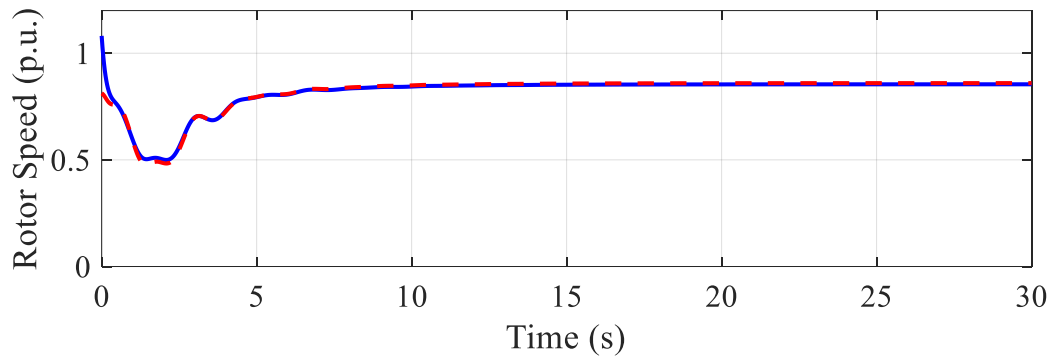


Figure 5.7 Comparison between the true and estimated rotor speed from the reconstruction of the data-driven linear system when starting outside the training region

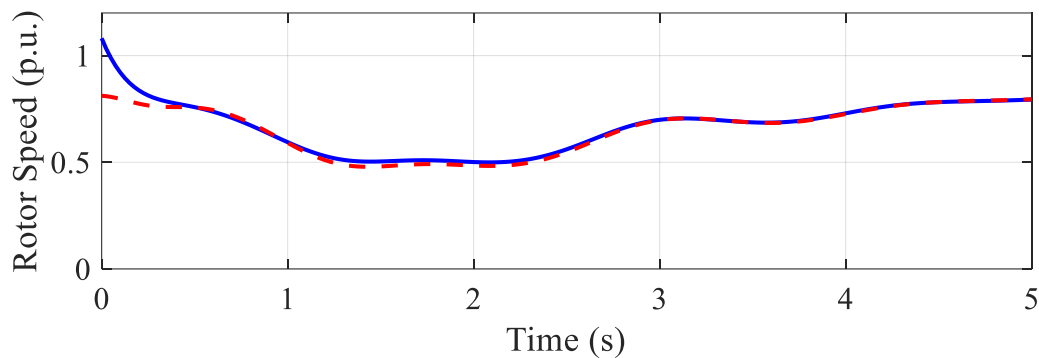


Figure 5.8 Comparison in the 1st 5 seconds between the true and estimated rotor speed from the reconstruction of the data-driven linear system when starting outside the training region

The phenomenon of stalling is an important behavior of the induction motor and is the reason for the large amount of non-linearity in the behavior of the IM. To validate whether the derived data-driven model is able to capture this behavior, a low voltage input is provided to the dynamic model and the resulting rotor speeds are compared between the true model and the data-driven model. Figure 5.9 plots the voltage inputs that initiate stalling as the magnitude of the voltage is ~ 0.6 p.u. at its peak. The motor is initialized close to synchronous speed and the applied voltage will cause the motor to quickly decelerate and reach a speed ~ 0.2 p.u. Figure 5.10 plots the true and estimated speed of the rotor and it can be seen that the estimated speed also decelerates just like the actual model and is indeed able to capture the overall stalling

behavior accurately. The maximum error occurs at the nadir of the rotor speed and is clear in the zoomed plot shown in Figure 5.11. The decelerating motor behavior in the lifted space is important as it enables the stability monitoring using the data-driven model.

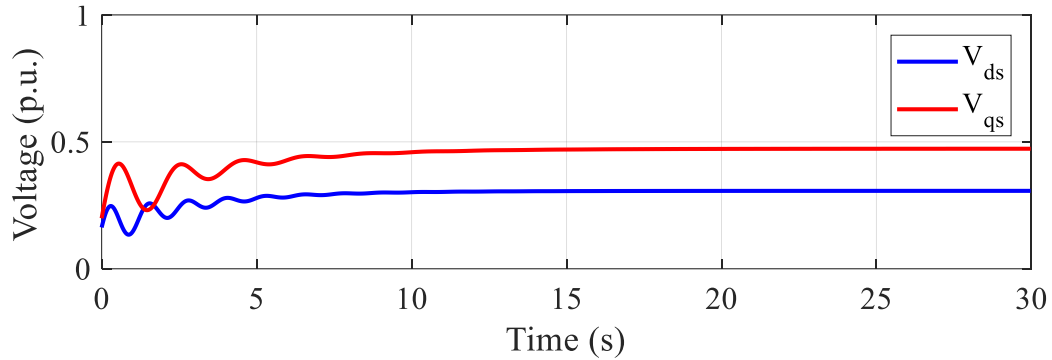


Figure 5.9 Variation of the inputs to the linear model used for validation to initiate stalling in the data-driven model

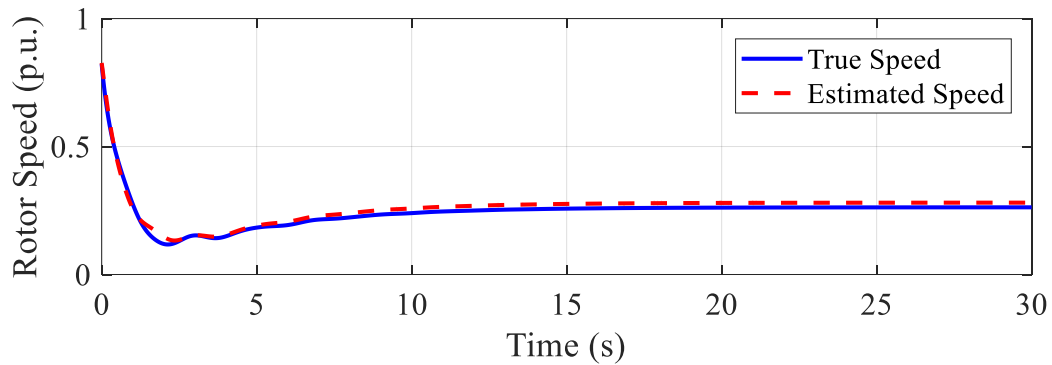


Figure 5.10 Comparison between the true and estimated rotor speed from the reconstruction of the data-driven linear system when stalling occurs.

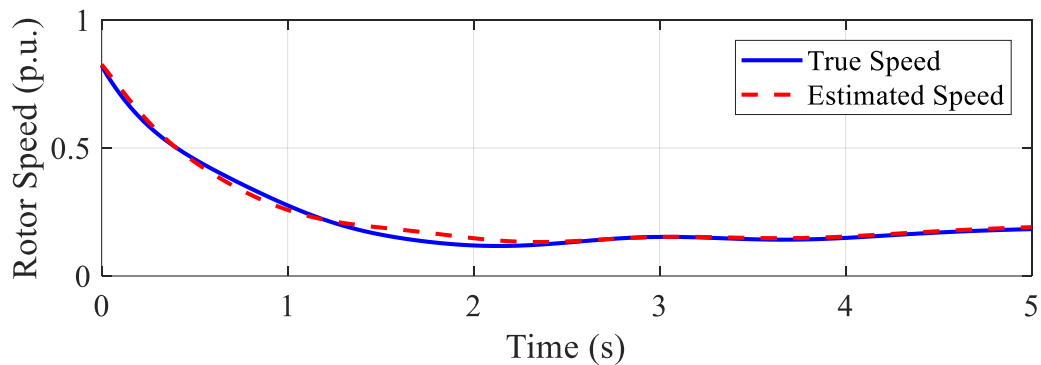


Figure 5.11 Comparison in the 1st 5 seconds between the true and estimated rotor speed from the reconstruction of the data-driven linear system when stalling occurs

5.4 Application of Linear Model of Induction Motor

5.4.1 Estimating the rotor speed from admittance measurements

As the data-driven linear model is able to accurately reconstruct the states, specifically the rotor speed, and the admittance outputs from the full model, we can now exploit techniques from linear dynamical systems to monitor the system for stalling behavior and track the speed in an online manner after a dynamic event. As the voltage input to the model is measured by the PMU, The equations for the state evolution and output of measured can be written as (5-21) and (5-22). The matrices $\mathbf{A}[i]$ & $\mathbf{C}[i]$ are a function of the inputs which can be estimated by the measurement device if the matrices $\mathbf{K}, \mathbf{B}_1, \mathbf{B}_2, \mathbf{C}, \mathbf{D}_1$ & \mathbf{D}_2 are known. It can be seen that the form of equations (5-21) and (5-22) for state trajectory and output are in the form for a linear system and so measuring the y_{IM} over a time window will enable us to estimate the state Ψ and will allow us to track it in real time. Furthermore, as this is a linear formulation, the computation necessary is minimal and is suitable for stability applications where time is of essence. Once the lifted state is estimate, the reconstruction expression in (5-22) can be used to estimate the physical states, and specifically the rotor speed.

$$\Psi[i + 1] = (\mathbf{K}^t + V_{ds}^2[i] \cdot \mathbf{B}_1 + V_{qs}^2[i] \cdot \mathbf{B}_2) \cdot \Psi[i] = \mathbf{A}[i] \cdot \Psi[i] \quad (5-21)$$

$$y_{IM}[i] = (\mathbf{C} + V_{ds}^2[i] \cdot \mathbf{D}_1 + V_{qs}^2[i] \cdot \mathbf{D}_2) \cdot \Psi[i] = \mathbf{C}[i] \cdot \Psi[i] \quad (5-22)$$

As a demonstration, two scenarios are tested – one in which the IM stalls and another in which the IM recovers. The PMU measures the admittances for 10 time steps – 0.25 s – and then estimates the lifted state using linear least square methods. The estimated state is then propagated using the inputs measured at the IM load terminal. The reconstruction of the rotor speed is done for every time step and can be used as a monitoring index. Figure 5.12 plots the

true and estimated speed for a case of inputs which lead to speed recovery after 5s. The estimated speed is accurate after ~ 0.3 s which was the time taken for the lifted state estimation using the admittances. It can be seen that the estimated speed is indeed tracking the actual speed for the entire time. Similarly, Figure 5.13 plots the true and estimated speed for a case of inputs which lead to recovery to a lower speed after 5s. For this scenario, the estimated speed had an error that was at the lowest speed in the true trajectory, but this accuracy is sufficient to take control actions and prevent the motor stalling and short term instability [3].

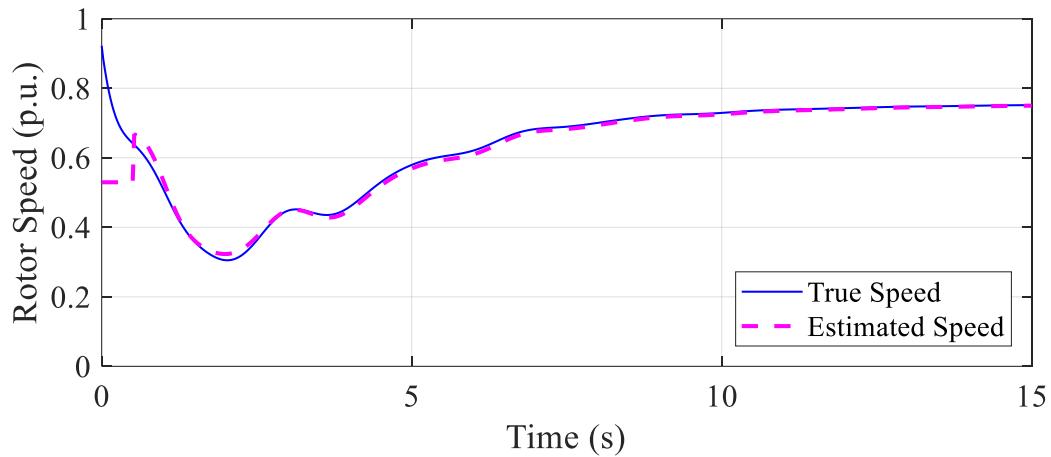


Figure 5.12 Comparison in the 1st 5 seconds between the true and estimated rotor speed from the reconstruction

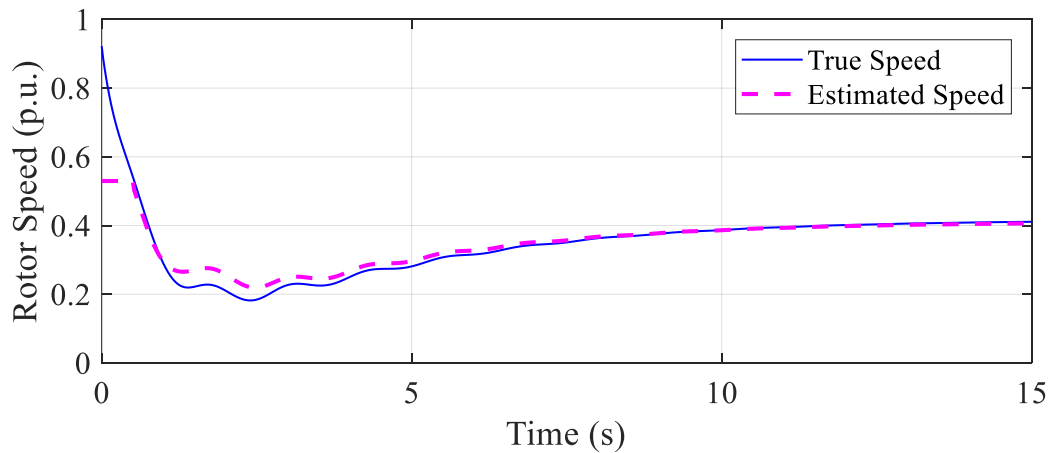


Figure 5.13 Comparison in the 1st 5 seconds between the true and estimated rotor speed from the reconstruction

5.4.2 Estimating fraction of 1-phase motor stalling

There can be situations when the PMU will measure a combination of loads and not a single load – such as the WECC composite load model [9]. The admittance measured by the PMU in this case will be a result of the combined dynamics of the load. In case of the WECC model, the admittance of the loads other than the motor-D can be estimated just from the load parameters and voltages. The admittance of motor-D is not easy to estimate as it depends on the proportion of motor that is stalled after a dynamic event. The expression for the admittance of the motor-D is given in (5-23) and is linear in the fraction of stall, given that the input voltage is measured. Thus, the total measured admittance is a linear function of the lifted state and the stalled fraction. As the stalled fraction does not change with time, this can also be estimated using the linear state estimation techniques introduced in Section 5.4.1. This enables the operator to accurately estimate the stalled proportion even when the IM dynamics exist.

$$y_{mD}[i] = \frac{(1 - f_{stall})}{V_{ds}^2[i] + V_{qs}^2[i]} \begin{bmatrix} P_{mD} \\ Q_{mD} \end{bmatrix} + f_{stall} \begin{bmatrix} G_{stall_{fill}} \\ B_{stall_{full}} \end{bmatrix} = \mathbf{C}_{mD}[i] \cdot f_{stall} \quad (5-23)$$

$$y_{meas}[i] = y_{IM}[i] + y_{mD}[i] = \mathbf{C}_{IM}[i] \cdot \Psi[i] + \mathbf{C}_{mD}[i] \cdot f_{stall} \quad (5-24)$$

The accuracy of the stalled proportion depends on the magnitude of \mathbf{C}_{mD} compared to \mathbf{C}_{IM} in (5-24) which depends on the load proportion of motor-D in the overall composite load. Table 5-1 lists the results for various trials with different fraction of Motor-D and stall proportion. The range given is the standard deviation of the estimated stall proportion after 100 trials. It can be seen that when the fraction of motor-D and stall proportion is low, then the error is the highest and as the motor-D fraction and the stall proportion increases, the estimation accuracy improves, and this is because the methodology is better able to split the overall

admittance into its constituent components easily. Thus, the linear data-driven model is able to estimate the fraction of motor stalled in an online manner that opens up the application for targeted load control.

Table 5-2 *The actual and estimated stall proportions using the linear model*

Fraction of Motor-D	True Motor-D Stall %	Estimated Stall %
20%	20%	15% \pm 2%
20%	50%	48% \pm 1%
20%	80%	82% \pm 1%
40%	20%	23% \pm 1%
40%	50%	51% \pm 0.5%
40%	80%	80% \pm 0.5%

5.5 Conclusion

In this paper a method to estimate a linear model from the non-linear 3-phase induction motor dynamics using techniques from linear operator theory is described. It is a data-driven approach that uses simulated data from the full non-linear IM and lifts the system into a functional space in which the trajectories of the simulated data follow a linear relation. The functional space is chosen so that the dynamic states and the outputs of the original system can be recovered from the lifted space in a linear manner. The proposed method is validated on a detailed induction motor model using Gaussian radial basis functions for lifting. The data-driven linear model is able to capture non-linear behavior of the induction motor such as stalling at low voltages and nominal operation for high voltages. This implies that the techniques from linear systems can be used to perform state estimation and reconstruction in an online manner from output admittance measurements at the PMU, enabling stability monitoring for the non-linear model without model approximations as is usually done in

literature. The proposed method can also be used to estimate the fraction of 1-phase motor stalling from PMU measurements of the admittance due to its linear nature making it the first time these two kinds of motors can be monitored at the same time.

5.6 References

- [1] Paul Krauss, “Analysis of Electric Machinery and Drive Systems”, 2nd Edition.
- [2] H. Bai, and V. Ajjarapu "A novel online load shedding strategy for mitigating fault-induced delayed voltage recovery" *IEEE Trans. Power Syst.* vol. 26 no. 1 pp. 294-304 Feb. 2011.
- [3] Y. Dong, et. al., "An Emergency-Demand-Response Based Under Speed Load Shedding Scheme to Improve Short-Term Voltage Stability," in *IEEE Trans. on Pow. Sys.*, vol. 32, no. 5, pp. 3726-3735, Sept. 2017
- [4] M. Budisic, R. Mohr, and I. Mezic, “Applied koopmanism,” *Chaos*, vol. 22, pp. 047510–32, 2012.
- [5] S. Peitz and S. Klus, “Koopman operator-based model reduction for switched-system control of pdes,” *arXiv preprint*, arXiv:1710.06759, 2017.
- [6] S. L. Brunton, et. al, “Koopman invariant subspaces and finite linear representations of nonlinear dynamical systems for control,” *arXiv preprint*, arXiv: 1510.03007, 2015.
- [7] M. O. Williams, I. G. Kevrekidis, and C. W. Rowley, “A data–driven approximation of the koopman operator: Extending dynamic mode decomposition,” *Journal of Nonlinear Science*, vol. 25, no. 6, pp. 1307–1346, 2015.
- [8] B. Huang and U. Vaidya, “Feedback Stabilization Using Koopman Operator,” *arXiv preprint*.
- [9] Modeling and validation work group, “WECC Dynamic Composite Load Model Specifications,” Western Electricity Coordinating Council, Technical Report, January 25, 2015

CHAPTER 6. SENSITIVITY BASED THEVENIN INDEX WITH SYSTEMATIC INCLUSION OF REACTIVE POWER LIMITS

Modified from a manuscript published in IEEE Transactions in Power Systems

Amarsagar Reddy Ramapuram Matavalam and Venkataramana Ajjrapu

*Department of Electrical and Computer Engineering, Iowa State University, Ames, IA 50011,
United States of America.*

Abstract

This paper presents proof for the relation between the Local Thevenin Index (LTI), measured at a Phasor Measurement Unit (PMU) that is used as an indicator of voltage stability, and the system operating condition. The derivation establishes that there is a direct connection between the sensitivity and the LTI and provides a mathematically rigorous justification to use LTI as a static long-term voltage stability indicator of the entire system. A Sensitivity based Thevenin Index (STI), calculated using Wide Area Measurements, is proposed and it can be used at the control center to authenticate the LTI being received from PMUs, to safeguard against malicious and spurious data. The association between the sensitivity and the LTI can also be used to predict the effect of various what-if scenarios on the LTI. As a demonstration, the impact of generator limits on the LTI is predicted, enabling the operator to anticipate the abrupt change in LTI before the limits are reached. Results are described in detail for a 5-Bus system, and verified on larger systems up to 300 buses, establishing the connection between the LTI and the sensitivities, and validating the prediction of impact of the generator reactive limits on the LTI

6.1 Introduction

The existing online long term voltage stability monitoring methods that utilize PMU measurements are either (a) local methods that only use quasi-static measurements at a single node or (b) central methods that use measurements over a wide-area at the control center. These methods have been developed independently in literature with no relation between the centralized and local methods and are unable to exploit the advantages of each of the methods. In order to see how a centralized method can be used to validate the local index, a mathematical relation is derived that relates the two kinds of methods [1]. This derivation proves that the local index is inherently related to the Jacobian of the system, via the sensitivities and provides the mathematical justification to use the local index as a measure of the system long term voltage stability for multi-bus systems. The relation between the sensitivities and the Thevenin index, called as the Sensitivity based Thevenin index (STI), can be used by the control center to validate the index being calculated at the PMU as the STI is much more robust to noise than the local index [1]. This validation is particularly important as the operator might activate control schemes based on the local Thevenin index, making it a cyber-security risk. The relation between the STI and the local index can also be used to estimate the change in the index after a generator reaches its reactive limit [1]. This predictive capability of the STI can be utilized at the control center to estimate the worst case impact of the reactive limit being reached and provides the operator with a better situational awareness of the system. Thus, the STI at the control center can ensure that the local index calculated can be used reliably for monitoring and control of long term voltage stability by overcoming the conventional limitations of robustness and including the reactive limits.

6.2 Sensitivity Based Thevenin Index

Figure 6.1 shows the 2-bus equivalent at a load bus where the rest of the system is reduced into an equivalent voltage E_{th} and an equivalent impedance Z_{th} .

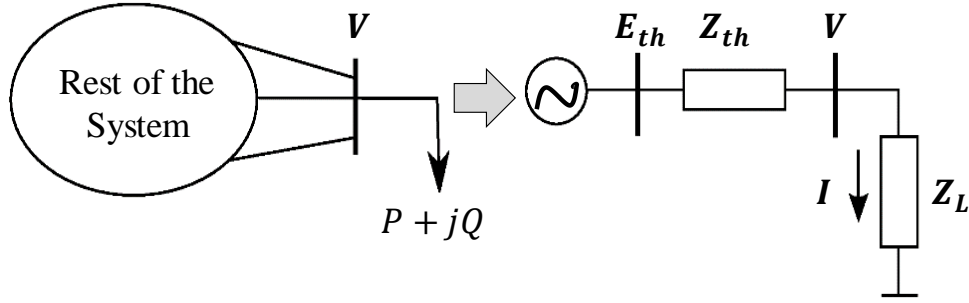


Figure 6.1 *The reduction of the rest-of-the-system into an equivalent Z_{th} and E_{th}*

In principle, two subsequent phasor measurements of the pair V & I can be used to compute Z_{th} under the assumption that the equivalent parameters do not change during the time interval between the two subsequent measurements [2]. This assumption is valid when the load increment ($\Delta\lambda$) between the two measurements is as close to 0 as possible. In practice, $\Delta\lambda$ between subsequent measurements is very small ($\sim 0.1\%$) and thus we can use this assumption but theoretically, the ideal value of the Z_{th} is determined when the load increment is as close to 0 as possible (i.e. $\Delta\lambda \rightarrow 0$).

The conventional Local Thevenin index (LTI) at a load Bus i , uses the Thevenin Impedance and the Load Impedance and can be determined by (6-1) to (6-3), using two distinct operating points [2].

$$\mathbf{Z}_{th_i} = -\frac{\mathbf{V}_i^{(2)} - \mathbf{V}_i^{(1)}}{\mathbf{I}_i^{(2)} - \mathbf{I}_i^{(1)}} = -\frac{\Delta\mathbf{V}_i}{\Delta\mathbf{I}_i} \quad (6-1)$$

$$\mathbf{Z}_{L_i} = \left(\frac{\mathbf{V}_i^{(1)}}{\mathbf{I}_i^{(1)}} \right) \quad (6-2)$$

$$LTI_i = \left| \frac{\mathbf{Z}_{th}}{\mathbf{Z}_L} \right| = \left| \frac{\Delta \mathbf{V}_i}{\mathbf{V}_i^{(1)}} \right| \cdot \left| \frac{\mathbf{I}_i^{(1)}}{\Delta \mathbf{I}_i} \right| \quad (6-3)$$

The closer the operating points are, the better the estimate of the Thevenin impedance and the accuracy of the LTI. For this derivation, it is assumed that there is no noise in the measurements, as this is the ideal scenario and will result in the ideal LTI value. The impact of noise on the LTI will be discussed later in Section 4.2.2.4. The LTI is calculated at every instant of time and at every bus with PMUs. Hence, for the sake of simplicity, the index of time, 't', and the index of the bus, 'i', is dropped from all equations in the derivation, as it is understood by the reader.

Let the load at bus i at the 1st instant be $(P + jQ)$ and the load at the 2nd instant be $(P + jQ)(1 + \Delta\lambda)$. We assume a load increase with constant power factor and this implies that $\Delta\lambda$ is a scalar. This is a valid assumption as the power factor in practice stays in a very tight range. For simplicity, the loading direction is assumed to be proportional to the initial load (this assumption will be later removed in Section 4.2.2.4) implying that the $\Delta\lambda$ at all the buses is same. Let the load voltage at the 1st instant be $(V)e^{j(\theta)}$ and at the 2nd instant can be expressed as $(V + \Delta V)e^{j(\theta + \Delta\theta)}$. We will attempt to get \mathbf{Z}_{th} in terms of $\theta, \Delta\lambda, \Delta V$ & $\Delta\theta$. The equations (6-4) to (6-8) are directly due to their definitions.

$$\Delta \mathbf{V} = (V + \Delta V)e^{j(\theta + \Delta\theta)} - (V)e^{j(\theta)} \quad (6-4)$$

$$\Delta \mathbf{V} = \mathbf{V}^{(1)} \left((1 + \Delta V/V) e^{j(\Delta\theta)} - 1 \right) \quad (6-5)$$

$$\mathbf{I}^{(1)} = \frac{(P - jQ)}{(V)e^{-j(\theta)}}; \mathbf{I}^{(2)} = \frac{(P - jQ)(1 + \Delta\lambda)}{(V + \Delta V)e^{-j(\theta + \Delta\theta)}} \quad (6-6)$$

$$\Delta \mathbf{I} = \mathbf{I}^{(1)} \left(\frac{1 + \Delta\lambda}{(1 + \Delta V/V) e^{-j(\Delta\theta)}} - 1 \right) \quad (6-7)$$

$$\frac{\mathbf{Z}_{th}}{\mathbf{Z}_L} = -\frac{\Delta V}{V^{(1)}} \cdot \frac{\mathbf{I}^{(1)}}{\Delta \mathbf{I}} = \frac{\left(\frac{\Delta V}{V} + 1\right) \cdot \left(\left(1 + \frac{\Delta V}{V}\right) - e^{-j(\Delta\theta)}\right)}{\left(1 + \Delta\lambda - \left(1 + \frac{\Delta V}{V}\right) e^{-j(\Delta\theta)}\right)} \quad (6-8)$$

Observe that in (6-8), $\Delta \mathbf{I}$ is in the denominator, and so, this derivation is valid only for buses with non-zero loads. As explained before, the smaller the value of $\Delta\lambda$ (implying $\Delta\theta$ & ΔV are also small), the closer the two operating points and the better the estimate of the LTI. Using the power series expansion for $e^{-j(\Delta\theta)}$ in (6-8), and neglecting $(\Delta\theta)^2$ and higher order terms, (6-9) is obtained.

$$\frac{\mathbf{Z}_{th}}{\mathbf{Z}_L} = \left(\frac{\Delta V}{V} + 1\right) \cdot \frac{\left(\left(1 + \Delta V/V\right) - \left(1 - j(\Delta\theta)\right)\right)}{\left(1 + \Delta\lambda - \left(1 + \Delta V/V\right)\left(1 - j(\Delta\theta)\right)\right)} \quad (6-9)$$

Since $\Delta\theta$ & ΔV are small, 1 dominates $\Delta V/V$ in the first term and linear terms of $\Delta\theta$ & ΔV dominate the $(\Delta V)(\Delta\theta)$ term in the denominator. Thus, (6-9) can be simplified to (6-10) and the expression for the LTI can then be written as (6-11). As the LTI depends on the $\Delta\lambda$ chosen, it is explicitly written as a function of $\Delta\lambda$, using the expression $LTI(\Delta\lambda)$.

$$\frac{\mathbf{Z}_{th}}{\mathbf{Z}_L} = -\frac{\left(\frac{\Delta V}{\Delta\lambda} \cdot \frac{1}{V} + j\left(\frac{\Delta\theta}{\Delta\lambda}\right)\right)}{\left(1 - \frac{\Delta V}{\Delta\lambda} \cdot \frac{1}{V} + j\left(\frac{\Delta\theta}{\Delta\lambda}\right)\right)} \quad (6-10)$$

$$LTI(\Delta\lambda) = \left|\frac{\mathbf{Z}_{th}}{\mathbf{Z}_L}\right| = \sqrt{\frac{\left(\frac{\Delta V}{\Delta\lambda} \cdot \frac{1}{V}\right)^2 + \left(\frac{\Delta\theta}{\Delta\lambda}\right)^2}{\left(1 - \frac{\Delta V}{\Delta\lambda} \cdot \frac{1}{V}\right)^2 + \left(\frac{\Delta\theta}{\Delta\lambda}\right)^2}} \quad (6-11)$$

The ideal value of LTI occurs by evaluating the limit of the expression in (6-11) as $\Delta\lambda \rightarrow 0$ and the terms $\Delta V/\Delta\lambda$ and $\Delta\theta/\Delta\lambda$ become $dV/d\lambda$ and $d\theta/d\lambda$ respectively. The terms $dV/d\lambda$ and $d\theta/d\lambda$ are the sensitivities of the voltage magnitude and the phase angle with respect to the load scaling factor. Hence, the proposed index is termed as the Sensitivity

based Thevenin Index (STI), to indicate that it connects sensitivity and the Local Thevenin Index. The expression of the STI is presented in (6-12) and is simplified into (6-13).

$$STI = \lim_{\Delta\lambda \rightarrow 0} LTI(\Delta\lambda) = \sqrt{\frac{\left(\frac{dV}{d\lambda} \cdot \frac{1}{V}\right)^2 + \left(\frac{d\theta}{d\lambda}\right)^2}{\left(1 - \frac{dV}{d\lambda} \cdot \frac{1}{V}\right)^2 + \left(\frac{d\theta}{d\lambda}\right)^2}} \quad (6-12)$$

$$STI = \sqrt{1 + \frac{\left(2 \frac{dV}{d\lambda} \cdot \frac{1}{V} - 1\right)}{\left(1 - \frac{dV}{d\lambda} \cdot \frac{1}{V}\right)^2 + \left(\frac{d\theta}{d\lambda}\right)^2}} \quad (6-13)$$

The terms $dV/d\lambda$ and $d\theta/d\lambda$ are well known in industry and academia and similar sensitivities have been conventionally used as voltage stability indicators at the control center, before the widespread deployment of PMUs [3]. As the above derivation shows, there is a direct connection between the LTI and the sensitivities and hence the LTI can also be used as an indicator of static long-term voltage stability.

Intuitively, the reason for using the sensitivities can be understood using the Figure 6.2 which shows a PV curve with 3 operating points Point A, B and C. Point A is the present operating point, point B corresponds to a negative load increment ($\Delta\lambda < 0$) and point C corresponds to a positive load increment ($\Delta\lambda > 0$). The LTI derived using the $\Delta\lambda$ is directly related to the slope of the secants AB or AC. As the ideal value of the LTI occurs when the $\Delta\lambda \rightarrow 0$, this corresponds to the slope of the tangent at point A (which is same as the sensitivity). Thus, the sensitivities at an operating condition can be used to calculate the ideal LTI at a particular bus.

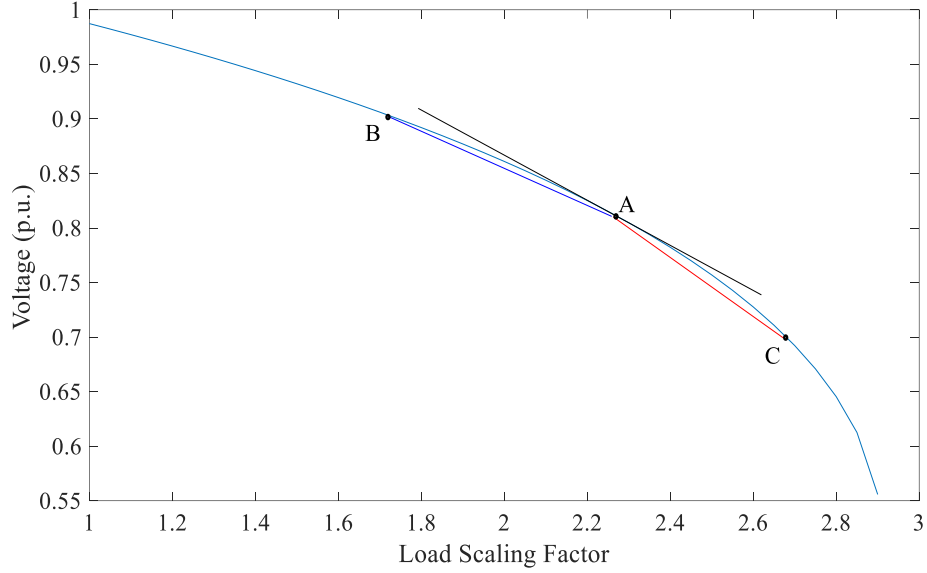


Figure 6.2 A PV curve indicating that the slope of tangent at a point, A, is between the slope of secants, AB ($\Delta\lambda < 0$) and AC ($\Delta\lambda > 0$).

The calculation of the sensitivities in power systems is a standard procedure and requires the Jacobian at an operating point [4]. Let $f(\bar{V}, \bar{\theta})$ be the set of expressions for the active power injection at all PV and PQ buses and let $g(\bar{V}, \bar{\theta})$ be the set of expressions for reactive power injection at all PQ buses. The sensitivities are determined by solving the linear system of equations given in (6-14).

$$\begin{bmatrix} f_{\bar{\theta}} & f_{\bar{V}} & \bar{P}_{\lambda} \\ g_{\bar{\theta}} & g_{\bar{V}} & \bar{Q}_{\lambda} \\ 0 & 0 & 1 \end{bmatrix} \cdot \begin{bmatrix} d\bar{\theta} \\ d\bar{V} \\ d\lambda \end{bmatrix} = \begin{bmatrix} 0 \\ 0 \\ 1 \end{bmatrix} \quad (6-14)$$

The submatrices $f_{\bar{\theta}}$ & $f_{\bar{V}}$ are the partial derivatives of the active power flow injection expressions with respect to the angles and voltages and can be extracted directly from the power system Jacobian at that operating point. Similarly, $g_{\bar{\theta}}$ & $g_{\bar{V}}$ correspond to the partial derivatives of the reactive power flow and are similarly extracted from the Jacobian. P_{λ} and

Q_λ are column vectors and correspond to how the active and reactive power injections vary as a function of $\Delta\lambda$. As described before, the voltage sensitivity at an operating point is essentially the slope of the tangent of the PV curve at that point and this method to determine sensitivities is numerically robust to noise, compared to numerically computing $\Delta V/\Delta\lambda$. Validation results comparing the behavior of the LTI and the STI are necessary for verification of the method and are described next.

6.2.1 Analytical Validation of Sensitivity Based Thevenin Index

The simplest way to check the validity of the derived expression in (6-12) is to analyze the range of the STI expression. It is a well-known fact that, if the system is in a valid operating point, the LTI has a value less than 1. This fact should also be true of the STI and can be directly deduced from (6-12). For any valid operating point, $dV/d\lambda < 0$ and so, $\left(1 - \frac{dV}{d\lambda} \cdot \frac{1}{V}\right)^2 > \left(\frac{dV}{d\lambda} \cdot \frac{1}{V}\right)^2$. Hence the denominator in (6-12) is larger than the numerator leading to a value less than 1 for a valid operating point.

The next step to validate the expression would be to determine its value at light loading and at heavy loading (close to the nose point). At light loading, the value of the conventional LTI is close to 0 while at high loading, the value of the conventional LTI is close to 1. This change in value with loading level is the main reason LTI is used in power system operations. The expression for STI should also behave in a similar manner at low and high loading.

At light loading, the sensitivities are small as there is sufficient power transfer capability in the network, hence $|dV/d\lambda| \sim 0$ and $|d\theta/d\lambda| \sim 0$. Observing (6-12), we can conclude that the STI for light loading is close to 0. In the region close to the nose point, the sensitivities are very high as the slope of the tangent increases and hence $|dV/d\lambda| \gg 1$ and $|d\theta/d\lambda| \gg 1$. For this scenario, (6-13) is analyzed, as (6-13) becomes an indeterminate form

of ∞/∞ and cannot provide a clear resolution. The denominator in (6-13) contains the term $(dV/d\lambda)^2$, while the numerator contains $(dV/d\lambda)$. Hence, the denominator dominates the numerator close to the nose point and the fraction in (6-13) approaches the value 0. Thus, the value of STI close to the nose point is around 1 and this behavior matches the observed behavior of LTI. Now that the analytical behavior of the STI is analyzed, the STI has to be numerically validated by comparing it with the calculated LTI and this is presented in the next subsection.

6.2.2 Numerical Validation of the Sensitivity Based Thevenin Index

The load power and the generation throughout the example systems are increased in proportion to the initial base case. The load power factor is kept constant and the reactive limits of the generators are not enforced. At every operating point, the proposed STI and the conventional LTI are calculated. As the LTI is a function of $\Delta\lambda$ at every operating point, the LTI is calculated using different $\Delta\lambda$ ($\Delta\lambda = -0.05, -0.02, 0.02$ & 0.05), to verify that the limiting case of LTI as $\Delta\lambda \rightarrow 0$ is indeed the STI. As explained before, the indices are only valid for buses with non-zero loads and so the indices are compared only at these buses.

6.2.2.1 Small 5-Bus system

The 5-Bus system consists of 3 Generators and 2 Loads. Figure 6.3 shows the single line diagram of the 5-Bus system with the Generator data, Load data & Line data in 100 MVA base. Gen-0 is the slack generator while Gen-1 and Gen-2 have reactive power limits of 200 MVAR and 450 MVAR respectively. The reactive limits are not enforced in the results for the present section and they will be considered in Section 4.3. Figure 6.4 plots the STI_3 and the LTI_3 for different $\Delta\lambda$ at every load level, from base load to the critical loading level.

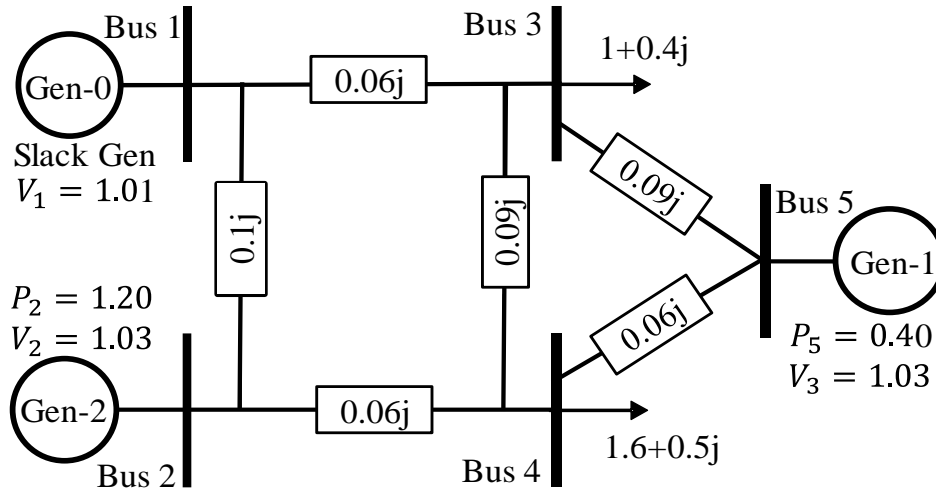


Figure 6.3 The single line diagram 5 Bus system with details of the Generator data, Load data & Line data in 100 MVA base.

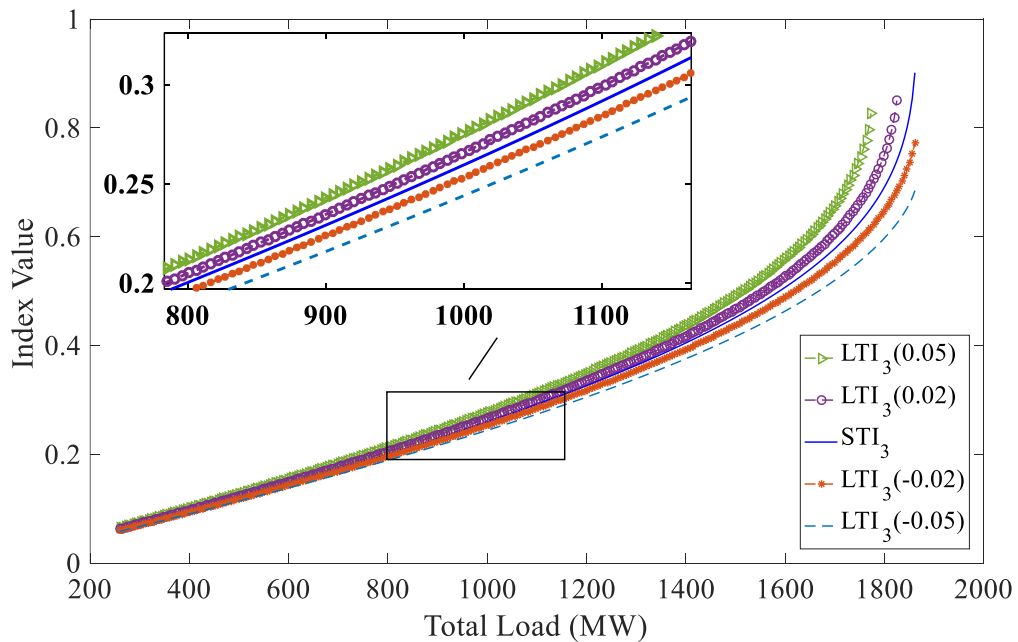


Figure 6.4 The STI and LTI at Bus 3 versus the system load for various $\Delta\lambda$ in the 5-Bus system. The STI always lies between LTI (0.02) and LTI(-0.02).

The first observation from Fig. 4 is that at the critical load, the STI_3 is around 1, while the $LTI_3(-0.05)$ is around 0.7 and $LTI_3(-0.02)$ is around 0.8. The reason why $LTI_3(0.05)$

and $LTI_3(0.02)$ reach 1 at a lower load is that their calculation uses a power flow with a higher load than the existing load level and this behavior is expected.

The next observation is that, for every loading level, the inequality relation $LTI_3(0.05) > LTI_3(0.02) > STI_3 > LTI_3(-0.02) > LTI_3(-0.05)$ holds. This is a consequence of the convex shape of the PV curve, due to which, the value of $\Delta V/\Delta\lambda$ is less than the $dV/d\lambda$ when $\Delta\lambda < 0$ and the reverse is true for $\Delta\lambda > 0$.

The final observation is that the difference between STI and each of the LTI increases as the load level increases. This is due to the increasing slope of the PV curve as the load increases. The increasing slope implies that the difference between the $\Delta V/\Delta\lambda$ and the $dV/d\lambda$ increases as the system goes closer to the critical load and this in turn increases the error between the STI and the LTI. As the utility of the Thevenin indices is mainly at high loading, the increasing error in the LTI at high loads diminish the usefulness of the LTI.

The explanations given are valid for all load buses and so the same observations can be made for the STI and LTI in general. Table 6-1 and Table 6-2 demonstrate the relation between STI and LTI at load buses in the 5-Bus system for system load of 1000 MW and 1700 MW respectively. It can be seen that the STI lies in between LTI with $\Delta\lambda < 0$ and with $\Delta\lambda > 0$ for both the buses at both the operating conditions.

Table 6-1 *Comparison of STI and LTI at Total Load of 1000 MW for the 5-Bus system*

Bus	STI	LTI with different $\Delta\lambda$			
		-0.05	-0.02	0.02	0.05
3	0.259	0.244	0.253	0.265	0.275
4	0.314	0.295	0.306	0.322	0.334

Table 6-2 Comparison of STI and LTI at Total Load of 1700 MW for the 5-Bus system

Bus	STI	LTI with different $\Delta\lambda$			
		-0.05	-0.02	0.02	0.05
3	0.578	0.520	0.553	0.606	0.657
4	0.675	0.601	0.643	0.711	0.780

6.2.2.2 IEEE 30-Bus System

The IEEE 30 Bus system has been traditionally used to study the long term voltage stability phenomenon in literature. It consists of 18 PQ buses which have loads, and where the STI and LTI can be calculated. The load power and the generation throughout the systems is increased in proportion to the base case. Figure 6.5 plots the STI along with the LTI for $\Delta\lambda = -0.05, -0.02, 0.02$ & 0.05 at Bus 30, versus the increasing system load.

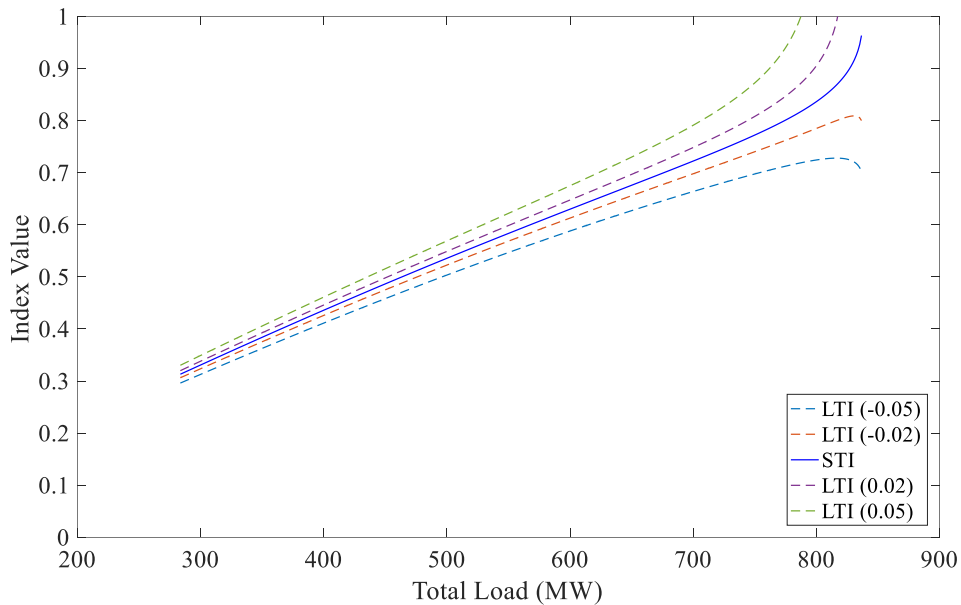


Figure 6.5 The STI and LTI at Bus 30 for various $\Delta\lambda$ in the 30-Bus system versus load. The STI is between the LTI with $\Delta\lambda > 0$ & $\Delta\lambda < 0$.

The first observation from Fig. 2 is that at the critical load, the STI is around 0.95, while the $LTI(-0.05)$ is around 0.7 and $LTI(-0.02)$ is around 0.8. $LTI(0.05)$ and $LTI(0.02)$ reach 1 at a lower load as their calculation uses a power flow with a higher load than the existing load level. The next observation is that, for every loading level, the inequality $LTI(0.05) > LTI(0.02) > STI > LTI(-0.02) > LTI(-0.05)$ holds at Bus 30. This is due to the fact that $\Delta V/\Delta\lambda < dV/d\lambda$ if $\Delta\lambda < 0$ and $\Delta V/\Delta\lambda > dV/d\lambda$ if $\Delta\lambda > 0$. The reason for this is explained in the previous subsection and is due to the convex shape of the PV curve.

The final observation is that the difference between STI and each of the LTI increases as the load level increases. This is caused by the increasing curvature of the PV curve as the load increases. The increasing curvature leads to an increasing difference between $\Delta V/\Delta\lambda$ and $dV/d\lambda$ as the system gets closer to the critical point, increasing the error between the STI and the LTI. The reasons for the observations are valid at all load buses and hence similar observations, for the STI and LTI, can be expected at all load buses. Table 6-3 displays the STI and LTI at a few load buses in the IEEE 30-Bus system for a system load of 330 MW. It can be observed from the table that STI lies between LTI with positive $\Delta\lambda$ and negative $\Delta\lambda$ for all the buses, validating the claim that STI is the ideal LTI.

Table 6-3 *Comparison of the STI and the LTI at a few buses in the IEEE 30-Bus system for a system load of 330 MW*

Bus	STI	LTI with different $\Delta\lambda$			
		-0.05	-0.02	0.02	0.05
26	0.340	0.321	0.332	0.348	0.359
29	0.348	0.329	0.340	0.356	0.367
30	0.362	0.343	0.355	0.371	0.383

A clearer way to display the relation between the STI and LTI, is by using a scatter plot of the LTI with different $\Delta\lambda$ versus the STI. This visualizing scheme allows us to compare the values of STI and LTI for all the non-zero load buses in a compact form. Figure 6.6 plots the LTI corresponding to $\Delta\lambda$ of 0.05 and -0.05, versus the STI at the same load as Table 6-3.

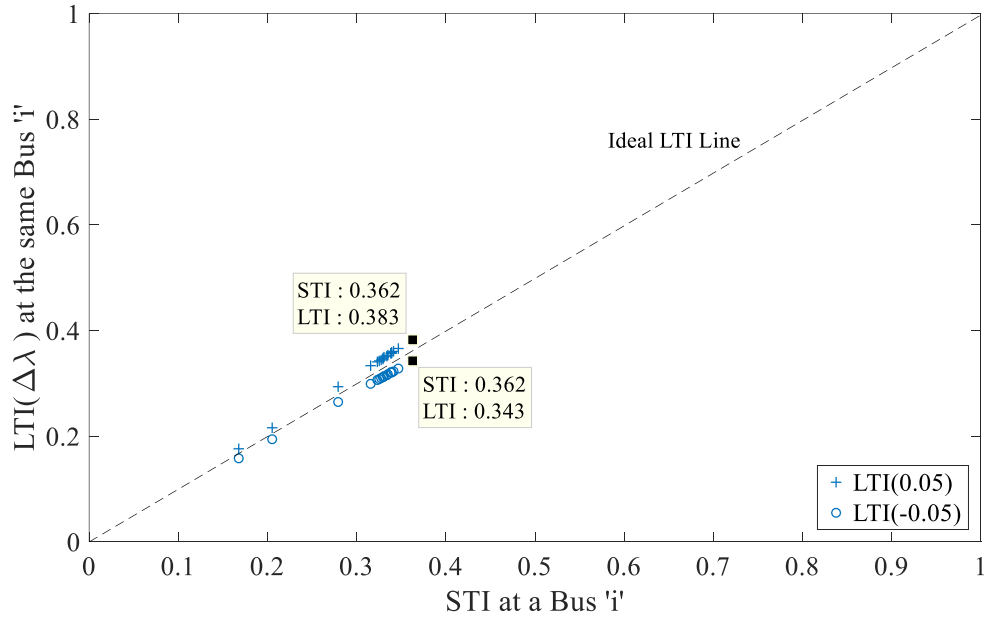


Figure 6.6 Scatter plot of the LTI versus the STI for various $\Delta\lambda$ at non-zero load buses in the 30-Bus system at load of 330 MW.

The dashed line is the line $LTI=STI$ and it indicates the ideal value of LTI. The data points corresponding to Bus 30 are identified in the plot and their values can be verified from the Table 1. The vertical distance of the LTI point from the line is an indication of the error. It can be seen from Fig. 3 that $STI=LTI$ line lies in between the $LTI(0.05)$ and $LTI(-0.05)$ at all the buses, implying that the relation $LTI(-0.05) < STI < LTI(0.05)$ holds for all the buses. To verify that this relation between STI and LTI holds at different load levels, the scatter plot of the LTI versus the STI is presented in Figure 6.7 for a system load of 760 MW.

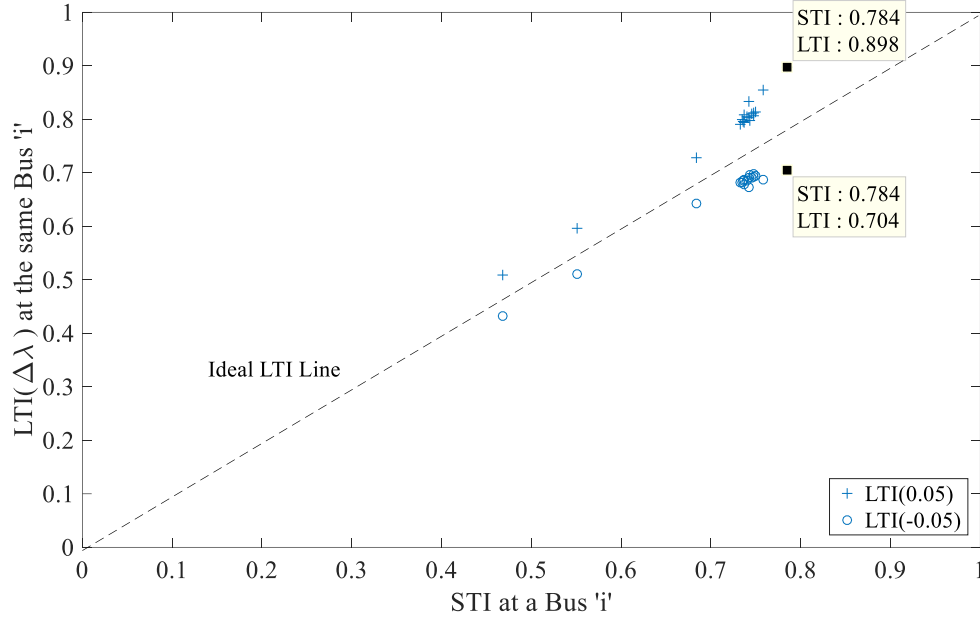


Figure 6.7 Scatter plot of the LTI versus the STI for various $\Delta\lambda$ at non-zero load buses in the 30-Bus system at load of 760 MW.

Similar to Figure 6.6, in Figure 6.7 the dashed line indicates the ideal value of LTI and the data points corresponding to Bus 30 are identified. As expected, the LTI and STI have increased at the buses due to the increased loading and the relation $LTI(-0.05) < STI < LTI(0.05)$ holds for all the buses at this load level as well. By visually comparing the Figure 6.6 and Figure 6.7, it can be observed that the data points have moved farther away from the dashed line, indicating that the error between the LTI and the STI increases as the load level increases. This can also be verified by comparing the data points for Bus 30 in Fig 3 and Fig 4. In all the cases, $LTI(0.02)$ and $LTI(-0.02)$ were closer to the dashed line than $LTI(0.05)$ and $LTI(-0.05)$ respectively, but are not plotted as they cluttered the plots. Thus, these results provide numerical validation for the claim that STI is the ideal value of LTI at all the non-zero load buses in the IEEE 30-Bus system.

6.2.2.3 MATPOWER 3120 Bus System

It is important to also validate the method with a large practical network and the MATPOWER 3120 Polish Summer Peak case is used to demonstrate the utility of the proposed method on large systems. This system consists of 2771 load buses, of which 1962 buses have non-zero loads, and the STI & LTI is calculated at these buses. Figure 6.8 plots the STI along with the LTI for $\Delta\lambda = -0.05, -0.02, 0.02$ & 0.05 at Bus 3111, versus the increasing system load.

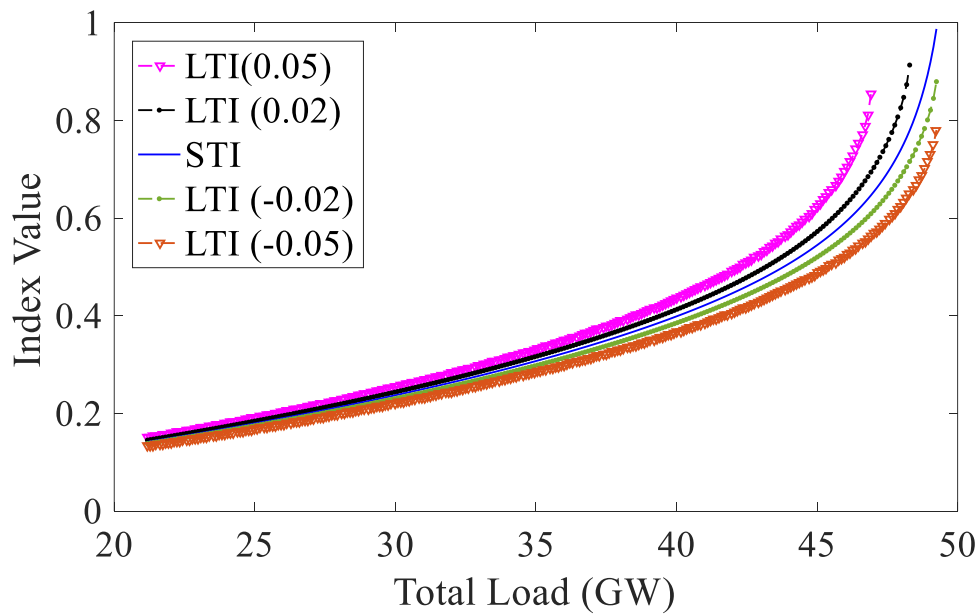


Figure 6.8 *The STI and LTI versus the load at Bus 3111 for various $\Delta\lambda$ in the MATPOWER 3120-Bus system.*

The following observations can be made at all load levels from Figure 6.8:

- STI lies in between the LTI curves with $\Delta\lambda < 0$ & $\Delta\lambda > 0$.
- The smaller the value of $\Delta\lambda$, the closer the LTI curve is to the STI
- The difference between STI and the LTI increases as the system loading increases

From these observations, it can be deduced that as the load increment is made smaller, the LTI curve moves closer to the STI curve, implying that the STI is indeed the ideal LTI

value. To demonstrate that this conclusion is true for all the buses, Figure 6.9 displays the scatter plot of the LTI ($\Delta\lambda = 0.05, 0.02, -0.02$ & -0.05) versus the STI at all load buses in the 3120-Bus system at system load of 45 GW.

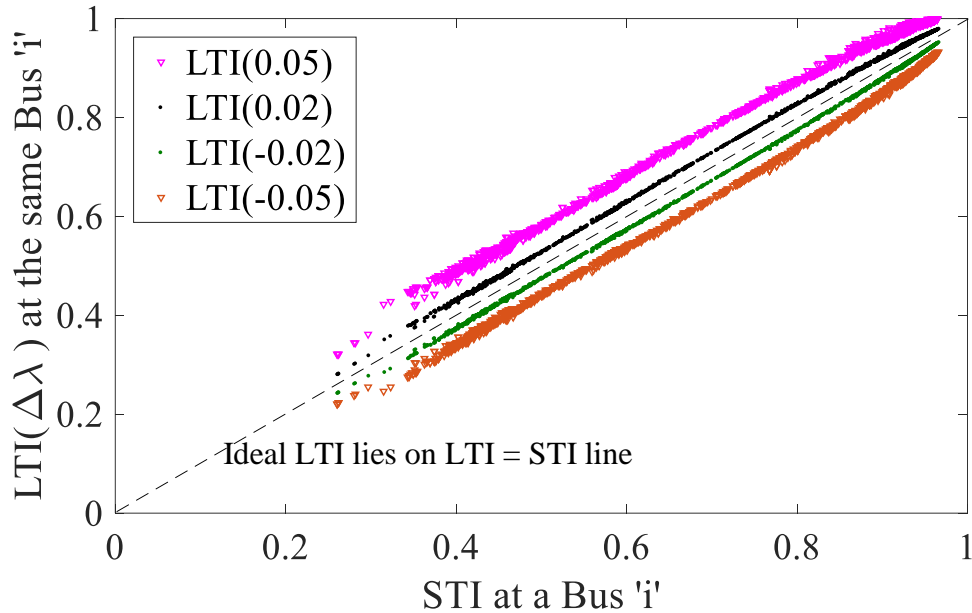


Figure 6.9 Scatter plot of the LTI ($\Delta\lambda = 0.05, 0.02, -0.02$ & -0.05) versus the STI at all load buses in the 3120-Bus system 45 GW load.

Comparing the LTI and the dotted line corresponding to LTI=STI in Figure 6.9, it is clear that $LTI(0.05) > LTI(0.02) > STI$ & $LTI(-0.05) < LTI(-0.02) < STI$ for all the buses. This confirms that the properties relating the STI and LTI can be generalized, proving that the ideal value of the LTI is indeed the STI at all buses and load levels.

6.2.2.4 Performance of STI and LTI in the presence of noise

In all the comparisons so far, the noise is assumed to be not present. In reality however, the noise at the measurement devices and the state estimation is important to consider. As per the PMU standards, the noise in current and voltage measurements is within ± 0.0002 p.u. [5]. As the LTI is calculated at PMUs using quasi steady state measurements, the increment ($\Delta\lambda$) is very small (0.1%-0.2%) and thus, the values of ΔV & ΔI in Eq. (2) are small enough to be

impacted by the measurement noise. The impact of noise on the LTI is derived in (6-15)-(6-16), where the subscript ‘meas’ corresponds to measured and subscript ‘true’ is what the value would be with no noise; ϵ_V & ϵ_I corresponds to noise in Voltage and Current measurements and they mainly impact ΔV & ΔI .

$$LTI_{meas} = \left| \frac{I^{(1)}}{V^{(1)}} \cdot \frac{\Delta V_{meas}}{\Delta I_{meas}} \right| \approx \left| \frac{I^{(1)}}{V^{(1)}} \cdot \frac{\Delta V_{true} + \epsilon_V}{\Delta I_{true} + \epsilon_I} \right| \quad (6-15)$$

$$LTI_{meas} \approx \left| \frac{I^{(1)}}{V^{(1)}} \cdot \frac{\Delta V_{true}}{\Delta I_{true}} \right| \left| 1 + \frac{\epsilon_V}{\Delta V_{true}} - \frac{\epsilon_I}{\Delta I_{true}} \right| \quad (6-16)$$

$$LTI_{meas} \approx LTI_{true} \left(1 + \frac{\epsilon_V}{\Delta V_{true}} - \frac{\epsilon_I}{\Delta I_{true}} \right) \quad (6-17)$$

As the noise levels in Current and Voltage are similar [1], we assume $\max(\epsilon_V) = \max(\epsilon_I) = \epsilon_{max}$. As ϵ_V & ϵ_I are independent random variables, the highest impact of noise occurs when $\epsilon_V = -\epsilon_I$. The maximum and minimum values of the LTI for a given value of ΔV_{true} & ΔI_{true} are as follows.

$$LTI_{max} \approx LTI_{true}(1 + \eta); \quad LTI_{min} \approx LTI_{true}(1 - \eta); \quad (6-18)$$

$$\eta = \epsilon_{max} \left(\frac{1}{\Delta V_{true}} + \frac{1}{\Delta I_{true}} \right) \quad (6-19)$$

Hence, for a given $\Delta\lambda$, which fixes the ΔV_{true} & ΔI_{true} , the maximum and minimum LTI vary linearly with the noise level. Reducing $\Delta\lambda$ reduces ΔV_{true} & ΔI_{true} and leads to more variation in LTI. The impact of measurement noise on the STI can be determined by the variation in the sensitivities due to the noise and can be done in a straightforward manner using linear stochastic methods [6]. As the Jacobian of the system and its entries depend on the voltage phasors (V), the sensitivities vary comparatively less for the same noise level and so the variation in the STI is much lesser than the LTI for the same amount of noise.

To demonstrate how the range of LTI and STI vary with noise, Figure 6.10 plots their upper and lower limits for the 30 Bus system at a loading of 600 MW with $\Delta\lambda = 0.2\%$, versus noise from 0 to ± 0.0002 p.u. To visualize how the LTI and STI vary over time, the IEEE 30 bus system is operated at 600 MW with a $\Delta\lambda$ of 0.2% for 300 sec with Gaussian additive noise of ± 0.0002 p.u. to voltage and current measurements and the results are plotted in Figure 6.11.

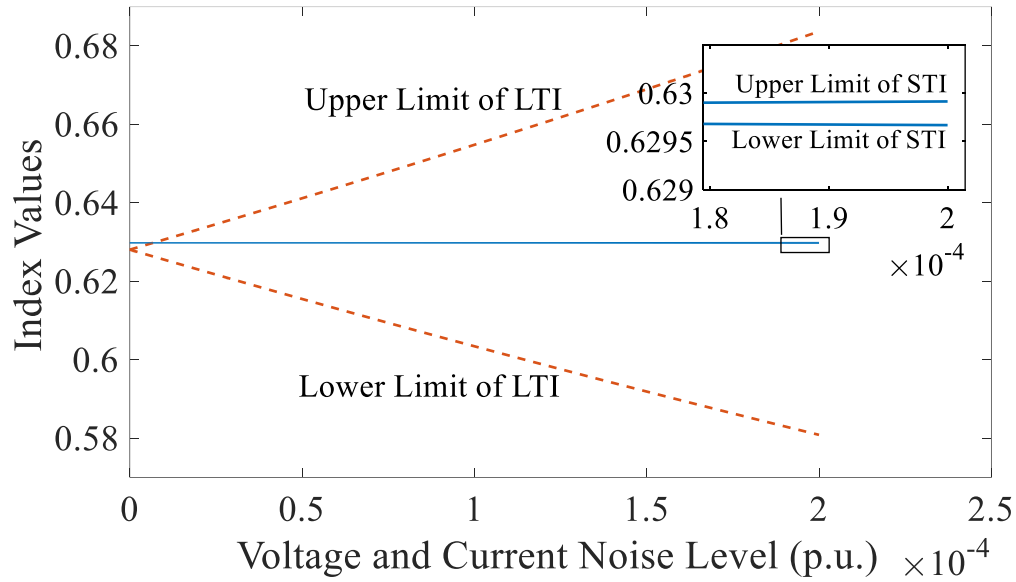


Figure 6.10 The upper limits and lower limits of STI and LTI versus the noise level ϵ_{max} for the 30 Bus system at a system loading of 600 MW with a $\Delta\lambda$ of 0.2%.

It can be seen from Figure 6.10 that the upper and lower limits of the LTI vary linearly as the noise level increases, as derived in Eq. (12). When there is no noise level, the LTI is very close to the STI and as the noise reaches ± 0.0002 p.u., the LTI varies between 0.58-0.68, i.e. a variation of $\pm 8.5\%$ from the STI of 0.63. This range can be verified from Figure 6.11 in which the LTI varies between 0.58-0.68 over the 300s of operation while the STI stays almost constant at 0.63.

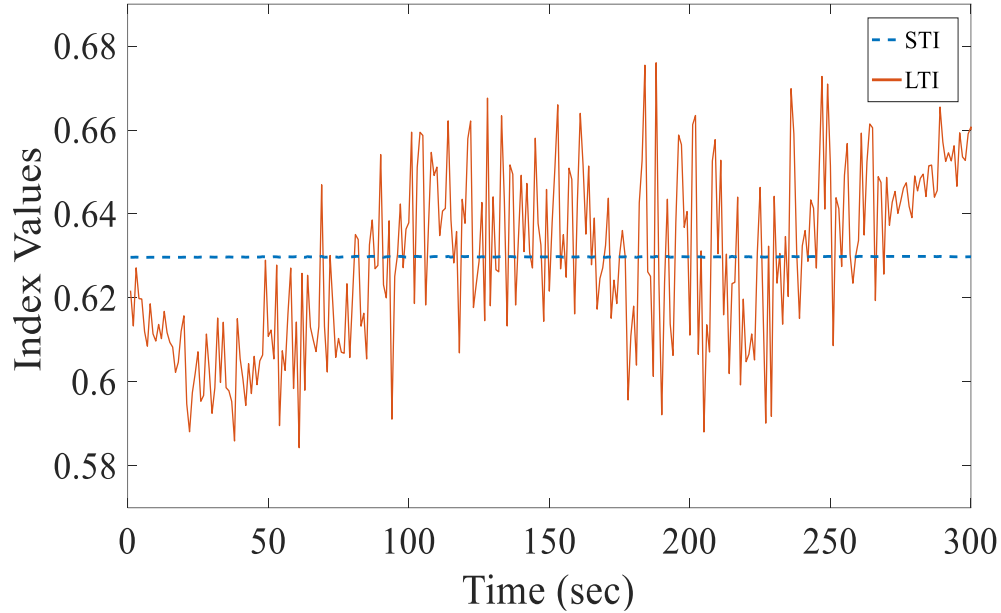


Figure 6.11 Behavior of the LTI and STI over 300s of operation with $\epsilon_{max} = \pm 0.0002$ p.u. for the 30 Bus system at a system loading of 600 MW with a $\Delta\lambda$ of 0.2%.

The LTI uses data over a time period to filter the noise and recover the true value of the index [7]. However, these methods might not recover the true value of LTI if the noise was deliberately introduced by a malicious actor or if the system behavior is unexpected (forced oscillations, etc.). While state estimation can detect bad data, the errors in this case are in the range of ± 0.0002 p.u. making it too small to be flagged by the state estimation packages. Thus, using the STI at the control center to verify if the calculated LTI is valid before performing a control action is a practical and straightforward application of the proposed methodology. A large difference between the STI and the LTI could indicate the presence of a data injection cyber-attack and help in preventing any damage.

In the future, we expect increasing penetration of renewables to lead to a more dynamic grid with increased fluctuations. This will lead to even more noise as the assumptions for constant sine waveforms at the PMU will not be totally valid. Figure 6.12 plots the variation in STI assuming the noise increases to 5 times the present range, i.e. ± 0.001 p.u. It can be

observed that the STI variation has increased (by about 5 times). Despite this, its performance is much better than the LTI performance at the same noise level. The LTI varied from 0.4 – 0.8 and is not plotted as it was too noisy. The high robustness to noise implies that the STI will be even more useful in the grid of the future.

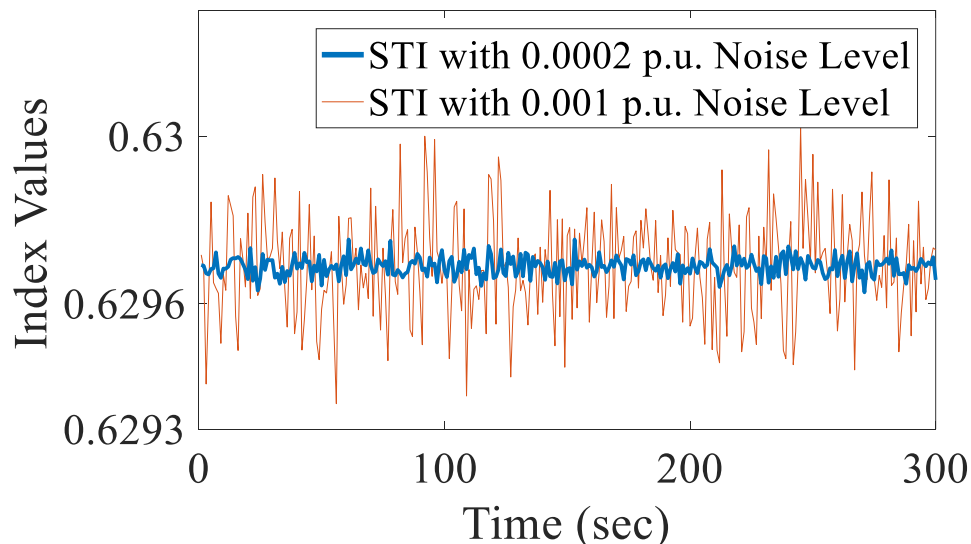


Figure 6.12 *The STI for the 30 Bus system at a system loading of 600 MW with noise level ± 0.001 p.u and ± 0.0002 p.u.*

6.2.3 Consequences of the Equivalence between LTI and STI

Traditionally, Thevenin methods used a 2-bus equivalent of the power system and used the maximum power transfer theorem to justify using LTI as a static long-term voltage stability indicator. The derivation in section 4.2.1 proves the connection between the system Jacobian and the LTI (via the sensitivities) and thus, provides a more mathematically rigorous justification to use LTI as a stability indicator of the entire system and can be used to explain behavior of the LTI that were previously only explained intuitively. For example, take the case of the 5-bus system discussed previously. As the system load increases, it is known that the LTI at Bus 3 and Bus 4 both go to 1 (i.e. reach instability) at the same time. Figure 6.13 plots the LTI at Buses 3 and 4 in the 5-bus system as the load increases.

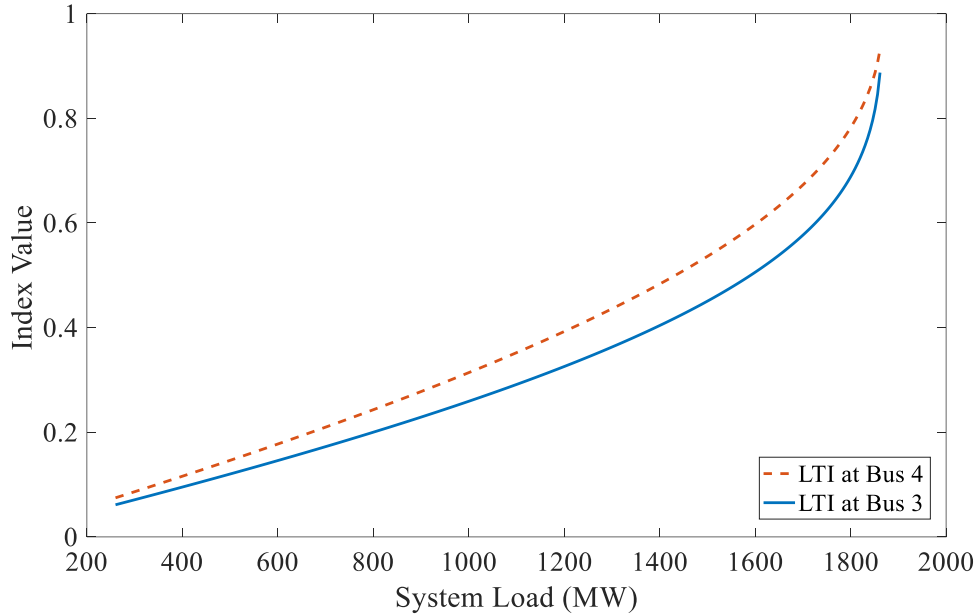


Figure 6.13 *The LTI at Bus 3 and 4 as the system load increases in the 5-Bus system. Both the LTI approach 1 at the critical system loading.*

There is no mathematical reasoning for this fact in literature other than the intuition about the system behavior. This fact can be explained due to the relation between the LTI and the Jacobian (via the sensitivities), that is derived in Section 4.2.1. As the system loading increases, the Jacobian becomes closer to becoming singular and this in turn increases the sensitivities at all the buses and thus the STI & LTI at all the buses at the long-term voltage stability limit is 1.

As far as the author is aware, this is the first time an analytical proof, showing the relation between the LTI and network parameters (through the sensitivities), has been presented. There is no analytical proof in existing literature that demonstrates definitively that the LTI should approach 1 at any load bus at critical loading for a multi-bus system. It is this connection between the LTI and the sensitivities, which proves rigorously that the critical value of LTI is 1 at any load bus and is the reason why LTI can be used as an indicator of system stability.

6.3 Predicting the Impact of Reactive-Limits on STI & LTI

The voltage stability problem is intrinsically linked to reactive power resources in the system and so, one of the main factors that influences the voltage stability phenomena, in a practical power system, is the relative power limits of generators. An ideal VSI should consider the limits on reactive resources into calculations, especially the reactive limits of generators. This will provide a more realistic view of the power system to the operator at the control center, enabling better situational awareness.

However, as the LTI uses only measurements around an operating point, it cannot account for the generator reactive limits. This drawback in the LTI methodology can be rectified using the relation between sensitivities and the LTI. By understanding and predicting the sensitivities when a generator reaches its limit, we can predict what would happen to the LTI under the same scenario.

Figure 6.14 shows the PV curve at Bus 3 in the 5-Bus system (introduced in the previous section) after enforcing the generator reactive limits. The reactive limit of Gen 1 is reached first, at a system load of 830MW and Gen 2 reaches its limit at a system load of 1225MW. The reactive limits of the generators lead to sharp corners in the PV curve. Thus, the slope of the PV curve increases abruptly at these points and this corresponds to a sudden increase in $dV/d\lambda$ sensitivities. Similarly, $d\theta/d\lambda$ sensitivities also abruptly increase at the same time. These observations lead us to conclude that a sudden rise in the STI & LTI can be expected when a generator reaches its limit. The reason for the sudden change in the sensitivities can be deduced from the change in the Jacobian when a generator reaches its limit. The PV bus, at which the reactive power limit is reached, is switched to a PQ bus, and so the Jacobian changes dimension.

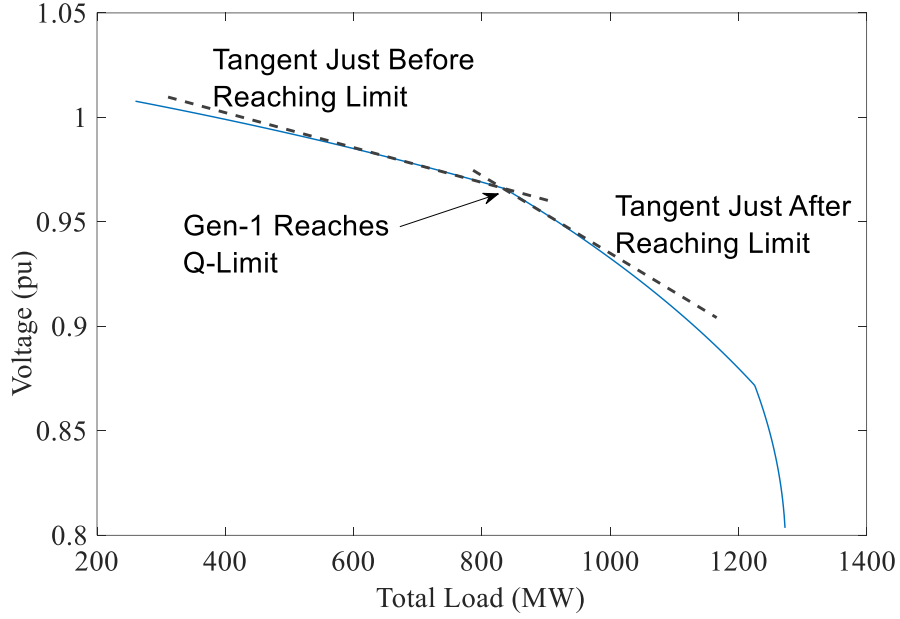


Figure 6.14 PV Curve of Bus 3 in the 5-Bus system with Reactive Limits enforced. The slope of the tangent changes abruptly when a generator Q-limit is reached.

Let $g^{(m)}$ be the expression of the power flow equations for the reactive power at Bus m . If the Gen at Bus m reaches its limit, then the bus is switched from PV bus to PQ bus and the voltage magnitude at Bus m , V_m , is now a variable. The new sensitivities are determined by solving (6-20). Since the reactive limit is reached at Bus m , the derivative of the Q at Bus m is 0.

$$\begin{bmatrix} f_{\bar{\theta}} & f_{\bar{V}} & f_{V_m} & \bar{P}_\lambda \\ g_{\bar{\theta}} & g_{\bar{V}} & g_{V_m} & \bar{Q}_\lambda \\ g_{\bar{\theta}}^{(m)} & g_{\bar{V}}^{(m)} & g_{V_m}^{(m)} & 0 \\ 0 & 0 & 0 & 1 \end{bmatrix} \cdot \begin{bmatrix} d\bar{\theta} \\ d\bar{V} \\ dV_m \\ d\lambda \end{bmatrix} = \begin{bmatrix} 0 \\ 0 \\ 0 \\ 1 \end{bmatrix} \quad (6-20)$$

To verify that the LTI and STI abruptly change when the generator reactive limit is reached, the STI and LTI for different $\Delta\lambda$ at Bus 3 in the 5-Bus system at different load levels are plotted in Figure 6.15 after enforcing the reactive limits of the generators. As expected, a sudden increase in the LTI and the STI is observed at the instant when the reactive limits of

generators are reached. The close match between the STI and LTI after enforcing the reactive limits provides corroborating evidence for this explanation. Furthermore, the amount of shift in LTI cannot be predicted just by using the voltage and current measurements before the limit is reached. Thus, even if the operator knew that a generator is close to its limit, the change in the LTI if this generator hit the limit cannot be determined – the increase could be as low as 0.01 (for a non-critical generator) or as high as 0.5 (for a critical generator).

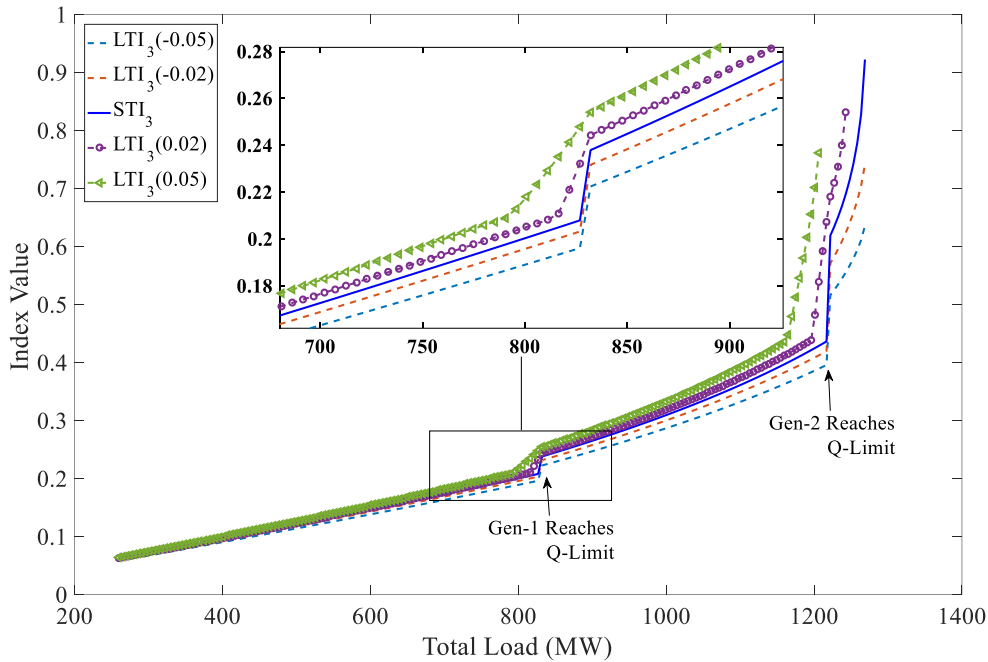


Figure 6.15 The STI and LTI at Bus 3 for various $\Delta\lambda$ in the 5-Bus system with Reactive Limits enforced. The STI always lies between LTI (0.02) and LTI(-0.02).

These properties of the LTI prevent the operator from considering and carrying out any proactive action. Completely trusting the LTI measured might lead to an optimistic assessment of voltage stability of the system and lull the operators into a false sense of security. Thus, there is a need to modify the STI and LTI by incorporating the generation limits into the calculation.

Due to the close match between STI and LTI, even after the reactive limits are reached, predicting the Q-impact of the reactive limits on STI will also predict the impact of Q-limits on LTI. Suppose, the power system is operating at a loading level and we are interested to know what would happen to the STI if a Generator, with index 'k' and connected at Bus 'm', just reaches its reactive limit at this operating point. This requires the sensitivities with the Bus 'm' as a PQ bus, which can be calculated from the Jacobian for this new condition. At first glance, it seems that this requires a new power flow solution.

However, an interesting property can be exploited with regards to the two Jacobians (the Jacobian with generator bus as a PV bus and the Jacobian with generator bus as PQ bus) if the limit is just reached right at that operating point. By comparing (6-14) and (6-20), it is observed that, the new Jacobian is essentially an addition of a column and a row to the previous Jacobian. Further, it can be observed from Figure 6.14 that the PV curve has two slopes at the point when a generator just reaches its limit, and they correspond to the two Jacobians. As they both are at the same operating point, the new Jacobian can be constructed by augmenting a row and a column to the original Jacobian (not just the expression but also the values) as shown in (6-20). There is no need for another power flow solution.

This observation can be used to calculate $STI_i^{(k)}$ at an operating condition (the STI at Bus-i, assuming Gen-k just reaches reactive limit at this condition and no other Gen reaches the limit) efficiently. If, it is possible to determine the generator that is going to reach the reactive limit first [8], then, the $STI_i^{(k)}$ is calculated for that generator. However, if this information is not available, a conservative approach is to calculate the impact for each generator, one at a time, and analyze all their values. Thus, at Bus-i, in addition to STI_i , the values $STI_i^{(1)}, \dots, STI_i^{(N_G-1)}$ are also calculated. The calculation of $STI_i^{(k)}$ is not done for the

slack bus as the power flow expressions at this bus are not used in (6-20). The steps for the method are described in the algorithm below.

Algorithm to calculate $STI_i^{(k)}$ at an operating condition

- 1: At an operating point, calculate the Jacobian, J , and the STI for all non-zero load buses.
 - 2: Gen 0 is the slack bus. START with Gen Index $k = 1$
 - 3: Determine the Bus m to which Gen. k is connected
 - 4: Create the Jacobian, J_m , assuming Bus m is a PQ bus by augmenting the J as shown in (6-20)
 - 5: Calculate the STI_i^k at every bus by calculating sensitivities using J_m
 - 6: If all generators are accounted for, then STOP, else clear J_m and go to Step 7
 - 7: Increment Generator index, k , by 1 and go to Step 3
-

As the power system becomes more stressed when a PV bus switches to a PQ bus, it is expected that, usually $STI_i^{(k)} > STI_i$. The difference between $STI_i^{(k)}$ and STI_i can be used as a measure of the influence of Gen k on the load at Bus i . This difference can be used by the operators or other programs at the control center to get a better understanding of the system.

6.3.1 Numerical Validation of STI Including the Generator Reactive Limits

In the 5-Bus system, there are 3 generators including the slack bus, thus two $STI_i^{(k)}$ are possible, one each for Gen-1 and Gen-2. Gen-1 reaches its reactive limit at a system load of 830 MW while Gen-2 reaches the limit at 1225 MW. If the information that Gen-1 reaches its limit first is available, then only $STI_i^{(1)}$ is calculated till Gen-1 reaches the limit and after which $STI_i^{(2)}$ is calculated. However, if this information is unknown, then both the $STI_i^{(k)}$ are

calculated and analyzed. Table 3 displays the values of all the STI's calculated at Bus 3 for the 5-Bus system at different load levels.

Table 6-4 Comparison of STI_3 , $STI_3^{(1)}$ & $STI_3^{(2)}$ for different load levels in the 5-Bus system.

System Load	STI_3	$STI_3^{(1)}$	$STI_3^{(2)}$
600 MW	0.145	0.162	0.151
1000 MW	0.307	0.307	0.397
1250 MW	0.704	0.704	0.704

From Table 3 it can be seen that $STI_3^{(k)} > STI_3$ at 600 MW load. This operating point is before any generator reaches its limit and so the inequality relation is expected. At a load of 1000 MW, Gen-1 has already reached its limit and so at this point, $STI_3^{(1)} = STI_3$. This is because the PV bus is already converted to a PQ bus and there is no need to augment the Jacobian to calculate $STI_3^{(1)}$. Similarly, at a load of 1250 MW, Gen-2 has also reached its limit and so $STI_3^{(2)} = STI_3$.

An interesting observation can be made regarding the influence of Gen-2 on Bus 3. At a load of 600 MW, the difference between $STI_3^{(2)}$ & STI_3 is 0.006 while at a load of 1000 MW, the difference is 0.09. There is a large change in the difference and it implies that the influence of Gen-2 increased after Gen-1 reached its limit. This makes sense as any further increase in reactive load, after Gen-1 reached its limit, needs to be supplied by Gen-2, thereby increasing its influence on loads. Thus, if a generator reaches its limit, it is expected that there will also be a sudden rise in all the other $STI_i^{(k)}$ as well.

Plotting the 3 STI values at Bus 3 for every load level gives more insight into the behavior of the indices and Figure 6.16 presentations this information. The first observation

that can be made from Figure 6.16 is that the estimate $STI_3^{(1)}$ just before Gen 1 reaches limit matches with the value of STI_3 after Gen 1 reaches its limit. The same is true for Gen 2 and $STI_3^{(2)}$. Thus, the $STI_i^{(k)}$ is successfully able to predict the change in the STI_i for Gen k reaching the reactive limit. This is exactly what the operator needs to understand the true status of the system.

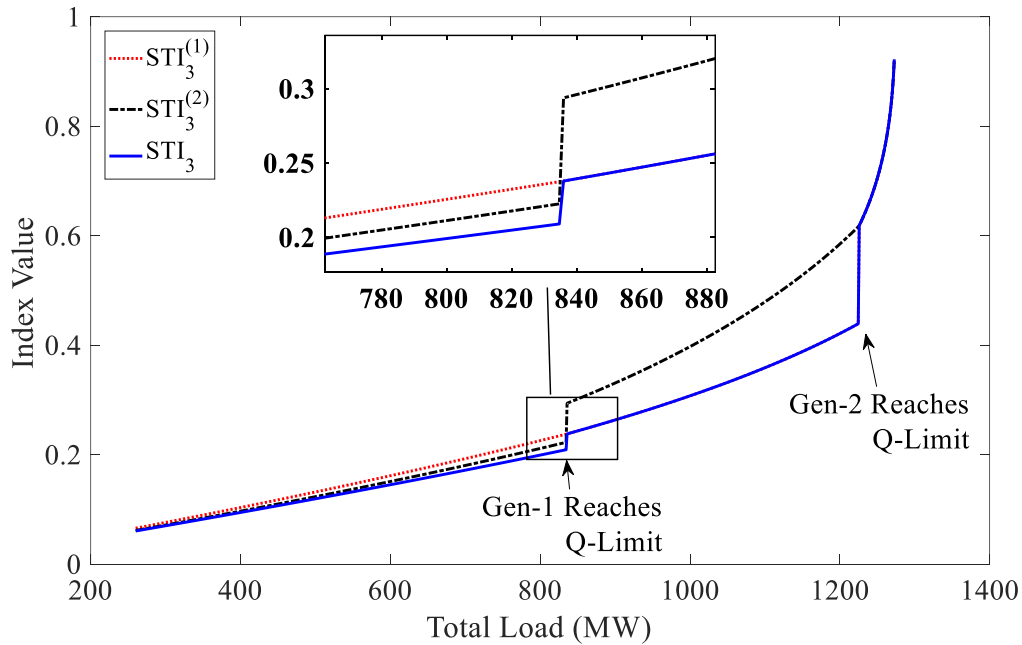


Figure 6.16 Comparison between STI_3 , $STI_3^{(1)}$ & $STI_3^{(2)}$ in the 5-Bus system with Q-limits enforced. $STI_3^{(1)}$ ($STI_3^{(2)}$) can predict the change in STI_3 when Gen-1 (Gen-2) reaches the reactive limit.

The second observation is that $STI_3^{(2)}$ also has a sudden jump when Gen 1 reaches the limit. This implies that the influence of Gen 2 increases suddenly after Gen 1 reaches its limit and as explained before, this occurs due to the lack of reactive resources in the system. This increase in the influence is verified by the matching value of $STI_3^{(2)}$ just before Gen 2 reaches the limit and STI_3 after Gen 2 reaches the limit.

Usually, alarms are signaled if LTI is in the range of 0.45-0.55 and controls are triggered if it is higher than 0.55. If the operator only observed STI_3 , the situation would be alright until 1225 MW. At this instant, Gen-2 reaches its limit and the STI_3 suddenly increases from 0.4 to 0.6. This unexpected increase will cause operators to initiate abrupt controls to rectify the issue. Being able to predict the jump before the Q-limit is reached provides the operator with time to arm various controls to mitigate the impact of the limit being reached.

As the load increases to 1100 MW, the value of $STI_3^{(2)}$ is in the warning range, implying that the STI_3 can enter the warning range if Gen-2 reaches its limit. Thus, the operators will be alert and will not be alarmed when the Gen-2 reaches the limit. Furthermore, control actions before Gen-2's limit is reached can be triggered if it is reasonable to perform conservative controls. Hence, the $STI_3^{(k)}$ enables the operators and other applications at the control center to take proactive controls such as re-dispatching generators, by anticipating the sudden rise in the STI_3 due to Q-limits and ensuring that the system is prepared to cope with the Q-limit being reached.

Displaying and analyzing the individual $STI_i^{(k)}$ is possible for small systems. However, as number of generators increase, consolidating the information present in all $STI_i^{(k)}$ into a single index is necessary. One way is to define an index as in (6-21).

$$STI_i^{(u)} = \max\{STI_i^{(1)}, \dots, STI_i^{(N_G-1)}\} \quad (6-21)$$

This index is the maximum value of $STI_i^{(k)}$ at Bus-i and thus, $STI_i^{(u)}$ provides an upper bound for the rise in STI_i in case a generator reaches its limit. Hence, providing the $STI_i^{(u)}$ to the operator, instead of the individual $STI_i^{(k)}$ values, leads to a simplified, but also a conservative, view of the system. For the 5 Bus system, $STI_3^{(u)} = STI_3^{(1)}$ until Gen-1 reaches

the limit and $STI_3^{(u)} = STI_3^{(2)}$ until Gen-2 reaches the limit. After Gen-2 reaches its limit, $STI_3^{(u)} = STI_3$, as all the PV buses have all switched to PQ buses.

Figure 6.17 plots the STI_{30} & $STI_{30}^{(u)}$ for IEEE 30-Bus system with reactive limits enforced. As expected, the $STI_{30}^{(u)}$ at every load level provides an upper bound for the STI_{30} , in case a reactive limit is reached. As soon as a Gen reaches its reactive limit, the value of STI_{30} suddenly increases. At the same time, the value of $STI_{30}^{(u)}$ also increases, as it is considering the most severe impact of the next generator to reach the limit.

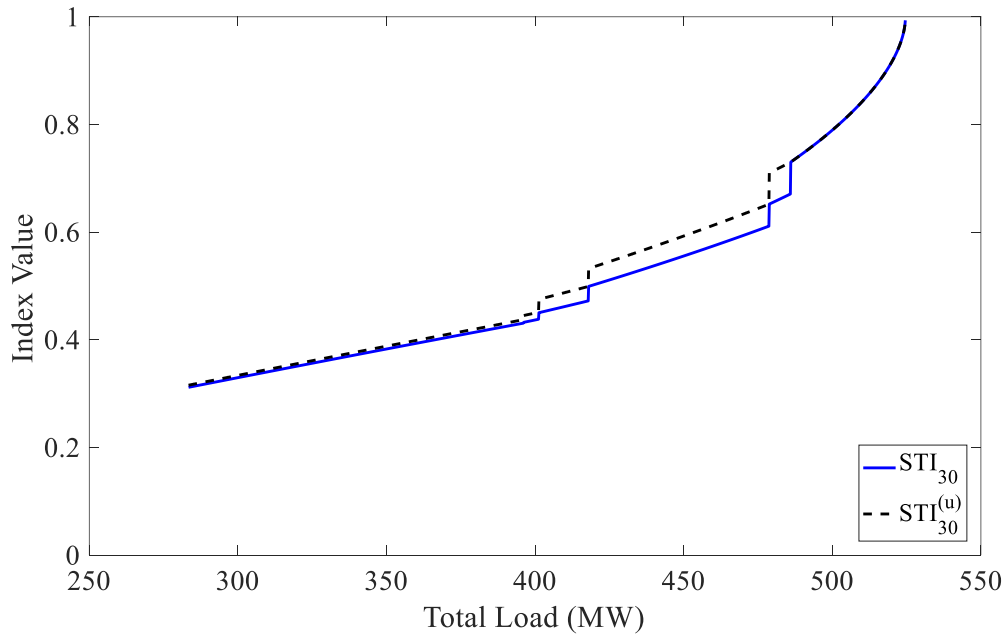


Figure 6.17 Comparison between STI_{30} & $STI_{30}^{(u)}$ for IEEE 30-Bus system with reactive limits enforced. $STI_{30}^{(u)}$ is greater than or equal to STI_{30} , even when limits are reached.

Thus, if the information of $STI_i^{(u)}$ is provided at every operating point, then, the operator will still be able to take proactive controls, based on $STI_i^{(u)}$ or the difference between $STI_i^{(u)}$ and STI_i . Similar results as Figure 6.17 were obtained for the IEEE 118 and 300 bus systems.

6.4 Feasibility of Implementing STI in Practical EMS Software

As the LTI at a bus is calculated in real-time, the time required for the calculation of STI_i needs to be considered for practical implementation. Determining the STI essentially boils down to solving the linear equation $Ax=b$, where A is the power flow Jacobian, and this is precisely what the power flow solvers do very efficiently. Thus, the time taken to calculate the STI is less than the time taken for a single iteration of a newton power flow solver and efficient routines exist in commercial programs (PSSE, PSLF, etc.) using efficient algorithms (LU decomposition, etc.) to solve $Ax=b$ within a few seconds for practical systems. Hence, using the converged state estimation solution to calculate the STI in the control center and using it to validate the LTI should be possible in the online time scale and is the most likely use-case scenario. In MATLAB, the time taken to calculate the STI for the 3120 Bus system is ~ 0.2 seconds.

As the study of reactive limits on the LTI is more of a predictive analysis, it is not expected to do this calculation in an online manner. Instead, the calculation of $STI_i^{(u)}$ needs to be completed within the operational time scale (usually 5 min) for practical systems. The time taken to compute all the $STI_i^{(u)}$ at an operating point is 30ms, 95ms and 240ms for the IEEE 30, 118 and 300 bus systems. There are two features in the methodology of $STI_i^{(u)}$ that seem to make it challenging to implement in a real system. The first feature is that $STI_i^{(k)}$ needs to be calculated for every generator in the system, which is essentially solving the $Ax=b$ equation, where A changes for each generator. As a large component of the matrix 'A', is same, the LU decomposition can be significantly simplified. Commercial programs exploit similar ideas to simplify calculations for what-if scenarios and solve the $Ax=b$ equation a few thousand times for practical systems ($\sim 30,000$ buses) in around 2-3 minutes. This is within the time frame of

the long-term voltage stability phenomenon and so this method can be implemented for practical systems within the operational time scale. Further reduction in time can be achieved by defining a region of interest and only calculating sensitivities for these buses, instead of all the buses.

The second feature is the conservative nature of the $STI_i^{(u)}$. Reducing or providing bounds on the conservativeness of $STI_i^{(u)}$ is recommended as it would reflect the true status of the system. The variation of generator reactive power with time can be used to deduce a set of candidate generators that are likely to reach the limit [8]. The $STI_i^{(u)}$ are calculated only for this set of generators, reflecting a more realistic status of the system. This modification has the added advantage of reducing the overall calculation time due to reduction in the number of generators.

A reduction in the computations necessary can also be achieved by converting a set of PV buses into PQ buses in a single step, instead of converting them one-by-one. The collection of PV buses to be converted into PQ buses at the same time can be determined by implementing methods such as [9], where the limit reaching generators were determined using a cubic formula. Thus, the STI method proposed can be implemented on practical systems with minor modifications.

6.5 Conclusion

In this chapter, the relation between the Linear Thevenin Index (LTI) at a PMU and the sensitivities is obtained, providing a mathematically rigorous justification to use LTI as a static long-term voltage stability indicator of the entire system. Using this relation, a Sensitivity based Thevenin Index, which uses PMU/WAMS data and (linear) state estimator data to address the following challenges associated with Thevenin-based voltage stability indices – (a)

Robust calculation of the stability index; (b) Verification of the local index by the system operator & (c) Accounting for generator reactive limits on the index. The ability of the STI to validate the local Thevenin index safeguards the operator against spurious and malicious data and makes this a useful property, especially with the current emphasis on cyber security. The generator reactive limits can be taken into account by modifying the Jacobian to anticipate the PV-PQ bus switching facilitating the operators with better situational awareness of the grid. The speed of the STI calculation make it a promising method to be implemented in the control center for operations. These claims are verified with examples using various standard IEEE test systems and the results confirm the proposed methodology. Thus, the Sensitivity based Thevenin Index provides the operator with better situational awareness even under the presence of noisy/malicious data.

6.6 References

- [1] A. Ramapuram-Matavalam; V. Ajjarapu, "Sensitivity based Thevenin Index with Systematic Inclusion of Reactive Power Limits," accepted for publication in IEEE Transactions on Power Systems
- [2] K. Vu, M. M. Begovic, D. Novosel and M. M. Saha, "Use of local measurements to estimate voltage-stability margin," in IEEE Transactions on Power Systems, vol. 14, no. 3, pp. 1029-1035, Aug 1999
- [3] C. Canizares, A. De Souza, and V. Quintana, "Comparison of performance indices for detection of proximity to voltage collapse," IEEE Trans. Power Syst., vol. 11, no. 3, pp. 1441–1450, 1996.
- [4] V. Ajjarapu and C. Christy, "The continuation power flow: a tool for steady state voltage stability analysis," IEEE Trans. Power Syst., vol. 7, no. 1, pp. 416–423, 1992.
- [5] M. Brown, M. Biswal, S. Brahma, S. J. Ranade and H. Cao, "Characterizing and quantifying noise in PMU data," 2016 IEEE PES General Meeting (PESGM), Boston, MA, 2016, pp. 1-5
- [6] Handbook of Linear Algebra, 2nd edition, Chapman & Hall/CRC, New York, 2014
- [7] S. Corsi and G. Taranto, "A real-time voltage instability identification algorithm based on local phasor measurements," IEEE Trans. Power Syst., vol. 23, no. 3, pp. 1271–1279, 2008.

- [8] M. Glavic and T. Van Cutsem, "Wide-Area Detection of Voltage Instability from Synchronized Phasor Measurements. Part I: Principle," in IEEE Trans. on Pow. Sys., vol. 24, no. 3, pp. 1408-1416, Aug. 2009
- [9] H. Y. Su and C. W. Liu, "Estimating the Voltage Stability Margin Using PMU Measurements," in IEEE Transactions on Power Systems, vol. 31, no. 4, pp. 3221-3229, July 2016

**CHAPTER 7. MONITORING LONG TERM VOLTAGE INSTABILITY DUE TO
DISTRIBUTION & TRANSMISSION INTERACTION USING UNBALANCED
 μ PMU & PMU MEASUREMENTS**

Modified from a manuscript published in the IEEE Transactions in Smart Grids

Amarsagar Reddy Ramapuram Matavalam, Ankit Singhal and Venkataramana Ajjarapu

*Department of Electrical and Computer Engineering, Iowa State University, Ames, IA
50011, United States of America.*

Abstract

This paper extends the idea of the Thevenin equivalent into unbalanced 3ϕ circuits and proposes a 3ϕ long-term voltage stability indicator (VSI) that can identify critical loads in a 3ϕ system. Furthermore, in order to identify whether the voltage stability limit is due to the transmission network or a distribution network, a transmission-distribution distinguishing index (TDDI) is proposed. The novelty in the proposed indices is that they can account for the unbalance in the lines and loads, enabling them to use unbalanced phasor measurements naturally. This is supported by mathematical derivations and numerical results. A convex optimization formulation to estimate the 3ϕ Thevenin equivalent using PMU & μ PMU measurements is proposed, making it possible to calculate VSI and TDDI in an online model-free manner. Numerical simulations performed using co-simulation between Pypower and GridlabD are presented for the IEEE 9 bus and the 30 bus transmission networks combined with several modified IEEE 13 node and 37 node distribution networks. These case studies validate the proposed 3ϕ -VSI and TDDI over a wide range of scenarios and demonstrate the importance of μ PMU measurements in identifying the regions causing long term voltage instability.

7.1 Introduction

There is increasing pressure on power system operators to utilize the existing grid infrastructure to the maximum extent possible and this mode of operation can lead to long-term voltage stability problems. To handle this, operators are adopting real-time tools using PMUs that provide them better situational awareness of the long-term voltage stability in the transmission network (TN) [1][2]. However, all these methods assume an aggregated load at the transmission level (≥ 115 kV) and do not consider the sub-transmission or the distribution network where the loads are actually present. To address this shortcoming and to monitor the distribution network (DN) voltage stability, recent papers have proposed methods using analytical techniques & μ PMU measurements. μ PMUs, also referred to as distribution PMUs (DPMUs) are synchronized measurement devices that can measure the electrical quantities in the electrical grid at the distribution and sub-transmission voltage levels (33 kV – 2.5 kV) [3]. These devices can support a range of monitoring, diagnostic and control applications [3] and are being deployed by utilities to capture transient phenomenon in distribution systems [4] and for load modeling.

The analytical methods [5][6] study the solvability of distribution power flow equations and relate them to voltage stability. These approaches need information about the network (topology, etc.) and lead to a better estimation of the DN voltage stability while incorporating the unbalanced nature of multi-phase networks. In contrast, the measurement based approaches [7][8] estimate a simplified network from measurements, leading to a slight error, but are fast and do not need much information about the network. However, these approaches usually assume a balanced network or no coupling between the phases, which can lead to large errors when the DN is unbalanced. In practice, the unbalance between the phases as seen by the transmission system is low, but the unbalance in the individual DN feeders could be high and

this can lead to a reduction in the stability margin. In the worst case, if only 1 phase in a DN feeder is loaded, the effective impedance is much higher than a balanced load and can have a large impact on the overall voltage stability margin of the system. More details about impact of unbalance in distribution on the overall loadability of the system can be found in [9].

The interaction between the transmission and distribution system can cause the overall voltage stability margin to be different from the individual networks. The voltage stability of the overall system can be either due to the TN or DN. [10] proposes a method for single phase networks to detect the limiting network (TN or DN) from PV curves and demonstrated that identifying the limiting network will lead to better control schemes to improve voltage stability. In [11], a faster identification method for single phase networks is proposed by estimating equivalent impedances for TN & DN from measurements to detect the limiting network. Thus, there is a need for a 3 ϕ measurement based voltage stability monitoring scheme that can account for unbalance and coupling between the phases. This scheme also needs to identify the critical bus and if the TN or the DN are the limiting network.

7.2 Impact of Distribution Network on Voltage Stability Indicator at the Transmission Network

The Thevenin equivalent is a methodology that has been utilized for monitoring the voltage stability of the grid using PMUs [1]. It is defined for each load bus and equivalences the rest of the network into an equivalent voltage (E_{eq}) and impedance (Z_{eq}), as shown in Figure 7.1.

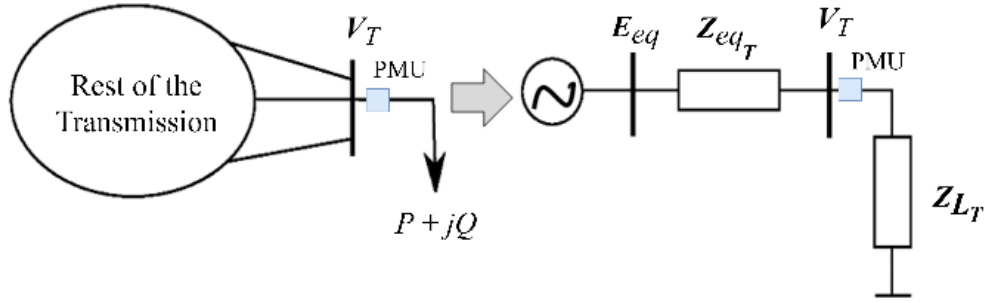


Figure 7.1 Structure of the conventional Thevenin Equivalent

This has been traditionally done for TNs with only the positive sequence component being modeled as the TNs are balanced. The Thevenin equivalent can be estimated from quasi-steady state measurements at a PMU. The maximum load power in the Thevenin equivalent occurs when the load impedance (\mathbf{Z}_{L_T}) matches the Thevenin impedance and the voltage stability indicator (VSI_T) for the equivalent circuit is given by (7-1) [2]. The VSI_T is 0 at no load condition and is 1 at the maximum loading. Recently it was shown that the VSI_T is closely related to the power flow jacobian and the VSI_T becomes 1 when the jacobian becomes singular, indicating that the critical point has been reached. Thus, the VSI_T value can be used to monitor the long term voltage instability of the grid in a data-driven manner using only measurements at a PMU.

$$\text{VSI}_T = \frac{|\mathbf{Z}_{eqT}|}{|\mathbf{Z}_{L_T}|}; \text{VSI}_D = \frac{|\mathbf{Z}_{eqT} + \mathbf{Z}_{eqD}|}{|\mathbf{Z}_{L_D}|} \quad (7-1)$$

One of the key assumptions in the derivation [2] of the VSI_T is that the load increase occurs at the transmission bus. In reality, the loads are located in the sub-transmission and distribution networks (DNs) and so this has to be incorporated into the Thevenin model. This is conceptually done in the modified Thevenin equivalent represented in Figure 7.2 where the impedance \mathbf{Z}_{eqD} represents an aggregation of the distribution feeders in a load area and the equivalent load impedance is given by \mathbf{Z}_{L_D} . For this simple case, the VSI_D is given in (7-1) as

the load increase is in the DN. It is important to stress that this is a conceptual example as the node connected to the distribution load is a virtual node and is not a physical site.

Comparing the two equivalents in Figure 7.1 and Figure 7.2, it can be seen that $\mathbf{Z}_{L_T} = \mathbf{Z}_{L_D} + \mathbf{Z}_{eq_D}$. As the load is present at the distribution node, at the critical loading $|\mathbf{Z}_{L_D}| = |\mathbf{Z}_{eq_T} + \mathbf{Z}_{eq_D}|$. Combining this information with (7-1) it can be deduced that the VSI_T at the critical load for the modified Thevenin equivalent including the DN is less than 1. To understand why this is the case, consider a simplified network with $\mathbf{Z}_{eq_T} = X_{eq_T} \cdot j$, $\mathbf{Z}_{eq_D} = X_{eq_D} \cdot j$ & $\mathbf{Z}_{L_D} = R_{L_D}$. For this case, the critical load impedance value is given by (7-2) and the VSI_T at the critical load is given by (7-3) which can be simplified into (7-5) which is less than 1 as $X_{eq_D} > 0$ & $X_{eq_T} > 0$.

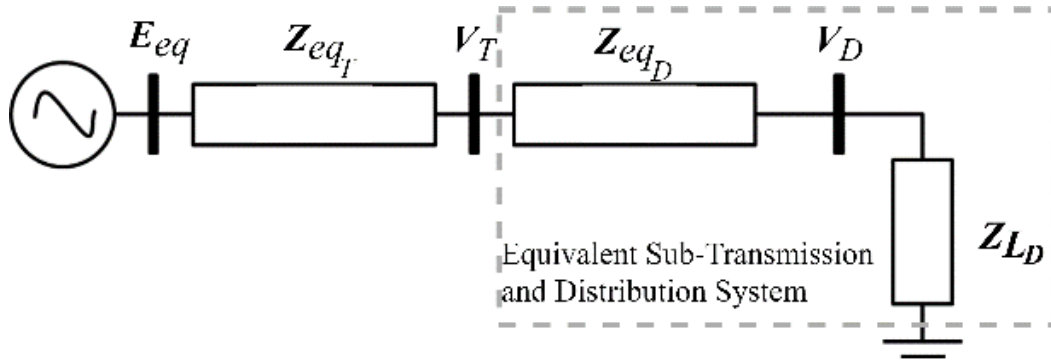


Figure 7.2 Structure of the Thevenin Equivalent including distribution network

$$R_{L_D-crit} = X_{eq_T} + X_{eq_D} \quad (7-2)$$

$$VSI_{T-crit} = \frac{|X_{eq_T} \cdot j|}{|X_{eq_D} \cdot j + R_{L_D-crit}|} \quad (7-3)$$

$$VSI_{T-crit} = \frac{X_{eq_T}}{|X_{eq_T} + (1 + j) \cdot X_{eq_D}|} \quad (7-4)$$

$$VSI_{T-crit} = \frac{1}{|1 + (1 + j) \cdot X_{eq_D}/X_{eq_T}|} < 1 \quad (7-5)$$

To verify the analysis presented above, several cases with fixed transmission impedance and varying distribution impedance (in per unit) as shown in Table 7-1 are simulated with unity power factor load. The varying distribution system impedance is analogous to different distribution feeders and the amount of variation in the impedance is comparable to the variation in impedance of line configurations present in the IEEE distribution test systems [13]. The maximum power in per unit is also listed in Table 7-1 for each case along with the VSI_T and VSI_D at the critical loading. The plot of the calculated VSI_T and VSI_D versus the load power is plotted for case 1 in Figure 7.3.

It can be seen that the VSI_{D-crit} for all the scenarios is 1 while the VSI_{T-crit} is less than 1 and is different for the various cases, implying that the critical VSI_T actually changes with Z_{eqD} . Case-1 is similar to the scenario analyzed in (7-2) – (7-5) with $X_{eqT} = 0.08$ and $X_{eqD} = 0.02$ and the VSI_{T-crit} calculated by (7-5) is equal to 0.79 which matches the value numerically obtained, validating the analysis presented.

Table 7-1 Various cases and the corresponding P_{crit} , VSI_{T-crit} & VSI_{D-crit}

	Z_{eqT}	Z_{eqD}	P_{crit}	VSI_{T-crit}	VSI_{D-crit}
Case-1	$0.08 \cdot j$	$0.01(0 + 2j)$	5	0.79	1
Case-2	$0.08 \cdot j$	$0.01(1 + 2j)$	4.5	0.69	1
Case-3	$0.08 \cdot j$	$0.01(2 + 2j)$	4.1	0.63	1

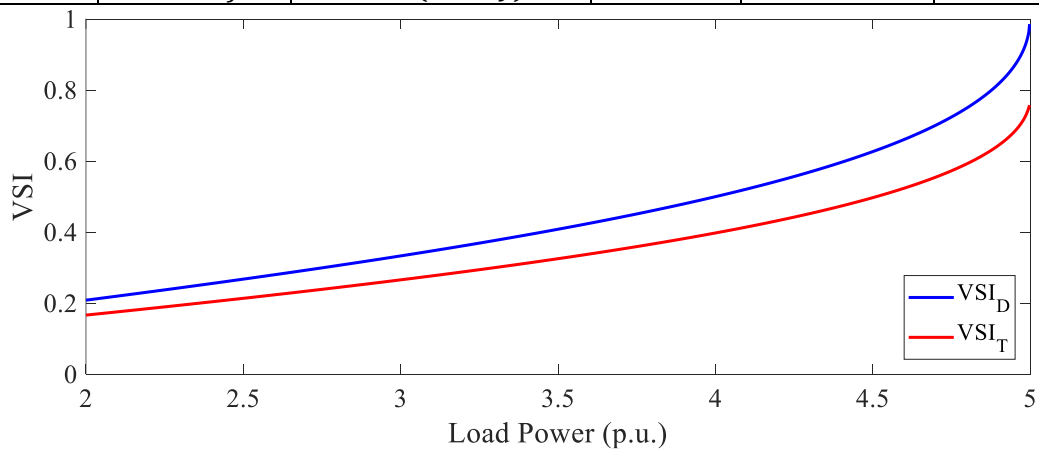


Figure 7.3 Variation of VSI_T and VSI_D versus load for case-1 in Table 7-1

The varying critical value of the VSI_T makes it challenging to monitor voltage stability using only the PMU measurements, as we cannot estimate the \mathbf{z}_{eqD} from only measurements at the PMU. Utilities instead use the measurement based techniques mainly to trigger more detailed model based techniques that account for the downstream network, either explicitly or by using a proxy impedance for the substation transformer. Thus, a method to estimate the equivalent Thevenin circuit including the DN equivalent would be desirable as it would allow better monitoring using only measurements. The estimation of the circuit parameters using μ PMU measurements in combination with PMU measurements is explained for 1- ϕ networks next.

7.2.1 Estimation of Equivalent Circuit Parameters from PMU & μ PMU Measurements for 1 ϕ Circuits

In order to determine the parameters (\mathbf{E}_{eq} , \mathbf{Z}_{eqT} , \mathbf{Z}_{eqD} & \mathbf{Z}_{LD}) of the circuit shown in Figure 7.2, synchronized measurements from the transmission and distribution buses over a time period with varying quasi steady-state load are necessary. Let there be M measurements of voltage and current at the T & D buses in Figure 7.2, then the following equations (7-6) - (7-8) can be written for the equivalent circuit from Ohms law where the index inside the square brackets is the measurement index.

$$\mathbf{Z}_{LD} \cdot \mathbf{I}_{LD}[k] = \mathbf{V}_D[k], k = 1 \dots M \quad (7-6)$$

$$\mathbf{E}_{eq} - \mathbf{Z}_{eqT} \cdot \mathbf{I}_{LD}[k] = \mathbf{V}_T[k], k = 1 \dots M \quad (7-7)$$

$$\mathbf{V}_T[k] - \mathbf{Z}_{eqD} \cdot \mathbf{I}_{LD}[k] = \mathbf{V}_D[k], k = 1 \dots M \quad (7-8)$$

The equations (7-6) - (7-8) are linear equations in the unknowns and thus, a standard least square formulation can be used to estimate the unknown parameters. Instead of writing a single optimization to estimate all the parameters at once, the parameters can be independently

estimated by solving smaller optimization formulations. Furthermore, as the VSI expressions only include the impedances, they are estimated from equations (7-9) - (7-11).

$$\min \sum_{k=1}^M |\mathbf{Z}_{L_D} \cdot \mathbf{I}_{L_D}[k] - \mathbf{V}_D[k]|_2^2 \quad (7-9)$$

$$\min \sum_{k=1}^M |\mathbf{Z}_{eq_T} \cdot (\mathbf{I}_{L_D}[k] - \mathbf{I}_{L_D}[1]) + (\mathbf{V}_T[k] - \mathbf{V}_T[1])|_2 \quad (7-10)$$

$$\min \sum_{k=1}^M |\mathbf{Z}_{eq_D} \cdot \mathbf{I}_{L_D}[k] + \mathbf{V}_D[k] - \mathbf{V}_T[k]|_2 \quad (7-11)$$

The optimization problems can be solved very quickly as this is the standard least square formulation. This approach to estimate the circuit parameters and the VSI using measurements is tested on the 3 cases shown in Table 7-1 and the estimated parameter values matched the actual values and were able to estimate the VSI accurately. In reality, the measurements in the DN are likely to be unbalanced 3ϕ measurements and so the formulations above need to be extended to handle 3ϕ measurements to estimate the equivalent impedances that are complex 3×3 matrices. Furthermore, the stability indicator in (7-1) has to be extended to handle DN characteristics of unbalance, etc. Extending the VSI for a 3ϕ equivalent is not straightforward as the impedances are complex 3×3 matrices. Thus a new stability indicator for 3ϕ networks that incorporates the unbalanced equivalent voltage, impedance and load needs to be defined. Both the challenge of a 3ϕ -VSI and equivalent circuit estimation from μ PMU measurements are addressed in the following sections.

7.3 3Φ Voltage Stability Indicator and Transmission-Distribution Distinguishing Index

To extend the VSI to 3ϕ circuits, we utilize a property of the Thevenin equivalent that relates the power loss in \mathbf{Z}_{eq} to the power demanded by the load. Multiplying the numerator

and denominator of (7-1) with the load current, we can see that the VSI is the ratio of the magnitude of total apparent power loss and total apparent load power as shown in (7-12).

$$VSI_D = \frac{|I_L|^2 |Z_{eqT} + Z_{eqD}|}{|I_L|^2 |Z_{LD}|} = \frac{|S_{lossT} + S_{lossD}|}{|S_{LD}|} \quad (7-12)$$

This definition can be extended naturally to the 3ϕ circuits by replacing S_{loss} and S_L with the total 3ϕ apparent power loss and apparent load and the expression for the $VSI_{D-3\phi}$ is given by (7-13) - (7-16) where the * signifies complex conjugate transpose.

$$VSI_{D-3\phi} = \frac{|S_{lossT-3\phi} + S_{lossD-3\phi}|}{|S_{LD-3\phi}|} \quad (7-13)$$

$$S_{lossT-3\phi} = I_{L-3\phi}^* \cdot Z_{eqT-3\phi} \cdot I_{L-3\phi} \quad (7-14)$$

$$S_{lossD-3\phi} = I_{L-3\phi}^* \cdot Z_{eqD-3\phi} \cdot I_{L-3\phi} \quad (7-15)$$

$$S_{LD-3\phi} = I_{L-3\phi}^* \cdot Z_{LD-3\phi} \cdot I_{L-3\phi} \quad (7-16)$$

To show that the proposed $VSI_{D-3\phi}$ works as a stability indicator, we will first prove that the expression in (7-13) will reduce to (7-1) when the lines and load are balanced. Then, we will numerically demonstrate the index performance with examples having unbalanced load.

Proposition: In case of a balanced network and balanced load, the $VSI_{D-3\phi}$ reduces to the VSI_D with the transmission, distribution and load impedances replaced by their positive sequence impedances.

Proof: In case of balanced load and lines, the structure of the impedance matrices $Z_{eqT-3\phi}$, $Z_{eqD-3\phi}$ & $Z_{LD-3\phi}$ and the load current $I_{L-3\phi}$ are as shown in (7-17) - (7-19).

$$\mathbf{Z}_{eqT-3\phi} = \begin{bmatrix} \mathbf{Z}_{sT} & \mathbf{Z}_{mT} & \mathbf{Z}_{mT} \\ \mathbf{Z}_{mT} & \mathbf{Z}_{sT} & \mathbf{Z}_{mT} \\ \mathbf{Z}_{mT} & \mathbf{Z}_{mT} & \mathbf{Z}_{sT} \end{bmatrix} \quad (7-17)$$

$$\mathbf{Z}_{eqD-3\phi} = \begin{bmatrix} \mathbf{Z}_{sD} & \mathbf{Z}_{mD} & \mathbf{Z}_{mD} \\ \mathbf{Z}_{mD} & \mathbf{Z}_{sD} & \mathbf{Z}_{mD} \\ \mathbf{Z}_{mD} & \mathbf{Z}_{mD} & \mathbf{Z}_{sD} \end{bmatrix} \quad (7-18)$$

$$\mathbf{Z}_{LD-3\phi} = \begin{bmatrix} \mathbf{Z}_{LD} & 0 & 0 \\ 0 & \mathbf{Z}_{LD} & 0 \\ 0 & 0 & \mathbf{Z}_{LD} \end{bmatrix}; \mathbf{I}_{L-3\phi} = \mathbf{I}_0 \begin{bmatrix} 1 \angle 0 \\ 1 \angle -\frac{2\pi}{3} \\ 1 \angle +\frac{2\pi}{3} \end{bmatrix} \quad (7-19)$$

From the structure of the impedance matrices and standard identities 0 we get expressions (7-20) - (7-21).

$$\mathbf{Z}_{eqT-3\phi} \cdot \mathbf{I}_{L-3\phi} = \mathbf{I}_0 \begin{bmatrix} \mathbf{Z}_{sT} & \mathbf{Z}_{mT} & \mathbf{Z}_{mT} \\ \mathbf{Z}_{mT} & \mathbf{Z}_{sT} & \mathbf{Z}_{mT} \\ \mathbf{Z}_{mT} & \mathbf{Z}_{mT} & \mathbf{Z}_{sT} \end{bmatrix} \begin{bmatrix} 1 \angle 0 \\ 1 \angle -\frac{2\pi}{3} \\ 1 \angle +\frac{2\pi}{3} \end{bmatrix} \quad (7-20)$$

$$= (\mathbf{Z}_{sT} - \mathbf{Z}_{mT}) \mathbf{I}_0 \begin{bmatrix} 1 \angle 0 \\ 1 \angle -\frac{2\pi}{3} \\ 1 \angle +\frac{2\pi}{3} \end{bmatrix} = (\mathbf{Z}_{sT} - \mathbf{Z}_{mT}) \mathbf{I}_{L-3\phi} \quad (7-21)$$

Substituting (7-21) in (7-14) and utilizing the fact that the transmission positive sequence impedance ($\mathbf{Z}_{T_{pos}}$) is equal to $(\mathbf{Z}_{sT} - \mathbf{Z}_{mT})$ and $\mathbf{I}_{L-3\phi}^* \cdot \mathbf{I}_{L-3\phi} = 3|\mathbf{I}_0|^2$ and the expression for $\mathbf{S}_{lossT-3\phi}$ for the balanced case is simplified into (7-22). A similar expression for $\mathbf{S}_{lossD-3\phi}$ can be derived in terms of $\mathbf{Z}_{D_{pos}}$ and $\mathbf{S}_{LD-3\phi}$ in terms of \mathbf{Z}_{LD} and are given in (7-23) - (7-24).

$$\mathbf{S}_{lossT-3\phi} = (\mathbf{Z}_{sT} - \mathbf{Z}_{mT}) \cdot \mathbf{I}_{L-3\phi}^* \cdot \mathbf{I}_{L-3\phi} = 3 \cdot (\mathbf{Z}_{T_{pos}}) |\mathbf{I}_0|^2 \quad (7-22)$$

$$\mathbf{S}_{lossD-3\phi} = 3 \cdot (\mathbf{Z}_{D_{pos}}) |\mathbf{I}_0|^2 \quad (7-23)$$

$$S_{L_{D-3\phi}} = 3 \cdot (Z_{L_D}) |I_0|^2 \quad (7-24)$$

Substituting equations (7-22) - (7-24) into (7-23), we get the expression (7-25) for the $VSI_{D-3\phi}$ which is same as VSI_D and thus the proof that the proposed $VSI_{D-3\phi}$ for balanced 3ϕ circuits is equal to the VSI_D is complete.

$$VSI_{D-3\phi\text{-balanced}} = \frac{|Z_{T_{pos}} + Z_{D_{pos}}|}{|Z_{L_D}|} = VSI_D \quad (7-25)$$

7.3.1 A. Discussion on Load Model

The long term voltage stability depends on the ZIP parameters of the load. In the proposed method the load is always an impedance whose value is calculated online based purely on the measurements and requiring the ZIP parameters. Hence, the proposed methodology incorporates the behavior of the load model indirectly via the varying load impedance. The proposed index (7-1) is a version of the maximum power transfer theorem and so the index has a value of 1 at the maximum load power. The operating point with maximum load power corresponds to the long term instability point in case of purely constant power loads. In case the loads are not purely constant power type, the index still reaches a value of 1 at the maximum power point, which need not be the initiation of instability but is still an important critical point (see C6-C7 in discussion in [2]).

This is actually an advantageous feature of the index as it can detect the transition of the system from the top of the PV curve to the bottom of the PV curve. Even if an operating point on the bottom of the PV curve is stable, it is not a desirable operating point as the total loss in the network is more than the power supplied to the load, making it an uneconomical and an unsafe region to operate. Utilizing the proposed index will enable the operator to prevent this mode of operation, without requiring the ZIP parameters of the load. To also demonstrate

that the $VSI_{D-3\phi}$ is a voltage stability indicator for unbalanced 3ϕ circuits with different ZIP parameters, numerical validation results are shown in the next sub-section.

7.3.2 Validating Results on Unbalanced Load

Results for two cases with balanced source voltage and T&D lines with unbalanced loads are shown. The 3ϕ load and the T&D line parameters for the two cases are shown in Table 7-2 with constant impedance loads. In scenario-1 all the loads have the same lagging power factor while in scenario-2 phase-a has a leading power factor and the remaining phases have lagging power factor. Scenario-3 is same as scenario-1 with 70% load proportion constant impedance type and 30% load constant current type. Scenario-4 is same as scenario-2 with 50% load proportion constant impedance type and 50% load constant current type.

Table 7-2 *Network parameters for validating the $VSI_{D-3\phi}$ for unbalanced load*

T/D network parameters	$\mathbf{Z}_{sT} = 0.8 + 1.6j$; $\mathbf{Z}_{mT} = 0.25 + 0.9j$; $\mathbf{Z}_{sD} = 0.2 + 0.4j$; $\mathbf{Z}_{mD} = 0.05 + 0.1j$;
Source Voltage	$\mathbf{E}_a = 1$; $\mathbf{E}_b = 1\angle -2\pi/3$; $\mathbf{E}_c = 1\angle 2\pi/3$
Load Scenario-1	$\mathbf{S}_a = 1.5 + 0.6j$; $\mathbf{S}_b = 0.5 + 0.2j$; $\mathbf{S}_c = 1.0 + 0.4j$
Load Scenario-2	$\mathbf{S}_a = 1.5 - 0.6j$; $\mathbf{S}_b = 0.5 + 0.2j$; $\mathbf{S}_c = 1.0 + 0.4j$
Load Scenario-3	Same as Scenario-1 with ZIP parameters = [0.7, 0.3, 0]
Load Scenario-4	Same as Scenario-2 with ZIP parameters = [0.5, 0.5, 0]

For each scenario, continuation power flow is used to determine the load voltage and the $VSI_{D-3\phi}$ index at varying loading conditions. Figure 7.4 – Figure 7.7 plot the load voltages in the three phases for scenarios 1-4 respectively. It can be seen that the voltages of all the phases have different profiles due to the load unbalance. The maximum total load power (which corresponds to the nose point) in scenarios 1-4 is 0.59 p.u., 0.67 p.u., 0.56 p.u. and 0.63

p.u. respectively. The lowest active power load for all scenarios is on phase-B and so the highest voltage in all scenarios occurs in phase-B. In scenario-2 and scenario-4, the load on Phase-A is capacitive and so the injection of reactive power increases the voltage in Phase-A & phase-B (least loaded phase) as the loading increases initially.

The load impedance can be estimated from measurements (explained in Section V) and the $VSI_{D-3\phi}$ index can be calculated. Figure 7.8 plots the $VSI_{D-3\phi}$ index versus the total active load for all the scenarios. It can be observed from Figure 7.8 that the $VSI_{D-3\phi}$ index goes to 1 exactly at the nose point of the PV curve for all scenarios, irrespective of the load composition. This verifies that the proposed $VSI_{D-3\phi}$ index can identify the point of maximum loadability and can serve as a voltage stability indicator for 3ϕ unbalanced circuits for different load compositions.

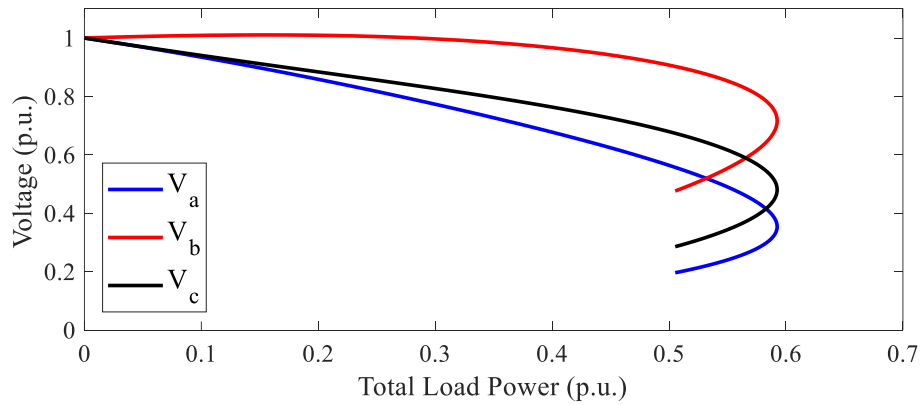


Figure 7.4 Voltage versus total load power with unbalanced load scenario-1

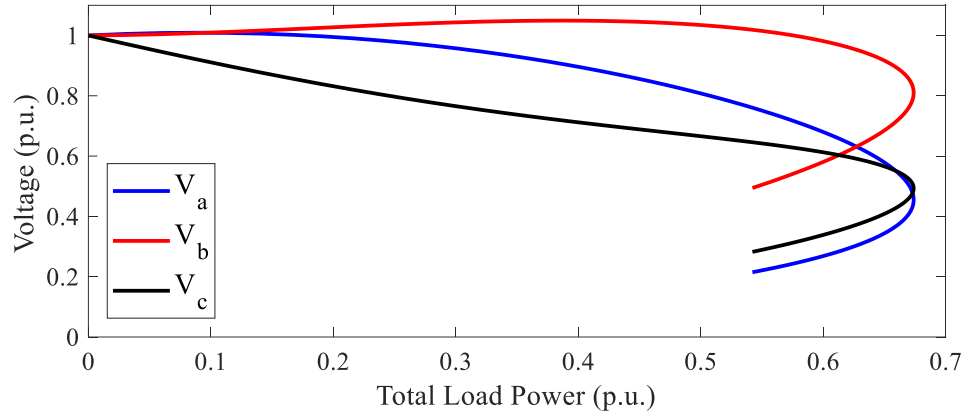


Figure 7.5 Voltage versus total load power with unbalanced load scenario-2

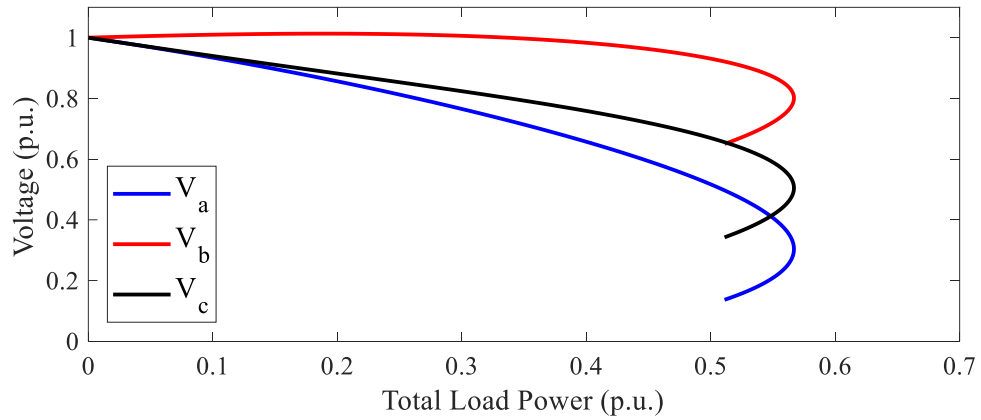


Figure 7.6 Voltage versus total load power with unbalanced load scenario-3

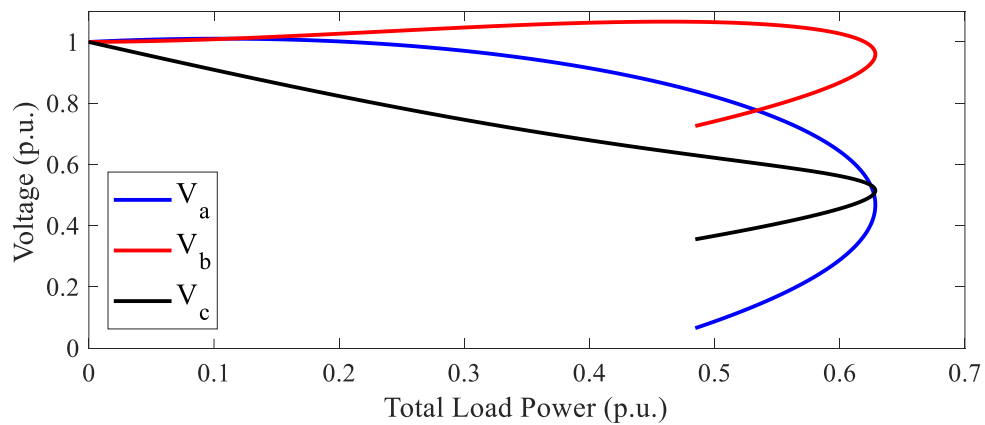


Figure 7.7 Voltage versus total load power with unbalanced load scenario-4

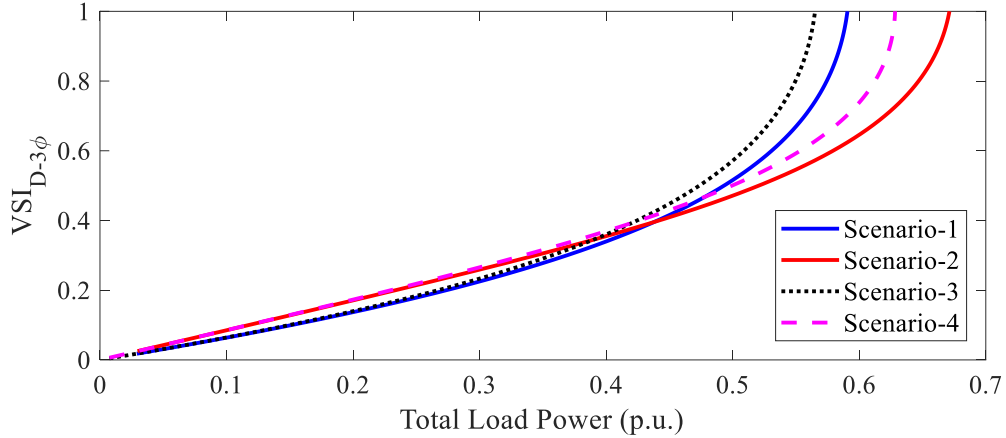


Figure 7.8 $VSI_{D-3\phi}$ versus total load power for the load scenarios in Table 7-2

7.3.3 Transmission-Distribution Distinguishing Index

It can be seen from the examples above that the maximum power reduces as the DN impedance increases and there can be a case when the maximum power limit is mainly due to the DN. For 1ϕ circuits the component which has a larger voltage drop is the main limiting network for voltage stability. Thus, if the transmission impedance is more than the distribution impedance ($|Z_{eqT}| > |Z_{eqD}|$), then the transmission network is the limiting factor. Hence, the ratio between the impedances can be used as a way to distinguish between transmission and distribution limited networks. Instead of directly using the ratio, a Transmission-Distribution Distinguishing Index (TDDI) [11] is defined to distinguish between the transmission limited and distribution limited cases. The identification of the reason for maximum loadability enables a better choice of control [10].

If the ratio $|Z_{eqT}|/|Z_{eqD}|$ is greater than 1 (transmission limited), then the value of TDDI is positive; if the ratio is less than 1 (distribution limited), the value of TDDI is negative; and if the ratio is equal to 1, the value of TDDI is zero. The logarithm function is used in (7-26) for better quantification and is explained in detail in [11]. The TDDI has to be calculated at the critical node, which is the node with the highest VSI and it is shown in [11] that the

TDDI is able to detect transmission limited and distribution limited networks from only PMU and μ PMU measurements with balanced lines and loads. Thus, in a manner similar to the VSI, the TDDI is also extended to 3ϕ circuits using the loss in the transmission and distribution impedances as shown in (7-26). The ability to distinguish between transmission and distribution limited systems will enable the operators to quickly choose between various controls (e.g. DG in a particular distribution system, switching in transmission lines, injecting reactive power via shunts in the transmission system, etc.) that will lead to a larger improvement in the margin.

$$TDDI = \log \frac{|Z_{eqT}|}{|Z_{eqD}|}; TDDI_{3\phi} = \log \frac{|S_{lossT-3\phi}|}{|S_{lossD-3\phi}|} \quad (7-26)$$

Now that a simple circuit has been analyzed, applying the proposed method to a multi-bus network requires a way to estimate the equivalent circuit parameters ($Z_{eqT-3\phi}$ & $Z_{eqD-3\phi}$) from measurements and this is presented in the next section.

7.4 Estimation of Thevenin Equivalent Parameters using PMU and μ PMU Measurements

The measurements are at the substation PMU and μ PMUs located at a few of the distribution nodes in the DN. Instead of a single equivalent at the substation, we will create a Thevenin equivalent for each μ PMU+PMU pair and so the impedance of the transmission will be different for different nodes in the same distribution feeder as the equivalent essentially splits the transmission lines among the loads based on the individual powers, as shown in Fig. 9. Even though μ PMUs are not present at some of the loads, the impact of the load increase at these nodes is reflected in the voltage measurements at all the μ PMUs and the substation PMU present in the corresponding DN. The decoupling of the Thevenin equivalent for each load is a standard technique in literature [1] and does not mean that these loads are independent. The

coupling between the loads is present in the measurements and so the impedances of the Thevenin equivalents will vary gradually with varying operating condition.

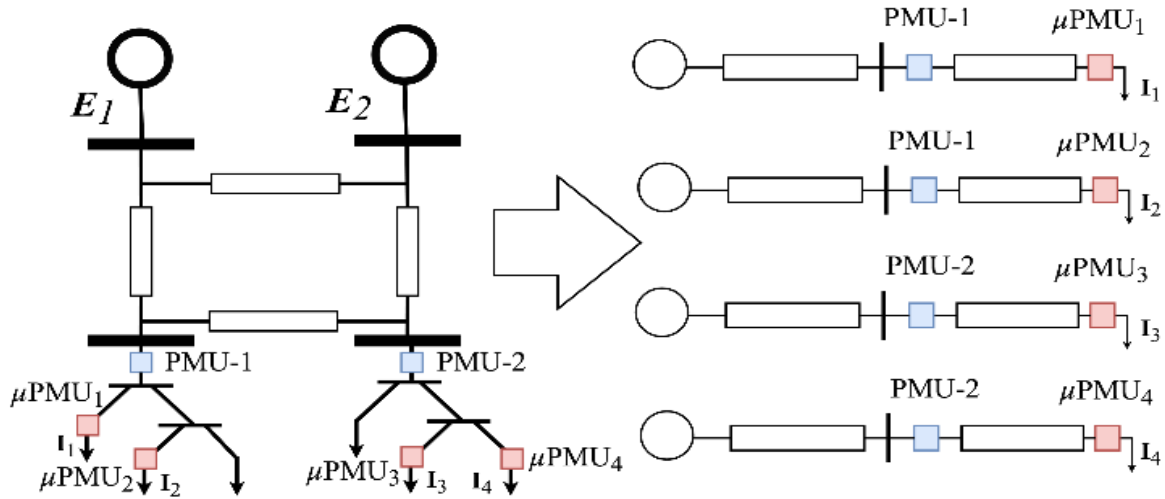


Figure 7.9 Conceptual example showing the proposed methodology splitting TN & DN so that each load μ PMU + substation PMU has a separate equivalent circuit

In order to determine the Thevenin equivalent circuit parameters, M synchronized measurements over a time period are used and we assume that the equivalent circuit is reasonably constant for the operating conditions in this time period. This assumption is usually valid due to the quasi steady state behavior of the power system. The load can be varying at all the nodes in this time period, even at the nodes with no μ PMUs. The measurements are the 3ϕ distribution load voltage and current from μ PMUs and the 3ϕ substation voltage from PMU. These measurements are 3×1 column vectors as they are 3ϕ measurements. The load impedance is the ratio of the mean voltage and current in each phase as shown in (7-27) where the division is element wise (this follows directly by extending (7-9) to 3ϕ circuits). Next, (7-28) - (7-29) are valid for every μ PMU and corresponding PMU phasor measurements just as in (7-7) - (7-8). We write the equations for measurements at i^{th} bus in the DN and the index inside the square brackets is the measurement index. The load impedance can be estimated by extending the expression in (7-9) to 3ϕ circuits as it is a diagonal matrix.

$$\mathbf{Z}_{L_{D_i}} = \min_{\mathbf{Z} \in \text{Diag}} \sum_{k=1}^M \left| \mathbf{Z} \cdot \mathbf{I}_{L_{D_i}}[k] - \mathbf{V}_{D_i}[k] \right|_2^2 \quad (7-27)$$

$$\mathbf{E}_{eq_i} - \mathbf{Z}_{eq_{T_i-3\phi}} \cdot \mathbf{I}_{L_{D_i}}[k] = \mathbf{V}_T[k], k = 1 \dots M \quad (7-28)$$

$$\mathbf{V}_T[k] - \mathbf{Z}_{eq_{D_i-3\phi}} \cdot \mathbf{I}_{L_{D_i}}[k] = \mathbf{V}_{D_i}[k], k = 1 \dots M \quad (7-29)$$

Defining the terms $\Delta \mathbf{V}_T[k]$, $\Delta \mathbf{V}_{D_i}[k]$ & $\Delta \mathbf{I}_{L_{D_i}}[k]$ as follows and substituting (7-28) - (7-29) into (7-30) - (7-31), the expressions (7-33) - (7-34) are derived.

$$\Delta \mathbf{V}_T[k] = \mathbf{V}_T[k] - \mathbf{V}_T[1] \quad (7-30)$$

$$\Delta \mathbf{V}_{D_i}[k] = \mathbf{V}_{D_i}[k] - \mathbf{V}_{D_i}[1] \quad (7-31)$$

$$\Delta \mathbf{I}_{L_{D_i}}[k] = \mathbf{I}_{L_{D_i}}[k] - \mathbf{I}_{L_{D_i}}[1] \quad (7-32)$$

$$\mathbf{Z}_{eq_{T_i-3\phi}} \cdot \Delta \mathbf{I}_{L_{D_i}}[k] = -\Delta \mathbf{V}_T[k] \quad (7-33)$$

$$\mathbf{Z}_{eq_{D_i-3\phi}} \cdot \Delta \mathbf{I}_{L_{D_i}}[k] = \Delta \mathbf{V}_T[k] - \Delta \mathbf{V}_{D_i}[k] \quad (7-34)$$

As the proposed VSI and the TDDI only utilize the impedance values and the load current, there is no need to estimate the Thevenin voltage. The equations (7-33) - (7-34) are linear in the impedance terms and after a sufficient number of measurements, we can solve for the equivalent impedance using least squares, just as in (7-10) - (7-11). Since the impedance matrices need to be symmetric, this constraint also needs to be incorporated while estimating the equivalent 3ϕ impedance matrices and a simple optimization formulation as shown in (7-35) & (7-36) can be used.

$$\begin{aligned} & \min \sum_{k=1}^M \left| \mathbf{Z}_{eq_{T_i-3\phi}} \cdot \Delta \mathbf{I}_{L_{D_i}}[k] + \Delta \mathbf{V}_T[k] \right|_2^2 \\ & \text{subject to } \left| \mathbf{Z}_{eq_{T_i-3\phi}} - \text{transpose}(\mathbf{Z}_{eq_{T_i-3\phi}}) \right|_F \leq \xi_T \end{aligned} \quad (7-35)$$

$$\begin{aligned} & \min \sum_{k=1}^M \left| \mathbf{Z}_{eq_{D_i-3\phi}} \cdot \Delta \mathbf{I}_{L_{D_i}}[k] + \Delta \mathbf{V}_{D_i}[k] - \Delta \mathbf{V}_T[k] \right|_2^2 \\ & \text{subject to } \left| \mathbf{Z}_{eq_{D_i-3\phi}} - \text{transpose}(\mathbf{Z}_{eq_{D_i-3\phi}}) \right|_F \leq \xi_D \end{aligned} \quad (7-36)$$

For an actual physical 3-phase line, the mutual impedance between any two phases is the same, no matter which direction the mutual impedance is measured – i.e. the mutual impedance of Phase-A on Phase-B is same as the mutual impedance of Phase-B on Phase-A. This property of physical 3-phase lines makes the impedance matrix symmetric. To ensure that the equivalent 3-phase impedance matrix determined from the measurements has a similar property, the inequality constraint is imposed on $\mathbf{Z}_{eq_{T_i-3\phi}}$ and $\mathbf{Z}_{eq_{D_i-3\phi}}$ in the optimization formulation. The values of ξ_T & ξ_D are ideally zero, but as it calculated over a range of operating points, they are non-zero and their values correspond to the non-ideality expected in the transmission and distribution equivalent. These values need to be small and values in between 0.01-0.05 gave good results in the numerical simulations in Section VI. Values of ξ_T & ξ_D smaller than 0.01 sometimes made the problem infeasible and values larger than 0.05 sometimes made the equivalent lines capacitive, even when all the intermediate lines were inductive. The subscript ‘F’ in the constraint above is the Frobenius-norm and the subscript ‘2’ in the optimization is the 2-norm of the vector. The optimization problem is convex as the Frobenius norm of a matrix is a convex function [15] and the objective is convex. Thus, the proposed optimization formulation can be solved efficiently in an online manner, even for a large number of measurements. Once the equivalent impedances for the T&D networks have been determined, the VSI and TDDI can be estimated.

7.4.1 PMU and μ PMU Placement in TN and DN

As the proposed method depends on measurements from the grid, the placement of PMUs and μ PMUs needs to be done in a systematic manner. The placement of μ PMUs is a

multi-objective problem as various conflicting objectives (cost, visibility, phenomenon of interest, etc.) need to be considered. This is a challenging problem in its own right and is beyond the scope of this paper. For the numerical simulations in this paper, it is assumed that PMUs are present in every node of the TN and μ PMUs are present in all the nodes of the DN. This is not a requirement of the proposed method as the equivalent circuit is determined only using measurements from a μ PMU and the PMU at the corresponding substation. As the impact of all loads in the DN is indirectly present in the measurements at a particular μ PMU, there is no need to have multiple μ PMUs in the same DN. In all the numerical simulations for the cases in Section VI, it is observed that the critical nodes all correspond to the nodes that are farthest from voltage controlled nodes in the DN or have large loads with significant unbalance. μ PMUs placed at these nodes were able to identify the voltage instability and so utilizing this as a criteria for placement of μ PMUs will be explored in the future

The flowchart in Figure 7.10 summarizes the data flow and the calculations required for monitoring voltage stability in the overall system and distinguishing between TN & DN limited networks from μ PMU and PMU measurements.

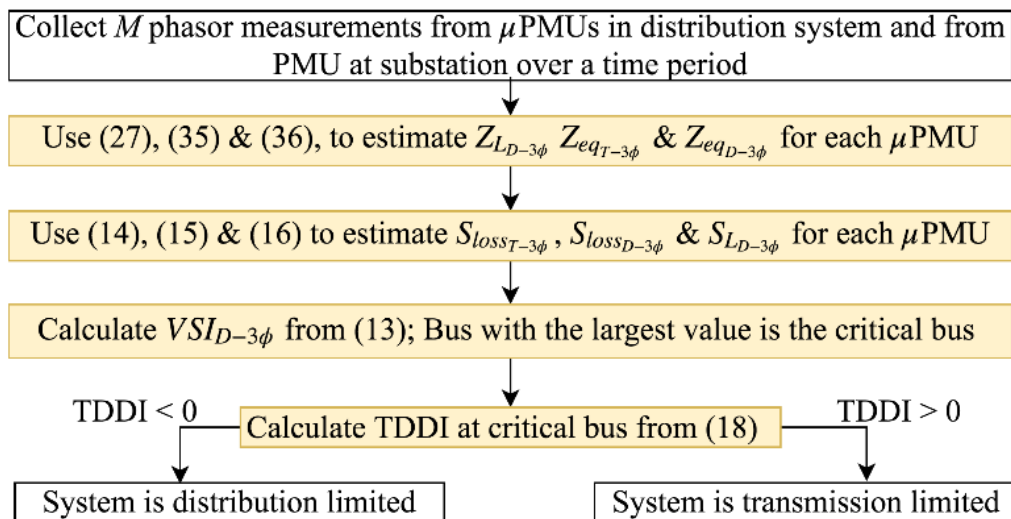


Figure 7.10 Flowchart using the measurements to estimate $VSI_{D-3\phi}$ and TDDI

7.5 Numerical Results

7.5.1 Simulation and Validation Setup

An integrated transmission-distribution co-simulation framework has been used to simulate the TN-DN interaction and validate the numerical results on test cases. A python based power flow solver ‘Pypower’[17] is utilized to model the TN. Similarly, an unbalanced three-phase solver ‘GridlabD’[18] is used to model and solve the DN. Both the solvers communicate and exchange the variables at the interface which is developed using a software Framework for Network Co-Simulation (FNCS)[19]. All three software are open-source, and GridlabD and FNCS are developed by Pacific Northwest National Laboratory (PNNL). Aggregated loads at the transmission buses are replaced by the several distribution feeders and interchange the variables as shown in Figure 7.11 For a particular operating point (loading condition), distribution feeders solve the power flow and send the net substation active and reactive power information to the transmission solver via FNCS. Transmission solver runs power flow for the received loading and sends the resultant voltage to the DNs via FNCS. This interchange of variables occurs until convergence is reached. References [9], [20], [21] & [22] contain more details about co-simulation methods for solving the power flow equations. References [9] & [22] specifically deal with describing the need for co-simulation for voltage stability analysis by considering unbalance and distribution generation.

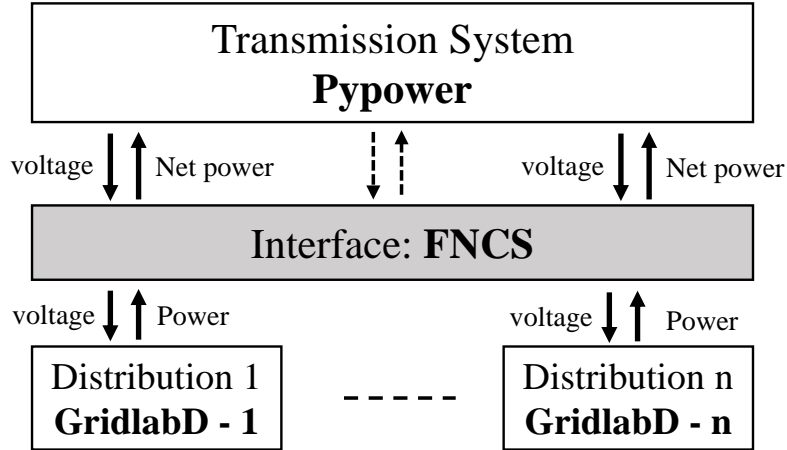


Figure 7.11 *Co-simulation methodology between Pypower and GridlabD*

For the load increase scenario, the loads at all the distribution buses and generation at all transmission buses are increased with the same scaling factor λ , where base operating point corresponds to $\lambda = 1$. Maximum loading condition (λ_{max}) is considered when either transmission or distribution power flow stops converging. The bus voltage and load currents in the TN & DN are used as simulated PMU and μ PMU measurements are recorded at each bus for each load level. These measurements are used to estimate the equivalent circuit parameters at each load in the DN by solving the optimization formulation (7-35) - (7-36). To solve optimization formulations (7-35) - (7-36) we used CVX, a package for specifying and solving convex programs [16] in Matlab and the time taken to estimate the equivalent parameters is around 1s. The $VSI_{D-3\phi}$ and the TDDI can then be calculated from the equivalent circuit. Two test systems are simulated to validate the $VSI_{D-3\phi}$ and the TDDI.

7.5.2 Small Test Case: 9 bus TN + 13 node DN

In order to better explain and validate the numerical results, a smaller test case is presented first. IEEE 9 bus test system is used as TN and the loads at all three load buses 5, 7 and 9 are replaced with the IEEE 13 bus distribution test feeders as shown in Figure 7.12. Several identical feeders are attached at each TN bus to ensure that the TN bus sees the same

load as the base load from the TN specification – i.e. the losses in the DN are considered as TN load while setting up the base case. For this test system, we use 3 different types of distribution feeders which are modified versions of IEEE 13 DN (see appendix for details). The base loading of these feeders is the same while the impedances are varied. The variation in the impedances is comparable to the various line configurations present in the IEEE distribution test systems [13]. We create 3 cases by attaching different DN feeders at TN buses shown in Figure 7.12 along with the maximum loading. As the line impedances in the DN are increasing for the feeders from case 1 to case 3, it is expected that the maximum loading will decrease and the results for λ_{max} show this trend

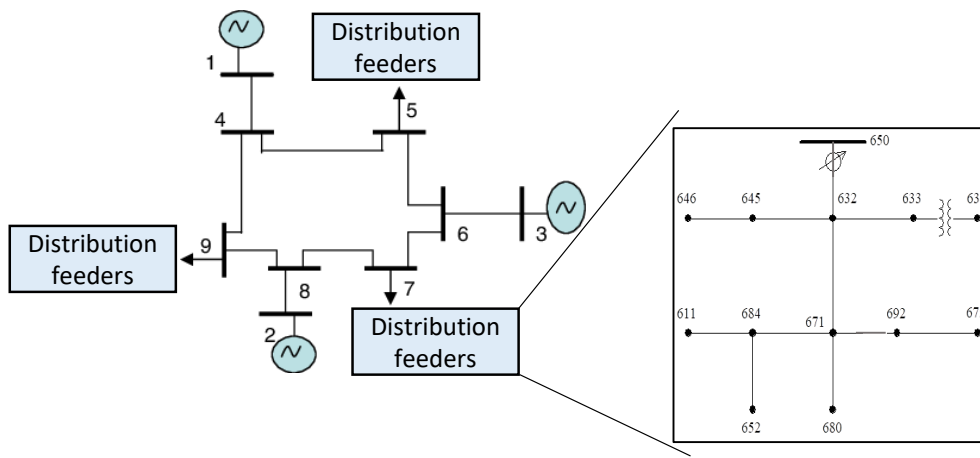


Figure 7.12 Topology of the 9 bus TN and 13 node DN

Table 7-3 Feeder configuration at various TN buses and critical load

Case	TN bus 5	TN bus 7	TN bus 9	λ_{max}
Case 1	13A	13A	13A	1.84
Case 2	13B	13A	13A	1.56
Case 3	13C	13A	13A	1.26

Feeder 13A, 13B & 13C – impedances are scaled by 0.5, 1 and 1.4 of the original 13-node feeder 0 respectively. From the simulated μ PMU and PMU measurements, \mathbf{Z}_{eqT_i} & \mathbf{Z}_{eqD_i}

are estimated by solving convex optimization (7-35) - (7-36) in Matlab at each load level for each case which took around 1 second to solve for a given λ . Then the $VSI_{D-3\phi}$ & TDDI are calculated using (7-13) & (7-26). The VSI_T can also be estimated using (7-1) by using the PMU measurements. The $VSI_{D-3\phi}$ & VSI_T for the critical distribution and transmission nodes in case-1 are plotted in Figure 7.13. It can be seen that the VSI_T is only ~ 0.6 at TN bus 5 at the critical loading while the $VSI_{D-3\phi}$ goes to 1 at DN-675 in TN bus 5 at the critical loading. Similar behavior was observed for all cases and this verifies the need for μ PMUs for accurate voltage stability monitoring.

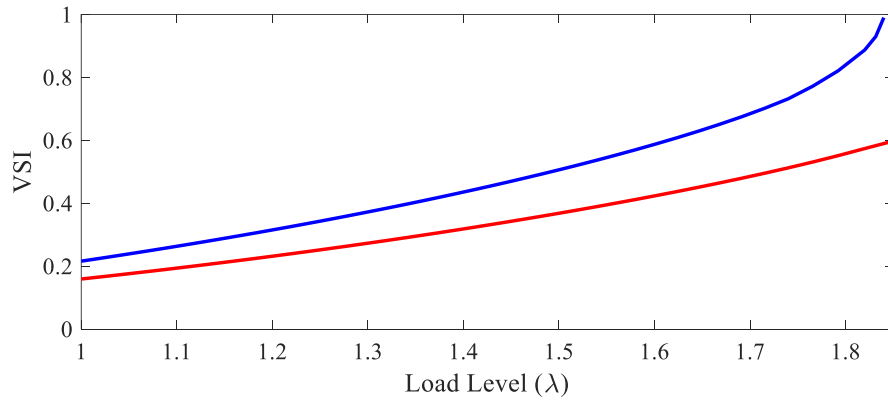


Figure 7.13 $VSI_{D-3\phi}$ at DN-675 at TN 5 & VSI_T at TN 5 v/s load scaling for case 1

The maximum value of $VSI_{D-3\phi}$ occurs at node 675 in the DN and this is the critical node in the DN. This makes sense as it is a large load at the end of the feeder. The value of $VSI_{D-3\phi}$ and TDDI at critical node (node 675) for the feeders connected to TN 5 and TN 9 are listed at the base loading in Table 7-4. The values at the critical node in the overall TN+DN system for each case is in bold font. It can be observed that value of the $VSI_{D-3\phi}$ at DN-675 node in TN bus 5 is increasing as the feeder at TN bus 5 changes from 13A to 13C, implying that the system is more stressed. This makes sense as the impedance of the distribution feeder increases from 13A to 13C. Observing the reducing value of TDDI at the critical node for the overall system, it can be seen that the system transitions from being T-limited on TN bus 5

(case 1) to being D-limited on TN bus 5 (case 2-3). Case 1 is on the edge between TN bus 5 and TN bus 9 as the value of the $VSI_{D-3\phi}$ at the critical nodes is similar.

In order to validate the inference drawn from $VSI_{D-3\phi}$ and TDDI, a 30 MVAR reactive power support is provided at bus 5 and 9 of TN and the critical loading is recalculated. The results of the increment in λ_{max} ($\Delta\lambda_{max}$) in percent are summarized in Table 7-5. As providing var support at the critical bus will have more impact on increasing the loadability limit of the system, we can use this as an indicator of the critical bus. It can be seen that for case 1, $\Delta\lambda_{max}$ is similar for TN 5 and TN 9, indicating that they are equally important. For cases 2-3, $\Delta\lambda_{max}$ is much more for var support at TN 5 than TN 9, implying that TN 5 is clearly the critical bus for the TN. These match the conclusions drawn from $VSI_{D-3\phi}$. In contrast, the VSI_T at TN bus 9 is greater than TN bus 5 for all the cases and leading to an incorrect conclusion that TN bus 9 is the critical node for the transmission system.

Table 7-4 $VSI_{D-3\phi}$ and TDDI at the critical DN node at different TN buses

Case	$VSI_{D-3\phi}$ at DN-675 node at		TDDI at DN-675 node at	
	TN 5	TN 9	TN 5	TN 9
1	0.224	0.218	0.636	1.201
2	0.341	0.227	-0.239	1.249
3	0.451	0.227	-0.590	1.312

In order to verify if TDDI can distinguish between T- limited and D-limited systems, new lines between the buses 4-9, 4-5 and 6-7 in the TN are added and the critical loading is recalculated. From the Thevenin equivalent, it can be seen that the more negative the TDDI, the lesser the $\Delta\lambda_{max}$ change due to reducing transmission line impedance, as the impedance in the DN dominates Thevenin equivalent. This is precisely the result observed from the simulations, thus validating the TDDI.

Table 7-5 Increment in critical load for var injection and line addition

Case	% $\Delta\lambda_{max}$ due to		
	Var support at TN 5	Var support at TN 9	Additional TN Lines 4-9, 4-5, 6-7
1	4.95	4.95	18.7
2	11.54	5.13	13.5
3	13.49	6.35	12.6

It is well known that the equivalent impedances change with the operating load and so the TDDI is a function of the load level. To understand the variation of TDDI with loading, TDDI at the critical node is plotted versus load scaling for the various cases in Figure 7-14. It can be observed that the overall profile of the TDDI is fairly flat and so the TDDI calculated at nominal or moderate loading can indicate if the overall system is T-limited or D-limited.

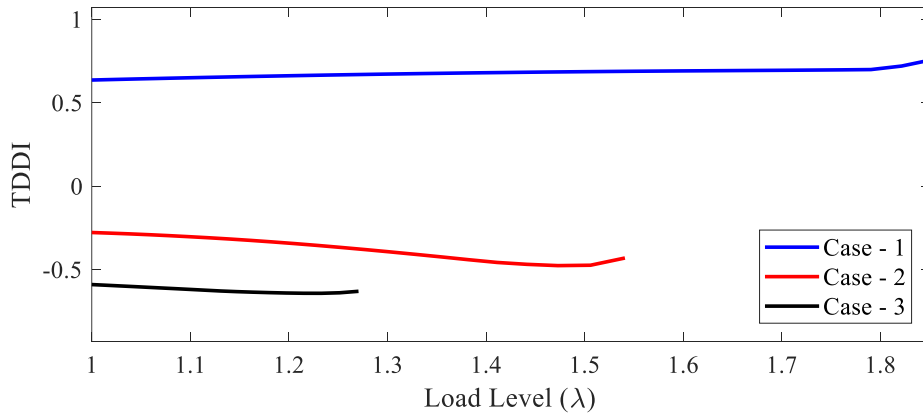


Figure 7.14 TDDI at DN-675 at TN 5 v/s load scaling for various cases

7.5.3 Larger Test Case: 30 bus TN + 37 node DN

For a larger test system, the IEEE 30 bus test system is considered as TN and two different feeders 37A and 37B are considered as DN. DN 37A and 37 B are modified versions of IEEE 37 node test DN (see Appendix for details). The base loading of these feeders is the same while the impedances are varied in a comparable manner to the variation present in the impedance of line configurations present in IEEE distribution test systems [13]. Loads at TN

buses 17, 19, 24, 26 and 30 are replaced with the multiple DNs so that the base load as seen by the transmission system remains the same. The 6 cases are created by changing the type of feeder at the various TN buses as shown in Table 7-6 along with the overall system critical loading. Case 1 is the scenario with only feeder 37A. Each of cases 2-6 is a variation of case 1 with feeders at one TN bus replaced by 37B. It can be seen that λ_{max} for case 1 is 5.44 while cases 2-6 are around 3 which implies replacing DN 37A with DN 37B has a large impact on the system, leading to a hint that cases 2-6 are distribution limited.

Table 7-6 *Feeder configuration at various TN buses and critical load*

Case	TN 17	TN 19	TN 24	TN 26	TN 30	λ_{max}
Case 1	37A	37A	37A	37A	37A	5.44
Case 2	37B	37A	37A	37A	37A	3.1
Case 3	37A	37B	37A	37A	37A	3.4
Case 4	37A	37A	37B	37A	37A	3.1
Case 5	37A	37A	37A	37B	37A	3
Case 6	37A	37A	37A	37A	37B	2.8

Feeder 37A & 37B – impedances are scaled by 0.5 and 1.25 of the original 37-node feeder 0 respectively. The $VSI_{D-3\phi}$, VSI_T & TDDI are calculated for each load level and just like in the previous system, the VSI_T at the critical TN bus is not 1 at the critical load while the $VSI_{D-3\phi}$ is 1. Similar behavior was observed for all cases and this reiterates the need for μ PMUs for accurate voltage stability monitoring. The critical node is estimated for each case from $VSI_{D-3\phi}$ and is found to be node 741, which is the furthest load in the distribution feeder [13]. This is a single phase load and the fact that proposed method identifies this as the critical loads shows the importance of using the 3ϕ extension of the VSI for analyzing distribution systems.

The $VSI_{D-3\phi}$ & TDDI at the critical node (node 741) for each DN at the TN are listed in Table 7-7 and Table 7-8 respectively. The values at the critical node in the overall system for each case is in bold font. It can be seen that the critical TN bus is 19 for case 1 and as the feeder 37B is attached to a TN bus, it forces that particular TN bus to become the critical bus. The TDDI for case 1 is positive, implying that the system in case 1 is T-limited. The value of TDDI is negative for all the cases 2-6 at the nodes with the largest $VSI_{D-3\phi}$ (where feeder 37B is located) and this implies that the DN is the cause of the voltage instability.

Table 7-7 $VSI_{D-3\phi}$ at the critical DN node in feeders at different TN buses

Case	$VSI_{D-3\phi}$ at weakest DN node at				
	TN 17	TN 19	TN 24	TN 26	TN 30
1	0.216	0.260	0.175	0.187	0.232
2	0.416	0.274	0.196	0.198	0.242
3	0.226	0.446	0.187	0.185	0.227
4	0.225	0.268	0.345	0.197	0.240
5	0.221	0.263	0.182	0.393	0.235
6	0.221	0.263	0.182	0.189	0.443

Table 7-8 TDDI at the critical DN node in feeders at different TN buses

Case	TDDI at weakest DN node at				
	TN 17	TN 19	TN 24	TN 26	TN 30
1	1.250	1.336	1.145	0.992	1.228
2	-0.312	1.639	1.337	1.244	1.493

3	1.743	-0.215	1.395	1.426	1.746
4	1.373	1.486	-0.455	1.147	1.374
5	1.419	1.583	1.250	-0.623	1.452
6	1.419	1.583	1.250	1.180	-0.430

In order to validate the inference drawn from the proposed index, 50 MVAR reactive power support is provided at TN buses 17, 19, 24, 26 & 30 and the critical loading is recalculated for each of the cases. The results of the increment in λ_{max} ($\Delta\lambda_{max}$) in percent are summarized in Table 7-9. For case 1, providing var support at TN 17, TN 19 and TN 30 has a small improvement in the critical loading. For cases 2-6, it can be seen that applying the var support at the buses with DN 37B has a large improvement in the critical loading compared to the other buses. These observations imply that the DN 37B is the reason for the system collapse in cases 2-6. Note that there is significant jump in critical loading in case 5 when the var support is at TN 26. In this particular case, the var support relieves the DN completely and the cause of instability shifts from DN to TN.

Table 7-9 *Increment in critical load for var injection at various TN buses*

Case	% $\Delta\lambda_{max}$ due to var support at				
	TN 17	TN 19	TN 24	TN 26	TN 30
1	1.10	2.57	0.00	0.00	1.08
2	12.90	3.23	0.00	0.00	0.00
3	3.57	17.86	0.00	0.00	0.00

4	0.00	0.00	11.76	8.24	0.00
5	0.00	0.00	6.45	75.48	0.00
6	0.00	0.00	0.00	0.67	33.33

These observations match the conclusions drawn from using the $VSI_{D-3\phi}$ and the TDDI, thus validating their behavior. Furthermore, as the $VSI_{D-3\phi}$ and the TDDI are calculated using only phasor measurements, the proposed methods perform the identification in an online manner which can be used to provide better situational awareness of the overall system. Thus, the utility of the proposed methodology will only increase in the measurement rich regime of the future.

7.6 Conclusion

In this paper, the importance of μ PMU measurements to identify regions causing long term voltage instability is established by extending the idea of the Thevenin equivalent to unbalanced 3ϕ circuits. To accomplish this, a 3ϕ long-term voltage stability indicator that can identify critical loads in a system is proposed. The proposed 3ϕ -VSI is proved to be equivalent to the conventional VSI for a balanced system and numerical results are presented that demonstrate its ability to monitor the long term voltage stability for unbalanced systems. In a similar manner, a 3ϕ transmission-distribution distinguishing index, which can distinguish between voltage stability limit due to the transmission network or a distribution network, is proposed for unbalanced networks. The estimation of the 3ϕ Thevenin equivalent is formulated as a convex optimization using PMU & μ PMU measurements, making it possible to calculate VSI and TDDI in a model-free online manner. Numerical simulations are performed using co-simulation between Pypower and GridlabD for the IEEE 9 bus and the 30 bus transmission

networks combined with IEEE 13 node and 37 node distribution networks. These case studies reveal that the VSI calculated from the transmission PMU can lead to the wrong estimation of the critical bus and using distribution μ PMU measurements leads to the correct estimation of the critical region for voltage stability. This proves the need to utilize distribution measurements to correctly estimate the critical region for long term voltage stability. Furthermore, it is shown that the TDDI is able to detect the transmission and distribution limit over a wide range of scenarios, validating the proposed methodology.

The $VSI_{D-3\phi}$ is derived by relating the impedances to the power loss and not from the power flow equations that are the root cause of voltage instability. Thus, relating $VSI_{D-3\phi}$ to the power flow equations would enable tap operations and capacitor switching to be also incorporated into $VSI_{D-3\phi}$ and is a research direction that will be explored in the future. Also, as there is a close relation to voltage stability and reactive support, utilizing the $VSI_{D-3\phi}$ to identify the most effective DERs to inject reactive power only from measurements in order to improve the voltage stability is another venue for further investigation. Finally, a robust optimization formulation for estimating the equivalent circuit is necessary as that the resulting equivalent would be robust to system variation and other sources of noise, making it possible to apply the proposed methods to measurements from the field.

7.7 References

- [1] M. Glavic and T. Van Cutsem, "A short survey of methods for voltage instability detection," Proc. 2011 IEEE PESGM, San Diego, USA, 2011.
- [2] K. Vu, M. Begovic, D. Novosel, and M. Saha, "Use of local measurements to estimate voltage-stability margin," IEEE Trans. Power Syst., vol. 14, no. 3, pp. 1029–1035, Aug. 1999
- [3] A. von Meier, et. al., "Precision Micro-Synchrophasors for Distribution Systems: A Summary of Applications", IEEE Transactions on Smart Grid, , vol. 8, no. 6, pp. 2926-2936, Nov. 2017

- [4] S. Robles, "2012 FIDVR Events Analysis on Valley Distribution Circuits". Prepared for LBNL by Southern California Edison, July 2013
- [5] C. Wang, et. al., "Existence and uniqueness of load-flow solutions in three-phase distribution networks," *IEEE Trans. Power Syst.*, 2016.
- [6] A. M. Kettner and M. Paolone" A Generalized Voltage-Stability Index for Unbalanced Polyphase Power Systems including Thevenin Equivalents and Polynomial Models", <https://arxiv.org/abs/1809.09922>, 2018.
- [7] L. Aolaritei, S. Bolognani and F. Dörfler, "Hierarchical and Distributed Monitoring of Voltage Stability in Distribution Networks", [online] <https://arxiv.org/abs/1710.10544>, 2017.
- [8] A. Bidadfar, H. Hooshyar, M. Monadi and L. Vanfretti, "Decoupled voltage stability assessment of distribution networks using synchrophasors," *Proc. 2016 IEEE PESGM*, Boston, MA, 2016, pp. 1-5.
- [9] A. K. Bharati and V. Ajjarapu, " Investigation of Relevant Distribution System Representation with DG for Voltage Stability Margin Assessment", under review in *IEEE Transactions on Power Systems*, [online] <https://arxiv.org/abs/1903.06002>, 2019.
- [10] A. Singhal and V. Ajjarapu, "Long-term voltage stability assessment of an integrated transmission distribution system," 2017 North American Power Symposium (NAPS), Morgantown, WV, 2017, pp. 1-6.
- [11] A. R. Ramapuram Matavalam, A. Singhal, and V. Ajjarapu, "Identifying Long-Term Voltage Stability Caused by Distribution Systems vs Transmission Systems", *Proc. 2018 IEEE PESGM*, Portland, USA, 2018. Available: <http://arxiv.org/abs/1809.10540>
- [12] A.R. Ramapuram Matavalam and V. Ajjarapu, "Sensitivity based Thevenin Index with Systematic Inclusion of Reactive Power Limits," in *IEEE Trans. on Power Systems*, vol. 33, no. 1, pp. 932-942, Jan. 2018.
- [13] IEEE Distribution System Analysis Subcommittee. Radial Test Feeders[Online].Available: <http://sites.ieee.org/pes-testfeeders/>
- [14] William H. Kersting, "Distribution system modeling and Analysis", CRC. Press, 2012.
- [15] S. Boyd and L. Vandenberghe, "Convex Optimization", Cambridge University Press, 2004.
- [6] CVX Research, Inc. CVX: Matlab software for disciplined convex programming, version 2.0. <http://cvxr.com/cvx> , April 2011.
- [17] Pypower, Available: <https://github.com/rwl/PYPOWER>

- [18] D.P. Chassin, et. al. "GridLAB-D: An agent-based simulation framework for smart grids." *Journal of Applied Mathematics* 2014 (2014).
- [19] Selim Ciraci, et. al. "FNCS: a framework for power system and communication networks co-simulation." *Proc. of the Symposium on Theory of Modeling & Simulation-DEVS Integrative*, 2014.
- [20] A. Singhal and V. Ajjarapu, "A Framework to Utilize DERs' VAR Resources to Support the Grid in an Integrated T-D System", *Proc. IEEE PESGM, USA*, 2018. Available: <https://arxiv.org/abs/1712.07268>
- [21] H. Sun, et. al., "Master-slave-splitting based distributed global power flow method for integrated transmission and distribution analysis," *IEEE Trans. Smart Grid*, vol. 6, no. 3, pp. 1484–1492, May 2015
- [22] Z. Li, Q. Guo, H. Sun, J. Wang, Y. Xu and M. Fan, "A Distributed Transmission-Distribution-Coupled Static Voltage Stability Assessment Method Considering Distributed Generation," in *IEEE Transactions on Power Systems*, vol. 33, no. 3, pp. 2621-2632, May 2018.

CHAPTER 8. GENERAL CONCLUSION

8.1 Overall Conclusions

With the increasing need for economic operation of the power grid, the system is being operated closer to their limits and so there is a need to address the increasing risk of voltage instability in the power grid. In this work, we have proposed methods that can monitor and mitigate the both short-term and long-term voltage instability by utilizing Phasor Measurement Unit measurements in the power grid.

The initial methodology to understand and monitor FIDVR is based on the voltage measurements being made at the transmission substation. The Wasserstein metric is proposed to quantify the FIDVR phenomenon in real time while ensuring that it calculated at the PMU is robust and reliable. To determine the control, just utilizing the voltage did not provide sufficient information as several varying parameters of the load can lead to similar voltages. To overcome this, the composite load model is studied in detail and is simplified based on engineering judgment and it is shown that an admittance approach is well suited for this purpose. Analytical relations were derived by approximations of expressions and the time to recovery in terms of the measured admittance is derived. This is verified on PSSE simulations and the error between the expected times and the measured times to recovery were less than 1 second. The only control schemes that can mitigate FIDVR are shown to be the tripping of Air Conditioners or the injection of reactive power via Shunt devices. An analytical expression for the magnitude of control action as a function of trip time is derived and is tested in PSSE with accuracy of 1 second with control actions upto 30% Air conditioner tripping, providing a use case for the utilities to implement smart thermostats.

Next, a methodology to monitor and mitigate the phenomenon of FIDVR in the distribution networks is proposed using μ PMU measurements. The expressions for recovery time are derived by simplifying the composite load model during FIDVR. A linearization of the non-linear expressions is then done to estimate the change in recovery time under various control schemes and a linear optimization problem is formulated to estimate the minimal control action necessary to recover faster. Further, the simplified load model is used to quickly estimate the linear trajectory sensitivities to ensure that the voltage recovery satisfies voltage ride through criteria of DERs. The optimal control actions calculated by using the linear sensitivities are quickly ($<0.5s$) able to identify the critical regions for control for both recovery time improvement and adherence to VRT requirements of DERs. We demonstrate that optimal control reduces the amount of load control significantly and by incorporating Q-injection by DERs into the optimization, the load control is further reduced ($>35\%$). Thus, the proposed methodology enables online monitoring and mitigation of FIDVR by utilizing Q-injection from DERs with minimal load disconnection making it a promising application of μ PMU measurements to enhance operation of the distribution systems.

Next, to handle the dynamics of non-linear 3-phase induction motors which can lead to voltage instability, a linear operator theoretic approach is proposed that estimates a surrogate linear dynamical model of the non-linear IM. This is a data-driven approach that uses simulated data from the full non-linear IM and lifts the system into a functional space in which the trajectories of the simulated data follow a linear relation. The functional space is chosen so that the dynamic states and the outputs of the original system can be recovered from the lifted space in a linear manner. The proposed method is validated on a detailed induction motor model using Gaussian radial basis functions for lifting. The data-driven linear model is able to

capture non-linear behavior of the induction motor such as stalling at low voltages and nominal operation for high voltages. This implies that the techniques from linear systems can be used to perform state estimation and reconstruction in an online manner from output admittance measurements at the PMU, enabling stability monitoring for the non-linear model without model approximations as is usually done in literature. The proposed method can also be used to estimate the fraction of 1-phase motor stalling from PMU measurements of the admittance due to its linear nature making it the first time these two kinds of motors can be monitored at the same time.

Next, a Sensitivity based Thevenin Index (STI) which uses PMU/WAMS data and (linear) state estimator data to monitor long term voltage stability is proposed. The STI addresses the following challenges associated with conventional Thevenin-based indices – (a) Robust calculation of the stability index; (b) Verification of the local index by the system operator & (c) Accounting for generator reactive limits on the index. The ability of the STI to validate the local Thevenin index safeguards the operator against spurious and malicious data and makes this a useful property, especially with the current emphasis on cyber security. The generator reactive limits can be taken into account by modifying the Jacobian to anticipate the PV-PQ bus switching facilitating the operators with better situational awareness of the grid. The speed of the STI calculation make it a promising method to be implemented in the control center for operations. These claims are verified with examples using various standard IEEE test systems and the results confirm the proposed methodology. Thus, the Sensitivity based Thevenin Index provides the operator with better situational awareness even under the presence of noisy/malicious data.

Finally, the importance of μ PMU measurements to identify regions causing long term voltage instability is established by extending the idea of the Thevenin equivalent to unbalanced 3ϕ circuits. To accomplish this, a 3ϕ long-term voltage stability indicator that can identify critical loads in a system is proposed. The proposed 3ϕ -VSI is proved to be equivalent to the conventional VSI for a balanced system and numerical results are presented that demonstrate its ability to monitor the long term voltage stability for unbalanced systems. The estimation of the 3ϕ Thevenin equivalent is formulated as a convex optimization using PMU & μ PMU measurements, making it possible to calculate VSI in a model-free online manner. Numerical simulations are performed using co-simulation between Pypower and GridlabD for the IEEE 9 bus and the 30 bus transmission networks combined with IEEE 13 node and 37 node distribution networks. These case studies reveal that the VSI calculated from the transmission PMU can lead to the wrong estimation of the critical bus and using distribution μ PMU measurements leads to the correct estimation of the critical region for voltage stability. This proves the need to utilize distribution measurements to correctly estimate the critical region for long term voltage stability.

8.2 Overall Contributions

The overall contributions of the thesis are summarized below:

- In case of the FIDVR phenomenon, traditional methods have utilized the variation of the voltage and current phasors to quantify and mitigate FIDVR in an online manner. But these methods assume a simplified load model and do not utilize the composite load model dynamics. They are also prone to errors from the oscillations in the voltage time-series that occur due to other dynamics in the system such as generator exciter, etc. We have addressed both these drawbacks by proposing to use the load admittance

as the monitoring variable at the PMU and demonstrated its behavior on the IEEE 162 bus system. The load admittance provides the PMU at the substation with a reasonable estimate of the proportion of the load that is stalled and this information can be used to estimate the time to recovery and the proportion of the air conditioners to disconnect for recovering within a set amount of time. To test the real-time nature of the method, the FIDVR phenomenon is simulated in a real-time test-bed and the proposed method is able to mitigate FIDVR in an online manner.

- The phenomenon of FIDVR in the distribution system is studied and the various factors that cause this phenomenon are analyzed. This analysis leads to the admittance based load model that enables online estimation of the FIDVR trajectory in the distribution system and the online estimation of the trajectory sensitivities of the FIDVR to various control schemes. These trajectory sensitivities are used in a linear formulation to derive control actions for a recovery voltage satisfying the fault ride through criteria and prevent DER disconnection due to fault voltage ride through. The reactive support from DERs is also used to minimize load control and demonstrate the utility of reactive support during dynamic events.
- To handle the dynamics of non-linear 3-phase induction motors which can lead to voltage instability, a linear operator theoretic approach is proposed that estimates a surrogate linear dynamical model of the non-linear IM. This is a data-driven approach that uses simulated data from the full non-linear IM and lifts the system into a functional space in which the trajectories of the simulated data follow a linear relation. The proposed method can estimate the fraction of 1- ϕ IM stalled from measurements making it the first time the two kinds of motors can be monitored at the same time.

- In case of the long term voltage stability phenomenon, existing methods utilize the Thevenin index for large systems but the theory is only valid for the simple two-bus system. This lack of theoretical basis for utilizing the Thevenin index is the reason why the existing local index methods cannot be validated at the control center leading to a cyber-security concern. To improve the understanding of the Thevenin index, we have derived an analytical relation between the local index and the system Jacobian, and thus we provided a mathematical justification for the use of the local index as an indicator for global stability.
- The significance of the relation between the local index and the system Jacobian can be understood by the inclusion of the what-if scenarios (reactive limit reached, line outage, etc.) into the index calculation process. This enables the operator to assess the true state of the system with the ability to predict the Limit Induced Bifurcation which is not the case using present indices.
- Furthermore, the importance of distribution networks on measurement based voltage stability assessment is established and a methodology to utilize phasor measurements from the distribution network for voltage stability assessment is described. A 3 ϕ long-term voltage stability indicator using the idea of a 3 ϕ Thevenin equivalent that can identify critical loads in an unbalanced multi-phase system is proposed. The estimation of the 3 ϕ Thevenin equivalent is formulated as a convex optimization using PMU & μ PMU measurements, making it possible to calculate VSI in a model-free online manner, enabling the accurate long term voltage stability monitoring of the overall system.

8.2 Possible Extensions of Work

- **Wide area method to recover from FIDVR:** At present the topology of the network is not being used and the disconnection of ACs is being done locally. However, a wide area methodology is better as a certain location might be the main cause of the FIDVR. Thus, a wide area method to assess the time to recovery and control actions based on the topology of the load area is a possible future direction. Also, utilizing DVARs from Distributed Generation devices to recover faster from FIDVR needs to be investigated using this approach.
- **Data driven techniques for speeding up simulations:** The linear data-driven model is much easier to simulate numerically than the non-linear model and can be used to speed up dynamic simulations for use in stability assessment.
- **Control schemes to improve long term voltage stability:** The proposed sensitivity based Thevenin index can be used for determining the control scheme to improve the long term voltage stability by clustering loads based on the index to understand which nodes are contributing to instability. Then either the voltage of the generators closest to them is increased or more power is re-dispatched from these generators.
- The proposed sensitivity based Thevenin index can be extended to provide an indicator for Limit Induced Bifurcation also. Furthermore, incorporating the impact of line outage and other component outages into the proposed index will enable the operator to have an indicator to the true critical point.
- In the future, the coordination of these methods with the emerging field of the control of distributed energy resources in the sub-transmission system will provide the operator with even more flexibility to steer the system to respond quickly to large disturbances

and ensure that the system remains stable even for stressed scenarios and this will be demonstrated.

8.4 Publications

8.4.1 Journals

[J1] A. Ramapuram-Matavalam; V. Ajjarapu, "Sensitivity based Thevenin Index with Systematic Inclusion of Reactive Power Limits," in *IEEE Transactions on Power Systems*, vol. 33, no. 1, pp. 932-942, Jan. 2018.

[J2] A. Ramapuram-Matavalam; V. Ajjarapu, "PMU based Monitoring and Mitigation of Delayed Voltage Recovery using Admittances," accepted for publication in *IEEE Transactions on Power Systems*

[J3] A. Ramapuram-Matavalam, A. Singhal; V. Ajjarapu, "Monitoring Long Term Voltage Instability due to Distribution & Transmission Interaction Using μ PMU & PMU Measurements," accepted for publication in *IEEE Transactions on Smart Grids*

8.4.2 Conferences

[C1] A. R. R. Matavalam, A. Singhal and V. Ajjarapu, "Identifying Long Term Voltage Stability Caused by Distribution Systems vs Transmission Systems", in *IEEE PES General Meeting*, 2018, vol., no., pp.1-5, Aug 2018.

[C2] A. R. R. Matavalam and A. K. Bharati, "Reliability Assessment of Industrial Circuit Breakers with Design Enhancements", in *International Conference on Probabilistic Methods Applied to Power Systems*, 2018, vol., no., pp.1-5, July 2018.

[C3] A. R. R. Matavalam and V. Ajjarapu, "Validation of the Sensitivity based Thevenin Index on Large Systems," *2017 IEEE Power & Energy Society General Meeting*, Chicago, IL, 2017

[C4] A. R. R. Matavalam and V. Ajjarapu, "Implementation of user defined models in a real-time cyber physical test-bed," *2016 National Power Systems Conference (NPSC)*, 2016,

[C5] A. Reddy and V. Ajjarapu, "PMU based real-time monitoring for delayed voltage response," *2015 North American Power Symposium (NAPS)*, Charlotte, NC, 2015, pp. 1-6.

[C6] A. R. R. Matavalam and V. Ajjarapu, "Calculating the long term voltage stability margin using a linear index," *2015 IEEE Power & Energy Society General Meeting*, Denver, CO, 2015, pp. 1-5.

[C7] A. Reddy, K. Ekmen, V. Ajjarapu and U. Vaidya, "PMU based real-time short term voltage stability monitoring — Analysis and implementation on a real-time test bed," *2014 North American Power Symposium (NAPS)*, Pullman, WA, 2014, pp. 1-6.

[C8] A. R. R. Matavalam and V. Ajjarapu, "Long term voltage stability thevenin index using voltage locus method," *2014 IEEE PES General Meeting / Conference & Exposition*, National Harbor, MD, 2014, pp. 1-5.

APPENDIX A. WASSERSTEIN METRIC BASED QUANTIFICATION OF FIDVR

The Wasserstein metric, also called as the earth movers distance, can be understood as the minimal amount of work done to transform a shape of a probability density function, PDF_1 into another probability density function, PDF_2 . This can be formalized as the following linear programming problem.

Let $P = \{(p_1, w_{p1}), \dots, (p_n, w_{pn})\}$ be the first PDF signature with the probability given by w_{pi} for the p_i th bin. Similarly let $Q = \{(q_1, w_{q1}), \dots, (q_n, w_{qn})\}$ be the second PDF signature with the probability given by w_{qi} for the q_i th bin. Finally, let $D = [d_{ij}]$ be the ground distance matrix where d_{ij} is the distance between clusters p_i and q_j and f_{ij} the flow between p_i and q_j . The work necessary to transform P to Q is given by $\sum_{i=1}^n \sum_{j=1}^n f_{ij} \cdot d_{ij}$. The formulation of the optimization problem to calculate the minimum work is given as:

$$\min \sum_{i=1}^n \sum_{j=1}^n f_{ij} \cdot d_{ij} \quad (A-1)$$

Subject to:

$$f_{ij} \geq 0 \quad 1 \leq i, j \leq n$$

$$\sum_{j=1}^n f_{ij} \leq w_{pi} \quad 1 \leq i \leq n$$

$$\sum_{i=1}^n f_{ij} \leq w_{qj} \quad 1 \leq j \leq n$$

$$\sum_{i=1}^n \sum_{j=1}^n f_{ij} = 1$$

Once the optimization problem is solved and the optimal f_{ij} is known, the final Wasserstein's distance is given by $\sum_{i=1}^n \sum_{j=1}^n f_{ij} \cdot d_{ij}$. This is a linear program and can be

solved efficiently, but it is preferred to determine this distance in a more direct manner for real-time applications. In the special case of the 1-Dimensional PDF functions that we are interested in, the above optimization can be simplified using cumulative probability functions. Suppose, $F_{1,i}$ and $F_{2,i}$ is the value of the cumulative probability functions of PDF_1 & PDF_2 in bin i respectively. Then the distance is given by the expression in equation (A-2) for W-index.

$$W - index = \sum_{i=1}^n |F_{1,i} - F_{2,i}| \quad (A-2)$$

Comparing the formulations of the KL divergence and the W-index in equations (3-2) & (A-2), the following observations can be made.

1. The W-index is symmetric as the absolute function is symmetric. The KL index is not symmetric and so is harder to intuitively interpret.
2. The W-index is incrementally linear, i.e. a small variation in the inputs causes a comparable change in the output value as the absolute function is incrementally linear. This is not the case for the KL divergence due to the logarithm function and the division. A small variation in the inputs can cause an unbounded change in the KL divergence. This property ensures that the W-index is a continuous function with no sudden changes.
3. The W-index is bounded. This is because the cumulative probability functions always lie between 0 and 1, the distance between them can be a maximum of 2. The KL divergence is not bounded again due to the logarithm function. The bounded nature is particularly useful in case of implementation where large results can lead to overflow problems.

To verify that the W-index can indeed be more appropriate in quantifying FIDVR from the voltage waveforms, Figure A.1 plots the voltage waveforms of the increasing percentages of 1-phase induction motor. The reference voltage waveform is exponentially rising and is the smooth red line in Figure A.1.

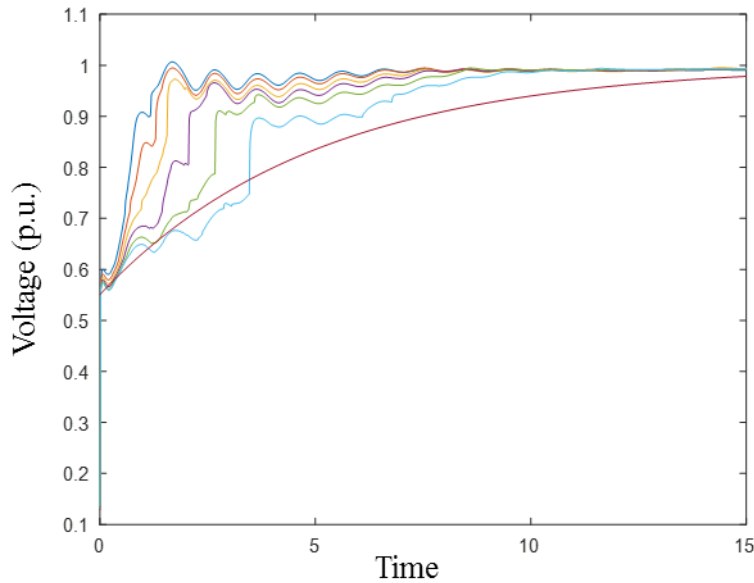


Figure A.1 *The voltage at the bus with increasing percentage of IM load along with the reference voltage waveform.*

The Wasserstein metric based Index of the FIDVR waveforms is shown in Figure A.2. It can be seen that the oscillations present in the voltage waveform are not present in the W-index plots. Also, voltages with the least FIDVR have the most negative value of the W-index while the voltages with the FIDVR violating the reference waveform have a W-index that goes to 0 quickly and also becomes positive in more severe cases.

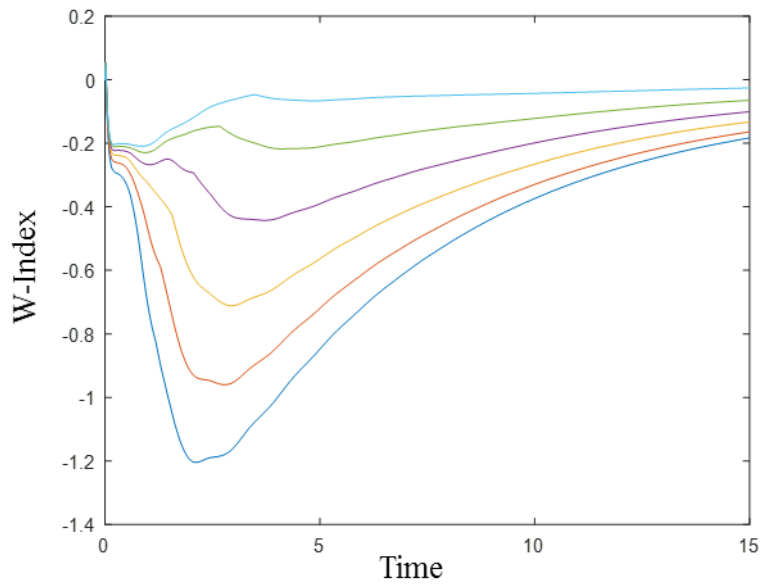


Figure A.2 *The Wasserstein metric based Index of the FIDVR waveforms. The more severe the FIDVR, the faster the index reaches 0.*

The W-index can differentiate between the waveforms almost from the start and its smoothness property can be used to reduce the moving time window to improve the computation speed and reduce the memory requirements. Figure A.3 plots the W-Index of the FIDVR waveforms using a moving time windows of 3s. Comparing Figure A.2 and Figure A.3, it can be seen that the essential information of the deviation from the reference is captured with minimal changes to the W-index waveform. Thus, the Wasserstein metric based Index of the FIDVR voltage can indeed detect and differentiate the various amounts of the FIDVR phenomenon. From a control perspective, the closer the W-index is to zero, the more the severity and a more aggressive control strategy is necessary. However, from this approach the amount of load to trip (control) cannot be determined directly as the voltage waveforms during FIDVR are determined by several parameters such as distance to closest generator, generator exciter parameters, topology of the transmission system, behavior of loads in the neighboring

buses, etc. To overcome this drawback, it is necessary to understand the load model that is demonstrating the FIDVR phenomenon.

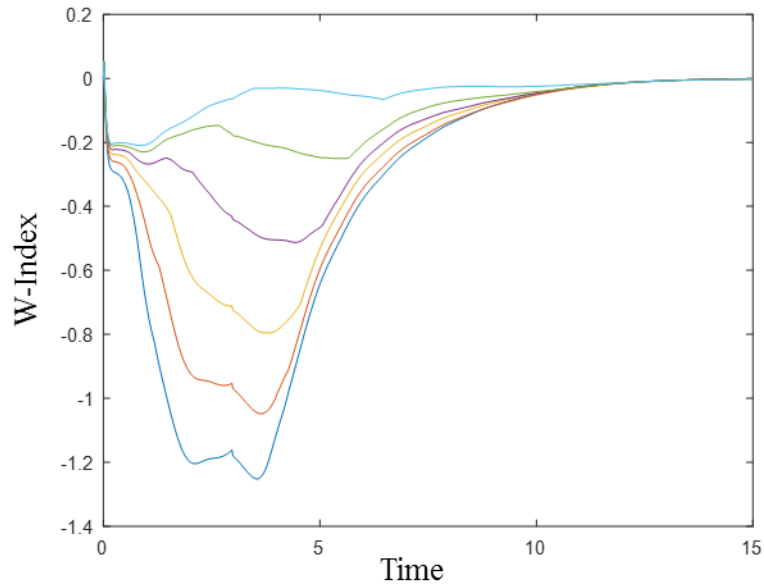


Figure A.3 *The Wasserstein metric based Index of the FIDVR waveforms using a moving time windows of 3s.*

APPENDIX B. COMPARISON OF POWER BETWEEN VARIOUS MOTORS DURING FIDVR

Consider an example CMLD load of 20 MW and 13 MVAR with $F_{mA} = 20\%$, $F_{mB} = 20\%$, $F_{mC} = 10\%$, $F_{mD} = 25\%$. The power demand of each of the components before and after fault (during FIDVR) is listed in Table B-1. The power demanded by the Motor-D significantly rises during FIDVR and dominates the behavior of the load during this phenomenon.

Table B-1 *Power distribution between the various components of the composite load model before and after the fault*

Type	Power Before Fault	Power After Fault (V=0.7) and UV relaying
Motor-A	4 MW + 3 MVAR	2 MW + 1.4 MVAR
Motor-B	4 MW + 3.3 MVAR	1.3 MW + 0.7 MVAR
Motor-C	2 MW + 1.7 MVAR	1 MW + 0.5 MVAR
Motor-D	5 MW + 2.3 MVAR	25 MW + 25 MVAR
Static Load	5 MW + 2.5 MVAR	4 MW + 2 MVAR

APPENDIX C. COMPOSITE LOAD MODEL PARAMETERS

The parameters of the CMLD model used for the results are listed below.

Table C-1 *Parameters of the CMLD model for the simulation results in Section 3.5*

Description	Value	Description	Value	Description	Value	Description	Value
Load MVA Base	100	Q2e	2	Ttr1B	999	CompPF	0.97
Substation shunt	0	Q2c	0	Ftr1B	0	Vstall	0.5
Rfdr	0	Qfrq	0	Vrc1B	999	Rstall	0.19
Xfdr	5.00E-02	MtypA	3	Trc1B	999	Xstall	0.19
Fb	0	LFmA	0.8	Vtr2B	9999	Lfadj	0
Xxf	0.1	RaA	0.035	Ttr2B	9999	Kp1	0
Tfixhs	1	LsA	2.894	Ftr2B	0	Np1	1
Tfixls	1	LpA	0.248	Vrc2B	9999	Kq1	6
LTC	0	LppA	0.248	Trc2B	9999	Nq1	2
Tmin	0.9	TpoA	0.1637	MtypC	3	Kp2	12
Tmax	1.1	TppoA	0.1637	LFmC	0	Np2	3.2
Step	6.30E-03	HA	1.5	RaC	-1	Kq2	11
Vmin	1.02	etrqA	1	LsC	-1	Nq2	2.5
Vmax	1.04	Vtr1A	0	LpC	-1	Vbrk	0.86
TD	30	Ttr1A	999	LppC	-1	Frst	0
TC	5	Ftr1A	0	TpoC	-1	Vrst	0.95
Rcmp	1.00E-02	Vrc1A	999	TppoC	-1	CmpKpf	1
Xcmp	0.11	Trc1A	999	HC	-1	CmpKqf	-3.3
FmA	0.15	Vtr2A	9999	etrqC	-1	Vc1off	0.5
FmB	0.15	Ttr2A	9999	Vtr1C	-1	Vc2off	0.4
FmC	0	Ftr2A	0	Ttr1C	-1	Vc1on	0.6
FmD	0.25	Vrc2A	9999	Ftr1C	-1	Vc2on	0.5
Fel	0.05	Trc2A	9999	Vrc1C	-1	Tth	20
Pfel	0.95	MtypB	3	Trc1C	-1	Th1t	0.9
Vd1	0	LFmB	0.8	Vtr2C	-1	Th2t	1.5
Vd2	0	RaB	0.035	Ttr2C	-1	Fuvr	0
PFs	0.9798	LsB	2.894	Ftr2C	-1	UVtr1	0.8
P1e	1	LpB	0.248	Vrc2C	-1	Ttr1	0.2
P1c	1	LppB	0.248	Trc2C	-1	UVtr2	0.9
P2e	2	TpoB	0.1637	Tstall	0.033	Ttr2	5
P2c	0	TppoB	0.1637	Trestart	30		
Pfrq	0	HB	0.11	Tv	0.02		
Q1e	1	etrqB	1	Tf	0.05		
Q1c	0	Vtr1B	0	CompLF	1		

APPENDIX D. REAL-TIME TEST-BED RESULTS

In order to make sure that the entire setup works as expected and to validate the results from the test-bed, the WECC 9 Bus system is simulated and the voltage waveform corresponding to the fault at Bus 5 for 0.05 sec (3 cycles) are compared between PSSE, RTDS, PMU and Matlab and shown below in Fig. 2.

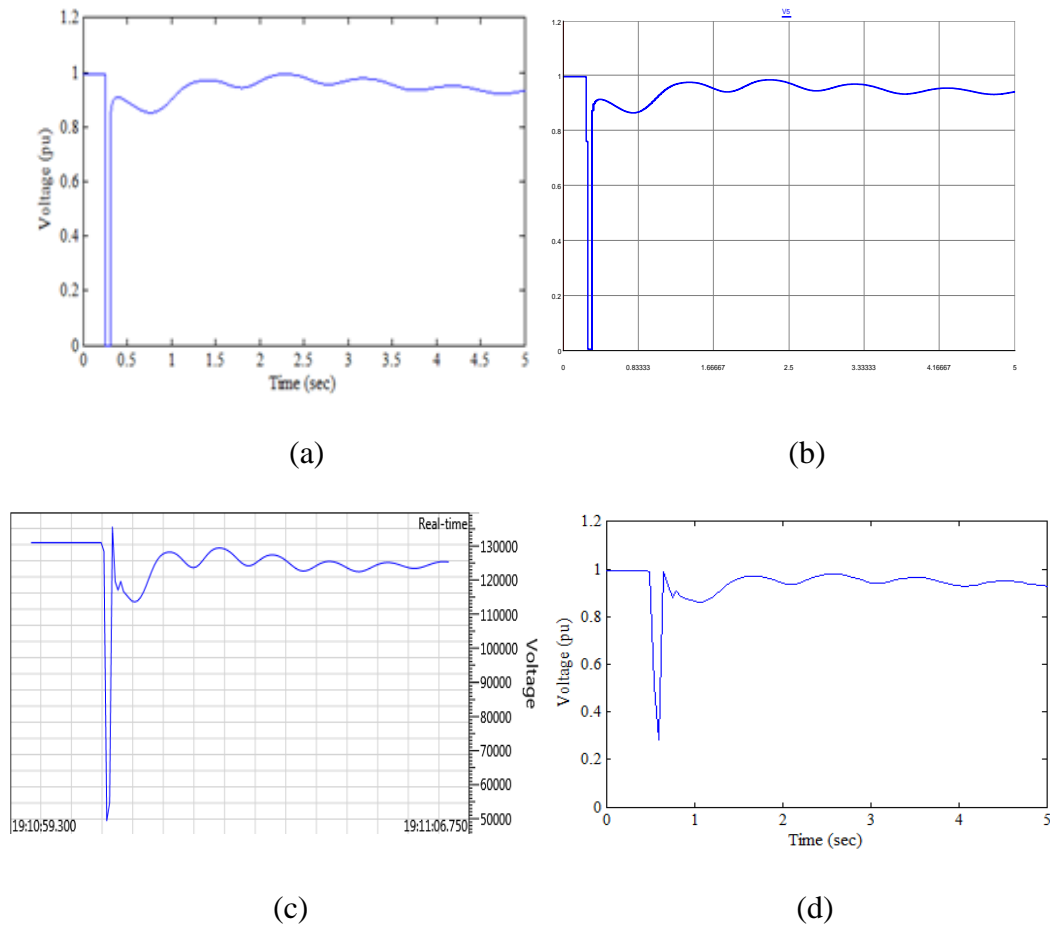


Figure D.1 Comparison between the voltage at Bus 5 in (a) PSSE, (b) RTDS, (c) PMU and (d) Matlab.

It can be observed that the all the voltage waveforms agree very well with one another, confirming that all the components in the setup are properly configured. The difference between the RTDS and the PMU voltage is that it does not go to zero during the fault and also

has a voltage spike when the fault is cleared. This is due to the analog electronics present in the PMU that do not allow sudden changes in the voltage input to the internal Digital to Analog converter. Another difference is that the sharp voltage spikes present in the PMU data after the fault is cleared are reduced in the Matlab data. This is due to the filtering done in the PDC to filter out high frequency noise. Thus, the setup seems to perform as expected

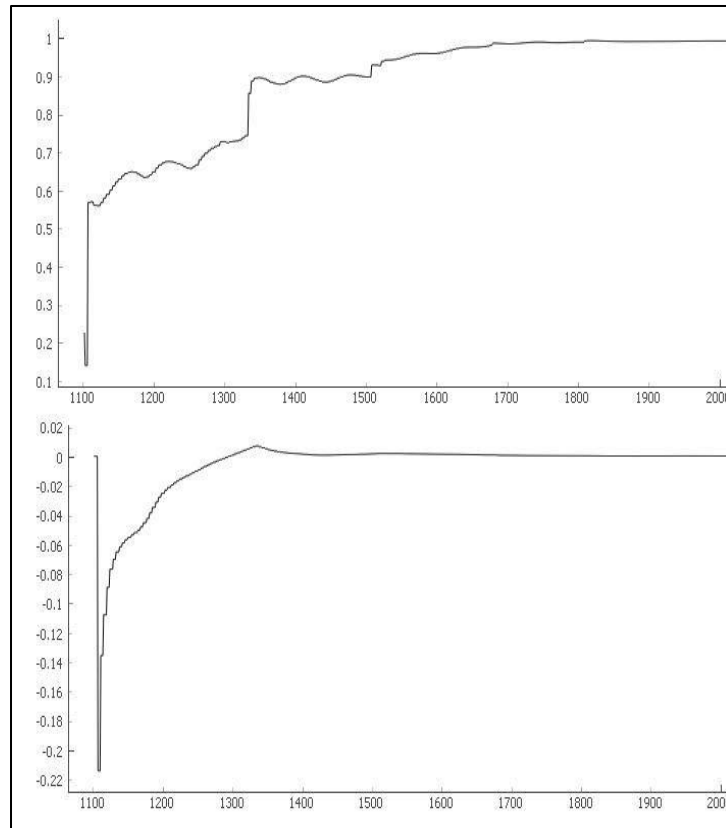


Figure D.2 *Delayed voltage response (top) and the corresponding W-index (bottom) vs the time in samples (60 samples per sec).*

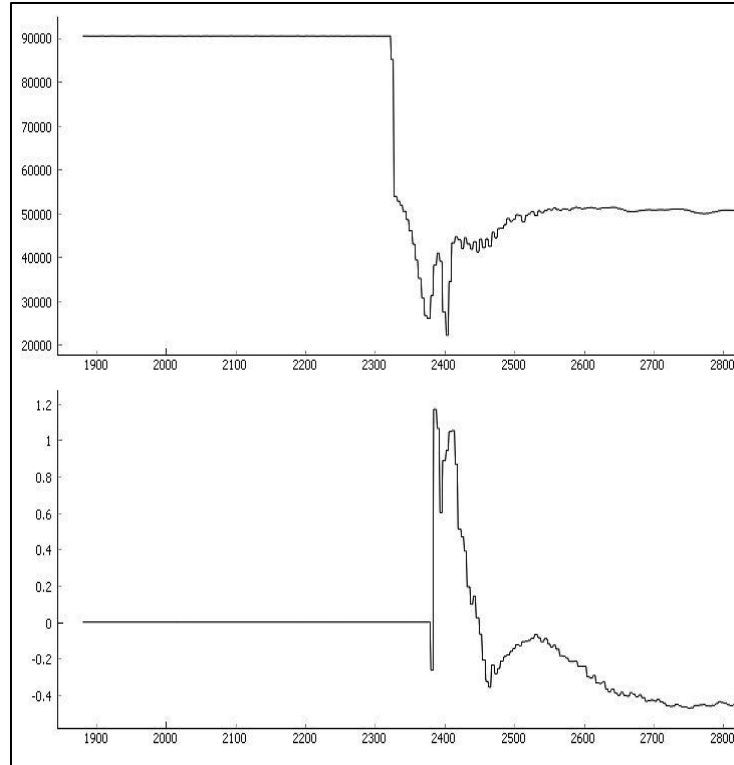


Figure D.3 *Voltage instability event (top) and the corresponding Lyapunov Exponent (bottom) vs the time in sample (60 samples per sec).*